Improvement in Orientation Predictions of High-Aspect Ratio Particles in Injection Mold Filling Simulations

Syed Makhmoor Mazahir

Dissertation submitted to the faculty of the Virginia Polytechnic Institute and State University in partial fulfillment of the requirements for the degree of

Doctor of Philosophy
In
Chemical Engineering

Donald G. Baird, Chair
Peter Wapperom, Co-Chair
Stephen Michael Martin
Eugene G. Joseph

Jan 30, 2013
Blacksburg, VA

Keywords: Fiber Orientation, Center-Gated Disk, Injection Molding, Fountain Flow, Advancing Front, Radial Evolution, Coupled Flow, Finite Element Analysis, Interface Methods, Folgar-Tucker Model, Bead-Rod Model

Improvement in Orientation Predictions of High-Aspect Ratio Particles in Injection Mold Filling Simulations

Syed Makhmoor Mazahir

ABSTRACT

Glass fiber based polymer composites based injection molded parts provide a light-weight high-strength alternative for use in automobile applications. The mechanical properties of these composities are dependent on the orientation of fibers and one of the major challenges in processing of these composites is to control the fiber orientation in the final product.

The evolution of short glass fiber orientation in a center-gated disk was experimentally determined along the radial direction at three different heights representative of the shell, transition and core layers, respectively. Orientation data along the shell and transition layers in the lubrication region show shear flow effects, which tends to align the fibers along the flow direction. In the core layer, where the extension in the θ-direction dominates, fibers tend to get aligned along the θ-direction. In the frontal flow region orientation in the flow direction drops in all three layers due to fountain flow effects.

Fiber orientation predictions in coupled and decoupled transient simulations using the Folgar-Tucker model, and the two slow versions of the Folgar-Tucker model, namely the slip Folgar-Tucker model and the reduced strain closure (RSC) model were compared with the experimental data. Measured inlet orientation was used in all simulations and model parameters were determined by fitting model predictions to rheological data under startup of shear. Pseudo-concentration method was implemented for the modeling of the advancing front and fountain flow effects in the region near the front. Discontinuous Galerkin finite element method and a third order Runge-Kutta total variance diminishing time integration scheme were implemented for the solution of the orientation and transport equations. In the lubrication region of the shell layer, all three orientation models provided a good match with the experimental data. In the frontal region, fountain flow simulations showed characteristic features seen in r- and z-profiles of orientation, although the experimental data showed these features at a relatively larger distance behind the front while the simulations predicted these effects only upto a small distance behind the front. On the other hand, orientation predictions with the Hele-Shaw flow approximation showed significant over-predictions in the frontal region. With model parameters determined from fitting to rheological data,

coupling did not show any significant improvements. However, with the use of a smaller value of the fiber interaction parameter, coupling showed significant improvement in orientation predictions in all three layers in the frontal region.

The simulation scheme was extended to long fiber systems by comparing available long fiber orientation data in a center-gated disk with model predictions using the Bead-Rod model which considers fiber bending, a property exhibited by long semi-flexible fibers. The Bead-Rod model showed improvements over rigid fiber models in the lubrication region of the shell layer. However, close to the front, both models showed similar predictions. In fountain flow simulations, the flow features seen in the *r*- and *z*-profiles were much better predicted with both the models while Hele-Shaw flow approximation showed over-prediction of orientation in the flow direction, especially in the shell layer.

Acknowledgements

I would like to express my sincere gratitude to my advisors, Drs. Donald G. Baird and Peter Wapperom for their guidance, support and encouragement throughout my PhD project. I would like to especially thank my primary advisor Dr. Donald Baird, who has been a great advisor and mentor, for giving me the direction of research, and for his invaluable advice which helped me develop confidence in my work. I would also like to offer special thanks to my co-advisor, Dr. Peter Wapperom for his continuous involvement and for his insightful suggestions that helped me find solutions to problems I faced in my research. I look upto my advisors for their extensive knowledge and sharp intellect and without whose continuous support, this work would not have been possible. I would like to thank my committee members, Dr. Eugene Joseph and Dr. Stephen Martin for their help and encouragement during this work. Their thought provoking discussions and feedback on my work have been very helpful in improving the quality of my work.

I am grateful to the Institute for Critical Technology and Applied Science (ICTAS) for awarding me the doctoral scholar fellowship to conduct my research without having to worry about financial considerations. The four year fellowship program allowed me to focus my efforts in the right direction and work on some of the novel ideas in my project. I would like to especially thank Dr. Roop Mahajan for initiating this program and for promoting an environment where graduate students are encouraged to work on innovative ideas.

I am thankful to my coworker Gregorio M. Vélez-García, with whom I spent numerous hours discussing various ideas, for helping me understand various concepts in the beginning and for always being there whenever I needed help in my research, professionally and personally. I would also like to thank my past and present coworkers, Dr. Jianhua Huang, Dr. Chris McGrady, Dr. Myoungbae Lee, Neeraj Agarwal, Dr. Michael Heinzer, Dr. Kevin Ortman, Dr. Chen Chen, Kevin Meyer, John Hoffman, John Quigley, Kevin Herrington, Mark Celinski, Rebecca Mink, Chen Qian and Hongyu for their help and the good times we shared.

The financial support for this work from the National Science Foundation and the Department of Energy through grant No. DMI-0521918 and National Science Foundation through grant No. CMMI-0853537 is gratefully acknowledged.

I would like to take this opportunity to thank my late father, Syed Mazahir Ali, my mother, Najma Mazahir, and my brother, Syed Peman Mazahir for their unconditional love and invaluable prayers throughout my life. I am indebted to my wife, Deena Khan, for her love and support in my professional and personal life and for making my stay at Blacksburg wonderful and enjoyable with our two children,

Sarah and Ameen. I offer my sincere gratitude to my father-in-law, Dr. Abdul Qayyum Khan and my mother-in-law, Shehla Khan, who have been very helpful and supportive of me. I am also thankful to my sister-in-laws, Tila Khan, Yusra Khan and Amra Khan, and brother-in-laws, Mohammed Rabius Sunny, Hussain and Taha for their love and affection. In the end, I hope I will be able to return the favors all my family and friends have done to me.

Syed Makhmoor Mazahir

Blacksburg, February 2013

Format of Dissertation

This work has been done as part of the PhD program at the Department of Chemical engineering, Virginia Polytechnic Institute and State University, Blacksburg, Virginia, United States. This dissertation is written in journal format. Chapters 3, 4, and 5 are self-contained papers that are in the process of submission for publication. Each paper separately describes the experiments, models, numerical methods, and results. With the exception of Chapter 1 and 2, the figures are presented at the end of each chapter.

Original contributions

The following are considered to be significant original contributions of this work:

- Assessment of slow orientation models along the radial direction in the lubrication region in a center-gated disk using Hele-Shaw flow approximation by comparing model predictions with the experimental fiber orientation data in a center-gated disk at three different heights representative of the shell, transition and core layers, respectively.

- Fitting model parameters to available rheological data under startup of shear and using these model parameters in coupled and decoupled simulations for orientation predictions along the flow direction in a center-gated disk

- Experimental measurement of fiber orientation in the frontal region of a center-gated disk, spanning a region from 90% of fill length to 99% of fill length along the radial direction at three different heights.

- Implementation of an explicit third order explicit total variance diminishing time integration scheme for the solution of hyperbolic equations that appear in the solution of the pseudo-concentration variable and the orientation tensors.

- Use of the pseudo-concentration method for orientation predictions in long fiber systems using the Bead-Rod model. With the use of the pseudo-concentration method, fountain flow was predicted which improved orientation predictions in the frontal region of a center-gated disk.

Table of Contents

List of Figures

CHAPTER 1. INTRODUCTION

Polymer composites containing high aspect ratio particles as reinforcing phase provide an attractive alternative to other industrial materials used in the automotive industry. These light-weight and high-strength materials provide greatly enhanced mechanical properties as compared to pure polymers. Among various reinforcing materials, glass fibers are one of the popular and low-cost materials being used in polymer composites. Glass fibers can be classified into two categories, short and long, based on their length. Short glass fibers (SGF) have an average length less than 1 mm and are considered rigid. Long glass fibers (LGF) have an average length more than 1 mm and are considered flexible or semi-flexible. The enhancement achieved in the mechanical properties of glass fiber / polymer composites highly depends on the orientation of these fibers and the microstructure developed inside the final solidified part during processing. Therefore, one of the major challenges in processing of these composite materials is to control the fiber orientation in the final product. In order to optimize industrial processing, mold design, and the desired properties of the final part, correct prediction and control of fiber orientation during processing becomes necessary. This motivates us to assess and improve the current models and methods used in the prediction of fiber orientation by implementation in a simulation program and validation of simulation results with experimental data.

Various models have been proposed to predict fiber orientation in fiber/polymer suspensions []. However, the available models make use of various simplifying assumptions in the prediction of fiber orientation. The model most commonly used for prediction of fiber orientation is the Folgar Tucker (F-T) model [2]. The model is based on earlier theories for suspensions with dilute fiber concentrations while most of the industrial composites lie in the concentrated regime of fiber concentration [2]. Fiber orientation predictions with the F-T model in complex flows are qualitatively good [4-11] . However, the model predicts a rapid evolution of fiber orientation to final steady state values while experimental observations of fiber orientation in simple flows suggest slow evolution kinetics. There have been improvements proposed to the original F-T model in order to slow down the kinetics of fiber orientation as observed experimentally [12-14]. The improved models either keep the model objective [14] or make it non-objective [12, 13]. The model parameters appearing in these models are empirical in nature and need to be determined accurately for predictions to match with the experimental values. However, there is no established standard method to determine these parameters. Recently, there have been attempts to

determine these parameters from simple flow experiments by fitting the parameters to stress and orientation curves [13-15].

One of the characteristic features in mold filling of polymer melts / suspensions is advancing front, or a moving front. It is the interface between the polymer melt and the air inside the mold cavity as the melt fills the mold. Figure 1.1 shows an advancing front between two parallel plates. The advancing front presents experimental and numerical challenges in polymer processing due to the complex nature of flow in the region behind the front.

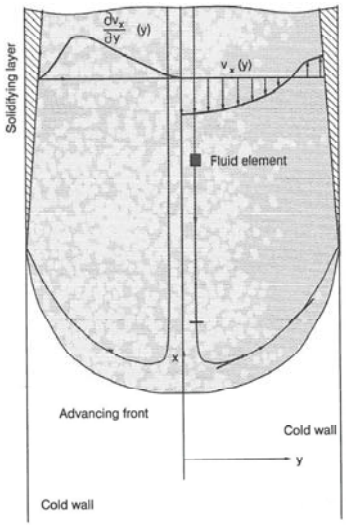

Figure 1.1 Flow patterns behind the advancing front for flow between two parallel plates as observed in a moving reference frame attached to the advancing front [16].

The advancing front moves with the average velocity of the filling fluid at the front which is less than the velocity of the fluid approaching the front around the midplane and more than the velocity of the fluid near the mold walls. This results in a deceleration of the fluid around the midplane as it approaches the slow moving front and a spill or flow of melt from the center to the walls causing a fountain-like phenomenon. This outflow of melt from the center to the walls behind the advancing front is known as fountain flow phenomenon [17].

For flow of fiber suspensions, the streamlines in the fountain flow region behind the advancing front take the fibers along with the suspending medium from the center of the mold and lays them on the sides of the mold, thereby significantly affecting the orientation in the region close to the walls. In a homogenous shear field, fibers along the walls would align along the flow direction due to presence of high shear near the walls. However, the presence of fountain flow behind the advancing front disrupts that orientation by transporting the fibers from a region of low shear to the region of high shear. Experimental studies on characterization of fiber orientation in injection molding flows provide evidence of the effect

of fountain flow on fiber orientation near the walls [6, 18]. Figure 1.2 shows A_{rr} component (the flow direction component) of fiber orientation as a function of the thickness direction for flow of fiber suspension in a center-gated disk. As can be seen from the figure, A_{rr} drops off close to the mold walls ($z/H = \pm 1$) as a result of the effect of the advancing front. Figure 1.3 shows the fiber orientation in the same geometry and flow field but tracked along the radial direction at a thickness position close to the mold wall ($z/H = 0.75$). As is evident from the figure, the orientation along the mold walls in a center-gated disk is high far behind the advancing front because of alignment in the flow direction due to high shear at the walls. However, the orientation drops close to the front because the fountain flow carries the transversely aligned fibers from extension-dominated central layers and lays them along the walls resulting in a drop in fiber orientation near the walls.

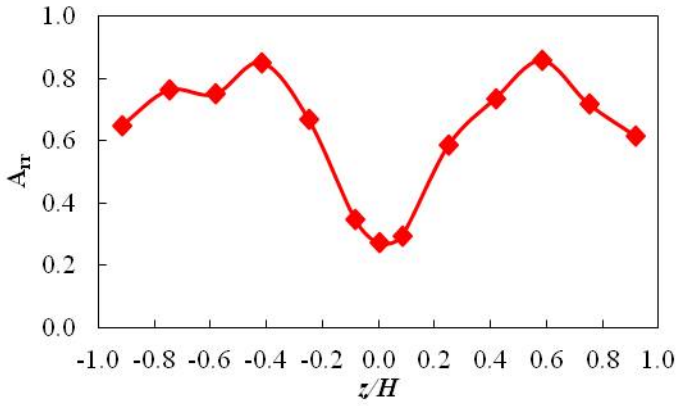

Figure 1.2 A_{rr} component of fiber orientation tensor measured in a center-gated disk at $r/H = 32.45$ as a function of thickness position (z/H) [13].

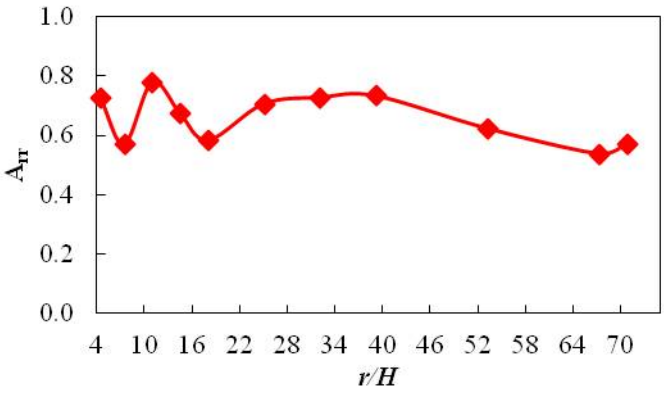

Figure 1.3 A_{rr} component of fiber orientation tensor measured in a center-gated disk at $z/H = 0.75$ as a function of radial position (r/H).

Current simulation schemes used in commercial simulation packages use a lubrication approximation known as Hele-Shaw flow approximation due to its computational efficiency. Hele-Shaw

flow ignores the transverse component of the velocity and treats the front as a flat interface moving with the average velocity of the fluid. With this simplification, fountain flow behind the advancing front is completely discarded in the velocity calculations leading to erroneous results for the velocity near the advancing front. As a result of the incorrect velocity field, fiber orientation predictions are not accurate near the mold walls. Hele-Shaw flow over-predicts fiber orientation near the walls [7, 9-11, 19-21]. It has been demonstrated that Hele-Shaw flow cannot correctly predict the fiber orientation near the mold walls and it is necessary to include the advancing front to improve orientation predictions near the walls [7, 22]. As can be seen in Figure 1.4 the prediction of fiber orientation with the advancing front effects are significantly better than the predictions with Hele-Shaw flow approximation when compared with experimental data.

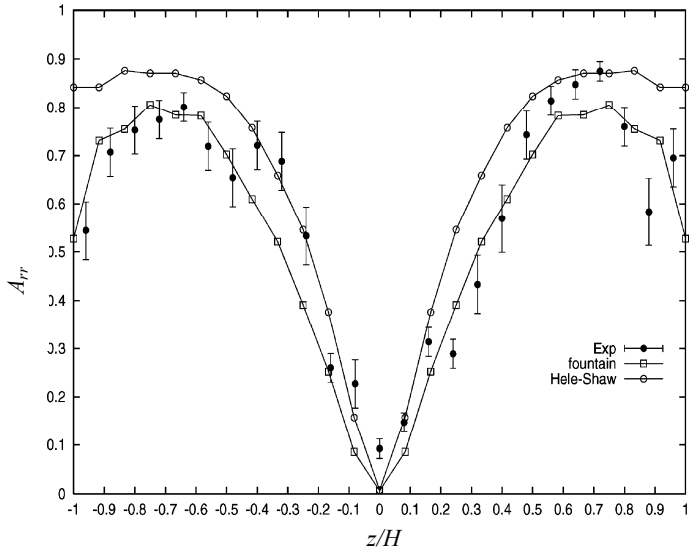

Figure 1.4 Comparison of A_{rr} component of fiber orientation predicted with advancing front and Hele–Shaw flow for a non-Newtonian fiber suspension in a center-gated disk as a function of the thickness position at r/b = 22.8 [7]

Equation for the prediction of fiber orientation and the equation for the prediction of the shape and the position of the advancing front are both hyperbolic partial differential equations. In order to handle the convective nature of these hyperbolic equations, the popular method of choice has been streamline upwinding Petrov-Galerkin (SUPG) method [4, 5, 7, 22]. However, the disadvantages of this method include introduction of artificial diffusion which smoothens the discontinuities and higher computational time due to solution of huge matrices. These disadvantages make the scheme unfit for commercial applications. Another numerical method to handle the convective problems is the discontinuous Galerkin finite element method (DGFEM) which is computationally much more efficient and keeps the sharpness at the interfaces and the discontinuities. In order to make the simulations for fiber orientation predictions commercially viable, it is necessary to use numerical schemes such as DGFEM

which is more accurate and efficient. DGFEM has been previously used to solve fiber orientation equations in a standard benchmark problem of planar contraction [23]. However, it has not been used in the prediction of fiber orientation in 2-D injection mold flows which is the focus of this study. In this work, we propose to use DGFEM to solve the hyperbolic partial differential equations describing the evolution of fiber orientation and the advancing front.

There are very few publications available in the literature that provide experimentally measured orientation in injection molded parts as a way to experimentally validate the predictions of fiber orientation in injection molded parts [6, 18]. The experimental results of Bay [6] for a center-gated disk and a film-gated strip have been considered as a benchmark study for experimental validation of fiber orientation prediction. However, in this study only the thickness direction was considered for orientation measurement. Moreover, fiber orientation data as a function of the flow direction is not available in the literature. Numerical studies with fiber orientation predictions that have been published have compared predictions with Bay's experimental data in the thickness direction only at three locations in the flow direction [7, 9, 22]. There is a need to experimentally track fiber orientation along the flow direction because the fibers follow the streamlines and their orientation evolves as they move along the streamlines. Fiber orientation tracked along the streamlines will be a better validation of the fiber orientation predictions. With this idea, in the current work, we aim to experimentally validate our predictions using the orientation tracked in the direction of the flow at various locations as shown in Figure 1.3. Experimental study currently underway in our group is aimed at measuring fiber orientation in most of the flow domain in order to have benchmark data in the entire domain of the mold cavity.

Most of the injection mold filling simulations for fiber suspensions have been limited to the mold cavity, while in the real process, the fiber suspension passes through a sprue and turns at the gate before entering the mold. There have been attempts to include sprue as part of the computational domain in fiber orientation predictions [4, 7] in order to improve the fiber orientation predictions, especially near the gate. Verweyst [4] computed the fiber orientation in a center-gated disk including the sprue but only steady state was considered while Chung [7] considered the transient filling of the sprue. However, in both of these studies, random inlet orientation was assigned at the inlet of the sprue. We plan to further improve upon the simulations of the sprue by using measured orientation at the inlet of the sprue as the inlet conditions for the orientation equations.

In order to make the simulation package commercially attractive, we plan to extend the scheme developed above to long glass fibers. Because of the flexibility of long glass fibers, Folgar Tucker model is not enough to describe their orientation. A bead-rod model has been recently proposed as one of the

first attempts at predicting long glass fiber orientation [24, 25]. We plan to use this model to predict long glass fiber orientation in a center-gated disk and compare predicted results with long glass fiber orientation measured as part of an experimental study currently undergoing at our lab.

With the above background, we are motivated to define the objectives of assessing and improving fiber orientation predictions in injection molded composites. The research objectives for this work are discussed in the following section.

1.1 Research Objectives

The primary goal of this research is the improvement in the prediction of fiber orientation in injection molded complex flow geometries and validation of the simulation results with experimental data. With regard to this goal, following objectives have been formulated:

1. To experimentally characterize the evolution of fiber orientation in a center-gated disk by measuring fiber orientation along the radial direction at three different heights, representative of the shell, transition and core layers, in the lubrication and frontal region, in order to investigate the effects of different flows (shear and extension) on fiber orientation in different regions of a disk.
2. To develop a numerical scheme for the prediction of fiber orientation under the effects of fountain flow in two dimensional (2D) geometries and use this numerical scheme to predict fiber orientation along the radial direction in a center-gated disk using the standard Folgar-Tucker model and its slow versions, the delayed Folgar-Tucker model and the reduced strain closure (RSC) model.
3. To assess the effects of inlet conditions in a center-gated disk by comparing model predictions with random orientation and measured orientation assigned at the inlet of the mold.
4. To extend the scheme to semi-flexible fibers and assess the effects of the advancing front on the prediction of orientation of long semi-flexible fibers in a center-gated disk using the Bead-Rod model by comparing model predictions with experimentally measured orientation.

1.2 References

[1] G.B. Jeffery, The motion of ellipsoidal particles immersed in a viscous fluid, in: Proceedings of the Royal Society of London, Series A, The Royal Society, 1922, pp. 161-179.

[2] F. Folgar, C.L. Tucker, Orientation behavior of fibers in concentrated suspensions, Journal of Reinforced Plastics and Composites, 3 (1984) 98-119.

[3] J.H. Phelps, C.L. Tucker III, An anisotropic rotary diffusion model for fiber orientation in short- and long-fiber thermoplastics, Journal of Non-Newtonian Fluid Mechanics, 156 (2009) 165-176.

[4] B.E. Verweyst, C.L. Tucker, Fiber suspensions in complex geometries: Flow/orientation coupling, Canadian Journal of Chemical Engineering, 80 (2002) 1093-1106.

[5] B.E. VerWeyst, C.L. Tucker, P.H. Foss, J.F. O'Gara, Fiber orientation in 3-D injection molded features: Prediction and experiment, International Polymer Processing, 4 (1999) 409-420.

[6] R.S. Bay, C.L. Tucker, Fiber orientation in simple injection moldings. Part II: Experimental results, Polymer Composites, 13 (1992) 332-341.

[7] D.H. Chung, T.H. Kwon, Numerical studies of fiber suspensions in an axisymmetric radial diverging flow: The effects of modeling and numerical assumptions, Journal of Non-Newtonian Fluid Mechanics, 107 (2002) 67-96.

[8] J. Ko, J.R. Youn, Prediction of fiber orientation in the thickness plane during flow molding of short fiber composites, Polymer Composites, 16 (1995) 114-124.

[9] K.H. Han, Y.T. Im, Numerical simulation of three-dimensional fiber orientation in injection molding including fountain flow effect, Polymer Composites, 23 (2002) 222-238.

[10] S.T. Chung, T.H. Kwon, Coupled analysis of injection molding filling and fiber orientation, including in-plane velocity gradient effect, Polymer Composites, 17 (1996) 859-872.

[11] S.T. Chung, T.H. Kwon, Numerical simulation of fiber orientation in injection molding of short-fiber-reinforced thermoplastics, Polymer Engineering and Science, 35 (1995) 604-618.

[12] M. Sepehr, G. Ausias, P.J. Carreau, Rheological properties of short fiber filled polypropylene in transient shear flow, Journal of Non-Newtonian Fluid Mechanics, 123 (2004) 19-32.

[13] G.M. Vélez-García, S.M. Mazahir, P. Wapperom, D.G. Baird, Simulation of injection molding using a model with delayed fiber orientation, International Polymer Processing, 26 (2011) 331-339.

[14] J. Wang, J.F. O'gara, C.L. Tucker, An objective model for slow orientation kinetics in concentrated fiber suspensions: Theory and rheological evidence, Journal of Rheology, 52 (2008) 1179.

[15] A.P.R. Eberle, D.G. Baird, P. Wapperom, G.M. Vélez-García, Using transient shear rheology to determine material parameters in fiber suspension theory, Journal of Rheology, 53 (2009) 685-705.

[16] D.G. Baird, D.I. Collias, Polymer Processing: Principles and Design, Wiley, 1998.

[17] W. Rose, Fluid-fluid interfaces in steady motion, Nature, 191 (1961) 242-243.

[18] G.M. Vélez-García, P. Wapperom, D.G. Baird, A.O. Aning, V. Kunc, Unambiguous orientation in short fiber composites over small sampling area in a center-gated disk, Composites Part A: Applied Science and Manufacturing, 43 (2012) 104-113.

[19] R.S. Bay, C.L. Tucker, Fiber orientation in simple injection moldings. Part I: Theory and numerical methods, Polymer Composites, 13 (1992) 317-331.

[20] M.C. Altan, S. Subbiah, S.I. Güçeri, R.B. Pipes, Numerical prediction of three-dimensional fiber orientation in hele-shaw flows, Polymer Engineering and Science, 30 (1990) 848-859.

[21] M. Gupta, K.K. Wang, Fiber orientation and mechanical properties of short-fiber-reinforced injection-molded composites: Simulated and experimental results, Polymer Composites, 14 (1993) 367-382.

[22] J.M. Park, T.H. Kwon, Nonisothermal transient filling simulation of fiber suspended viscoelastic liquid in a center-gated disk, Polymer Composites, 32 (2011) 427-437.

[23] B.D. Reddy, G.P. Mitchell, Finite element analysis of fibre suspension flows, Computer Methods in Applied Mechanics and Engineering, 190 (2001) 2349-2367.

[24] U. Strautins, A. Latz, Flow-driven orientation dynamics of semiflexible fiber systems, Rheologica Acta, 46 (2007) 1057-1064.

[25] K.C. Ortman, Assessing an orientation model and stress tensor for semi-flexible glass fibers in polypropylene using a sliding plate rheometer: For the use of simulating processes, in: PhD Thesis, Chemical Engineering,Virginia Tech Polytechnic Institute and State University,2011

CHAPTER 2. LITERATURE REVIEW ON COMPLEX FLOW SIMULATION OF SHORT GLASS FIBER POLYMER COMPOSITES

The injection mold filling process is increasingly being used for manufacturing automotive parts from glass fiber filled polymer composites. Glass fibers provide mechanical strength and stiffness to the polymer matrix. The objective in the processing of these materials is to control the orientation so as to achieve maximum enhancement of mechanical properties. Processing of glass fiber polymer suspensions and prediction of fiber orientation presents a tough challenge for the polymer processing industry because of the difficulty in controlling the fiber orientation in the parts during the mold filling process. The fiber orientation usually sets in during the filling phase and evolution of fiber orientation during this phase is governed by the velocity fields present in the mold cavity. The behavior of the suspending polymer matrix and the fibers during this phase must be well described in order to predict the orientation of the fibers. However, the description of the behavior of the fluid is difficult due to the non-Newtonian nature of the polymeric matrix, such as viscoelasticity or shear-thinning behavior, and the complex rheological effects introduced due to the presence of the fibers. Moreover, the effects of the characteristic fountain flow that is present behind the advancing front in mold-filling flows of polymeric matrices need to be included in order to correctly predict fiber orientation near the mold walls [1, 2]. Any numerical simulation aiming to predict fiber orientation needs to address the modeling and the numerical issues in order to correctly predict the orientation. In this chapter, a review of governing equations describing the kinematics of the mold filling process and the orientation evolution is presented in section 2.1. This is followed by section 2.2 which briefly covers some of the numerical methods used in mold filling simulations of fiber suspensions. Section 2.3 provides an overview of the mold filling simulations of fiber suspensions and some key results published in the literature in the past three decades.

2.1 Governing Equations

This section provides an overview of the governing equations describing the filling stage in injection molding process. The filling conditions inside the mold are assumed to be isothermal. The isothermal conditions during mold filling are justified on the basis of fast filling times compared to the time required for solidification of polymer melt. There are two main governing equations that

describe the isothermal mold filling process for a fiber suspension: mass and momentum balance equations, and orientation evolution equations. This section is divided in three subsections based on these two governing equations. Section 2.1.1 provides an overview of the mass and momentum balance equations that govern the flow of a fluid with a given rheological behavior and under certain boundary conditions. This section discusses constitutive equations for Newtonian and generalized Newtonian fluids. Viscoelastic effects are excluded because the current effort is only limited to Newtonian and generalized Newtonian fluids. The section is concludes with a discussion of the boundary conditions for the balance equations encountered in injection mold filling simulations. Section 2.1.2 provides a description of orientation for short glass fibers and the Folgar Tucker model [3] and its variations, which is the most promising model to date for modeling fiber orientation evolution.

2.1.1. Mass and momentum balance equations

The set of equations defining a fiber suspension with constant mass, negligible inertia and local acceleration (due to the high viscosity of the polymer melt) flowing into a mold cavity during the filling stage of an injection molding process are:

$$\nabla \cdot \mathbf{v} = 0 \tag{1}$$

$$\nabla \cdot \boldsymbol{\sigma} = 0 \tag{2}$$

where $\boldsymbol{\sigma}$ is the total stress tensor defined as:

$$\boldsymbol{\sigma} = -p\boldsymbol{\delta} + \mathbf{T} \tag{3}$$

where p is the pressure, $\boldsymbol{\delta}$ denotes the unit tensor, and $\mathbf{T}$ is the extra stress tensor.

The key to simulate injection molding process of fiber suspensions is the specification of the extra stress tensor [4]. The extra stress tensor for a high aspect ratio glass fiber / polymer suspension consists of two components,

$$\mathbf{T} = \mathbf{T}^{fibers} + \mathbf{T}^{matrix} \tag{4}$$

where $\mathbf{T}^{fibers}$ is the stress due to the movement of the high aspect ratio glass fibers in the fluid and $\mathbf{T}^{matrix}$ is the stress contribution from the polymer matrix. In this research study, we do not include

the stress contributions due to fibers, i.e. $\mathbf{T}^{fibers} = 0$. This is known as the decoupled approach in prediction of fiber orientation.

2.1.1.1. Constitutive equations for polymeric matrices

Constitutive equations for polymer melts describe the relationship between the stresses developed in a fluid under a given strain. To understand the behavior of the material, it is necessary to develop an equation that relates the flow phenomena to the stress. When a suspension of high aspect ratio fibers in a viscoelastic melt is considered, the stresses due to the matrix and the fibers have to be considered. One arises from the deformation due to the kinematics of the fluid and the other from the drag produced by the fluid as it flows past the fibers.

Rheological constitutive equation for a polymer melt can be developed using a continuum approach or molecular approach, among other approaches. The continuum approach does not distinguish between the constituents and consists of empirical modifications to the constitutive equation to fit their response, depending on the terms included in the equations. This approach has been useful in the development of the constitutive equations for Newtonian and shear-thinning non-Newtonian fluids. In addition, it can be used to develop constitutive equations for the viscoelastic fluids under large deformation (non-linear viscoelastic fluids) by introducing convected derivatives in the constitutive relation. The molecular approach takes into account the molecular components of the system to build equations for the macroscopic stresses [5].

2.1.1.1.1. Newtonian model

A Newtonian constitutive equation describes the behavior of a fluid of low molecular weight and polymeric solutions or disperse systems at low polymer or disperse phase concentrations, respectively. The stress in a Newtonian matrix is given by:

$$\mathbf{T}^{matrix} = 2\eta\mathbf{D} \tag{5}$$

where η is the Newtonian viscosity and $\mathbf{D}$ the rate of deformation tensor defined as:

$$\mathbf{D} = \frac{1}{2}\left(\nabla\mathbf{v}^T + \nabla\mathbf{v}\right) \tag{6}$$

where $\nabla\mathbf{v}$ is the velocity gradient tensor and the superscript ^{T} denotes the transpose. The above constitutive equation indicates that the stress tensor is linearly related to the rate of deformation

tensor. In extension flows, the Newtonian model predicts that extensional viscosity is 3 times the shear viscosity, i.e. $\eta_E = 3\eta$.

As the complexity of the molecular structure increases, such as for concentrated solutions and polymers melts the fluids deviate from the Newtonian behavior. Such fluids are known as non-Newtonian fluids. Non-Newtonian fluids exhibit certain characteristic behaviors such as shear thinning, normal stress differences, and viscoelastic (memory) effects. Such characteristic behaviors shown by non-Newtonian fluids have to be described by an equation different from the Newtonian constitutive equation. The Newtonian model can be used to approximate the behavior of such Non-Newtonian fluids only at low deformation rates [6].

2.1.1.1.2. Matrix viscosity enhancement at high shear rate

At high shear rates, the contribution of the inelastic matrix to the total extra stress is significant and can be modeled as a viscous contribution [7]. At low shear rates, the contribution to the total extra stress due to the matrix accounts for the isotropic contributions from the fluid and the fibers, as described by Eq. (5) with viscosity (η) defined as the solvent or the matrix viscosity (η_s). Typical shear thinning effects at high shear rates affect the values of the suspension viscosity [8]. The viscosity is enhanced by the addition of the fiber, as shown in Figure 2.1. The amount of displacement is proportional to the relative viscosity (η_r) defined as

$$\eta_r = \frac{\eta_{suspension}}{\eta_{matrix}} \tag{7}$$

where the ratio η_r is a measure of the effective enhancement of the shear rate in the matrix when a large volume fraction is occupied by the fibers [7]. When the relative viscosity is used in the matrix stress, the equation for the matrix stress becomes

$$\mathbf{T}^{matrix} = 2\eta_r \eta_s \mathbf{D} \tag{8}$$

where η_s is the solvent viscosity.

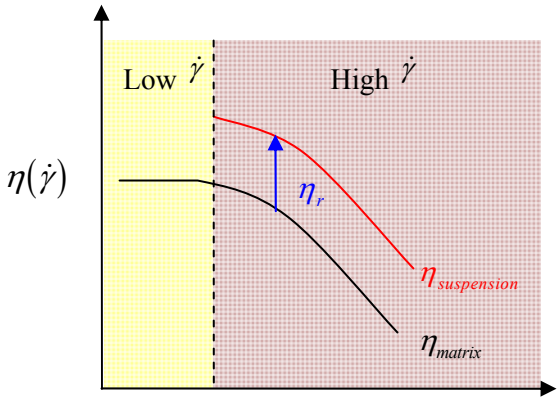

Figure 2.1 Typical enhancement of suspension viscosity at high shear rate.

Doraiswamy and Metzner [7] have suggested empirical relationships for the relative viscosity. These relationships depend on the type of flow, i.e. shear or extensional, volume fraction (ϕ_v), and aspect ratio of the fibers (a_r). The relative viscosity in shear flows is given by:

$$\eta_r = \left(1 - \frac{\phi_v}{K}\right)^{-2} \tag{9}$$

where K is an experimental constant. In elongational flow, relative viscosity is

$$\eta_r = 1 + \frac{4}{9}\frac{\phi_v a_r^{\,2}}{\ln\left(\pi/\phi_v\right)} \tag{10}$$

The format of these equations can be used to assess the viscosity enhancement due to the fibers in shear and extensional flows. In shear flows the viscosity enhancement grows exponentially for concentrations below the K value while in extensional flows it grows linearly with the concentration and quadratically with the aspect ratio.

2.1.1.1.3. Generalized Newtonian models

The generalized Newtonian constitutive equation describes the fluids which show shear thinning behavior. However, it does not predict normal stresses in shear and memory effects. The generalized Newtonian constitutive equation is given by

$$\mathbf{T}^{matrix} = 2\eta\left(II_D, III_D\right)\mathbf{D} \tag{11}$$

where $\eta(II_D, III_D)$ is a function that describes the dependence of the viscosity on the second (II_D) and third (III_D) invariants of the rate of deformation tensor, defined as:

$$II_D = 2\mathbf{D}:\mathbf{D} \tag{12}$$

$$III_D = \det(\mathbf{D}) \tag{13}$$

For shear dominated flows, (III_D) is not taken into account for the viscosity (η) because in shear-dominated flows, there are no terms on the diagonal [9]. The difference between the Newtonian and the generalized Newtonian constitutive equations is due to the difference in the description of the viscosity function of shear rate.

2.1.1.1.3.1. Power-law model

For many polymer melts, viscosity (η) vs. the second invariant of the rate of deformation tensor or the strain rate II_D plotted on a log-log scale shows a shows linear shear thinning behavior over a range of strain rates typical in polymer processing operations [10]. Power law model is a simple constitutive model with only two parameters which fits this shear thinning behavior quite well. The power law model is given by:

$$\eta = m(II_D)^{n-1} \tag{14}$$

where m is known as the consistency index and n is called the power-law index. These are empirical parameters and depend on a particular fluid and temperature, but independent of the strain rate. For a Newtonian fluid, $n = 1$, for shear-thinning behavior, $n < 1$, and for a dilatants or a shear-thickening fluid, $n > 1$. One of the limitations of the power law model is that it does not give good predictions for the limiting zero-shear-rate viscosity, η_0. However, the simplicity of the model makes it one of the most attractive models for rheological behavior of polymer melts.

2.1.1.1.3.2. Carreau-Yasuda model

Carreau-Yasuda model is a five-parameter model that provides a good estimate of the viscosity for a wide range of shear rates. In general for polymer melts, at low shear rates, the viscosity profile must show a plateau, and with increase in the shear rate, it should show a shear thinning behavior, i.e. a reduction in the viscosity. In addition, the curve must include a transition region between the plateau and the shear thinning behavior. The Carreau-Yasuda model predicts all

of these behaviors of the viscosity curve and is widely used for polymer melts [9]. The model is given by:

$$\eta = (\eta_0 - \eta_\infty)\left[1 + \left(\lambda\sqrt{II_D}\right)^{\alpha}\right]^{(n-1)/\alpha} + \eta_\infty \tag{15}$$

where λ is a time constant approximately representing the reciprocal of the shear rate for the onset of shear thinning behavior [9], η_0 the zero-shear viscosity, η_∞ the viscosity as II_D or $dv_1/dx_3 \to \infty$, α represents the width of the transition region between η_0 and the power law region, and $n$represents the degree of deviation from the Newtonian behavior at higher shear rates.

2.1.1.2. Boundary conditions

In injection molding process, the boundary conditions are the result of fluid-solid (melt suspension-wall) or fluid-fluid (i.e. melt suspension-air) interactions depending on the solution approach. In Lagrangian methods, melt suspension-air interface is considered as a boundary while in Eulerian methods, it is considered as part of the continuum. The boundary conditions for the flow equations encountered in injection mold filling process are described as follows [11].

Inlet

At the inlet, either a velocity profile is prescribed based on a given flow rate or pressure is prescribed based on the pressure drop across the flow domain. In the case of a given flow rate, velocity profile is prescribed as:

$$u(x_1) = f(x_3) \tag{16}$$

where the coordinate system is described as: 1: flow direction, 2: transverse direction, 3: cavitywise direction.

Mold walls and air vents (outlets)

The boundary conditions specified at the mold walls and air vents are based on the PC method. The details of the PC method are provided in 2.2.1.2.7. In the PC method for mold filling, adjustable Robin boundary conditions for the velocity and the stress components (u_t and σ_t) are specified at the mold walls and air vents [12]. This results in no slip boundary condition for the polymer and a free-slip condition for the air at the mold walls in tangential direction.

$$au_t + \sigma_t = 0 \qquad \forall x \in \Gamma_w \cup \Gamma_v \tag{17}$$

where Γ_w is mold wall boundary and Γ_v is the air vent boundary and the dimensionless 'Robin penalty parameter' a is defined as

$$a = a(F) = \begin{cases} \geq 10^4 & \text{if } F \geq 0.5 \text{ no-slip} \\ 0 & \text{if } F < 0.5 \text{ free-slip} \end{cases} \tag{18}$$

Moreover, polymer or air are not allowed to pass through the mold walls. Since mold walls are impermeable, except at air vents where air is allowed to leave freely, the following boundary conditions are imposed for normal component of velocity at the walls and vents

$$u_n = 0 \qquad \forall x \in \Gamma_w \tag{19}$$

$$au_n + \sigma_n = 0 \qquad \forall x \in \Gamma_v \tag{20}$$

where a is given by Eq. (18). In Lagrangian methods, a no-slip boundary condition at the wall is prescribed indicating that the normal and tangential components of the fluid velocity are zero.

$$u_n = u_t = 0 \qquad \forall x \in \Gamma_w \tag{21}$$

Free surface

In Lagrangian methods which consider melt-air interface as a boundary, following boundary conditions are imposed:

$$\sigma_n = (\boldsymbol{\sigma} \cdot \mathbf{n}) \cdot \mathbf{n} = 0 \tag{22}$$

$$\sigma_t = (\boldsymbol{\sigma} \cdot \mathbf{n}) \cdot \mathbf{t} = 0 \tag{23}$$

$$\mathbf{v} \cdot \mathbf{n} = 0 \tag{24}$$

where **t** is the tangent and **n** is the normal vector to the curve, σ_n the normal stress, σ_t the tangential stress. The last equation indicates that there is no flow through the interface. The boundary conditions at the free surface which are defined by Eqs. (22)-(24) represent a moving boundary. In Eulerian methods, the interface forms part of the continuum and is not treated as a boundary.

Symmetry

For symmetry boundaries, following boundary conditions are prescribed:

$$\boldsymbol{\sigma}\cdot\mathbf{t}=0,\mathbf{v}\cdot\mathbf{n}=0 \tag{25}$$

Eq. (25) indicates the absence of tangential stress and normal velocity components along the centerline and other symmetry boundaries.

2.1.2. Orientation equations for high aspect ratio fibers

2.1.2.1. Particle orientation

Typically, high aspect ratio particles such as glass fibers are described by their geometrical features and their concentration in the suspending matrix. These fibers are assumed to be uniform, axisymmetric, and characterized by the aspect ratio (a_r), which is defined as

$$a_r=\frac{l}{d} \tag{26}$$

where l and d are the length and diameter of the fiber, respectively. The suspending medium is assumed to be a Newtonian solvent. Suspensions with fibers are characterized by the fiber volume fraction (ϕ_v) and aspect ratio simultaneously in three regimes of concentration:

Dilute regime: $\phi_v << a_r^{-2}$

Semi-dilute regime: $a_r^{-2} < \phi_v < a_r^{-1}$

Concentrated regime: $\phi_v > a_r^{-1}$

The spatial orientation of a single fiber can be described using the spherical coordinates with the azimuthal (ϕ) and the zenith (θ) angle as shown in Figure 2.2. In this spherical coordinate system, an orientation unit vector **p** can be constructed parallel to the backbone of the fiber as:

$$\mathbf{p}=p_1\boldsymbol{\delta}_1+p_2\boldsymbol{\delta}_2+p_3\boldsymbol{\delta}_3 \tag{27}$$

where the components of p are given by:

$$p_1=\sin\theta\cos\phi \tag{28}$$

$$p_2 = \sin\theta \sin\phi \tag{29}$$

$$p_3 = \cos\theta \tag{30}$$

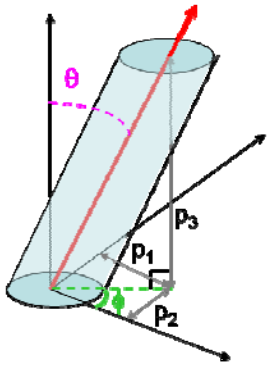

Figure 2.2 Description of high aspect ratio fiber orientation in spherical coordinates.

The orientation description of a population of such fibers can be developed from the orientation description of a single fiber using statistical methods. The most general description of the orientation state at any point in the domain is given by the probability distribution function $\psi(p)$ or $\psi(\theta, \phi)$ also known as the orientation distribution function. This function is defined such that the probability of finding a fiber between angles θ_1 and $\theta_1+\Delta\theta$ and ϕ_1 and $\phi_1+\Delta\phi$ is given by [13]:

$$P(\theta_1 \le \theta \le \theta_1 + \Delta\theta, \phi_1 \le \phi \le \phi_1 + \Delta\phi) = \psi(\theta_1, \phi_1)\sin\theta_1 \Delta\theta\Delta\phi \tag{31}$$

where the left hand side denotes the probability of finding a fiber with orientation angles between θ_1 and $\theta_1+\Delta\theta$ and ϕ_1 and $\phi_1+\Delta\phi$.

The orientation distribution function ψ must satisfy two conditions: the two ends of a fiber must be indistinguishable from each other, i.e.

$$\begin{aligned} &\psi(\theta,\phi) = \psi(\theta - \pi, \pi + \phi) \quad \text{or} \\ &\psi(p) = \psi(-p) \end{aligned} \tag{32}$$

and it should be normalized, i.e. the total probability must be 1, i.e.

$$\int_{\theta=0}^{\pi}\int_{\phi=0}^{2\pi}\psi(\theta,\phi)\sin\theta d\theta d\phi = \oint\psi(p)dp = 1 \tag{33}$$

When the fibers are present in a fluid and are changing orientation with time due to the bulk motion of the fluid, then ψ may be regarded as a convected quantity. In that case, ψ must also satisfy the continuity condition which is given by:

$$\begin{aligned}\frac{D\psi}{Dt} &= -\frac{\partial}{\partial\theta}\cdot\left(\dot{\theta}\psi\right) - \frac{1}{\sin\theta}\frac{\partial}{\partial\phi}(\dot{\phi}\psi) \quad \text{or} \\ \frac{D\psi}{Dt} &= -\frac{\partial}{\partial\mathbf{p}}\cdot\left(\psi\dot{\mathbf{p}}\right)\end{aligned} \tag{34}$$

The continuity condition given by Eq. (34) is also referred to as Smoluchowski equation [14], and describes the evolution of ψ with time, once an appropriate expression for average angular velocities $(\dot{\theta},\dot{\phi})$ or $\dot{\mathbf{p}}$ is chosen.

Although complete and unambiguous, the disadvantage of the orientation distribution function is high computational cost that is associated with it. Bay and Tucker [15] estimated the number of degrees of freedom required for $\psi(\theta,\phi)$ in a typical injection molding simulation and concluded that the description of $\psi(\theta,\phi)$ in a realistic injection molding simulation using 5000 nodes would require four million degrees of freedom.

Advani and Tucker [13] used orientation tensors to approximate the orientation distribution. Orientation tensors are formed by taking the dyadic product of the vector **p** with itself and integrating its product with the orientation distribution function over all possible directions. Because the distribution function is even, odd order tensors are zero but an infinite set of even order tensors can be developed. Second and fourth order orientation tensors are given by:

$$\mathbf{A} = \mathbf{A}_{ij} = \left\langle p_i p_j \right\rangle = \int_{\phi=0}^{2\pi}\int_{\theta=0}^{\pi} p_i p_j \psi(\theta,\phi)\sin\theta d\theta d\phi \tag{35}$$

$$\mathbf{A}_4 = \mathbf{A}_{ijkl} = \left\langle p_i p_j p_k p_l \right\rangle = \int_{\phi=0}^{2\pi}\int_{\theta=0}^{\pi} p_i p_j p_k p_l \psi(\theta,\phi)\sin\theta d\theta d\phi \tag{36}$$

where **A** is the second order orientation tensor and $\mathbf{A}_4$ is the fourth order orientation tensor with the components of each tensor given by $\mathbf{A}_{ij}$ and $\mathbf{A}_{ijkl}$ respectively. $\langle\cdot\rangle$ represents the ensemble average of the dyadic product of the unit vectors **p** over all possible orientations. Orientation tensors are symmetric and satisfy the normalization condition, i.e. $tr(\mathbf{A}) = 1$. Due to symmetry and normalization conditions, **A** has only five independent components and $\mathbf{A}_4$ has fourteen independent components. The advantage of using orientation tensors over the orientation distribution function is the compactness, efficiency and a manageable computation time. For the injection molding case considered in Bay and Tucker [15] with 5000 nodes, if **A** is used instead of $\psi(\theta,\phi)$, 25,000 degrees of freedom are required, which is less than 1% of the number required for $\psi(\theta,\phi)$. However, the use of orientation tensors introduces the necessity for a closure approximation to express the higher order tensors in terms of lower order tensors in order to get a closed set of orientation evolution equations.

2.1.2.2. Folgar Tucker model

Folgar and Tucker [3] developed a model using orientation distribution function for the evolution of fiber orientation in non-dilute suspensions based on Jeffery's model [16] for dilute suspensions of ellipsoidal particles by adding a phenomenological term to account for fiber-fiber interactions. The following assumptions are considered in developing the Folgar Tucker model in addition to the original assumptions of Jeffery's model:

- The fibers are rigid rods of uniform length and diameter
- The fibers are sufficiently large so that the Brownian motion can be neglected
- The fibers are uniformly distributed throughout the matrix

Advani and Tucker [13] replaced the orientation distribution function in the Folgar Tucker model with the more compact orientation tensor notation . The evolution equation for second order orientation tensor **A** can be written as:

$$\frac{D\mathbf{A}}{Dt} = \left(\mathbf{W}\cdot\mathbf{A} - \mathbf{A}\cdot\mathbf{W}\right) + \lambda\left(\mathbf{D}\cdot\mathbf{A} + \mathbf{A}\cdot\mathbf{D} - 2\mathbf{A}_4 : \mathbf{D}\right) + 2D_r\left(\mathbf{I} - 3\mathbf{A}\right) \tag{37}$$

where $\mathbf{W} = [(\nabla\mathbf{v})^T - (\nabla\mathbf{v})]/2$ is the vorticity tensor, $\mathbf{D} = [(\nabla\mathbf{v})^T + (\nabla\mathbf{v})]/2$ is the rate of strain tensor. Velocity gradient is defined as $\nabla\mathbf{v} = \partial v_j / \partial x_i$, and λ is the shape factor defined as

$$\lambda = \frac{a_r^2 - 1}{a_r^2 + 1} \tag{38}$$

For high aspect ratio particles such as glass fibers, λ = 1. **I** is the identity tensor and D_r is the isotropic rotary diffusivity and accounts for fiber-fiber interactions in non-dilute suspensions. It depends on the fiber size, and the viscosity and temperature of the suspending fluid [17]. For a single fiber, D_r is zero and the Folgar Tucker model reduces to Jeffery's model.

The first parentheses on the right hand side accounts for the rotational motion of the fibers and the second parentheses indicates that the fibers are convected with the macroscopic flow field keeping their length constant [18]. The isotropic diffusivity term is added to randomize the flow induced orientation in an analogous way as Brownian motion since the randomizing effect in a fiber suspension is similar to Brownian motion. However, the randomizing effect in glass fiber suspensions stops when the flow stops, which means that this term should go to zero as the flow stops. Therefore, Folgar and Tucker proposed the following form for D_r:

$$D_r = C_I \dot{\gamma} \tag{39}$$

where $\dot{\gamma}$ is the scalar magnitude of the rate-of-deformation tensor (**D**) and C_I is an empirical constant known as interaction coefficient. Substituting D_r from Eq. (39) in Eq. (37), Folgar Tucker model is given by:

$$\frac{D\mathbf{A}}{Dt} = \left(\mathbf{W}\cdot\mathbf{A} - \mathbf{A}\cdot\mathbf{W}\right) + \lambda\left(\mathbf{D}\cdot\mathbf{A} + \mathbf{A}\cdot\mathbf{D} - 2\mathbf{A}_4 : \mathbf{D}\right) + 2C_I\dot{\gamma}\left(\mathbf{I} - 3\mathbf{A}\right) \tag{40}$$

The presence of $\dot{\gamma}$ in this term ensures that it goes to zero when the flow stops. Phelps [19] suggested a typical range of C_I = 0.006 to 0.01 for short glass fiber composites. There is no established model yet for the prediction of the interaction coefficient C_I. Therefore, it is empirically determined by comparing predictions with the experiments. Folgar and Tucker [3] observed fiber orientation for various suspensions in semi-concentrated and concentrated regimes and tried to obtain values for C_I by fitting the numerical predictions with the experimental data. The values of C_I obtained were in the range of $O(10^{-1})$ and $O(10^{-3})$. There have been a few attempts to develop an empirical model for the interaction coefficient depending on fiber volume fraction. Bay [20] conducted experiments on fiber suspensions of various fiber concentrations and found that for non-

concentrated regimes, C_I decreased with fiber but increased in the high concentration regime and suggested an exponential form for C_I in the concentrated regime as a function of $\phi_v a_r$:

$$C_I = 0.0184 \exp\left[-0.7148 \phi_v a_r\right] \tag{41}$$

Eq. (41) predicts that the fiber interactions reduce at high volume fractions. Ranganathan and Advani [21] proposed a theoretical expression for C_I based on the average inter-fiber spacing as:

$$C_I = \frac{K}{a_c / l} \tag{42}$$

where K is a proportionality constant, a_c the average inter-fiber spacing and l the fiber length. In this model, a_c depends on fiber orientation states. The authors showed that the inter-fiber spacing increases with increasing orientation strength. Therefore, this model predicts that the value of C_I is high for randomly oriented fibers and decreases with increasing fiber orientation. Ramazani et al. [22] suggested that the interaction coefficient depends on polymer configuration to better fit the shear viscosity data and developed a modified version of Eq. (42) as follows:

$$C_I = \frac{K}{a_c / l} \frac{1}{(\mathbf{A} : \mathbf{C})^n} \tag{43}$$

where $\mathbf{C}$ is the polymer conformation tensor and n is a constant. According t o Eq. (43), as the polymer chains are stretched in the direction of fiber orientation, the fiber interaction reduces. Recently, Park and Kwon [23] proposed a model for the interaction coefficient using the irreversible thermodynamics approach for viscoelastic deformation of polymers. They introduced the anisotropic effect of the fiber orientation in the kinematic equation for the polymer in a manner of positive entropy production. The details of the model can be found elsewhere [23].

The use of the orientation tensors in the orientation equations introduces the necessity of using a closure approximation to expresss the higher order tensor appearing in the right hand side of the equation in terms of a lower order tensor in order t get a closed set of equations. Chung and Kwon [24] published a review of various closure approximations proposed for the fourth order tensor $\mathbf{A}_4$ appearing in Eq. (40). Advani and Tucker [13] have indicated certain requirements for an acceptable closure approximation, which are: the approximation must be constructed only from lower order orientation tensors and the unit tensor, the approximation must satisfy the normalization condition, i.e. $tr(\mathbf{A}) = 1$, $\mathbf{A}_{ijkl}=\mathbf{A}_{ij}$, and it should maintain the symmetries of the orientation tensors.

A hybrid closure is a simple and a stable closure and thus has been widely used in numerical predictions [13]. It is a linear combination of linear and quadratic closure approximations based on the level of orientation. Hybrid closure tends to overpredict the fiber orientation in comparison with the distribution function results [25]. Moreover, it does not satisfy the full symmetric property of $\mathbf{A}_4$.

Orthotropic closure approximations were developed by Cintra and Tucker [26] and improved upon by Chung and Kwon [27]. In these closure approximations, three independent components of $\mathbf{A}_4$ in the eigenspace, namely $\mathbf{A}_{ii}^{closure}$ are assumed to be polynomial functions of the two largest eigenvalues of $\mathbf{A}$. The orthotropic closures satisfy full symmetry condition and are quite successful in prediction simple flows. However, these closures require additional computation time due to transformations between the global coordinate system and the principal coordinate system. For low C_I values the orthotropic closures show non-physical oscillations in simple shear and radial diverging flows.

The invariant based optimal fitting closure [28] expresses the fourth order orientation tensor in terms of the symmetric second order tensor $\mathbf{A}$ and its invariants using the most general expression of a full symmetric fourth order tensor as:

$$\begin{aligned}\mathbf{A}_4 = {} & \beta_1 S(\mathbf{II}) + \beta_2 S(\mathbf{IA}) + \beta_3 S(\mathbf{AA}) + \beta_4 S(\mathbf{IA}\cdot\mathbf{A}) \\ & + \beta_5 S(\mathbf{AA}\cdot\mathbf{A}) + \beta_6 S(\mathbf{A}\cdot\mathbf{AA}\cdot\mathbf{A})\end{aligned} \tag{44}$$

where S is the symmetric operator and $\mathbf{I}$ is the unit tensor. The coefficients β_i's are functions of the second and third invariants of $\mathbf{A}$, $\beta_i = \beta_i(II_A, III_A)$. Invariant-based closure is as accurate as the eigenvalue-based closures, but requires much less computational time (about 30%) as compared to eigenvalue-based closures.

2.1.2.3. Slow orientation models

Even though the Folgar Tucker model (Eq. (40)) has been widely accepted for numerical predictions of fiber orientation, some experimental observations suggest that the actual kinematics of fiber orientation may be slower than the model predicts [29-31]. One of the simplest ways to capture slow orientation kinetics is to multiply the right hand side of the Folgar Tucker model by a factor $\alpha < 1$ as below:

$$\frac{D\mathbf{A}}{Dt} = \alpha\left[\left(\mathbf{W}\cdot\mathbf{A} - \mathbf{A}\cdot\mathbf{W}\right) + \lambda\left(\mathbf{D}\cdot\mathbf{A} + \mathbf{A}\cdot\mathbf{D} - 2\mathbf{A}_4 : \mathbf{D}\right) + 2C_I\dot{\gamma}\left(\mathbf{I} - 3\mathbf{A}\right)\right] \tag{45}$$

Sepehr and coworkers [30], Eberle and coworkers [32] and Garcia and coworkers [33] termed α the slip parameter. The slip parameter accounts for the non-affine motion of the fibers and slows down the orientation kinetics under fluid deformation. Hyun [34] called the reciprocal of slip parameter ($1/\alpha$) the strain reduction factor using the argument that the fibers are present in clusters and the strain they experience is less than that in the bulk. We will refer to Eq. (45) as the strain reduction factor (SRF) model. It reduces to Folgar Tucker model for $\alpha = 1$.

Although the SRF model is useful in describing slow orientation kinetics in simple flows [29-32], the model does not pass the rheological objectivity test and can give different answers when solved in different coordinate systems. The model is not invariant under rigid-body rotation. Therefore, its use may be limited to simple flows and it cannot be used for general flows [31]. Recently, Wang [31] developed an objective model for the slow orientation kinetics. To get this objective model, the equation for **A**, Eq. (40) is decomposed into rate equations for eigenvectors and eigenvalues of **A**, the equation for the eigenvalues is modified similarly as SRF model and the equations are then reassembled. After some algebra, the model takes the following form:

$$\frac{D\mathbf{A}}{Dt} = \left(\mathbf{W}\cdot\mathbf{A} - \mathbf{A}\cdot\mathbf{W}\right) + \lambda\left(\mathbf{D}\cdot\mathbf{A} + \mathbf{A}\cdot\mathbf{D} - 2\left[\mathbf{A}_4 + (1-\kappa)(\mathbf{L}_4 - \mathbf{M}_4 : \mathbf{A}_4)\right] : \mathbf{D}\right) + 2\kappa C_I\dot{\gamma}\left(\mathbf{I} - 3\mathbf{A}\right) \tag{46}$$

where $\mathbf{L}_4$ and $\mathbf{M}_4$ are defined in terms the terms of eigenvalues and eigenvectors of A as:

$$\mathbf{L}_4 = \sum_{i=1}^{3} \lambda_i (e_i e_i e_i e_i) \tag{47}$$

$$\mathbf{M}_4 = \sum_{i=1}^{3} e_i e_i e_i e_i \tag{48}$$

This model is different from the original Folgar Tucker model in the fourth-order orientation tensor term and the fiber interaction term. Now the closure approximation used to approximate the fourth order tensor $\mathbf{A}_4$ depends on κ which reduces the effect of straining on orientation. Hence, this model is known as 'reduced strain closure' or the RSC model.

The RSC model was able to fit the transient shear viscosity data better than the original Folgar Tucker model, especially near the shear strain where the viscosity has a peak. Fiber

orientation predictions in a center-gated disk using RSC model were also in better agreement with the experimental data [1]. Moreover, the RSC model is objective and is invariant under rigid-body rotation. Hence, it can be used in general flows.

2.2 Numerical Methods

The governing equations discussed in 2.1 are solved numerically using various numerical techniques. The balance equations are elliptic PDEs while the orientation equations are hyperbolic PDEs. The elliptic equations can be solved using standard Galerkin finite element method (GFEM). However, the hyperbolic PDEs are solved using discontinuous Galerkin finite element method (DGFEM). These methods are standard methods to solve these types of equations. Therefore they are not reviewed here. The transient filling of mold cavities involves a free moving front or an advancing front which makes it a moving interface problem. This interface evolves in time and changes its shape and position as the flow progresses. Section 2.2.1 reviews various approaches that have been considered to predict the evolution of this free moving interface. Section 2.2.2 gives the details of a time-discretization scheme that is used as an efficient stable scheme to solve the equation describing the evolution of free interfaces.

2.2.1. Advancing Front in Mold Filling Simulations

The advancing front is a free moving interface which is sometimes also referred to as 'moving front'. It is the interface between the polymer melt advancing in the mold cavity and the air present inside the cavity and evolves in shape and position with time during the mold filling process. Figure 1.1 shows the advancing front between two parallel plates. One of the characteristic flow features behind the advancing front is known as a fountain flow. The term 'fountain flow' was first introduced by Rose [35] to describe the kinematics of a wetting liquid displacing another immiscible liquid in a capillary channel. The interface formed between the wetting and the displaced liquid moves at a slower speed than the fluid particles approaching the slow moving interface. The fluid decelerates at the front and spills outward from the center towards the walls, thus creating a fountain effect. This kind of flow has been reported in the literature even before Rose coined this term [36-38]. Fountain flow behind the advancing front is critical to the study of mold filling simulations of fiber suspensions because all the fibers that are deposited near the walls practically pass through the fountain flow [39]. In fountain flow region behind the advancing front, streamlines carry the polymer matrix along with the fibers from the center of the mold towards the walls. The fibers, as they pass through the fountain flow region, undergo changes in orientation due

to the complex flow field present in the fountain flow region, and get laid along the walls thereby affecting the orientation near the walls. Therefore, it is necessary to include the fountain flow in fiber orientation predictions to get correct predictions of fiber orientation near the walls [1, 2, 15, 39-41].

The advancing front moves as the polymer melt fills the mold and creates a moving boundary with a moving contact point at the mold walls. As a result of this, numerical complications arise such as a stress singularity at the contact line in case of no slip boundary conditions for the filling fluid at the walls [42]. Various approaches have been suggested in the literature to solve the problem of viscous flows with moving contact points [43-45]. Some of the problems in the numerical treatment of such free boundaries or interfaces are: (1) their discrete representation, (2) their evolution in time and (3) the imposition of boundary conditions on them [46]. Solution of such problems requires a choice of an appropriate kinematical description of the continuum [47]. The choice of the description dictates the capability of the numerical method to handle huge distortions of the continuum and an accurate description of free surfaces and interfaces. In continuum mechanics, three methods have been used: Lagrangian, Eulerian and arbitrary Lagrangian Eulerian (ALE) for such description. In Lagrangian method, the frame of reference is attached to the moving fluid and the observer follows the fluid particles in motion as they move through the given space while in Eulerian methods, reference frame is stationary and the fluid particles are seen by a stationary observer as they move through the given space. ALE method is a combination of Lagrangian and Eulerian methods. Lagrangian methods are briefly discussed in section 2.2.1.1 and a detailed overview of Eulerian methods is given in section 2.2.1.2. ALE method is briefly discussed in section 2.2.1.3. The discussion of these methods in the following sections is restricted to two-dimensional problems unless stated otherwise, with a few remarks about their implementation in three dimensions.

2.2.1.1. Lagrangian methods

In Lagrangian methods, also known as interface tracking or moving mesh or surface methods, the reference frame moves with the fluid so that the fluid elements are always contained in the same elements. In these methods, mesh nodes always move along with the fluid particles with which they are associated. Interfaces are marked and tracked with calculations only on one phase based on the following conditions [48]:

1. Free surface is a sharp interface between two immiscible fluids without any flow across the interface (interface kinematic condition)
2. Forces acting on the free surface are in equilibrium (interface dynamic condition)

Lagrangian description of kinematics has certain advantages that make it a preferred method for problems with small displacements. In Lagrangian methods, it is easy to track free surfaces or interfaces between two immiscible fluids and to define their shapes. It also makes it easy to work with materials having history-dependent constitutive relations. However, in the case of large distortions in the continuum, there may be sizeable changes in the size and shape of mesh elements thereby requiring frequent remeshing operations [47].

2.2.1.2. Eulerian methods

In the Eulerian methods, a reference frame is chosen which employs a fixed or a static mesh through which the fluid moves under a given or computed velocity field. The advantages of this method include its ability to preserve mesh regularity i.e. its ability to handle large distortions in the continuum without any recourse to remeshing. This feature of the Eulerian methods is helpful in problems involving free boundaries, especially when the free boundaries undergo such large deformations that the Lagrangian methods cannot be used [46]. However, this comes at the expense of the resolution of the flow details and precise definition of the interfaces [47]. The accuracy of the interface position is limited by the mesh size.

In Eulerian fluid elements, body and surface forces are computed analogously to Lagrangian fluid elements. However, Eulerian methods differ in the manner in which fluid elements are moved to next positions using computed velocities at every time step [46]. In the Lagrangian method the mesh elements simply translate with the fluid velocity while in Eulerian case the mesh remains fixed and the fluid moves through the mesh elements. In order to advance a free moving interface in an element using the Eulerian method, flow properties such as viscosity and density in the element need to be averaged using the properties of the fluids on either side of the interface. This inherent averaging of flow properties for approximating the convective flux is one of the biggest shortcomings of Eulerian methods. This results in smoothing of the variations in flow quantities and a loss of resolution for free boundaries [46]. As noted above, the averaging process in Eulerian methods results in loss of resolution and in particular, blurring of discontinuities in case of free boundaries. This problem is overcome by introducing a treatment that identifies a discontinuity at free boundaries and prevents averaging of the flow properties across it [46].

Various Eulerian methods for tracking moving interfaces and free boundaries have been proposed. Sections 2.2.1.2.1 through 2.2.1.2.7 provide brief descriptions of selected methods used to predict the evolution of free moving interfaces in an Eulerian frame of reference. Advantages and disadvantages associated with each one of these methods are also discussed briefly in each section.

2.2.1.2.1. Height function method

A free boundary can be represented simply by defining its distance from a reference line as a function of position along the reference line. In case of a rectangular mesh with elements having width δx and height δy, the height of the free surface h from the bottom of the mesh can be defined for each column of elements. Such a description would approximate a curve $h = f(x,t)$ by assigning the values of h to discrete values of x [46]. The advantage of this method is its efficiency due to its requirement of only one-dimensional array for storing the values of surface height h. Moreover, the evolution of the height function also requires update of only one-dimensional array (e.g. [49]). However, the method does not work at all for multiple-valued surfaces having more than one y-value for a given x-value such as drops or bubbles, and does not work well when the boundary slope, $\partial h / \partial x$, exceeds the mesh element aspect ratio $\delta y / \delta x$.

For free fluid boundaries, the kinematic equation, Eq. (49) governs the time evolution of the height function.

$$\frac{\partial h}{\partial t} + u\frac{\partial h}{\partial x} = v \tag{49}$$

where (u,v) are components of fluid velocity in (x,y) coordinates. Eq. (49) states that a free fluid boundary moves with the fluid. As can be seen, Eq. (49) is Eulerian in the x direction while Lagrangian in the y direction. The method of the height function can be easily extended from two-dimensions to three-dimensions [50] for single-valued surfaces which can be described by $h = f(x, y, t)$.

2.2.1.2.2. Line segments method

The method of line segments is a generalization of the height function method. It utilizes chains of short line segments or points connected by multiple line segments (for example [51]) instead of a single line. In this method, the coordinates of each point need to be stored and for accuracy, the distance between the neighboring points should be less than the minimum mesh size,

δx or δy . This requires additional memory space for this method, but it is not limited to single-valued surfaces [46]. A chain of line segments evolves in time by moving with the fluid velocity determined by the interpolation in the surrounding mesh. This resembles the evolution of a Lagrangian mesh line. The chain of line segments is more flexible than a single line, because individual segments maybe easily added or deleted to get the desired resolution of the free boundary. One of the difficulties arises when two surfaces intersect or when a surface folds over itself. In such a case, segment chains can be reordered with possible addition or deletion of chains. However, in a general case, the identification of intersections and the decision on how a reordering should be performed is not trivial [46]. The applicability of the method is limited to two-dimensional analyses and cannot be easily extended to three dimensions because linear ordering of two-dimensional lines does not work for three-dimensional [52]. Consequently, identification of surface intersections and addition-deletion algorithms are more complex.

2.2.1.2.3. Level-set method

In the level-set method, interface is defined as the zero level set of a distance function from the interface [53]. This distance function Υ is a signed function that has a positive sign on one side of the interface and a negative sign on the other side. This function is a scalar variable which is advected with the local fluid velocity following the scalar transport equation, which is given by:

$$\frac{\partial \Upsilon}{\partial t} + \mathbf{v} \cdot \nabla \Upsilon = 0 \tag{50}$$

Level-set method is conceptually simple and relatively easy to implement and gives accurate results when the interface is advected parallel to one of the coordinate axes. However, when there is significant vorticity present in the flow or for significantly deformed interfaces, the method results in a loss of mass (or volume) [54].

2.2.1.2.4. Marker and cell (MAC) method

The marker and cell (MAC) method is one of the first methods that were developed to deal with free moving interfaces [55, 56]. In the MAC method, a fluid filled region is defined instead of a free surface as in the method of height function or the method of line segments. This method has been applied for numerical solution of problems concerning time-dependent, viscous flows of an incompressible fluid in several space dimensions. In this method, a Lagrangian set of marker particles is introduced to designate empty and fluid filled regions and the finite difference

approximation is employed on an Eulerian mesh to obtain the changes in the fluid configuration [57]. Surfaces or interfaces between immiscible fluids are defined by identifying the 'boundaries' dividing the regions with and without marker particles. An element containing marker particles with a neighboring element without any marker particles is marked as an element having the interface. Precise location of the free interface within the element can be determined by analyzing the distribution of the marker particles within the element and appropriate interface boundary conditions for the flow equations can be applied based on this information [58]. An interlaced grid system with pressure placed at the element center and velocity components centered at the element sides is used. This permits rigorous internal momentum conservation with minimal participation of neighboring elements and reduces the averaging usually required for computing the values of the variables at grid points where variables are not explicitly defined. Only such a grid allows the continuity equation to achieve a unique exact form [57].

In the MAC method, all elements in the computational domain are 'flagged'. The cells at the boundary of the computational domain are flagged as 'boundary' cells while interior cells filled with the fluid are marked as 'full', empty cells (cells not containing the fluid) are marked as 'empty' and cells containing the fluid and having at least one face contiguous with an empty cell are marked as 'surface' cells. Marker particles are created and their coordinates are stored for future reference. In the time-stepping loop, new velocity field is computed at every step and marker particles are advanced through the cells with this new velocity field. As the marker particles move through the cells filling up empty cells, cell flags are updated accordingly.

The method has been successful in treating transient incompressible viscous flows with free surfaces encountered in hydraulics, such as the splash of a falling column of water, draining of a tank, dam breaking, flow over an underwater obstacle, etc [57]. The method has also been applied to the problem of laminar mixing of two immiscible Newtonian fluids being sheared in a cavity with a moving and a fixed wall. The evolving interface between the two immiscible fluids which were initially stratified in the cavity was obtained as a function of time, processing conditions, and the ratio of the viscosities of the two fluids [59]. The method can also be easily extended to three-dimensional problems, although with added storage requirements because of the large increase in number of point coordinates corresponding to marker particles and high computational times [46, 60]. Due to finite number density of marker particles, false regions of empty spaces or voids may be generated in high shear regions of fluid flow (and hence high fluid extension). Another difficulty arises in obtaining good quantitative information on the orientation of the interface or partial cell

volume using this method, and applying free surface boundary conditions, especially pressure [61]. They are applied approximately often leading to instability at the free surface [61].

2.2.1.2.5. Flow analysis network (FAN) method

Flow Analysis Network (FAN) method is a simplified mathematical model that predicts the overall filling pattern in thin molds of some complexity for two dimensional, quasi steady-state and isothermal flows [62]. In the FAN approach, a parameter F_{fill} is defined that represents the ratio of the filled volume to the total volume in each control volume and is computed based on the net flow rates into each partially filled control volume [63]. Pressure distribution is obtained by dividing the flow region into a mesh of square elements with a node at the center of the element. Links with specified flow resistance interconnect adjacent nodes. The flow resistance of the links is determined by the local separation of the mold walls and the fluid flows through a network of links and nodes. When a melt front node is filled with the fluid, a value of one is assigned to the parameter F_{fill} at that location and the neighboring nodes in the flow direction become the new melt front nodes. The melt front nodes are convected from the starting node until the cavity is completely filled [64]. The method has good predictive capabilities under isothermal conditions. For filling conditions where no large melt temperature drops are expected, the advance of the flow front(s) and the locations of the weld lines can be predicted fairly well. Simulations with the FAN method also support the predictions that the overall filling patterns and flow front shapes are only a mild function of non-Newtonian nature of the filling fluids [57].

2.2.1.2.6. Volume of Fluid (VOF) method

A common method used to track advancing fronts is known as the Volume of fluid (VOF) method [46, 65]. In the VOF method, in every element of the computational mesh, a marker concentration function F (also known as color function or volume function or phase indicator function) denotes the proportion of volume filled by the fluid. The average value of F in an element represents the fractional volume of the element filled with the fluid. All the elements with the average value of F equal to unity represent fluid filled elements while the elements having an average value of zero for F represent empty elements. The elements having a value of F between zero and unity represent elements containing the free interface. Thus the location and the direction of steep gradients in F determine the location and the normal direction of the interface. Evolution of F is given by the transport equation (Eq. (50)) with Υ replaced by F as below:

$$\frac{\partial F}{\partial t} + \mathbf{v} \cdot \nabla F = 0 \tag{51}$$

where **v** is the velocity vector computed at time *t*. With the known values of *F* and the normal direction, a line that approximates the interface is constructed parallel to one of the coordinate axes through the elements containing the interface. Interface normal components are approximated from the neighboring elements; and based on relative magnitudes of these components, the interface normal is aligned parallel to one of the coordinate axes. This approximate interface location is then used to apply the velocity and other boundary conditions for mass and momentum balance equations. Eq. (51) states that *F* moves with the fluid and is the partial differential analog of marker particles. For a Lagrangian mesh, Eq. (51) reduces to the statement that *F* is constant in each cell and serves as a marker for fluid containing cells.

The VOF method [52] provides similar information about the interface as the marker and cell method while requiring storage for only one variable which is consistent with the storage requirements for all other dependent variables [46]. This conservative use of resources is highly advantageous in multi-dimensional computations. In principle, the method is applicable in tracking surfaces of discontinuity in material properties, tangential velocity, or any other property [46]. VOF method is a popular way for filling simulations in forming operations due to its simple representation of the free surface and it has been applied to existing numerical codes [66].

The problem of averaging of flow properties inside elements in the Eulerian methods is overcome in the VOF method by introducing a treatment that identifies a discontinuity at free boundaries and prevents averaging of the flow properties across it [46]. However, standard finite difference schemes or lower order schemes such as first order upwind method result in smearing of the function *F* due to numerical diffusion and standard higher order schemes result in numerical oscillations [54]. Thus, various volume advection schemes have been proposed for finite volume and finite difference meshes to keep the interfaces sharp and produce monotonic profiles of the function, *F*. Some of these schemes are donor-acceptor scheme [46], flux corrected transport [67], Lagrangian piecewise linear interface construction (PLIC) [68], simple line interface calculation (SLIC) [69], Young's method [70], compressive interface capturing scheme for arbitrary meshes (CICSAM) [71], and inter-gamma compressive scheme [72]. In the following sections, these methods are described in some detail.

2.2.1.2.6.1. Donor-acceptor scheme

In the Hirt and Nichols' VOF method [46], the interface is approximately constructed parallel to one of the coordinate axes. For fluxes in the direction perpendicular to the approximate interface, a donor-acceptor scheme is used while for calculating fluxes in the direction parallel to the interface, upwind fluxes are used. The method determines the slope of the interface and switches to upwind differencing when the smallest angle between the face of the control volume and the interface is more than 45^{O}. Figure 2.3 shows an example of a fluid configuration with a positive x-velocity at the face i+1/2. Element (i,j) and the downwind element (i+1, j) are both partially filled and $F_{i,j} > F_{i+1,j}$. Using the VOF scheme, reconstruction of the interface in element (i,j) is vertical. The donor-acceptor scheme computes the amount of F fluxed across the element face (i+1/2,j) in time step δt as [61]:

$$Q_{i+1/2,j} = \delta y\{MIN[F_{i,j}\delta x, U_{i+1/2,j}F_{i+1,j}\delta t + MAX(0.0, U_{i+1/2,j}(1.0 - F_{i+1,j})\delta t - (1.0 - F_{i,j})\delta x)]\} \quad (52)$$

The terms in the right hand side of Eq. (52) are:

i. $F_{i,j}\delta x$, the maximum amount of fluid available for the outgoing flux from the element (i, j)

ii. $U_{i+1/2,j}F_{i+1/2,j}\delta t$, the downwind approximation of F fluxed across the face $(i+1/2, j)$

iii. $U_{i+1/2,j}(1.0 - F_{i+1,j})\delta t$, the downwind approximation of the air fluxed across the face $(i+1/2, j)$

iv. $(1.0 - F_{i,j})\delta x$, the maximum amount of air that can be fluxed out from the element (i, j)

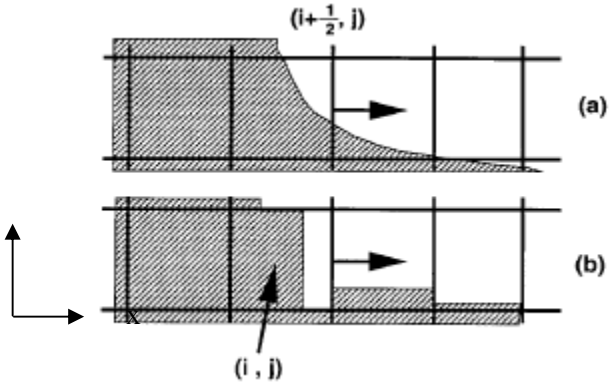

Figure 2.3 (a) True interface configuration and (b) interface reconstruction for Hirt-Nichols VOF [61]. Shaded region represents fluid while non-shaded region represents air.

The MIN function in Eq. (52) prevents the flux of more fluid through the face $(i+1/2, j)$ from the donor element (i, j) than that exists inside the element. In the process of fluxing out the fluid from the donor element, the air also gets fluxed out and MAX function ensures that the air that is fluxed out is not more than the air that exists inside element (i, j). The method combines first-order up and downwind fluxes in such a way as to minimize diffusion and ensure stability. The method can be considered as a flux-corrected algorithm in which MIN and Max functions limit the non-monotonic downwind flux of fluid ensuring that no new extrema is created in the element.

2.2.1.2.6.2. Flux-corrected transport

Flux-corrected transport (FCT) is a scheme that is based on a combination of upwind and downwind fluxes such that it eliminates both the instability of the downwind scheme and the diffusiveness of the upwind scheme. It is built on the idea of adjusting fluxes calculated with a non-monotonic higher order advection scheme to improve the monotonicity of the final solution [67, 73]. The scheme comprises several stages of calculation. First, an intermediate value of *F*, denoted by F^*, is calculated using a diffusive monotonic advection scheme. The solution scheme for one-dimensional version of Eq. (51) at time level *n* for mesh element *i* can be written as:

$$F_i^* = F_i^n - \frac{1}{\delta x}\left(Q_{i+1/2}^L - Q_{i-1/2}^L\right) \tag{53}$$

where Q^L is the lower-order flux. An anti-diffusive flux is then defined in an attempt to correct the numerical diffusion resulting from the lower order solution scheme. This anti-diffusive flux, denoted by Q^A is initially approximated as the difference between higher and lower order flux approximations:

$$Q_{i+1/2}^A = Q_{i+1/2}^H - Q_{i+1/2}^L \tag{54}$$

Application of this anti-diffusive flux in its entirety results in an unstable higher order flux being used introducing numerical oscillations, and thus it is limited by introducing correction factors, denoted by *q*. The correction factors are so as to ensure that no new extrema are introduced in the solution after applying anti-diffusive fluxes. The range of fluxes allowed for a mesh element *i* is based on the values of F^n and F^* in element i and its two neighboring elements, $i-1$ and $i+1$.

Details of the method for limiting fluxes can be found elsewhere [73]. The final step in FCT method is to apply the corrected anti-diffusive fluxes and obtain the values of F at the new time level:

$$F_i^{n+1} = F_i^* - \frac{\left(q_{i+1/2}Q_{i+1/2}^A - q_{i-1/2}Q_{i-1/2}^A\right)}{\delta x} \tag{55}$$

Multi-dimensional FCT-VOF

The one-dimensional FCT scheme can be extended to two-dimensions in two ways, The first one is by using the fully two-dimensional FCT algorithm [73] and the second is by implementing a direction-split implementation [61].

In the two-dimensional algorithm, an approximate value of F is calculated by two-dimensional fluxing using the lower order solution scheme. The anti-diffusive fluxes are then estimated and limited using F^n and F^* in five-neighborhood of the element. Rudman tested this scheme with the advection of a 2-D step function in a uniform velocity field. The interface remained extremely thin but the interface shape was not maintained. The key source of error in two-dimensional scheme comes from the limiting of fluxes, in which the direction of the major component of the diffusive error cannot be determined [61].

In direction-split implementation in two dimensions, the entire mesh is swept in the *x*-direction using the 1D algorithm, updating F, followed by a sweep in the *y*-direction [61]. The order of sweeps in *x*- and *y*-directions is interchanged at every time step to avoid introduction of a systematic error. In this method, a problem is encountered that is not seen in Zalesak's multi-dimensional algorithm. After the first sweep, values of F may exceed the value of unity resulting in a problem in the next step because these values greater than unity are used in calculating the fluxes for the next time step. This results in the elements in the fluid domain attaining F values less than unity, which is unacceptable. One of the ways to overcome this problem is to make allowance for effective change in the area of an element during each one-dimensional sweep of the mesh. Letting $\delta a_{i,j} = \delta x \delta y$ be the area of the element (i, j) at the beginning of each time step, the following calculations are made for the x-sweep:

$$\widetilde{F}_{i,j} = F^n_{i,j}\delta a^n_{i,j} - (Q^x_{i+1/2,j} - Q^x_{i-1/2,j}),$$
$$\delta a^{n+1/2}_{i,j} = \delta a^n_{i,j} - \delta t\delta y(u_{i+1/2,j} - u_{i-1/2,j}), \tag{56}$$
$$F^{n+1/2}_{i,j} = \frac{\widetilde{F}_{i,j}}{\delta a^{n+1/2}_{i,j}}.$$

Similar calculations are performed in the y-sweep. After the two sweeps, $\delta a_{i,j}$ is set equal to $\delta x\delta y$. This scheme is equivalent to solving Eq. (57) in the x-direction with an analogous equation in the y-direction.

$$\frac{\partial F}{\partial t} + \frac{\partial uF}{\partial x} = F\frac{\partial u}{\partial x} \tag{57}$$

It is important to calculate the element volume change occurring in each one-directional sweep when calculating the lower order diffused solution F^*, because otherwise the integrity of the method is severely degraded. One last correction to avoid accumulation of round-off errors and boundedness of the solution, is implemented at every time step, which is that all the negative F-values are set to zero and all the F-values greater than unity are set to unity. However, if such a procedure is not implemented, the values of F used in the calculation of up and downwind fluxes should be limited to the range [0, 1].

2.2.1.2.6.3. Simple line interface calculation (SLIC)

In the simple line interface calculation method, the interface in an element is reconstructed with a straight line parallel to one of the coordinate axes [69]. The method uses a direction-split scheme and in each direction sweep, only element neighbors in the direction of the sweep are considered for interface reconstruction. Because only element neighbors in the flux direction are considered for flux calculations, it is possible that an interface containing element may have different representations for each direction sweep as shown in Figure 2.4 (b and c). For the case of interface reconstruction between two fluids, there are nine possible interface element configurations, which reduce to three basic cases for flux determination. Details of these possible configurations are available elsewhere [69]. After approximate interface reconstruction, fluxes are geometrically calculated for each fluid.

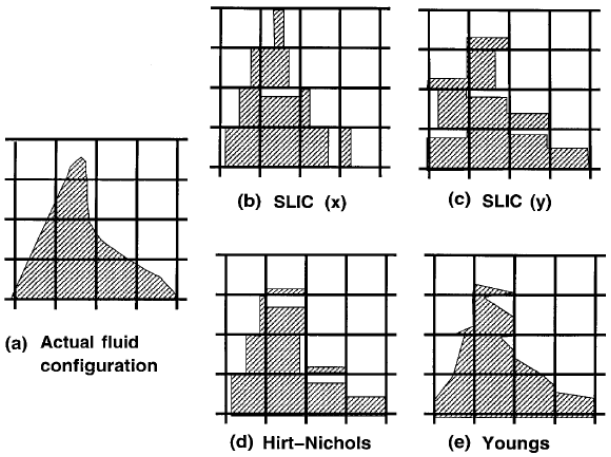

Figure 2.4 Interface reconstructions of actual fluid configuration show in (a): (b,c) SLIC (*x*- and *y*- sweep respectively); (d) Donor-acceptor scheme; (e) Young's method [61]

2.2.1.2.6.4. Young's method

Young's VOF (Y-VOF) method has more accurate interface reconstruction than Hirt-Nichol's VOF or SLIC [61]. Young's method is a direction-split method in which the interface normal, β, is first estimated [70]. The interface location in an element is then approximated by a straight line with an orientation β and cutting the element such that the fraction of the element filled by the fluid is equal to $F_{i,j}$.The geometry of the resulting fluid 'polygon' is then used to determine the fluxes of F through any of the element faces on which the velocity is directed out of the element. Compressive interface capturing scheme for arbitrary meshes (CICSAM)

CICSAM [74] is a high-resolution differencing scheme that falls in the category of composite schemes. Composite schemes were introduced to solve local boundedness which is not preserved in previous VOF schemes. CICSAM uses the concept of normalized variable diagram (NVD) [75] for applying boundedness criteria, in a discretized form of convection equation [76]. NVD is used to define a normalized expression for the volume fractions of donor elements and the element face, respectively as:

$$\widetilde{F}_D = \frac{F_D - F_U}{F_A - F_U} \tag{58}$$

$$\widetilde{F}_f = \frac{F_f - F_U}{F_A - F_U} \tag{59}$$

where subscripts A, D, U represent acceptor, donor and upwind elements as shown in

Figure 2.5.

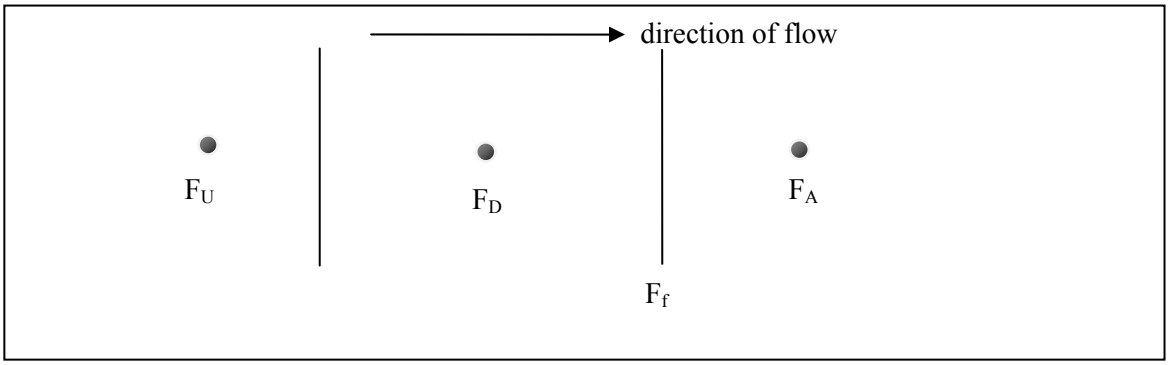

Figure 2.5 One-dimensional control volume.

CICSAM uses convection boundedness criteria (CBC) [77], shown in Figure 2.6, as the most compressive scheme with robust local bounds on $\widetilde{F}_f$ in order to reduce numerical diffusion. For explicit flow calculations, this can be represented as:

$$\widetilde{F}_{f_{CBC}} = \begin{cases} \min\left\{1, \dfrac{\widetilde{F}_D}{C_f}\right\} & when \quad 0 \le \widetilde{F}_D \le 1 \\ \widetilde{F}_D & when \quad \widetilde{F}_D \le 0, \widetilde{F}_D > 1 \end{cases} \tag{60}$$

where C_f is the Courant number defined at the face f as $C_f = \left|u_f\right| \delta t / \delta x$.

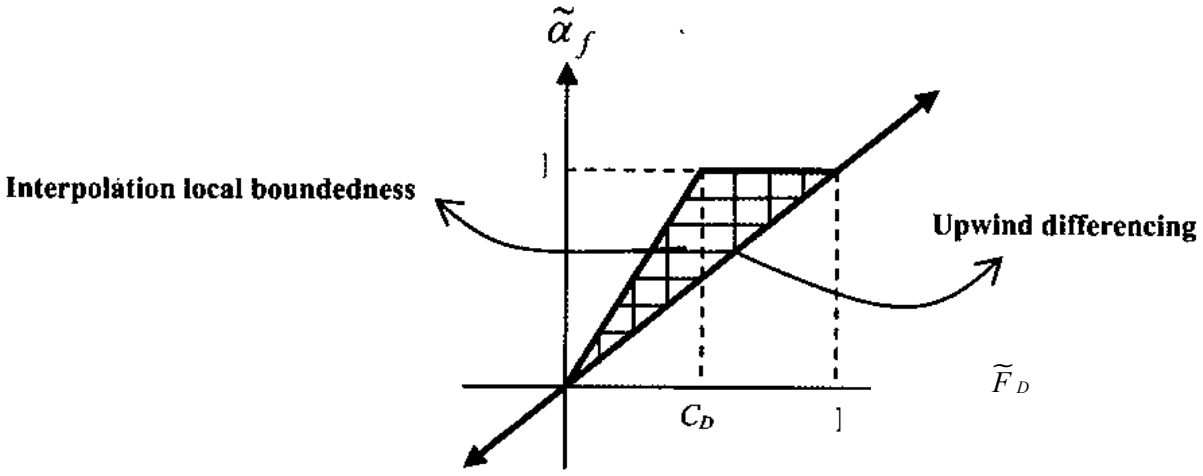

Figure 2.6 Convection boundedness criteria for explicit flow calculations [48].

CBC is a very compressive scheme and wrinkles the interface because it tends to compress any gradient into a step profile, even when the slope of the interface is almost tangential to the flow direction [46, 54]. So, CICSAM should be switched to another scheme known as the Ultimate-Quickest (UQ) [75] when the interface slope is tangential to the flow direction. UQ scheme, in the explicit form, can be represented as:

$$\widetilde{F}_{f_{UQ}} = \begin{cases} \min\left\{\dfrac{8C_f\widetilde{F}_D + (1-C_f)(6\widetilde{F}_D+3)}{8}, \widetilde{F}_{f_{CBC}}\right\} & when \quad 0 \le \widetilde{F}_D \le 1 \\ \widetilde{F}_D & when \quad \widetilde{F}_D \le 0, \widetilde{F}_D > 1 \end{cases} \tag{61}$$

A weighting factor in the range [0, 1] is introduced to switch between more compressive CBC scheme and less compressive UQ scheme as the angle between the slope of the interface and the flow direction changes from 90^o to 0^o, respectively.

When used for simple advection and other more real tests, CICSAM scheme is very accurate in keeping the interface sharp. The scheme is derived for arbitrary meshes and is flexible in terms of boundary fitted grid usage. In terms of mass loss, the errors for different test cases show that the scheme is fairly mass conservative. However, the limitation of the scheme is that the boundedness of the scheme is dependent on the local Courant number, and thus requiring very small time steps to keep the interface sharp (a sharp interface is an interface for which the gradient of the

volume fraction across the interface is very steep). For 1D problems, Courant number limit is Co < 1/2 while in multi-dimensions, Courant number limit is Co < 1/3 [54].

2.2.1.2.6.5. Inter-gamma differencing method

The inter-gamma differencing method [72] achieves the necessary compression of interface by introducing an extra, artificial compression term in the original transport equation, Eq. (51) instead of just using a compressive differencing scheme. The transport equation is modified as:

$$\frac{\partial F}{\partial t} + \nabla \cdot (\mathbf{v}F) + \nabla \cdot (\mathbf{v}^r F(1-F)) = 0 \tag{62}$$

where $\mathbf{v}^r$ is a velocity field introduced to compress the interface. This artificial term is active only in the interface region. There can be many possible formulations for $\mathbf{v}^r$. Rusche et al. [78] used Inter-gamma differencing method for interface capturing in two-phase flows and used a formulation for $\mathbf{v}^r$ based on maximum velocity magnitude in the interface region $(0 < F < 1)$. Since the compression is required to act perpendicular to the interface, maximum velocity magnitude was multiplied by the normal vector of the interface to get the maximum magnitude in the direction perpendicular to the interface. The inter-gamma differencing scheme bounds the solution to Eq. (62) between zero and one. Eq. (62) is rewritten in a modified form which is discretized and solved using inter gamma differencing scheme. The scheme is based on the donor-acceptor formulation of Leonard's normalized variable diagram [79]. The variables and the arrangement of the control volume is similar to the one used in CICSAM approach. The results of simple advection tests show that the scheme is highly dependent on CFL numbers limiting the time steps to very small values in order to get sharp interfaces. More practical test cases using low CFL numbers result in very good resolution of interface. Moreover, the method is completely mass conservative as there is no mass addition or deletion [54].

2.2.1.2.7. Pseudoconcentration method

The pseudoconcentration (PC) method [12] is related to the VOF method. However, in contrast with the VOF method which takes into account geometrical configurations, this method takes an algebraic approach and solves the transport equation, Eq. (51) numerically without any special geometrical treatment. The flow problem is solved on a fixed mesh that covers the entire domain that gets filled by the flowing fluid, namely polymer melt in the case of mold filling problems. In the context of mold-filling by a polymer melt, a fictitious fluid is introduced that

represents air downstream of the melt- air interface [80]. The density of the fictitious fluid is chosen to be similar to that of the air and viscosity is chosen such that it is small enough compared to the melt viscosity (about 10^{-3} times the polymer viscosity) in order to mimic the inviscid nature of air but still large enough (many orders of magnitude higher than air) to maintain numerical stability. We will call this fictitious fluid 'air' from now on. With this selection, the contribution of the air to pressure buildup in the mold is negligible as compared to that of the melt. Moreover, inertia for air is negligible and Reynolds number is small. This air is allowed to leave the mold at specified outlets or vents. The material label is a continuous function bounded by zero and one and is known as the pseudoconcentration function. This material label takes the value $F = 1$ for completely fluid filled regions, $F = 0$ for completely air filled regions and $F = 0.5$ defines the melt-air interface. This interface moves with the fluid as the material labels are convected with the local fluid velocity.

Material parameters such as viscosity and density are defined as discontinuous functions of pseudoconcentration as below:

$$\eta = \eta(F) = \begin{cases} \eta_{polymer} & if\ F \geq 0.5 \\ \eta_{air} & if\ F < 0.5 \end{cases} \tag{63}$$

Because quadratic shape functions are used for the pseudoconcentration field, negative values for material property such as viscosity and density may be encountered. This is avoided by piece-wise linear interpolation of the material properties at midpoints of the elements containing the interface [81] as shown in Figure 2.7.

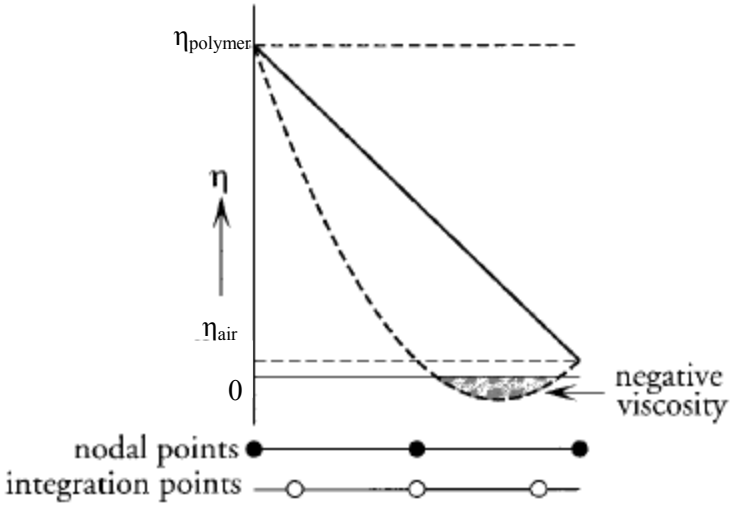

Figure 2.7 Piecewise linear interpolation of viscosity on a quadrilateral element to avoid negative values: original function (dashed line) and interpolated function (solid line) [12].

The advantages of the pseudoconcentration method over the VOF method are [82]:

1. The pseudoconcentration method makes use of an algebraic approach as compared to the VOF method which uses geometrical calculations to calculate fluxes across elements. In the pseudoconcentration method, a hyperbolic equation is directly solved to get the position of the flow front without the need for treatment of special cases or to define how volumes are filled since these equations use finite element basis functions.

2. Because a finite element scheme is used to solve a hyperbolic equation, it is easy to implement higher order schemes just by the choice of the basis functions.

3. The pseudoconcentration method is easy to implement in the discontinuous Galerkin finite element method (DGFEM) scheme and directly determines the shape and the position of the advancing front by solving the hyperbolic transport equation. The discontinuous Petrov-Galerkin formulation that is used to solve the hyperbolic differential equation is stable even for local CFL numbers greater than one [83].

In this work, we have used the pseudoconcentration method for the evolution of the advancing front due to its several advantages over other methods as listed above. The mass and momentum balance equations are solved with the boundary conditions specific to the pseudoconcentration method. The boundary conditions for the balance equations are discussed in section 2.1.1.2.

2.2.1.3. Arbitrary Lagrangian Eulerian methods

The arbitrary Lagrangian Eulerian (ALE) methods combine the advantages of the Lagrangian and the Eulerian methods while reducing their drawbacks [47, 84]. ALE methods include adaptive grid regeneration methods that involve remeshing at every time step. The mesh covers the filling fluid area and the flow equations are solved for this domain with appropriate boundary conditions. In addition to the continuity equation and stress balance equations, an equation for the mesh velocity is also solved at every time step and a convective velocity $\mathbf{v}_c$ is defined as

$$\mathbf{v}_c = \mathbf{v} - \mathbf{v}_m \tag{64}$$

where $\mathbf{v}$ is the fluid velocity and $\mathbf{v}_m$ is the mesh velocity. Such methods have been in use for two-dimensional simulations of mold filling processes. ALE description of kinematics comes in handy for moving boundary problems because in ALE formulation of the mesh following the moving boundaries is allowed while maintaining the regularity of the mesh [85]. In finite element formulations of ALE methods, nodes can either stay fixed or move with the fluid velocity at the nodes or move with a mesh velocity that is different from nodal velocity of the fluid providing a continuous remeshing capability [47, 86]. This ability of continuous remeshing at every time step gives the technique the capability of maintaining reasonable shapes for the elements while allowing for almost accurate description of free boundaries [87]. This gives the ALE formulation the advantage of easy tracking of moving surfaces while handling large distortions relatively easily [47]. Other advantages include the capability of the technique to keep mesh connectivity and the number of degrees of freedom constant during remeshing steps, and a reduction in computational cost [86].

2.2.2. Total variance diminishing (TVD) time discretizations

The solution to hyperbolic conservation laws such as Eq. (51) may develop discontinuities such as contact discontinuities and shocks, etc. even if the initial condition is a smooth function. Standard finite difference methods are not suitable for such equations, even if linearly stable and give poor results in the presence of shocks and other discontinuities [88]. Various methods have been proposed for constructing efficient time discretization schemes to solve Eq. (51) such as total variance diminishing (TVD), total variation bounded (TVB) and essentially non-oscillatory (ENO) methods. Eq. (51) is written here in the form:

$$F_t + \sum_{i=1}^{d} f_i(F)_{x_i} = 0, \qquad F(\mathbf{x},0) = F_0(\mathbf{x}) \tag{65}$$

where $\mathbf{x} = (x^1, x^2, ..., x^d)$, and any real combination of the Jacobian matrices $\sum_{i=1}^{d} \xi_i (\partial f_i / \partial F)$ has m real eigenvalues and a complete set of eigenvectors. Given a computational grid $x_j = j \cdot \Delta x,\ t_n = n\Delta t$. F_j^n represents the computed approximation to the exact solution $F(x_j, t_n)$ of Eq. (65). The above equation can be written in abstract from as

$$F_t = L(F) \tag{66}$$

where L is a spatial operator. For a hyperbolic conservation equation such as Eq. (65), Shu and Osher [88] use a conservative scheme:

$$F_j^{n+1} = F_j^n - \lambda(\hat{f}_{j+1/2} - \hat{f}_{j-1/2}), \qquad \lambda = \Delta t / \Delta x \tag{67}$$

with a consistent numerical flux given by

$$\hat{f}_{j+1/2} = \hat{f}(F_{j-1}, ..., F_{j+k}); \tag{68}$$

The total variation of a discrete scalar solution of above equation is given by

$$TV(F) = \sum_j \left| F_{j+1} - F_j \right| \tag{69}$$

The scheme can be said to be TVD if

$$TV(F^{n+1}) \le TV(F^n) \tag{70}$$

Runge Kutta methods are used to discretize Eq. (65), and the goal is to get a fully r^{th} order approximation to the differential equation of the form (66), giving

$$F^{n+1} = S(F^n) \tag{71}$$

where S is a linear expression. After algebraic manipulations using Taylor expansions, and manipulations of possible parameters, Shu and Osher [88] have suggested the following schemes:

:

1. Second order case, $m = 1$,

$$F^{(1)} = F^{(0)} + \Delta t L(F^{(0)})$$
$$F^{(2)} = \frac{1}{2}F^{(0)} + \frac{1}{2}F^{(1)} + \frac{1}{2}\Delta t L(F^{(1)}) \tag{72}$$

CFL coefficient = 1

2. Third order case, $m = 2$,

$$F^{(1)} = F^{(0)} + \Delta t L(F^{(0)})$$
$$F^{(2)} = \frac{3}{4}F^{(0)} + \frac{1}{4}F^{(1)} + \frac{1}{4}\Delta t L(F^{(1)}) \tag{73}$$
$$F^{(3)} = \frac{1}{3}F^{(0)} + \frac{2}{3}F^{(2)} + \frac{2}{3}\Delta t L(F^{(2)})$$

CFL coefficient = 1

For higher order cases, TVD schemes can increase CFL coefficients to at most slightly above 2/3. Results of numerical experiments with TVD schemes indicate good shock transitions without any noticeable oscillations and high accuracy in smooth regions, although contact discontinuities are more smeared than shocks [88].

The advantage of TVD schemes is high-order accuracy in smooth regions while resolving discontinuities without spurious oscillations. Moreover TVD schemes have a convergent (in L_1^{local}) subsequence as $\Delta x \to 0$ to a weak solution to (65). If an additional entropy condition, that implies uniqueness of weak solution to (65), then the scheme converges. However, the TVD schemes locally degenerate to first-order accuracy at nonsonic critical points [89].

TVD scheme in third order has been used to reduce the oscillations near the interface in mold-filling simulations in 2D geometries. Third order TVD scheme was tested against 2nd order Adams-Bashforth for time-stepping and was found to be more stable allowing for a relatively larger time step [90]. In this work, we have used the explicit TVD scheme of third order which is termed

as Runge Kutta 3rd order total variance diminishing (RK3-TVD) scheme for time integration of the convection problems, namely the transport equation and the orientation equation because of its advantages mentioned above.

2.3 Mold filling simulations of short glass fiber reinforced thermoplastic composites

This section covers a literature review of the numerical simulations and predictions of short glass fiber orientation in mold filling phase during processing of injection molded thermoplastic composites. Complex flow fields exist during the mold filling phase inside mold geometries which induce orientation of the fibers in the final solidified part. The problem of predicting fiber orientation really constitutes of two problems: prediction of correct flow fields by solving the flow equations and prediction of fiber orientation using the orientation models.

Significant amount of work has been done on the prediction of flow fields inside the mold. The focus of most of the studies in mold filling simulations has been on the advancing front and fountain flow in the region behind it. The problem has been solved in various reference frames using different numerical methods, some of which are described in Section 2.2.1. Section 2.3.1 covers the literature review of the advancing front and the fountain flow simulations. Note that these studies were conducted for pure polymers and no fibers were added to the polymer matrix because mold filing phenomenon is a research area in itself.

For past three decades, there has been significant interest in the prediction of fiber orientation in polymer composites. There have been improvements in the models being used for the evolution of fiber orientation and the numerical methods being used to solve the governing equations. Section 2.3.2 covers a review of the work done in numerical prediction of short glass fiber orientation in injection molding flows. The section is subdivided in three sections based on the approach taken for the solution of the flow fields and predictions of fiber orientation based on the solution of the flow fields. Section 2.3.2.1 discusses numerical simulations based on the simplified approach of Hele-Shaw flow approximation, which is a simplified model for solution of flow equations and completely discards the advancing front and the fountain flow phenomenon. This is followed by a discussion of simulations considering the polymer melt-air interface as a free boundary in section 2.3.2.2. These simulations are one step better than Hele-Shaw flow approximations since they incorporate the free-surface nature of the advancing front and show better orientation predictions. In the end, in section 2.3.2.3, a review of fiber orientation predictions

with the moving interface simulations is presented. These simulations consider the free moving interface as part of the continuum and let the flow fields decide the shape and the position of the interface. This is the most natural way of looking at the problem and these methods are the most flexible in terms of their applicability to different geometries.

2.3.1. Mold filling simulations for pure polymer melts

One of the first attempts at solving the Navier-Stokes equations to determine the flow field behind the moving interface was made by Bhattacharji [91] using a Lagrangian frame of reference. Approximate analytical solutions were obtained for the flow of a Newtonian incompressible fluid between parallel plates using full-slip condition at the wall-interface contact point and no slip condition far behind the interface. Kamal et al. [92] used the velocity expressions developed by Bhattacharji and computed the axial velocity in an Eulerian frame of reference. Kamal indicated finite and non-zero velocities at the wall even though an explicit slip boundary condition was not used in the fountain flow region.

Some of the recent work in mold-filling simulations has been done using the level-set method [93-96] for 2D channels and non-isothermal or non-Newtonian effects are investigated. Otmani et al. [93, 94] considered impermeable walls in their simulations and allowed air to leave only at specified air vents. The dynamic Robin boundary condition was imposed at the walls as described in section 2.1.1.2. The free moving interface evolved with time and assumed an almost semi-circular shape. Baltussen et al. [96] explored a range of viscosity ratios of the polymer and the fictitious fluid (representing air) and suggested a ratio of at least 1,000 to achieve a semi-circular shape of the interface. The problem of non-attaching flow for a semi-circular interface was also discussed and the problem was fixed by treating the walls as an interface by setting the level-set function to zero ($\gamma = 0$ is the interface iso-value in the level-set method) at the walls, thereby forcing the fluid to attach to the walls. However, this created the need for mass correction at every time step as some air was converted into polymer near the contact point and a small outflow of the fluid had to be prescribed at the inlet. Also, with this correction, the interface ceased to attach to the wall tangentially, rather a thin section of interface very close to the wall touched the wall almost in a perpendicular direction.

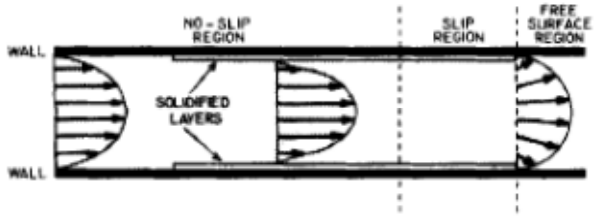

Figure 2.8 Flow regimes divided into two regions: no-slip and slip [92].

Mold filling simulations using the Marker and Cell (MAC) method have also been reported [57, 92, 97]. Mass and momentum balance equations are solved with no-slip boundary conditions at the wall and zero normal or tangential stresses at the interface. The interface evolves under non-equilibrium conditions as the melt front moves into the cavity. Kamal et al. [92] initially prescribed a flat profile for the interface and divided the wall boundary into two regions: no-slip and slip as shown in Figure 2.8.

Slip boundary condition alleviates the singularity at the interface-wall contact point, and thus oscillatory behavior, and also maintains an equilibrium shape of the melt-air interface. The characteristic fountain flow behind the advancing front is predicted and with the slip boundary condition, the fountain flow region goes farther behind the interface when compared to no-slip boundary conditions. The interface takes an almost semi-circular shape as it advances inside the mold.

One of the early techniques for mold filling simulations involves an ALE method with a moving frame of reference [98-100]. A reference frame is chosen that moves with the average fluid velocity in the flow direction. In this frame of reference, walls move backwards with the average velocity of the fluid. The mesh is generated for the entire domain with the geometry shown in Figure 2.9 and mass and momentum balance equations are solved for the fluid contained in this domain.

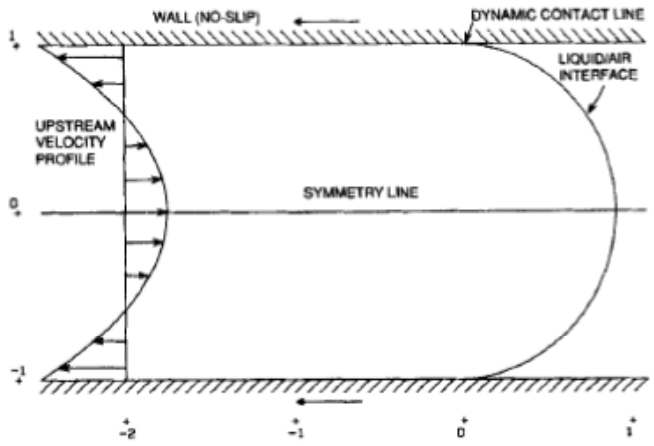

Figure 2.9 Schematic diagram of flow domain in a moving frame of reference [99].

A fully developed one-dimensional shear flow is imposed at the upstream boundary while no slip boundary conditions are imposed at the walls. The interface has an equilibrium shape and stays stationary in the chosen reference frame. For the interface boundary conditions, zero normal and tangential stresses and zero normal velocity through the interface are specified. The solution algorithm first chooses a location of the free surface either by an informed guess (semi-circle) or from previous iterations. Navier-Stokes and continuity equations are solved to give the velocity and pressure fields for the fluid. However, only stress boundary conditions are satisfied. The residual in the velocity boundary condition is used to adjust the location of the free surface and the process is repeated to convergence. With this technique, fountain flow is predicted behind the flow front and the free surface takes an almost semi-circular shape for Newtonian flow as suggested by Tadmor [101] and Hoffman [102].

Recently, Ale method has been used in steady state mold filling simulations [103, 104] with no slip at the mold walls and vanishing stresses at the free surface with no flow across it. Effects of various fluid mechanics parameters (including inertia, gravity, surface tension, compressibility, slip at the wall, etc.) on the fountain flow and the front shape were investigated and the authors concluded that a semi-circle is a good rough approximation of the free surface.

Flux corrected transport method was used in the simulation of fountain flow for viscoelastic fluids [105]. Sato et al. [106] simulated mold filling with this method for an Oldroyd-B fluid using the fringe element generation method. Mass and momentum balance equations were solved with this method using a fully developed Poiseuille flow (parabolic profile) at the inlet of the mold, no slip boundary conditions at the mold walls which were considered impermeable, symmetry

conditions at the centerline, and zero stresses at the interface. The velocity field was initialized as fully developed flow with zero stress in the entire domain. The interface which was initialized as a flat front evolved into a semi-circular shape and characteristic fountain flow was predicted in the region behind the interface. Free interface was approximated by a piece-wise linear segment in each element and fringe elements were generated fitting their one face to the linear free surface. In an interface containing element, three types of fringe elements (denoted by x in Figure 2.10) were formed: bilinear quadrilateral, a linear triangle, or three linear triangle elements as shown in Figure 2.10.

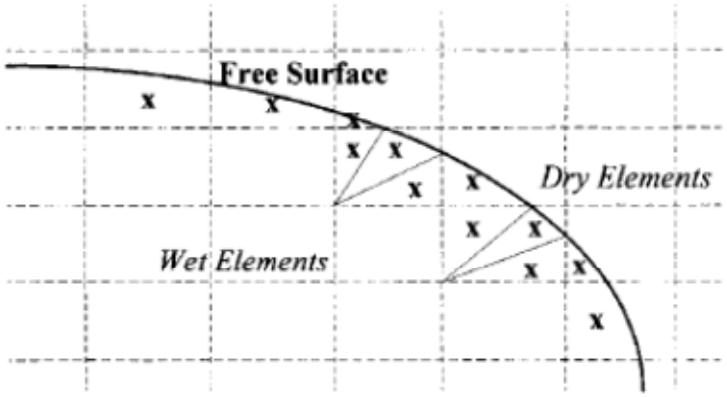

Figure 2.10 Fringe elements (x) in the original mesh (dashed lines) [105]. The interface is shown by the solid curve.

Sato highlighted the advantages of fringe element generation method as good applicability to arbitrarily-shaped molds and an accurate imposition of boundary conditions on the free interface.

The pseudoconcentration method and its variations have been used for mold-filling simulations [45, 80, 81, 107, 108] with different boundary conditions imposed at the mold walls. In Thompson's work [80], a no-slip condition was imposed at those parts of the mold walls that were wetted by the filling fluid without a clear description of the boundary conditions for the fictitious fluid. The mold filling example considered in his work showed a moving contact line that was significantly lagging behind with respect to the flow front. Also, the pseudoconcentration function was a continuously decreasing function that was severely distorted by the convection algorithm and had to be smoothed regularly. There was also a reported mass loss of about 10%. Fortin et al. [81] simulated two-dimensional mold filling of a polymer melt. The fountain flow effect was captured in their simulations with no-slip boundary conditions for the filling fluid, and free stress for the fictitious fluid in both normal and tangential directions. Their simulations with zero normal velocity

for air at the walls failed as a thin layer of air remained at the walls behind the flow front. Hetu et al. [109] imposed the same boundary conditions as did Fortin et al. [81]. However, their flow front results showed material appearing at the locations in the mold where the flow front was not yet reached. Moreover Hetu et al. do not show the fountain flow effect in their simulations. Medale and Jaeger [45] solved the transport equation in a steady flow field only in a small domain in the vicinity of the interface and corrected for mass losses by slightly modifying the value of the material label, $F_{\text{interface}}$, that defines the interface position. They imposed the same boundary condition (Eq. (17)) at the wall in tangential direction as did Haagh with $a = 0.01$.

In Haagh's work, pseudoconcentration technique was implemented for four test cases: filling of an axisymmetric cylinder with a polymer, flow front development in a two-dimensional bifurcation, three-dimensional flow in a rectangular cavity and expelling of a viscous fluid from a tube by a less viscous fluid. As can be noticed from these test cases, they were able to simulate filling of both two- and three-dimensional molds with this method. The fountain flow effect was predicted and a mass loss of about 2-4% was observed and good agreement was seen between the predicted shape and experimentally observed shape of the flow front for a Newtonian fluid filling an axisymmetric cylinder.

The Pseudoconcentration method has been used for filling simulations of 2D and 3D rectangular channels [82, 90, 110] in which the walls were considered solid for the polymer while air was allowed to pass through the walls. This was achieved by prescribing Robin boundary conditions for both normal and tangential components. This allowed for air to pass freely through the walls while retaining the polymer within the domain. Fountain flow was predicted in the region behind the flow front and the front assumed a semi-circular shape as the filling fluid filled the mold. Chung and Kwon [2] and Park and Kwon [1] used the pseudoconcentration method of Haagh and van de Vosse [12] to study mold filling simulation of concentrated fiber suspensions in an axisymmetric diverging flow. Center-gated disk geometry was selected and boundary conditions for all the boundaries were matched with those suggested by Haagh and van de Vosse. Chung et al. [2] showed fountain flow predictions in the region behind the advancing melt-air interface and the interface evolved to assume a shape that was curved but relatively flat at the center, due to deceleration associated with radial diverging flow.

2.3.2. Numerical studies of fiber orientation in injection molded composites

This section covers a literature review of numerical simulation and predictions of short glass fiber orientation in injection molded thermoplastic composites. Numerical predictions of fiber orientation in these processes follow one of the following two approaches: decoupled approach or coupled approach. In decoupled approach, the flow fields are first solved without considering the presence of the fibers and the fiber orientation is post-calculated using the solution of the flow equations. Decoupled approach in simulating fiber orientation has been successful in qualitatively predicting the fiber orientation. However, it fails to quantitatively match the experimentally measured orientation simultaneously in all regions of the mold cavities [111]. In coupled approach, the presence of fibers is taken into account while solving the flow equations. The presence of fibers results in a change in the rheological behavior of the polymer/fiber suspension and alters the viscosity. This change in viscosity due to the presence of fibers results in a change in the flow field and the flow field in turn governs the fiber orientation. This approach is known as coupled approach.

In either case (coupled or decoupled approach) the flow fields are computed either by fully solving the flow equations or by using Hele-Shaw flow approximation. Hele-Shaw flow approximation has been used to qualitatively predict the fiber orientation. However, it ignores some of the characteristic flow features present in the injection molding process such as fountain flow. Fountain flow is observed to play a significant role in the fiber orientation in injection molded parts, especially near the walls [39].

The orientation equations describing the evolution of fiber orientation contain terms that cannot be solved analytically with limited computational resources. Hence, predictions of fiber orientation are usually done by solving these equations numerically, and in some cases, validating the results with the experimental data collected from real injection molded parts or from the literature. Typical test geometries chosen for simulation are center-gated disk and end-gated plaque as shown in Figure 2.11. These geometries are simple enough so that various test cases can be considered because they provide a relatively good understanding of the flow fields and the stresses present during the filling phase. At the same time, these geometries can be directly scaled up to commercial injection molding process because they try to mimic the design and the gating arrangement of the commercial molds. However, experimental studies have been limited in number. One of the most commonly used experimental data for validation in a center-gated disk is that of Bay [39]. Bay used a center-gated disk with inner radius R_i = 3.81 mm, outer radius, R_o = 76.2 mm,

and thickness, $2b$ = 3.18 mm, and an end-gated rectangular plaque with flow direction length L = 203.2 mm, width, w = 25.4 mm, and cavity thickness $2b$ = 3.18 mm. Recently, Garcia [112] reported orientation data for a center-gated disk with inner radius R_i = 2.97 mm, outer radius, R_o =51.53 mm, and thickness, $2b$ = 1.38 mm.

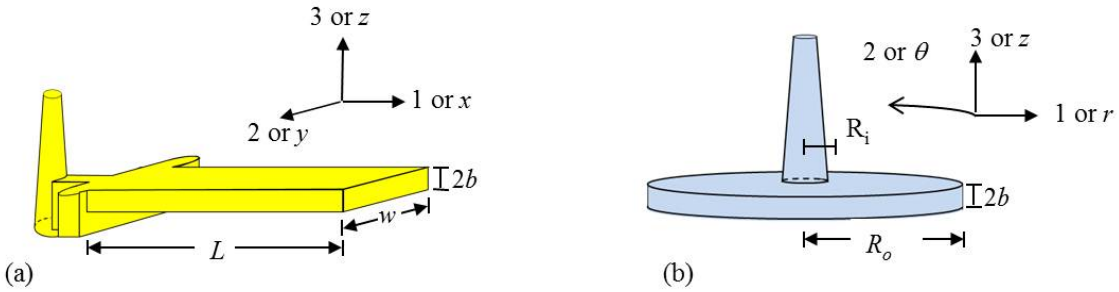

Figure 2.11 Typical geometries used simulations in (a) end gated plaque and (b) center-gated disk.

The most common flow domain considered in the literature for simulations is the mold cavity. However, very few simulations have included runner or the sprue also as part of the flow domain. Figure 2.12 shows the typical domains and the planes used for simulations in center-gated disk and end-gated plaque. The most common plane for both geometries (center-gated disk and end-gated plaque) is the 1,3 plane, though there are publications in which 1,2 planes have also been simulated.

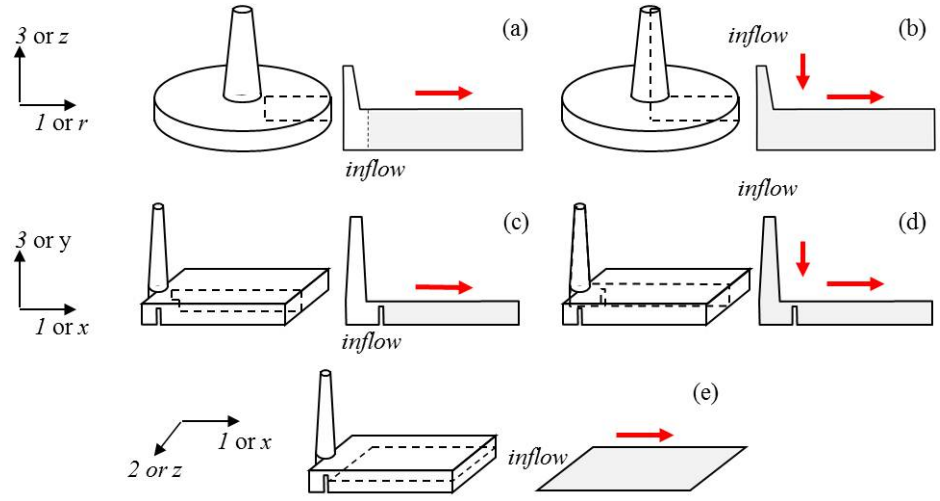

Figure 2.12 Typical planes used as domain for simulations in (a, b) rectangular plaque and (c-e) axisymmetric disk geometries. The arrow indicates the flow direction through the domain and the inflow indicates the location where the inlet conditions have been imposed.

Experimental measurements reveal a layered structure of fiber orientation. A skin layer containing a random planar orientation on the surface is formed due to cooling effects at the mold walls. Beneath the skin layer, a shell layer is observed having fibers aligned mostly in the flow direction due to high shear. At the center of the cavity, most of the fibers are aligned in the transverse direction due to presence of extensional flow around the center of the molds, especially in radial diverging flows. In between the shell and the core layers, a transition layer is observed in which the fiber orientation transitions from aligned in the shell layer to transverse towards the center. The predictions of fiber orientation in this section are reviewed in the context of this shell-transition-core structure.

The following sections review the work done on prediction of fiber orientation based on various approaches taken to solve the flow fields. Section 2.3.2.1 coves numerical simulations based on the simplified approach of Hele-Shaw flow approximation, a simplified model for solution of flow equations that ignores the advancing front and the fountain flow phenomenon. Section 2.3.2.2 reviews the simulations considering the polymer melt-air interface as a free boundary. In the end, in section 2.3.2.3, a review of fiber orientation predictions with the moving interface simulations is presented. These simulations consider the free moving interface as part of the continuum and let the flow fields decide the shape and the position of the interface.

2.3.2.1. Hele-Shaw simulations

Altan [113] used Hele-Shaw flow simulation to predict fiber orientation in the filling of a rectangular channel and a planar converging mold. The flow governing equations were decoupled from fiber orientation equations and an isothermal Newtonian fluid with fiber concentration in the dilute regime was considered. Fiber orientation was calculated for individual fibers along the fiber path at every time step from the velocity field using Jeffrey's model. The fourth order orientation tensor was used to describe the three-dimensional fiber orientation. Sixth order orientation tensor appearing in the orientation model was approximated using the quadratic closure approximation. No slip boundary conditions at the wall and uniform velocity and zero stress were prescribed at the inlet and the outlet. Fibers were introduced at discrete time intervals with random orientation at the inlet. The predictions were shown graphically in terms of the orientation ellipsoids as defined by the second order orientation tensor in planar, transverse and longitudinal directions. In the case of

channel flow, fibers aligned in the flow direction in the shell layers while at the midplane, fibers maintained random orientation. In converging flow, the effect of the extensional flow aligned the fibers along the flow direction. Since the fountain flow effects were ignored in this study, the introduction of the first set of fibers in the flow domain was retarded by a certain amount so that fibers do not reach the flow front region.

Gupta [114] predicted fiber orientation in a thin end-gated cavity by modeling the flow of the suspension as a generalized Hele-Shaw formulation for an incompressible, inelastic, non-Newtonian fluid under non-isothermal conditions. Flow equations were decoupled from the fiber orientation equations. Flow and energy equations were solved together by using hybrid finite element/finite difference scheme [115] with a control-volume approach [116] for handling the melt front advancement. In this approach, nodal fill factor, defined as the filled fraction of the nodal control volume and lies in the range [0,1] is assigned to each node. Nodes having values of fill factor greater than zero and less than unity are considered as the flow front nodes. Nodal fill factor is updated at every time step according to the mass balance in the control volume constructed around each node. The simulations were performed in the plane of the cavity for the planar components of the orientation tensor. Results of the simulations were reported for two levels, mid-plane and the surface of the cavity. Folgar Tucker model was used with $C_I = 0.001$ and hybrid closure approximation for the fourth order orientation tensor. Only in-plane components of the orientation tensor were predicted from the orientation equations while out-of-plane components were assumed in agreement with their values obtained from simple shear flow and numerical experimentation not discussed in the paper. The effect of fountain flow was neglected in this paper. For the elements that were filled during a time step, the orientation tensor was initialized by averaging its values at the same cavitywise location over the neighboring elements that were previously filled. It was found that the cavitywise-converging flow due to the growing layer of solidified polymer at the walls aligns the fibers near the entrance of the mold while near the advancing front, cavitywise-diverging flow due to the diminishing solidified layer tends to align the fibers transverse to the flow. The effect of cavitywise converging-diverging flow was especially found to be significant in thin cavities molded at slow injection speeds due to presence of thicker solidified layers.

Chung and Kwon [117] coupled the flow equations with three dimensional fiber orientation equations for non-isothermal filling of a 2-D and a 3-D mold cavity using Hele-Shaw simulation. Cross model was used for the polymer matrix constitutive equation and Folgar Tucker model was

used for the orientation evolution with hybrid closure for the fourth order orientation tensor and a constant C_I = 0.001. Dinh-Armstrong model [18] was used for the coupling of flow and orientation equations. Finite element / finite difference scheme was employed for the non-isothermal flow equations. Control volume approach was used for the advancement of the flow front. The orientation was calculated at each thickness layer, by using a fourth-order Runge-Kutta method for the time integration. Because of extra viscous contribution from fiber orientation, simulated velocity vector was not in the direction of $-\nabla P$ which is different from a fundamental solution of Hele-Shaw type of flows. An upwinding scheme was adopted for the spatial derivatives in the orientation equation. The authors considered three schemes for the initialization of the orientation in newly filled elements at the flow front: i) by convecting the orientation state at each layer from the neighboring upwind element, ii) by applying the convected fiber orientation from the central layer to all the layers, and iii) by introducing random orientation to all the layers except the central layer, where the convected fiber orientation is applied. The predictions from the three different schemes were found to be indistinguishable from each other and the authors adopted the first scheme for the simulations. A dogbone cavity was selected as a 2-D test geometry. Two inlet conditions for fiber orientation were considered: random and flow-aligned, to assess the effects of the inlet conditions on the final fiber orientation. It was observed that the fiber orientation away from the inlet (gate) is not affected by the inlet conditions. Also, close to the gate, the difference in the orientation for the two cases was much less closer to the walls due to the presence of high shear rates that aligned the fibers in the flow direction. By increasing the fiber volume fraction, velocity profile near the gate was found to be more flattened and by increasing C_I to 0.05, the orientation predictions approached a randomized orientation state.

The scheme developed in [117] was extended to radial diverging flow in a center-gated disk [118] in order to include the in-plane velocity gradients due to the extensional effects in the θ-direction. The inlet conditions for the fiber orientation were determined from steady state solution of orientation equations using hybrid closure and C_I = 0.002 under isothermal Newtonian velocity field. At the wall, the orientation state was assumed to be the same as that just at the first layer below the wall. Simulation results showed that the effects of the in-plane velocity gradients on the predicted pressure are quite small because of the cancelling effects of the in-plane stress terms. However, the effects of the stresses due to the in-plane velocity gradients are significant near the gate, more so with non-isothermal effects. The authors also showed that the orientation based on the

fourth-order orientation tensor reached steady state more rapidly than that based on the second-order orientation tensor.

Bay and Tucker [15] developed a decoupled finite-difference scheme to predict fiber orientation in thin cavities using Hele-Shaw flow approximation for the lubrication region and a special treatment to include the effects of the fountain flow region near the flow front. The simulation was performed with generalized Newtonian fluid described by power law and Arrhenius model under non-isothermal conditions with a variable heat capacity. Orientation equations were solved with Folgar Tucker model using hybrid closure approximation. The location of the nodes at the flow front was temporarily adjusted at any given time during the simulation to match the spatial location of the front. Upwind differencing was used for the convective terms in the energy and the orientation equations. However, for the time derivative, an implicit scheme was employed for the energy equation, while an explicit scheme, second order accurate in time, was used in the orientation equations. The orientation equations used a smaller time step than the momentum and energy equations. Time step control in the orientation equations was based on Jeffrey's number defined as:

$$Je = \dot{\gamma}\Delta t \tag{74}$$

A value of 0.2 is recommended for *Je* since significant changes in orientation take place when Je is ~O(1) [15].

For the fountain flow region, finite element package FIDAP was used and a moving frame of reference was chosen that was attached to the front. The 2-D velocity field and the position of the front were calculated starting with an initial guess of semi-circular front based on a simplified method proposed by Dupret and Vanderschuren [119]. This method was used to obtain initial orientation for the newly filled-nodes. The location of the inlet boundary for the fountain flow region was set at $0.5b$ (b being the half-thickness of the mold) behind the contact point based on the reasoning that the velocity field behind this location is nearly that of the lubrication region. At the inlet to the fountain flow region, velocity profile for fully developed channel flow was prescribed and power law was used to describe the fluid viscosity. Newton-Raphson scheme was used to solve the nonlinear finite element equations. The temperature was assumed uniform in the fountain flow region. For the fiber orientation calculations, a fiber tracing scheme was used in which individual fibers were injected into the flow field with a specified initial position and orientation state and their

position and orientation were tracked with time. Inlet orientation states included a range of $\mathbf{A}_{11}$ with other components fixed. Orientation equations were formulated as ordinary differential equations (O.D.E.'s) with $D\mathbf{A}/Dt$, the material derivative, on the left hand side, and were integrated using a fourth order Runge-Kutta scheme. The mold cavity was divided into two regions along the vertical direction using a pivot point based on the fluid velocity. For the nodes with velocity greater than the front velocity (nodes closer to mid-plane) orientation was convected from the upwind nodes and for the nodes with velocity less than the front velocity (nodes closer to the wall), orientation was convected from the fountain flow region and applied to the flat front at that height. With this technique, the authors observed that the orientation of a fiber exiting the fountain flow region depended on the orientation at the inlet of the fountain flow region and the height at which it entered. The fibers entering close to the midplane and exiting close to the wall showed large orientation changes while the fibers entering and exiting near the pivot point showed little change. The final value of the flow direction component of the orientation tensor was found to be nearly a linear function of the initial value with the slope and the intercept depending on the initial z-height of the fiber.

Bay and Tucker [39] used the numerical method of Bay [15] to predict and experimentally validate fiber orientation in two geometries: film-gated strip and center-gated disk for a fiber suspension with 43 wt% short glass fibers in Nylon matrix. The inlet orientation at the gate prescribed for the film-gated strip was chosen to match experimental data near the gate ($\mathbf{A}_{11}$=0.5, $\mathbf{A}_{22}$=0.2, $\mathbf{A}_{33}$=0.3, $\mathbf{A}_{12}$=$\mathbf{A}_{13}$=$\mathbf{A}_{23}$=0.0). For the center-gated disk, inlet orientation at the gate was assumed to be random ($\mathbf{A}_{11}$= $\mathbf{A}_{22}$= $\mathbf{A}_{33}$= 1/3, $\mathbf{A}_{12}$=$\mathbf{A}_{13}$=$\mathbf{A}_{23}$=0.0). It was found that C_I = 0.01 provided a good fit to orientation data in the film-gated strip, hence it was used for center-gated disk also. Orientation predictions showed good correlation with the experimental data near the gate but only qualitative agreement at locations away from the gate. For locations away from the gate, in general, a thinner core was predicted than experimentally observed and orientation near the walls was overpredicted. The authors cite closure approximation as the main source for difference in experimental and predicted orientation. A sensitivity analysis was also performed to assess the effects of various parameters such as inlet and wall temperatures, fill time, matrix properties and the effect of fiber interaction coefficient. It was found that neither injection time nor the mold wall temperature has a significant effect on the final orientation pattern. However, slow filling results in a thicker shell layer and possibly a skin layer at the wall while fast filling gives a thicker core. Moreover, shear thinning behavior or a large heat of fusion produces a flatter velocity profile and a

thicker core. The authors mention that the primary factors controlling the fiber orientation are the shape of the cavity and the location of the gate. One limitation in the simulations was the assumption of symmetry for the orientation about the midplane when comparing with experimental data which showed asymmetry around the midplane.

Han and Im [41] used a slightly modified version of the numerical method developed by Bay and Tucker [15]. The variation came from the use of Jeffrey's model for fiber orientation in the fountain flow region, and the use of random orientation at the inlet of this region. It should be noted here that Bay [39] interpolated the orientation results from the flat front to obtain the inlet boundary conditions for the fountain flow region. This interpolation algorithm limited its application to simple cavities. In Han's work, the pivot point for deciding the direction of convection in the fountain flow region was set a $z/b = 1/\sqrt{3}$. Han tested three closure approximations: hybrid, modified hybrid, and closure equation for $C_I = 0$ (CEQ). C_I values most appropriate for each closure approximation were selected by comparing simulated and experimental values near the wall (where effects of inlet orientation can be ignored due to high shear). Simulations were compared with experimental data of Bay [39] and it was found that fountain flow effects improved the orientation predictions near the wall. Comparison of different closures revealed that the modified hybrid (C_I = 0.001) and CEQ (C_I = 0.001) closures provided better prediction for the out-of-plane component A_{13} for both geometries as compared to the hybrid closure (C_I =0.01). Test simulations were also performed for a dashboard panel, and it was shown that the numerical method can effectively predict orientation in complex parts.

2.3.2.2. Free boundary simulations

One of the first attempts at predicting fiber orientation considering the effects of the fountain flow in injection molding processes were based on the solution of Jeffrey's model in a steady state reference frame [120, 121]. Givler [120] used a finite element method to solve a steady state planar flow of fiber suspension in a generalized Newtonian matrix using the decoupled approach. Simulations were performed in a coordinate system attached to the moving front which helps to convert the transient problem of fountain flow to a steady state problem. The moving front was considered as a streamline and its shape was determined iteratively starting from an initial guess of a semi-circle. Orientation equations were solved using the method of integration along the streamlines using a second-order Runge-Kutta scheme. Individual fibers were considered in the simulation and statistical averages for the orientation were obtained at each point in the domain by averaging the orientation of individual test fibers.

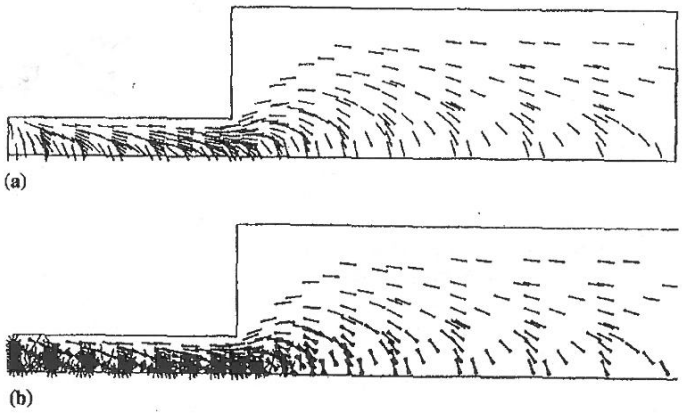

Figure 2.13 Predicted fiber orientation in planar expansion with inlet fiber orientation perpendicular to the flow (a) and as random orientation (b) [111].

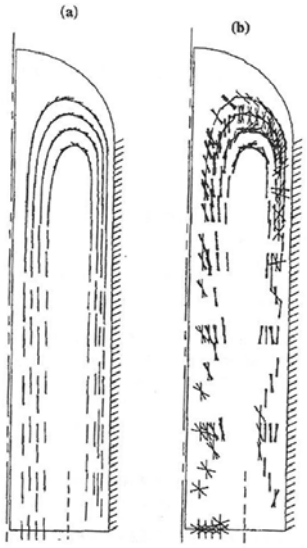

Figure 2.14 Predicted fiber orientation in the fountain flow region with inlet fiber orientation perpendicular to the flow (a) and as random orientation (b) [111].

Two cases: planar expansion and fountain flow, were simulated for prediction of fiber orientation with two inlet conditions for fiber orientation: random and transverse to the flow direction. In planar expansion, for both inlet conditions, fibers were predicted to align themselves predominantly perpendicular to the flow direction along the centerline while they aligned in the flow direction close to the walls as shown in Figure 2.13. In fountain flow simulations, the fibers aligned themselves along the streamlines. For both cases of inlet conditions, fibers near the walls aligned themselves predominantly parallel to the wall as shown in Figure 2.14.

Gillespie [121] employed the numerical scheme developed by Givler [120] for the determination of fiber orientation and compared the predictions with experimentally observed fiber orientation for a short glass phenolic thermoset (33% glass fiber, 57% phenolic resin, 10% filler by volume) in an end-gated cavity with a pin at the center. The surface and the mid-plane of the part were simulated. The inlet conditions employed for fiber orientation were based on the microscopy results: fibers aligned parallel to the flow direction near the surface and transverse to the flow direction near the mid-plane. The change in the orientation due to the presence of the pin hole was also compared with experimental data. The orientation was experimentally measured at two locations along the centerline equidistant from the pin hole and matching with the inlet/outlet regions of the finite element mesh. The predicted fiber orientation was compared quantitatively with the experimental values using the planar orientation parameter f_p:

$$f_p = 2\left\langle \cos^2\theta \right\rangle - 1 \tag{75}$$

$$\left\langle \cos^2\theta \right\rangle = \int_{-\pi/2}^{\pi/2} \cos^2\theta \, d\theta \tag{76}$$

where θ is relative to a reference direction, usually the local flow direction. Experimentally measured value of f_p at the inlet was found to be $f_p = 0.4$ which was used as inlet condition for the simulation. At the outlet, measured values of f_p was $f_p = 0.8$ while the simulations predicted $f_p = 1$. The authors ascribed this over-prediction to the inability of the Jeffrey's model to handle fiber interaction. Simulation results also showed a core region where the orientation was less than the prescribed inlet fiber orientation and this was attributed to the diverging nature of the flow in the vicinity of the pin hole.

Vincent and Agassant [122] predicted the fiber orientation for a 30 wt % fiber suspension in a center-gated disk mold cavity using decoupled approach and compared the results with the experimental data. They considered Newtonian viscosity model for the matrix and Jeffrey's equation for the fiber orientation. The method of integration along the streamlines was used to solve the fiber orientation equations. They used an alternative form of scalar measurement for the planar orientation as below:

$$f = \frac{2\left\langle \cos^2\theta \right\rangle - 1}{2} \tag{77}$$

$$\left\langle \cos^2\theta \right\rangle = \frac{\sum_i N_i \cos^2\theta}{\sum_i N_i} \tag{78}$$

where N_i is the number of fibers in the θ-direction relative to a reference direction (usually the local flow direction). The inlet orientation condition prescribed at the inlet of the mold cavity was a function of the cavity height with fibers perpendicular to the flow direction in the center and parallel to the flow direction close to the walls. The predicted orientation in the disk shows a skin-shell-core structure with fibers slightly aligned in the flow direction very near the walls (skin layer), highly aligned in the flow direction beneath the skin layer (shell layer) and almost perpendicular to the flow direction near the center (core layer) which is qualitatively in agreement with the experimental measurements.

Devilers and Vincent [123] predicted the influence of the fountain flow on the fiber orientation for a dilute suspension with a moving mesh based on ALE method. The computation of flow kinematics was based on a method developed by Magnin [124] in which fully developed Poiseuille flow is prescribed at the inlet, no slip boundary conditions are prescribed at the walls and zero stresses are prescribed at the free surface. Flow equations were solved in a decoupled manner using a mixed velocity pressure Galerkin finite element method and Jeffrey's model was used to calculate fiber orientation. Random orientation for the fibers was prescribed at the inlet and the individual fibers were tracked along their trajectories inside the mold. Two geometries, center-gated disk with and without sprue were considered. In the disk without the sprue, the fibers close to the centerline have a higher velocity than the fibers close to the wall. When the fibers close to the centerline reach the fountain flow region, fibers move outwards towards the wall until they reach a gapwise position close to the wall and move slowly after that. Fibers close to the centerline are almost perpendicular to the flow direction in the plane of the disk and as they move in the fountain flow region, they rapidly change orientation passing through a random orientation state and align themselves in the flow direction as they move out towards the walls. In simulations with the sprue, the fibers in the sprue close to the centerline are predicted to orient perpendicular to the flow direction and the radial direction. At the junction of the disk and the sprue, fibers close to the centerline of the sprue move towards the opposite wall where they tend to align in the flow direction. The fibers near the wall inside the sprue tend to align in the flow direction.

Vincent [125] simulated fiber orientation by tracking individual fibers in a tube and a disk cavity (without the sprue) with a generalized Newtonian matrix using a decoupled approach. Simulations were performed with Folgar-Tucker model to account for fiber-fiber interaction with interaction coefficient, $C_I = 0.001$. Flow kinematics calculations were done in a decoupled manner using the ALE method. Authors also performed simulations with $C_I = 0.0$ (Jeffrey's model). In the tube flow with $C_I = 0.0$, the fibers were predicted to orient in the flow direction due to shear flow. As they move in the z-direction and reach the fountain flow region, the fibers align themselves mainly in the θ-direction and reorient themselves in the flow direction as they get close to the wall. In the disk flow with $C_I = 0.0$, the fibers orient themselves in the θ-direction in the extensional flow region (close to the centerline). As the fibers enter the fountain flow region, a complex behavior is observed for A_{rr} with an increase in A_{rr} followed by a decrease and finally an increase due to shear flow near the walls. Authors indicate that the introduction of the interaction coefficient ($C_I = 0.001$) slightly disorients the fibers with respect to the plane (A_{zz} around 0.2) of the disk which makes shear flow near the walls more important in aligning the fibers.

Ko and Youn [126] used a Lagrangian scheme for the simulation of fiber orientation in the thickness plane of injection molded parts. Flow equations for a generalized Newtonian fluid were solved with similar boundary conditions as described above in the work of Devilers and Vincent [123] without the effects of fibers on the flow field. Lagrangian mesh was generated with quadrilateral elements at each time step using linear shape functions that resulted in a volumetric loss of about 1%. Numerical simulation results showed the evolution of the moving front into a semi-circular shape and presence of fountain flow behind the moving front. At the inlet boundary, two inlet conditions were prescribed: random orientation and fully flow-aligned orientation. Out of plane components of orientation tensor were not considered in the solution of orientation equations and a fiber interaction coefficient of $C_I = 0.1$ was used. Hybrid closure approximation was used for the fourth order orientation tensor. Authors showed the orientation ellipses and the maximum eigenvalues of the orientation tensor to describe the orientation field. The simulation results with both inlet conditions showed the maximum eigenvalues in the fountain flow region near the wall and large values were also found along the walls. For the case of fully-aligned inlet orientation, the predicted orientation was significantly rearranged due to fountain flow and a minimum degree of orientation was obtained just behind the flow front. In the core region, the orientation differed considerably where the effects of shear and fountain flow were very small and the inlet orientation was convected with the flow. Authors used the technique to show orientation patterns for two

geometries: a Z-shape crank as a typical shape of a single path channel and a T-shape crank as a typical shape of dividing flow.

Ranganathan and Advani [127] used a finite difference formulation for coupled steady state simulation with semi-concentrated fiber suspensions in a Newtonian matrix in an axisymmetric diverging radial flow. Folgar Tucker model was used for fiber orientation and Shaqfeh-Fredrickson model [128] was used to determine the stress contribution of the fibers. The orientation field was described by the fourth order orientation tensor and the sixth order term in the Folgar Tucker model was approximated using the hybrid closure approximation. The following boundary conditions were prescribed: uniform radial velocity at the inlet, no-slip velocity at the wall, symmetry boundary conditions at the centerline, and a zero gapwise velocity and a zero derivative in the normal direction at the outlet boundary. Random inlet orientation was prescribed at the inlet boundary. Method of integration along the streamlines was used to compute the orientation at every time step with fully aligned orientation prescribed at the wall. The results showed that the flow develops much slowly in fiber suspensions with non-zero fiber volume fraction as compared to Newtonian fluid without any fibers. This is due to the effect of fibers on the rheology of the suspension. The centerline velocity was observed to increase from the inlet gate value, go through a maximum and then decrease. This is because the shear viscosity at the wall initially increases which results in the suspension to slow down at the walls and accelerate at the centerline initially. However, as the flow progresses, shear flow at the wall dominates and aligns the fibers near the wall reducing the viscosity at the wall. This results in a reverse effect, i.e. an increase in velocity near the wall and a decrease at the centerline. The centerline velocity overshoot was seen in all suspensions considered in this work [127]. The effect of the fiber volume fraction (ϕ_v) on the flow kinematics was compared for two cases, $\phi_v = 0.01$ and $\phi_v = 0.05$. It was noticed that as the fiber volume fraction increased, the velocity profile was more plug-like, i.e. most of the shearing was observed near the wall. Three different orientation regions were identified: i) near the wall where fibers tend to align along the flow direction due to high shear, ii) around the centerline where fibers are aligned in the transverse direction due to extensional effects, and iii) around midway between the wall and the centerline where the flow-direction orientation increases with the radial distance due to expansion of shear dominated region. Orientation at a height $b/2$ was plotted against the dimensionless radial location for coupled and decoupled solutions and in the radial direction. The radial plot shows an initial increase in the flow direction orientation component due to shear in the 1,3-plane followed by a decrease due to extensional effects in 1,2-plane and then a monotonic increase because of increasing

shear effects. The coupled solution showed a slow evolution in the region of monotonic increase in orientation. The effect of inlet conditions with decoupled scheme were also tested at a height $b/2$ by comparing random inlet orientation and flow-aligned inlet orientation and it was suggested that the maximum difference due to different inlet conditions should be seen in this region which is away from the wall and the centerline and the inlet conditions are not washed away due to shear or extensional effects.

Verweyst and Tucker [40] performed a finite element simulation for coupled isothermal steady state problem with semi-concentrated fiber suspensions in axisymmetric flows. The suspending fluid was taken to be a Newtonian fluid and Folgar Tucker model was used for the evolution of fiber orientation. The orientation field was described by the second order orientation tensor and orthotropic closure developed by Wetzel [129] was used to approximate the fourth order term in the orientation equation. The value of the fiber interaction in the model was taken to be C_I = 0.001. A center-gated disk with a sprue was included as one of the test geometries. The boundary conditions used were parabolic velocity profile at the inlet of the sprue, no slip condition at the cavity walls, symmetry boundary condition along the center-line in the sprue with $A_{13} = 0$ and traction free boundary at the outlet. For the orientation equations, random orientation was assigned at the sprue inlet. The governing equations were solved using a Galerkin finite element method with streamline upwinding to handle the hyperbolic nature of the orientation equation. It was found that a steady-state solution would seldom converge, unless the flow geometry were very simple (such as parallel plates). Hence, the solution was obtained by time-marching the transient equations using fully implicit treatment for the time derivative starting from random orientation in the entire domain.

Verweyst [40] showed the non-physical orientation states at stagnation points in the flow such as at the location $r = 0$ on the bottom wall opposite the sprue. The orientation components A_{11}, A_{33} and A_{13} around this point were plotted along the bottom wall and it was observed that the A_{11} and A_{13} have constant positive values in the vicinity of this point with a different value at this point and A_{13} changes sign at this point. Numerical simulation on a finite-size mesh around this point showed oscillations and produced non-physical results such as $A_{11} > 1$. Such non-physical values did not distort the remainder of the solution with streamline upwinding technique. Hence they were accepted as part of the solution for the orientation. However, for coupled problems, these non-physical values were corrected to physically acceptable values before using them in constitutive and

momentum equations. The details of these corrections in the orientation tensor components can be found in Verweyst [40].

For the center-gated disk with a sprue, decoupled and coupled simulations were performed. In decoupled simulations, the results showed that the streamlines rapidly turn in the radial direction as the flow enters the disk cavity from the sprue and the flow develops very quickly in the radial direction as shown in . Fibers also quickly align themselves in the radial direction near the upper wall of the disk while the fibers take a little longer to align in the radial direction. In the center of the disk, velocity develops much more quickly than fiber orientation. For the coupled problem, the streamlines are displaced towards the bottom of the disk as the flow enters the cavity. The authors suggest that this is due to rapid radial alignment of the fibers near the upper wall which results in enhanced shear viscosity thereby reducing the local velocity which causes the streamlines to shift downward. However, the orientation results did not show much difference from decoupled solution and the differences diminished with increasing distance from the center of the disk.

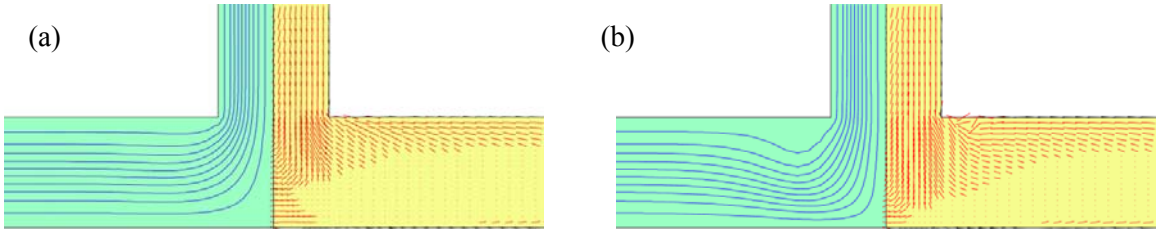

Figure 2.15 Streamlines and fiber orientation vectors in a center-gated disk with sprue using (a) decoupled and (b) coupled steady state simulations in Newtonian matrix assuming random inlet orientation at the sprue inlet [40].

2.3.2.3. Moving interface simulations

Verweyst [130] developed a two-level finite-element program on top of FIDAP software [131] for predicting fiber orientation in 3-D parts. In the proposed approach, Hele-Shaw simulation is first used to model the entire part and the results of this simulation provide the boundary conditions for a more detailed second level simulation of selected 3-D features. Decoupled simulations were performed for non-isothermal, non-Newtonian matrix having fiber concentration in the semi-concentrated regime. Folgar Tucker model was used to describe the evolution of fiber orientation described by second order orientation tensor and an ORT closure developed by Wetzel [129] was used to approximate the fourth order orientation tensor appearing in the evolution

equation. The fiber interaction coefficient was chosen as $C_I = 0.0035$ to match the experimental data for the $\mathbf{A}_{11}$ tensor component in the shell region of the strip for a 30 wt% glass fiber filled polycarbonate resin using the ORT closure. Moving flow front in the second level simulation was simulated using the VOF method [46]. Galerkin finite element method was used to solve for the governing equations using fully implicit time integration. The hyperbolic nature of the orientation equation was controlled by adding streamline upwinding. The boundary conditions imposed in the first level Hele-Shaw simulation were: pressure prescribed at the inlet and the outlet, and no slip at the walls. For the second level simulation, full balance equations were solved for a smaller more specific domain inside the mold. The boundary conditions at the inlet for this smaller domain were taken from the first level solution. This included specifying velocity, pressure, temperature and fiber orientation as a function of position on the boundary. No slip velocity was prescribed at the walls and zero surface traction was imposed on the free moving interface and the orientation inside the simulation domain was initialized with a random orientation state. A film-gated strip with transverse and flow-direction ribs made from 30 wt% fiber filled polycarbonate resin was used as a test geometry. The ribs were separately simulated as a test case for the second level simulation and results were compared with experimentally observed orientation in the ribs. A complete filling analysis was performed for the transverse rib while only steady state simulations were done for the flow-direction rib due to computational limitations. The predictions of orientation inside the ribs are in qualitative agreement with the experimental data. However the discrepancies in the core and the skin layer for the transverse rib were attributed to the errors in the frontal flow introduced by the implementation of the VOF method. The simulation results for the transverse rib show a semi-circular flow front approaching the rib. However, as the flow front passes the rib, there are slight irregularities due to discretization errors in the VOF method. A very narrow core region is predicted in the main channel and the predictions for A_{11} show a slight upward shift in the core in direction of the surface containing the rib. The steady state results for the flow-direction rib show only qualitative agreement and fail to predict the orientation at the tip of the rib. The discrepancies in this rib are attributed to steady state being used for simulation which discards the fountain flow effect and the transient nature of the flow because most of the orientation changes take place during the transient phase.

Chung and Kwon [2] used a finite-element formulation for coupled, non-isothermal transient simulation of semi-concentrated fiber suspensions in a non-Newtonian matrix in axisymmetric flows. The evolution of fiber orientation was modeled using Folgar Tucker model

with C_I = 0.001 and coupling of momentum and orientation equations was done using Dinh-Armstrong model. The evolution of the melt-front interface was modeled through the pseudoconcentration (PC) method [12]. The following boundary conditions were prescribed: parabolic velocity profile at the inlet boundary, symmetry boundary conditions at the symmetry boundaries, and adjustable Robin boundary conditions at the mold walls and outlet boundaries [12]. Random orientation was prescribed at the inlet boundary of the axisymmetric geometry. The orientation field was described by second order orientation tensor and the fourth order term appearing in the Folgar Tucker model was approximated using IBOF closure approximation [28]. Governing equations were solved using a Galerkin formulation and the hyperbolic nature of orientation and the pseudoconcentration equations were handled using streamline-upwinding Petrov-Galerkin (SUPG) method. Crank-Nicholson implicit finite difference method was used for the temporal discretization. Simulation results for a center-gated disk without a sprue showed that coupled velocity profile is more flat than the decoupled case. The effect of coupling on orientation was more significant when fountain flow was taken into account as compared to the case of Hele-Shaw flow in which fountain flow is neglected. Fountain flow results in a sudden decrease in $\mathbf{A}_{rr}$ far downstream and fountain-flow affected region was larger for the shell layer as compared with other layers. A general observation was made that coupling effect is more significant in the core and transition layers which is in agreement with the results of Ranganathan and Advani [127], Chung and Kwon [118] and Verweyst [129]. A comparison of A_{rr} values predicted by Hele-Shaw flow and flow including the effects of fountain flow was done with experimental data from Bay [39] for decoupled non-isothermal, non-Newtonian flow. The simulation results obtained by including the fountain flow showed better match with the experimental data, especially in the shell layer while Hele-Shaw flow consistently over-predicted A_{rr} in the shell layer. Effect of inlet conditions were also investigated by comparing disk flow with and without sprue and random orientation being specified at the inlet of each geometry. In the disk with the sprue, the gapwise orientation measured at the inlet of the disk, shows an asymmetric profile with more alignment in the upper half of the disk cavity as compared to that in the lower half as shown in Figure 2.16.

Orientation predictions for A_{rr} with and without sprue were compared in the radial direction at different heights in the disk cavity that were representative of core, transition and shell layers for various and also in the gapwise direction at different radial locations. It was found that the entrance effects persist mostly in the core and the transition layers in both upper and lower half of the disk. A_{rz} was found to be significantly affected by the presence of the sprue, especially in the core layer.

For the region around the melt-front in the shell layer, A_{rz} showed a rapid flip-over phenomenon. $A_{\theta\theta}$ component showed fiber alignment transverse to the flow direction in the core layer, and in the shell layer around the melt-front region, it showed a more rapid flip-over phenomenon than A_{rz}. The authors mention that the presence of the sprue affects $A_{\theta\theta}$, especially in the core and the transition layers.

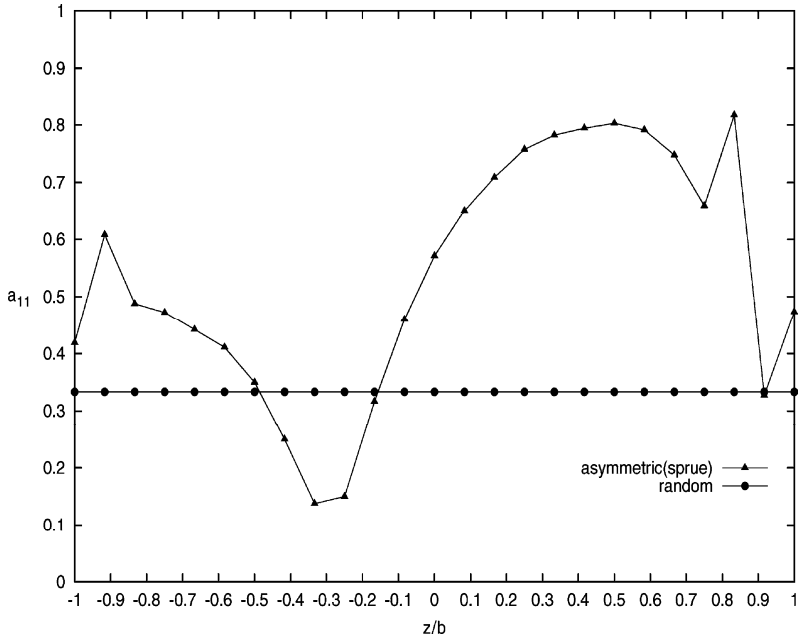

Figure 2.16 Cavitywise profile of A_{rr} at the inlet of the cavity when the computation domain includes sprue with random inlet orientation prescribed at the sprue inlet [2].

.

Park and Kwon [1] used the same formulation as Chung [2] for non-isothermal transient filling simulation of fiber suspensions in a center-gated disk. However, Dinh-Armstrong rheological model was modified to include viscoelasticity and delayed objective Folgar-Tucker model was used for the fiber orientation with a modified form of C_I. The modified form of C_I introduced by Park is based on the following phenomenological model [23]:

$$C_I = \frac{C_I^*}{\frac{h}{L}\left(\frac{1}{M}\sum_{i=1}^{M} tr(\mathbf{A}\cdot\mathbf{c}_i)\right)^n} \tag{79}$$

where C_I^* is an empirical parameter, h is the average spacing between neighboring fibers, L is the fiber length, M is the total number of relaxation modes, and $\mathbf{c}_i$ is the finger strain tensor which evolves according to the following equation:

$$\frac{D\mathbf{c}_i}{Dt} - \nabla\mathbf{v}^T \cdot \mathbf{c}_i - \mathbf{c}_i \cdot \nabla\mathbf{v} = f_i(\mathbf{A}, \mathbf{c}_i) \tag{80}$$

where $f_i(\mathbf{A}, \mathbf{c}_i)$ represents the dissipation process of the polymer. Park and Kwon [23] have proposed a form of f_i in which the anisotropy due to the fibers is introduced in a manner of positive entropy production. The details of the model can be found in their original paper [23]. In order to handle the viscoelasticity and high Weissenberg number issues related to viscoelasticity ($We = \bar{\theta}\bar{\dot{\gamma}}$ where $\bar{\theta}$ is the characteristic time of the fluid and $\bar{\dot{\gamma}}$ is the characteristic strain rate), discrete-elastic-viscous split stress (DEVSS) method and matrix logarithm formulation for $\mathbf{c}_i$ was used in the simulations. Numerical simulation results were compared with experimental data from Bay [39]. The kinematics result for the isothermal filling showed a diminishing effect of coupling with the radial distance. In non-isothermal conditions, the best fit to experimental data in overall geometry was seen for κ = 0.4. The effect of reducing the filling time was also assessed and it was observed that the velocity profile was more flat with reduction in filling time due to viscoelastic nature of the matrix and the thickness of the solidified layer near the wall also decreased. As a result of the flatter velocity profile, the core and transition layers became thicker for reduced filling times and shell layer approached the wall. Overall, the fiber-coupled viscoelastic model did have a little effect on the fiber orientation predictions while slow orientation kinetics did significantly improve the predictions. Authors also mention that viscoelasticity would have insignificant effects on orientation as compared to other issues such as closure approximations.

2.4 References

[1] J.M. Park, T.H. Kwon, Nonisothermal transient filling simulation of fiber suspended viscoelastic liquid in a center-gated disk, Polymer Composites, 32 (2011) 427-437.

[2] D.H. Chung, T.H. Kwon, Numerical studies of fiber suspensions in an axisymmetric radial diverging flow: The effects of modeling and numerical assumptions, Journal of Non-Newtonian Fluid Mechanics, 107 (2002) 67-96.

[3] F. Folgar, C.L. Tucker, Orientation behavior of fibers in concentrated suspensions, Journal of Reinforced Plastics and Composites, 3 (1984) 98-119.

[4] J.A. Dantzig, Tucker, C.L., Modeling in materials processing, Cambridge University Press, Cambridge, UK, 2001.

[5] F.A. Morrison, Understanding Rheology, Oxford University Press, New York, Oxford, 2001.

[6] R. Lapasin, Pricl, S., Rheology of Industrial Polysaccharides: Theory and Applications, Springer, 1995.

[7] D. Doraiswamy, Metzner, A.B. , The rheology of polymeric liquids crystals, Rheol Acta, 25 (1986).

[8] A.B. Metzner, Rheology of suspensions in polymeric liquids, J Rheol, 26 (1985) 739-775.

[9] D.G. Baird, D.I. Collias, Polymer Processing: Principles and Design, Wiley, 1998.

[10] W. Ostwald, About the rate function of the viscosity of dispersed systems, Kolloid Z, 36 (1925) 99-117.

[11] C. Cuvelier, Segal, A., vanSteenhoven, A.A., Finite element methods and navier-stokes equations, D. Reidel Publishing Co, Dordrecht, 1986.

[12] G. Haagh, F. Van De Vosse, Simulation of three-dimensional polymer mould filling processes using a pseudo-concentration method, International Journal for Numerical Methods in Fluids, 28 (1998) 1355-1369.

[13] S.G. Advani, C.L. Tucker III, The use of tensors to describe and predict fiber orientation in short fiber composites, Journal of Rheology, 31 (1987) 751-784.

[14] R.G. Larson, The Structure and Rheology of Complex Fluids, Oxford University Press, New York, 1999.

[15] R.S. Bay, C.L. Tucker, Fiber orientation in simple injection moldings. Part I: Theory and numerical methods, Polymer Composites, 13 (1992) 317-331.

[16] G.B. Jeffery, The motion of ellipsoidal particles immersed in a viscous fluid, in: Proceedings of the Royal Society of London, Series A, The Royal Society, 1922, pp. 161-179.

[17] C.L. Tucker, Advani, S.G., Processing of short-fiber systems, in: S.G. Advani (Ed.) Flow and rheology in polymer composites manufacturing, Elsevier, Amstendarm, 1994, pp. 147-197.

[18] S.M. Dinh, R.C. Armstrong, A rheological equation of state for semiconcentrated fiber suspensions, Journal of Rheology, 28 (1984) 207-227.

[19] J.H. Phelps, C.L. Tucker III, An anisotropic rotary diffusion model for fiber orientation in short- and long-fiber thermoplastics, Journal of Non-Newtonian Fluid Mechanics, 156 (2009) 165-176.

[20] R. Bay, Fiber orientation in injection-molded composites: A comparison of theory and experiments, in: PhD Thesis, Mechanical Engineering,University of Illinois at Urbana-Champaign,1991

[21] S. Ranganathan, S.G. Advani, Fiber-fiber interactions in homogeneous flows of nondilute suspensions, Journal of Rheology, 35 (1991) 1499-1522.

[22] A.R.S. A, A. Ait-Kadi, M. Grmela, Rheology of fiber suspensions in viscoelastic media: Experiments and model predictions, Journal of Rheology, 45 (2001) 945-962.

[23] J.M. Park, T.H. Kwon, Irreversible thermodynamics based constitutive theory for fiber suspended polymeric liquids, Journal of Rheology, 55 (2011) 517-543.

[24] D.H. Chung, T.H. Kwon, Fiber orientation in the processing of polymer composites, Korea-Australia Rheology Journal, 14 (2002) 175-188.

[25] J.M. Park, S.J. Park, Modeling and simulation of fiber orientation in injection molding of polymer composites, Mathematical Problems in Engineering, 2011 (2011).

[26] J.J.S. Cintra, C.L. Tucker III, Orthotropic closure approximations for flow-induced fiber orientation, Journal of Rheology, 39 (1995) 1095-1122.

[27] D.H. Chung, T.H. Kwon, Improved model of orthotropic closure approximation for flow induced fiber orientation, Polymer Composites, 22 (2001) 636-649.

[28] D. Chung, T.H. Kwon, Invariant-based optimal fitting closure approximation for the numerical prediction of flow-induced fiber orientation, Journal of Rheology, 46 (2002) 169.

[29] A.P.R. Eberle, G.M. Vélez-García, D.G. Baird, P. Wapperom, Fiber orientation kinetics of a concentrated short glass fiber suspension in startup of simple shear flow, Journal of Non-Newtonian Fluid Mechanics, 165 (2010) 110-119.

[30] M. Sepehr, G. Ausias, P.J. Carreau, Rheological properties of short fiber filled polypropylene in transient shear flow, Journal of Non-Newtonian Fluid Mechanics, 123 (2004) 19-32.

[31] J. Wang, J.F. O'gara, C.L. Tucker, An objective model for slow orientation kinetics in concentrated fiber suspensions: Theory and rheological evidence, Journal of Rheology, 52 (2008) 1179.

[32] A.P.R. Eberle, D.G. Baird, P. Wapperom, G.M. Vélez-García, Using transient shear rheology to determine material parameters in fiber suspension theory, Journal of Rheology, 53 (2009) 685-705.

[33] G.M. Vélez-García, S.M. Mazahir, P. Wapperom, D.G. Baird, Simulation of injection molding using a model with delayed fiber orientation, International Polymer Processing, 26 (2011) 331-339.

[34] H.M. Huynh, Improved fiber orientation predictions for injection-molded composites, in: MS Thesis, Universty of Illinois - Urbana Champaign,2001

[35] W. Rose, Fluid-fluid interfaces in steady motion, Nature, 191 (1961) 242-243.

[36] R. Ballman, H. Toor, Orientation in injection molding, Modern Plastics, 38 (1960) 113-120.

[37] G.D. Yarnold, The motion of a mercury index in a capillary tube, Proceedings of the Physical Society, 50 (1938) 540.

[38] M. Schwartz Anthony, A. Rader Charles, E. Huey, Resistance to flow in capillary systems of positive contact angle, in: Contact angle, wettability, and adhesion, American Chemcial Society, 1964, pp. 250-267.

[39] R.S. Bay, C.L. Tucker, Fiber orientation in simple injection moldings. Part II: Experimental results, Polymer Composites, 13 (1992) 332-341.

[40] B.E. Verweyst, C.L. Tucker, Fiber suspensions in complex geometries: Flow/orientation coupling, Canadian Journal of Chemical Engineering, 80 (2002) 1093-1106.

[41] K.H. Han, Y.T. Im, Numerical simulation of three-dimensional fiber orientation in injection molding including fountain flow effect, Polymer Composites, 23 (2002) 222-238.

[42] C. Huh, L. Scriven, Hydrodynamic model of steady movement of a solid/liquid/fluid contact line, Journal of Colloid and Interface Science, 35 (1971) 85-101.

[43] J.M. Floryan, H. Rasmussen, Numerical methods for viscous flows with moving boundaries, Applied Mechanics Reviews, 42 (1989) 323-341.

[44] R.W. Lewis, A.S. Usmani, J.T. Cross, Efficient mould filling simulation in castings by an explicit finite element method, International Journal for Numerical Methods in Fluids, 20 (1995) 493-506.

[45] M. Medale, M. Jaeger, Numerical simulation of incompressible flows with moving interfaces, International Journal for Numerical Methods in Fluids, 24 (1997) 615-638.

[46] C.W. Hirt, B.D. Nichols, Volume of fluid (vof) method for the dynamics of free boundaries, Journal of Computational Physics, 39 (1981) 201-225.

[47] J. Donea, A. Huerta, J.P. Ponthot, A. Rodríguez-Ferran, Arbitrary lagrangian–eulerian methods, in: E. Stein, R.e.d. Borst, T.J.R. Hughes (Eds.) Encyclopedia of computational mechanics, John Wiley & Sons, Ltd, 2004.

[48] R. Panahi, E. Jahanbakhsh, M.S. Seif, Comparison of interface capturing methods in two phase flow, Iranian Journal of Science and Technology Transaction B-Engineering, 29 (2005) 539-548.

[49] C. Hirt, B. Nichols, N. Romero, Sola: A numerical solution algorithm for transient fluid flows, NASA STI/Recon Technical Report N, 75 (1975) 32418.

[50] B.D. Nichols, C.W. Hirt, Calculating three-dimensional free surface flows in the vicinity of submerged and exposed structures, Journal of Computational Physics, 12 (1973) 234-246.

[51] B.D. Nichols, C.W. Hirt, Improved free surface boundary conditions for numerical incompressible-flow calculations, Journal of Computational Physics, 8 (1971) 434-448.

[52] B.D. Nichols, C.W. Hirt, Proceedings first intern. Conf. Num. Ship hydrodynamics, in, Gaithersburg, MD, 1975.

[53] S. Osher, J.A. Sethian, Fronts propagating with curvature-dependent speed: Algorithms based on hamilton-jacobi formulations, Journal of Computational Physics, 79 (1988) 12-49.

[54] V.R. Gopala, B.G.M. van Wachem, Volume of fluid methods for immiscible-fluid and free-surface flows, Chemical Engineering Journal, 141 (2008) 204-221.

[55] F.H. Harlow, J.E. Welch, Numerical calculation of time-dependent viscous incompressible flow of fluid with free surface, Physics of fluids, 8 (1965) 2182.

[56] J.E. Welch, F.H. Harlow, J.P. Shannon, B.J. Daly, The mac method, in: Los Alamos Scientific Laboratory Report No. LA-3425, 1966.

[57] C.G. Gogos, C.-F. Huang, L.R. Schmidt, The process of cavity filling including the fountain flow in injection molding, Polymer Engineering & Science, 26 (1986) 1457-1466.

[58] M.F. Tomé, L. Grossi, A. Castelo, J.A. Cuminato, S. McKee, K. Walters, Die-swell, splashing drop and a numerical technique for solving the oldroyd b model for axisymmetric free surface flows, Journal of Non-Newtonian Fluid Mechanics, 141 (2007) 148-166.

[59] D. Bigg, S. Middleman, Laminar mixing of a pair of fluids in a rectangular cavity, Industrial & Engineering Chemistry Fundamentals, 13 (1974) 184-190.

[60] F.H. Harlow, A.A. Amsden, J.R. Nix, Relativistic fluid dynamics calculations with the particle-in-cell technique, Journal of Computational Physics, 20 (1976) 119-129.

[61] M. Rudman, Volume-tracking methods for interfacial flow calculations, International Journal for Numerical Methods in Fluids, 24 (1997) 671-691.

[62] E. Broyer, C. Gutfinger, Z. Tadmor, Theoretical model for cavity filling process in injection molding, Transactions of the Society of Rheology, 19 (1975) 423-444.

[63] Z. Tadmor, E. Broyer, C. Gutfinger, Flow analysis network (FAN) - a method for solving flow problems in polymer processing, Polymer Engineering & Science, 14 (1974) 660-665.

[64] D. Cardozo, A brief history of the filling simulation of injection moulding, Proceedings of the Institution of Mechanical Engineers, Part C: Journal of Mechanical Engineering Science, 223 (2009) 711-721.

[65] V.R. Voller, S. Peng, An algorithm for analysis of polymer filling of molds, Polymer Engineering & Science, 35 (1995) 1758-1765.

[66] S. Shin, Lee, W.I., Finite element analysis of incompressible viscous flow with moving free surface by selective volume of fluid method, International Journal of Heat and Fluid Flow, 21 (2000) 197-206.

[67] J.P. Boris, D.L. Book, Flux-corrected transport. I. Shasta, a fluid transport algorithm that works, Journal of Computational Physics, 11 (1973) 38-69.

[68] B.G.M. van Wachem, J.C. Schouten, Experimental validation of 3-D lagrangian vof model: Bubble shape and rise velocity, AIChE Journal, 48 (2002) 2744-2753.

[69] W. Noh, P. Woodward, Slic (simple line interface calculation), in: A. van de Vooren, P. Zandbergen (Eds.) Proceedings of the Fifth International Conference on Numerical Methods in Fluid Dynamics, Springer Berlin / Heidelberg, Twente University, Enschede, 1976, pp. 330-340.

[70] D. Youngs, K. Morton, M. Baines, Time-dependent multi-material flow with large fluid distortion, in: Numerical methods for fluid dynamics, Academic Press, New York, 1982, pp. 273–285.

[71] O. Ubbink, Numerical prediction of two fluid systems with sharp interfaces, in: PhD Thesis, Imperial College of Science, Technology and Medicine,1997

[72] H. Jasak, H. Weller, Interface-tracking capabilities of the intergamma differencing scheme, in: Technical report, Imperial College, University of London, 1995.

[73] S.T. Zalesak, Fully multidimensional flux-corrected transport algorithms for fluids, Journal of Computational Physics, 31 (1979) 335-362.

[74] O. Ubbink, R.I. Issa, A method for capturing sharp fluid interfaces on arbitrary meshes, Journal of Computational Physics, 153 (1999) 26-50.

[75] B. Leonard, The ultimate conservative difference scheme applied to unsteady one-dimensional advection, Computer Methods in Applied Mechanics and Engineering, 88 (1991) 17-74.

[76] J.D. Ramshaw, J.A. Trapp, Numerical technique for low-speed homogeneous 2-phase flow with sharp interfaces, Journal of Computational Physics, 21 (1976) 438-453.

[77] P. Gaskell, A. Lau, Curvature-compensated convective transport: Smart, a new boundedness-preserving transport algorithm, International Journal for Numerical Methods in Fluids, 8 (1988) 617-641.

[78] H. Rusche, Computational fluid dynamics of dispersed two-phase flows at high phase fractions, in: PhD Thesis, Mechanical Engineering,University of London,2002

[79] B.P. Leonard, Simple high-accuracy resolution program for convective modelling of discontinuities, International Journal for Numerical Methods in Fluids, 8 (1988) 1291-1318.

[80] E. Thompson, Use of pseudo-concentrations to follow creeping viscous flows during transient analysis, International Journal for Numerical Methods in Fluids, 6 (1986) 749-761.

[81] A. Fortin, A. Béliveau, Y. Demay, Numerical solution of transport equations with applications to non-newtonian fluids, in: Trends in applications of mathematics to mechanics, 1995, pp. 311-322.

[82] J.F. Hétu, D.M. Gao, A. Garcia-Rejon, G. Salloum, 3D finite element method for the simulation of the filling stage in injection molding, Polymer Engineering & Science, 38 (1998) 223-236.

[83] R. Courant, K. Friedrichs, H. Lewy, Über die partiellen differenzengleichungen der mathematischen physik, Mathematische Annalen, 100 (1928) 32-74.

[84] C. Stoker, Developments of the arbitrary lagrangian-eulerian method in non-linear solid mechanics: Applications to forming processes, in: Thesis, Universiteit Twente,1999

[85] M. Souli, Zolesio, J.P., Arbitrary lagrangian-eulerian and free surface methods in fluid mechanics, Comput Method Appl Mech Eng, 191 (2001) 451-466.

[86] S. Roels, Carmeliet,J., Hens, H., Mesh adaptative finite element formulation for moisture transfer in materials with a critical moisture content, Int. J. Numer. Meth. Engng., 46 (1999) 1001-1016.

[87] H. Braess, Wriggers, P., Arbitrary lagrangian eulerian finite element analysis of free surface flow, Comput Method Appl Mech Eng, 190 (2000) 95-109.

[88] C.-W. Shu, S. Osher, Efficient implementation of essentially non-oscillatory shock-capturing schemes, Journal of Computational Physics, 77 (1988) 439-471.

[89] C. Shu, Total-variation-diminishing time discretizations, SIAM J. Sci. and Stat. Comput., 9 (1988) 1073-1084.

[90] W.R. Hwang, W.-Y. Kim, S.H. Kang, S.J. Kim, Direct simulations on 2D mold-filling processes of particle-filled fluids, Korea-Australia Rheology Journal, 21 (2009) 193-200.

[91] S. Bhattacharji, P. Savic, Real and apparent non-newtonian behavior in viscous pipe flow of suspensions driven by a fluid piston, in, 1965, pp. 248-262.

[92] M.R. Kamal, S.K. Goyal, E. Chu, Simulation of injection mold filling of viscoelastic polymer with fountain flow, AIChE Journal, 34 (1988) 94-106.

[93] R. El Otmani, M. Zinet, M. Boutaous, P. Chantrenne, H. Benhadid, Numerical simulation of the filling phase in the polymer injection moulding process with a conservative level set method, International Journal of Material Forming, 1 (2008) 731-734.

[94] R. El Otmani, M. Zinet, M. Boutaous, H. Benhadid, Numerical simulation and thermal analysis of the filling stage in the injection molding process: Role of the mold-polymer interface, Journal of Applied Polymer Science, 121 (2011) 1579-1592.

[95] H.-S. Dou, B. Khoo, N. Phan-Thien, K. Yeo, R. Zheng, Simulations of fibre orientation in dilute suspensions with front moving in the filling process of a rectangular channel using level-set method, Rheologica Acta, 46 (2007) 427-447.

[96] M.G.H.M. Baltussen, M.A. Hulsen, G.W.M. Peters, Numerical simulation of the fountain flow instability in injection molding, Journal of Non-Newtonian Fluid Mechanics, 165 (2010) 631-640.

[97] M.R. Kamal, E. Chu, P.G. Lafleur, M.E. Ryan, Computer simulation of injection mold filling for viscoelastic melts with fountain flow, Polymer Engineering & Science, 26 (1986) 190-196.

[98] H. Mavridis, A. Hrymak, J. Vlachopoulos, Finite element simulation of fountain flow in injection molding, Polymer Engineering & Science, 26 (1986) 449-454.

[99] D.J. Coyle, J.W. Blake, C.W. Macosko, The kinematics of fountain flow in mold-filling, AIChE Journal, 33 (1987) 1168-1177.

[100] X. Jin, Boundary element study on particle orientation caused by the fountain flow in injection molding, Polymer Engineering & Science, 33 (1993) 1238-1242.

[101] Z. Tadmor, Molecular orientation in injection molding, Journal of Applied Polymer Science, 18 (1974) 1753-1772.

[102] R.L. Hoffman, A study of the advancing interface. I. Interface shape in liquid-gas systems, Journal of Colloid and Interface Science, 50 (1975) 228-241.

[103] E. Mitsoulis, Fountain flow revisited: The effect of various fluid mechanics parameters, AIChE Journal, 56 (2010) 1147-1162.

[104] E. Mitsoulis, Fountain flow of pseudoplastic and viscoplastic fluids, Journal of Non-Newtonian Fluid Mechanics, 165 (2010) 45-55.

[105] T. Sato, S.M. Richardson, Numerical simulation of the fountain flow problem for viscoelastic fluids, Polymer Engineering & Science, 35 (1995) 805-812.

[106] T. Sato, S.M. Richardson, Numerical simulation method for viscoelastic flows with free surfaces-fringe element generation method, International Journal for Numerical Methods in Fluids, 19 (1994) 555-574.

[107] R.W. Lewis, A.S. Usmani, J.T. Cross, Efficient mold filling simulation in castings by an explicit finite-element method, International Journal for Numerical Methods in Fluids, 20 (1995) 493-506.

[108] A.S. Usmani, J.T. Cross, R.W. Lewis, A finite-element model for the simulations of mold filling in metal casting and the associated heat-transfer, International Journal for Numerical Methods in Engineering, 35 (1992) 787-806.

[109] J.-F. He´tu, Y. Lauze´, A. Garcia-Rejon, Three-dimensional finite element simulation of mold filling processes, in: S.-F.S.-F. Shen, P. Dawson (Eds.) Numiform, Ithaca, NY, 1995, pp. 1135-1140.

[110] F. Ilinca, J.F. Hetu, Three-dimensional finite element solution of gas-assisted injection moulding, International Journal for Numerical Methods in Engineering, 53 (2002) 2003-2017.

[111] T.D. Papathanasiou, Flow-induced alignment in injection molding of fiber-reinforced polymer composites, in: T.D. Papathanasiou, D.C. Guell (Eds.) Flow-induced alignment in composite materials, Woodhead Publishing Limited, Cambridge, England, 1997, pp. 112-165.

[112] G.M. Vélez-García, P. Wapperom, D.G. Baird, A.O. Aning, V. Kunc, Unambiguous orientation in short fiber composites over small sampling area in a center-gated disk, Composites Part A: Applied Science and Manufacturing, 43 (2012) 104-113.

[113] M.C. Altan, S. Subbiah, S.I. Güçeri, R.B. Pipes, Numerical prediction of three-dimensional fiber orientation in hele-shaw flows, Polymer Engineering and Science, 30 (1990) 848-859.

[114] M. Gupta, K.K. Wang, Fiber orientation and mechanical properties of short-fiber-reinforced injection-molded composites: Simulated and experimental results, Polymer Composites, 14 (1993) 367-382.

[115] C.A. Hieber, S.F. Shen, A finite-element/finite-difference simulation of the injection-molding filling process, Journal of Non-Newtonian Fluid Mechanics, 7 (1980) 1-32.

[116] V.W. Wang, C. Hieber, Dynamic simulation and graphics for the injection molding of three-dimensional thin parts, Journal of Polymer Engineering, 7 (1986) 21-45.

[117] S.T. Chung, T.H. Kwon, Numerical simulation of fiber orientation in injection molding of short-fiber-reinforced thermoplastics, Polymer Engineering and Science, 35 (1995) 604-618.

[118] S.T. Chung, T.H. Kwon, Coupled analysis of injection molding filling and fiber orientation, including in-plane velocity gradient effect, Polymer Composites, 17 (1996) 859-872.

[119] F. Dupret, L. Vanderschuren, Calculation of the temperature field in injection molding, AIChE Journal, 34 (1988) 1959-1972.

[120] R.C. Givler, Crochet, M. J., Pipes, R.B., Numerical prediction of fiber orientation in dilute suspensions, J Compos Mater, 17 (1983) 330-343.

[121] J.W. Gillespie, Vanderschuren, J.A., Pipes, R.B., Process induced fiber orientation: Numerical simulation with experimental verification, Polym Composite, 6 (1985) 82-86.

[122] M. Vincent, Agassant, J.F., Experimental study and calculations of short glass fiber orientation in center gated molded disks, Polym. Composite, 7 (1986) 76-83.

[123] V. Devilers. E., M., Fibre orientation in injection moulding of a disk, in: W.R. Blain, De Wilde, W. P. (Ed.) Computer aided design in composite material technology (CADCOMP/94), Computational Mechanics, Southampton, UK, 1994, pp. 264-272.

[124] B. Magnin, Couplez, T., Vincent, M., Agassant, J.F., Numerical modeling of injection mold-filling with an accurate description of the frontal flow, in: J.L. Chenot, Wood, R.D., Zienkiewick, O.C. (Ed.) Proceedings of Numiform 1992: Numerical methods in Industrial forming processes, Valbonne, France, 1992, pp. 365-370.

[125] M. Vincent, Devilers, E., Agassant, J.F., Fibre orientation calculation in injection moulding of reinforced thermoplastics J Non-Newtonian Fluid Mech, 73 (1997) 317-326.

[126] J. Ko, J.R. Youn, Prediction of fiber orientation in the thickness plane during flow molding of short fiber composites, Polymer Composites, 16 (1995) 114-124.

[127] S. Ranganathan, S.G. Advani, A simultaneous solution for flow and fiber orientation in axisymmetric diverging radial flow, Journal of Non-Newtonian Fluid Mechanics, 47 (1993) 107-136.

[128] E.S.G. Shaqfeh, G.H. Fredrickson, The hydrodynamic stress in a suspension of rods, Physics of Fluids A: Fluid Dynamics, 2 (1990) 7-24.

[129] B.E. Verweyst, Numerical predictions of flow-induced fiber orientation in 3-D geometries, in: PhD Thesis, University of Illinois - Urbana Champaign,1998

[130] B.E. VerWeyst, C.L. Tucker, P.H. Foss, J.F. O'Gara, Fiber orientation in 3-D injection molded features: Prediction and experiment, International Polymer Processing, 4 (1999) 409-420.

[131] M. Engelman, Fidap 7.0 Theory Manual, 1st ed., Fluid Dynamics International Inc., 1993.

CHAPTER 3. EVOLUTION OF FIBER ORIENTATION IN RADIAL DIRECTION IN A CENTER-GATED DISK: EXPERIMENTS AND SIMULATION

S.M. Mazahir [a], G.M. Vélez-García [b], P. Wapperom [c,]*, and D. Baird [a]

[a] Department of Chemical Engineering, Virginia Tech, Blacksburg, VA, 24061, USA

[b] Macromolecules and Interfaces Institute, Virginia Tech, Blacksburg, VA, 24061, USA

[c] Department of Mathematics, Virginia Tech, Blacksburg, VA, 24061, USA

syedm@vt.edu, gvelez@vt.edu, pwappero@math.vt.edu, dbaird@vt.edu

*Author to whom correspondence should be addressed; email: pwappero@math.vt.edu, Tel: +1 540 231 7252, Fax: +1 540 231 5960

Abstract

The evolution of fiber orientation in transient simulations with the Folgar-Tucker model and its slip and reduced strain closure versions was assessed against experimental data measured in the shell, transition, and core layers for two center-gated disks. Decoupled and coupled transient simulations were performed using a measured orientation profile at the inlet of the mold. All three orientation models assessed here match the experimental data only in the steady region of the shell layer but are unable to predict the evolution of orientation in all three layers. Effects of coupling are very small and unable to account for the discrepancies between the experiments and simulations.

Keywords: A. Glass fibres, B. Directional orientation, C. Finite element analysis (FEA), E. Injection moulding

3.1 Introduction

Injection-molded thermoplastics are an alternative for making lightweight parts for use in semi-structural applications. The thermal, mechanical and electrical properties of these materials are dependent on fiber orientation developed during processing. However, because of complex velocity field inside the mold that induces fiber orientation, and the effect of inter-particle interactions due to

high fiber concentrations in commercial suspensions, prediction of fiber orientation with quantitative accuracy is a difficult task.

The Folgar-Tucker (FT) model [1] has been used for prediction of fiber orientation in injection molded parts, with varying degrees of success, and it has been used as the standard model in commercial simulation packages for prediction of fiber orientation. In the FT model the orientation of the fibers is attributed to the drag of the fluid on the fibers and the influence of fiber-fiber interactions on the orientation state. However, the inability to completely account for all fiber-fiber interactions for concentrated suspensions prevents precise description of orientation for molded parts within a fiber concentration of commercial interest. Rheological experiments suggest that the fiber orientation kinetics is much slower than the predictions of the FT model for glass fiber suspensions [2, 3]. In these experiments, the fiber suspension is first sheared to a very large strain, then the direction of the shear is reversed and transient stresses are measured. Some authors have suggested that the discrepancies between the predicted and the experimentally measured orientation for concentrated fiber suspensions arise from the reduction in the rate of rotation of fibers which are caused by the interactions between the fibers, at high concentrations [4, 5]. These interactions, which are not completely accounted for in the FT model play a major role in the evolution of the fiber orientation [6].

Two modifications to the FT model have been proposed to slow down the orientation kinetics [3, 5, 7] in concentrated fiber suspensions. One modification is the addition of a delay parameter known as the strain reduction factor (SRF) [7] or the slip parameter [3]. However, this modified FT model is non-objective. Wang et al. [5] proposed a modified version of the FT model, known as the reduced strain closure (RSC) model which slows down the orientation evolution while keeping the model objective. These modified versions of the FT model show improved transient fiber orientation predictions by slowing down the orientation kinetics in simple flow experiments such as start-up of shear, shear flow reversal [2, 3], and a combination of simple shear and planar elongation under transient conditions [5].

The slowdown in orientation kinetics with the modified versions of the FT model in complex flow experiments, such as a center-gated disk, has been assessed against the published experimental data [8, 9]. However, the published data on fiber orientation is measured in the thickness direction of the mold and *z*-profiles of orientation are reported. Moreover, these *z*-profiles are typically taken in the lubrication region where orientation has reached or almost reached a

steady value. Therefore, this set of data is not a good basis for assessing the slowdown in orientation. A more appropriate criterion for the assessment of slowdown in orientation is a comparison against the measured orientation data along the flow lines. For a center-gated disk, this implies measurement of orientation in the radial direction because it practically coincides with the direction of the flow lines. However, orientation data along the radial direction in a center-gated disk is not available in the literature and the simulation predictions of radial evolution in a center-gated disk have never been validated with experimental measurements [8-13]. Thus, there is a need to measure and report radial evolution of orientation in a center-gated disk in order to understand the behavior of fibers as they progress with the flow and to serve as a benchmark against which orientation evolution kinetics can be assessed.

In order to obtain accurate transient predictions, it is essential for an evolution equation, such as the FT model and its modified versions with reduced orientation evolution kinetics, to start from correct initial data. For injection molding geometries, the initial data for fiber orientation is usually prescribed at the inlet of the mold (also referred to as the gate). However, in most of the numerical studies of orientation in a center-gated disk, the inlet orientation is assumed as completely random orientation, i.e. $A_{rr} = A_{zz} = A_{\theta\theta} = 1/3$, or random in the plane, i.e. $A_{rr} = A_{\theta\theta} = 1/2$, $A_{zz} = 0$ [9-13]. Such an assumption may lead to erroneous conclusions about the slowdown in orientation when compared against the measured orientation along the direction of the flow lines. The best value of the orientation at the inlet for assessment of the transient predictions should be the experimentally measured inlet orientation. Recently, experimentally measured inlet orientation at the inlet of a center-gated disk has been reported showing an asymmetric profile through the thickness which is different from the standard assumption of random orientation [8].

The objectives of this paper are twofold. The primary objective is to report the evolution of orientation along the radial direction in a thin center-gated disk at thickness positions representative of the shell, the transition and the core layer in order to determine whether the slowdown in orientation evolution is present in complex flow geometry. The second objective is to assess whether the modified versions of the FT model are able to predict the slowdown in orientation evolution better than the FT model by comparing model predictions with the orientation data along the radial direction in a center-gated disk.

3.2 Problem Description

A 30 wt% short glass fiber polybutylene-terephthalate (PBT) suspension (Valox 420) was used to make two center-gated disks in an injection molding machine. The viscosity of the PBT matrix was determined on a Rheometrics Mechanical Spectrometer (RMS-800) at 533K from steady shear and dynamic oscillatory measurements [3]. The PBT matrix behaves as a Newtonian fluid with viscosity η = 350 Pa·s under shear rates ranging from 0.1 s^{-1} to 100 s^{-1} [8]. The dimensions of the glass fibers suspended in the PBT matrix were determined from a burn-off process for approximately 1000 fibers. The number average fiber length L_f was 362.8 μm and the average diameter d_f was12.9 μm. This corresponds to an aspect ratio of a_r = 28.1.

Two short-shot disks were made in a center-gated mold having internal radius r_{in} = 2.97 mm, outer radius r_{mold} = 57.0 mm, and thickness $2H$ = 1.38 mm. The disks filled approximately 90 % of the radial distance inside the mold. The purpose behind incomplete filling of the mold was to account for the evolution of orientation only during the mold filling phase of the injection molding operation. The dried resin was fed to the screw at 433 K and injected into the mold maintained at 363 K. The mold was filled using an injection pressure of approximately 20 MPa, for a fill time of approximately one second. This corresponds to a volumetric flow rate $q \approx 11.8$ cm^3/s. The disks were then allowed to cool inside the mold for one minute in order to minimize warpage. The average outer radius was r_{out} = 51.5 mm. Figure 3.1 shows the radial dimensions of the incomplete disk normalized by the half thickness of the disk, i.e. r_{in}/H = 4.30 and r_{out}/H = 74.7.

A center-gated disk is a model geometry for evaluating fiber orientation because it resembles the features of commercial molds. A multilayer structure with each layer exhibiting different fiber orientation has been proposed as shown in Figure 3.2 [14]. At least two distinguishable layers of orientation through the thickness have been identified experimentally, known as the shell and the core layer [15]. It has been observed that in the shell layer, fibers tend to align in the direction of the flow (r-direction) and in the core layer, fibers tend to align in the direction of the extension (θ-direction) [6, 16]. A third layer, the transition layer, located between the shell and the core layer exhibits non-preferential orientation [13]. A disk has three primary regions defined on the basis of the flow field: entry, lubrication and front [17]. In all these regions, complex flow is present comprising shear and extensional deformation with different degrees of each deformation type. The shear deformation tends to align the fibers in the direction of the flow lines and the extensional deformation tends to

align the fibers in the direction of the extension. Extensional deformation is dominant in the entry region and close to the centerline. In the lubrication region, a combination of shear and extensional deformation is present with shear dominating near the walls and extension dominating around the centerline.

3.3 Experimental evaluation of fiber orientation

Fiber orientation was measured at constant heights along the radial direction as a new strategy for assessing the evolution of fiber orientation in a center-gated disk. The orientation data obtained with this strategy provides a way for understanding the different effects of the flow field in different layers in the disk, with the layers as shown in Figure 3.2. This is because flow lines run parallel along the radial direction in the most part of the disk and the orientation evolves along these flow lines. In small regions, flow lines are not exactly parallel to the radial direction, such as in the entry region close to the gate where the fiber suspension turns and enters the mold cavity [18]. Such deviations are small compared to the height of the area selected for orientation measurement (bin) because the flow is primarily in the radial direction. Orientation measured with this new strategy is an improvement over the traditional method of orientation through the thickness because it shows the differences in the evolution of orientation in different layers as we move along the flow lines.

Measurements of orientation were made on optical micrographs taken from two independent disks having average dimensions and molding conditions described in Sec. 2. The sampling considerations and strategy are illustrated in Figure 3.3 and summarized as follows. The orientation was measured in rectangular sampling bins with a height $H/6$ and length approximately $2L_f$, as described by Vélez-García et al. [19]. Sampling heights representative of the shell layer near the wall, the transition layer beneath the shell layer, and the core layer around the centerline, were chosen as z_s/H = 0.75, 0.42, and 0.08, respectively, and the sampling bins for each layer were centered in the z-direction at these heights. The skin layer was excluded from this experimental study. The wall-to-wall distance in the micrographs was measured locally at each sample radial location and was normalized by the half-thickness H of the disk. The z_s/H locations for the bins were, therefore, determined independently for each radial location. The error introduced in the bin height due to independent measurement at each sampled radial location was insignificant. Twelve sampling areas along the radial direction were used to characterize the orientation for each layer, as shown in Figure 3.3. The sampling bins were centered in the r-direction at these locations. The radial sampling distribution was chosen to assess the variation in the orientation due to the presence of different flow regions inside the mold cavity, as indicated in Sec. 2. Five closely spaced sampling

regions, i.e. r_s/H = 4.8, 7.8, 11, 15 and 18 were selected near the gate in order to capture rapid changes in the orientation in the entry region. A larger separation between sampling areas was used at radial locations away from the gate, i.e. r_s/H = 18, 25, 33, 40, 47, 54, 61 and 68, because gradual changes in orientation are expected in the shear flow dominated lubrication region.

The procedure proposed by Vélez-García et al. [8, 19] was used to characterize the radial evolution of orientation. In this procedure, a modified version of the method of ellipses (MoE) was used to evaluate the orientation because of its simplicity and reliability. In the MoE, the elliptical footprints of fibers in a polished plane are used to obtain orientation angles, i.e. in-plane (ϕ_f) and out-of-plane (θ_f) angles, for every individual fiber, followed by the estimation of a volumetric average of orientation represented by a second order tensor. Vélez-García et al. extended the MoE to consider partially elliptical footprints in order to obtain reliable orientation data in small sampling areas and characterize regions with rapid changes in orientation. The modified MoE also includes the elimination of the ambiguity problem of two fibers having identical cross sections in the plane of measurements but with orientations ϕ_f and $\phi_f + \pi$. For this, a shadow and its location were identified for elliptical and partially elliptical footprints. The measurements of fiber orientation in this study were performed by means of image analysis of micrographic images (20X magnification) of a polished cross section containing the sampling area of interest. Using an in-house Matlab® code, each image containing the region of interest was divided into 12 bins and the orientation obtained from elliptical and partially elliptical footprints was evaluated for the bins of interest. Subsequently, the second-order orientation tensor and the sampling error were estimated following the procedure described by Bay and Tucker [20] and Mlekusch [21]. The orientation data reported here is calculated as a weighted average from two disks using the averaging method described by Vélez-García et al. [19].

Experimental orientation values are given in Figure 3.4 through Figure 3.6 for the shell, transition, and core layer, respectively. The values are averages from measurements performed on two center-gated disks. The orientation data from these two disks show good reproducibility for all radial locations selected in this study. The planar orientation state for most of the radial locations seen in these figures allows us to simplify the discussion and examine the effects on the diagonal components through the A_{rr} component. In the case of off-diagonal components, we focused on the A_{rz} and $A_{r\theta}$ components because $A_{\theta z} \approx 0$ for all layers.

Figure 3.4(a) shows the diagonal components of the orientation tensor at different radial locations for the shell layer. The shell layer is dominated by shear, which aligns the fibers in the *r*-direction. A sudden drop is observed in A_{rr} from the gate to r_s/H = 7.8 followed by an increase between r_s/H = 7.8 and 11 to a value higher than the inlet orientation. The A_{rr} component then drops back to about the same value as r_s/H = 7.8, but this drop happens over about twice the distance as compared to the first drop. This fluctuating pattern near the gate is reproducible as similar behavior is observed in the two disks that were considered for orientation measurements. The region between r_s/H = 18 and 25 shows an increase in orientation and the orientation remains stable between r_s/H = 25 and 61 (considering the relatively large error bar at r_s/H = 54). This region of stable orientation has A_{rr} values close to the A_{rr} value measured at the gate. The orientation then drops in the region between r_s/H = 61 and 68 with A_{rr} and $A_{\theta\theta}$ values converging to similar levels.

The A_{rz}, $A_{r\theta}$ and $A_{\theta z}$ components of the orientation tensor for the shell layer are shown in Figure 3.4(b). In order to have clarity, the error bars are shown for $A_{r\theta}$ only, which had the maximum observed error compared to other off-diagonal components. The profiles along the radial direction show fluctuations in these components with magnitudes dependent on the radial location. The value of the A_{ij} component represents the average tilt of the fibers projected on the *ij*- plane. In orientation terms, the values of these off diagonal terms indicate three possible conditions. Considering the $A_{r\theta}$ component, the possible values of $A_{r\theta} \approx 0$, $A_{r\theta} > 0$, and $A_{r\theta} < 0$ denote insignificant tilting, tilting in the counter-clockwise direction, and tilting in the clockwise direction, respectively, in the $r\theta$-plane. From Figure 3.4(b), we see that A_{rz} is close to zero at most r_s/H locations except close to the gate (r_s/H = 4.8). $A_{r\theta}$ starts close to zero at the gate, shows an increase for a distance upto r_s/H = 11 and then drops to a value close to zero at r_s/H = 18. There is an increase in $A_{r\theta}$ between r_s/H = 40 and 54 followed by a drop to values close to zero. $A_{\theta z}$ stays close to zero in the entire shell layer.

The evolution of orientation for the transition layer is shown in Figure 3.5. In this layer, both shear and extension are present. A sudden reduction is observed in A_{rr} similar to the shell layer between the gate and r_s/H = 7.8 as the influence of extension, which aligns the fibers in the θ-direction, is relatively large in this region. However, there is a steady increase in A_{rr} between r_s/H = 7.8 and 18 as shear becomes more dominant at larger r/H values, aligning the fibers in the *r*-direction. The orientation continues to increase between r_s/H = 18 and 40, although this increase is more gradual than the increase between r_s/H = 7.8 and 18. At r_s/H = 40, the orientation reaches its peak value which is higher than the orientation at the same radial location in the shell layer. The

profile qualitatively matches with the shell layer between r_s/H = 25 and 68 with orientation staying relatively flat between r_s/H = 25 and 61 and showing a drop between r_s/H = 61 and 68. However, A_{rr} values in this region are higher than A_{rr} values in the shell layer. In the case of the off-diagonal components, the evolution profiles qualitatively match with the evolution profiles in the shell layer.

The radial evolution of orientation in the core layer is shown in Figure 3.6. This layer is dominated by extension which aligns the fibers in the θ-direction. As a result, $A_{\theta\theta}$ increases and A_{rr} decreases in this layer. The drop in A_{rr} near the gate, is consistent with the drop in other layers between the gate and r_s/H = 7.8. A_{rr} continues to decrease in value upto r_s/H = 15. It is noticeable that the increase in $A_{\theta\theta}$ mirrors the decrease in A_{rr} in this region. Between r_s/H = 15 and 54, orientation stays relatively flat at about A_{rr} = 0.3. The orientation further drops between r_s/H = 54 and 61 and then stays relatively flat between r_s/H = 61 and 68. The off-diagonal components A_{rz} and $A_{\theta z}$ stay relatively flat close to zero for the most part of the flow domain. Variation of $A_{r\theta}$ shows tilting of fibers in the $r\theta$-plane with values between +0.15 and -0.15.

3.4 Modeling and simulation of fiber orientation

3.4.1. Governing equations

Folgar and Tucker [1] proposed a model for the evolution of the second order orientation tensor **A**:

$$\frac{D\mathbf{A}}{Dt} = \left(\mathbf{W}\cdot\mathbf{A} - \mathbf{A}\cdot\mathbf{W}\right) + \lambda\left(\mathbf{D}\cdot\mathbf{A} + \mathbf{A}\cdot\mathbf{D} - 2\mathbf{A}_4 : \mathbf{D}\right) + 2C_I\dot{\gamma}\left(\mathbf{I} - 3\mathbf{A}\right) \tag{1}$$

where D/Dt is the material derivative, $\mathbf{W} = [(\nabla\mathbf{v}) - (\nabla\mathbf{v})^T]/2$ the vorticity tensor and $\mathbf{D} = [(\nabla\mathbf{v}) + (\nabla\mathbf{v}^T)]/2$ the rate-of-strain tensor. The velocity gradient is defined as $\nabla\mathbf{v} = \partial v_j / \partial x_i$ and the shape factor $\lambda = \left(a_r^2 - 1\right)/\left(a_r^2 + 1\right)$, a_r being the aspect ratio of the fibers. For high aspect ratio particles such as glass fibers, $\lambda = 1$. $\mathbf{A}_4$ is the fourth order orientation tensor, **I** the identity tensor, C_I the interaction coefficient and $\dot{\gamma} = \sqrt{2\mathbf{D}:\mathbf{D}}$. The last term in Eq. (40) is the interaction term which introduces a randomizing effect in the model and is used to account for the semi-dilute-regime fiber interaction contributions to the orientation.

The FT model predicts too rapid evolution of orientation and does not match the kinetics of orientation evolution in transient shear flow [5, 7, 8]. Hence, two modifications were proposed to slow down the

orientation kinetics. One modification is to add a strain reduction factor (SRF) proposed by Huynh et al. [7] or a slip parameter proposed by Eberle et al. [3] to delay the orientation evolution:

$$\frac{D\mathbf{A}}{Dt} = \alpha\left[\left(\mathbf{W}\cdot\mathbf{A}-\mathbf{A}\cdot\mathbf{W}\right)+\lambda\left(\mathbf{D}\cdot\mathbf{A}+\mathbf{A}\cdot\mathbf{D}-2\mathbf{A}_4:\mathbf{D}\right)+2C_I\dot{\gamma}\left(\mathbf{I}-3\mathbf{A}\right)\right] \tag{2}$$

where the slip parameter α is a factor between 0 and 1. However, this modification renders the fiber orientation equation non-objective. Wang et al. [5] proposed the reduced strain closure (RSC) model where the objectivity is retained while the slowdown in the evolution of orientation is achieved,

$$\frac{D\mathbf{A}}{Dt} = \left(\mathbf{W}\cdot\mathbf{A}-\mathbf{A}\cdot\mathbf{W}\right)+\lambda\left(\mathbf{D}\cdot\mathbf{A}+\mathbf{A}\cdot\mathbf{D}-2\left[\mathbf{A}_4+(1-\kappa)(\mathbf{L}_4-\mathbf{M}_4:\mathbf{A}_4)\right]:\mathbf{D}\right)+2\kappa C_I\dot{\gamma}\left(\mathbf{I}-3\mathbf{A}\right) \tag{3}$$

where κ is the strain reduction factor with values between 0 and 1 and $\mathbf{L}_4$ and $\mathbf{M}_4$ are defined as:

$$\mathbf{L}_4 = \sum_{i=1}^{3}\lambda_i\mathbf{e}_i\mathbf{e}_i\mathbf{e}_i\mathbf{e}_i, \qquad \mathbf{M}_4 = \sum_{i=1}^{3}\mathbf{e}_i\mathbf{e}_i\mathbf{e}_i\mathbf{e}_i \tag{4}$$

where λ_i are the eigenvalues and $\mathbf{e}_i$ the eigenvectors of $\mathbf{A}$.

For the fourth order tensor $\mathbf{A}_4$, a closure approximation needs to be used to express it in terms of $\mathbf{A}$. Chung and Kwon [22] have proposed the invariant-based optimal fitting (IBOF) closure approximation for $\mathbf{A}_4$. The IBOF closure is as accurate as eigenvalue-based closures, but requires less computational time. We use the IBOF closure approximation for $\mathbf{A}_4$ in all simulations.

The flow of an incompressible fluid under creeping conditions is governed by the mass balance and the momentum balance equations, given by:

$$\nabla\cdot\mathbf{v} = 0 \tag{5}$$

$$\nabla\cdot\left(-p\mathbf{I}+2\eta_s\mathbf{D}+\mathbf{T}^{fiber}\right) = \mathbf{0} \tag{6}$$

where ∇ represents the gradient operator, $\mathbf{v}$ the velocity, p the pressure, $\mathbf{I}$ the identity tensor and η_s the matrix viscosity. The viscous extra-stress $\mathbf{T}^{fiber}$ is due to the presence of the fibers and the general form of this viscous extra-stress contribution is described by:

$$\mathbf{T}^{fiber} = 2\nu\zeta_{str}\mathbf{D}:\mathbf{A}_4 \tag{7}$$

where ν is the concentration of the fibers and ζ_{str} is the viscous drag coefficient [23]. For $\mathbf{A}_4$ we use the IBOF closure approximation in all simulations. The viscous component of the extra-stress is also described in terms of the particle number (N_p) and η_s, where N_p is an expression that represents the anisotropic contribution of the fibers, i.e. the effect of fibers on the rheology [18, 24]. The relation between the two forms is [25]:

$$\eta_s N_p = \nu \zeta_{str} \tag{8}$$

The most popular model used to determine the viscous drag coefficient in the simulation of injection molded thermoplastic composites has been the Dinh and Armstrong model [23], described by

$$\zeta_{str} = \frac{\pi \eta_s L_f^3}{12 \ln\left(2a_c / d_f\right)} \tag{9}$$

where a_c is the average inter-fiber distance that depends on the orientation of the fibers.

We have assumed isothermal filling conditions due to short injection time of about one second, in agreement with the findings of Wu et al. [26]. Isothermal conditions are further validated by roughly equal amounts of heat dissipated through viscous heating and the rate of heat loss by conduction through the mold walls. The maximum rise in the temperature due to viscous dissipation during filling time of one second was estimated to be about 3.5 K. Therefore, we do not consider thermal effects in our simulations.

3.4.2. Model parameters

The orientation evolution models (Eqs. (1-3)) contain model parameters (C_I, α, κ) which need to be determined from flow experiments. The orientation model parameters α and κ are factors between 0 and 1. When C_I is set to zero, a highly flow-aligned orientation state is predicted and the model reduces to Jeffery's model [27]. The values of C_I are typically in the range of 0.003-0.016 [28]. Eberle et al. [3] obtained the model parameters for Valox 420 from fitting model predictions using the FT model and its slip version to measured orientation data in startup of shear flow obtained at different strain values at a shear rate $\dot{\gamma} = 1\ \mathrm{s}^{-1}$. The model parameters were obtained as $C_I = 0.006$ for the FT model and (C_I, α) = (0.006, 0.30) for the slip version. Vélez-García et al. [8] used a slightly different fitting for the same suspension and obtained the model parameters as C_I = 0.012 for the FT model and (C_I, α) = (0.012, 0.40) for the slip version. Wang et al. [5] fitted the

model parameters to shear viscosity data for the same suspension using the RSC model and obtained a set of model parameters (C_I, κ) = (0.0112, 0.119).

In this work, model parameters for all three models are fitted using experimental orientation data in startup of shear flow obtained by Eberle et al. [3]. The model parameters for the three models under consideration are obtained as C_I = 0.0112 for the FT model, (C_I, α) = (0.0112, 0.40) for the slip version and (C_I, κ) = (0.0112, 0.40) for the RSC version. Parameter fitting using the RSC model predictions is shown in Figure 3.7. The value of C_I obtained with this method matches with the value obtained by Wang et al. [5]. However, the value of κ, which is primarily responsible for the transient behavior, is approximately four times the value obtained by Wang et al. [5].

The viscous model parameters $\nu\zeta_{str}$ are, in general, either calculated from theory or obtained from rheological studies on fiber suspensions. In this work, we fitted the stress predictions to stress data of Eberle et al. [4] considering only the steady state and using a value of C_I = 0.0112. The fitted value of the extra-stress parameters was obtained as $\nu\zeta_{str}$ = 6.18 which was used in all coupled simulations.

3.4.3. Numerical methods

The fiber suspension is injected in a center-gated disk with dimensions shown in Figure 3.1. The filling of the mold is a transient problem in which the suspension replaces the air as it fills the mold. One of the geometrical simplifications applied for injection molding of thin geometries is known as the Hele-Shaw flow approximation [29]. This simplification has a formulation developed for viscous and viscoelastic fluids under a creeping flow regime, assuming that normal stresses are negligible compared to shear stresses. This approximation is suitable for a center-gated disk geometry because the characteristic length in the z-direction is significantly less than characteristic lengths in other directions and the velocity gradient in the z-direction is significantly higher than those in in-plane directions. With this approximation, 2-D fountain flow is completely discarded and a 1-D radial flow is obtained in the entire domain.

The time-stepping scheme used for the transient mold filling solves three decoupled equations at every time step: the flow equations, orientation equations, and a transport equation to capture the suspension-air interface. Velocity is approximated by continuous quadratic polynomials. Discontinuous quadratic polynomials are used for the orientation and pseudo-concentration and discontinuous linear polynomials for the extra-stress. The choice of discontinuous polynomials for

the orientation and extra-stress is made because of the convective nature of the orientation equations that are solved to determine these variables. The solution at each time step is determined in the 2-D simulation domain shown as the shaded area in Figure 3.1. The details of solution schemes for the above equations are given below.

The Hele-Shaw equation for the filling of the fiber suspension takes the form

$$-\frac{\partial p}{\partial r}+\frac{\partial}{\partial z}\left(\eta_s \frac{\partial v_r}{\partial z}\right)+T_{rz}=0 \tag{10}$$

With the extra-stress taken into consideration, the flow is termed as coupled Hele-Shaw flow; while without the extra-stress, as decoupled Hele-Shaw flow. The decoupled Hele-Shaw flow is equivalent to analytical solution of Eq. (10) with T_{rz} = 0 which gives the velocity field as $v_r(r,z)=(K/r)[1-(z/H)^2]$, where K is a constant that depends on the dimensions of the disk, and the prescribed flow rate [29]. Several attempts to couple the Hele-Shaw flow with the computation of extra-stress can be found in the literature [11, 13, 30-32]. We take advantage of the 2-D simulation domain and spatially discretize the domain using 1-D finite elements in the z-direction at multiple r-locations. The 1-D velocity field is solved on these elements by solving a system of n + 1 equations (Eq. (10) at n nodes and the flow rate equation) in n + 1 unknowns (v_r at n nodes and $\partial p/\partial r$). This solution strategy requires significantly less computation time than the solution for the entire 2-D domain at once. In order to apply the 1-D finite element discretization, T_{rz} in Eq. (10) is calculated as a continuous quadratic field projected from the discontinuous linear extra-stress field.

Orientation evolution equations are discretized in space using the DGFEM of Lesaint and Raviart [33]. The time stepping is done with the explicit RK3-TVD scheme [34]. The DGFEM solves the equations on each element separately and handles the problem of oscillations associated with hyperbolic equations by taking into account a discontinuity at inter-element boundaries [35]. The explicit RK3-TVD scheme allows for stable solution without requiring large computation time and memory. The orientation is initialized as random in the empty mold. The boundary condition prescribed at the inlet for the orientation in all simulations is the weighted average of the orientation measured at the inlets of two center-gated disks using the averaging method of Vélez-García et al. [19].

The pseudo-concentration method is used to capture the advancing front in the transient filling simulation [36]. In this method, air is introduced as a fictitious fluid with zero density and

viscosity 0.1% of the filling fluid. A pseudo-concentration variable c is defined to distinguish between the filling fluid and air. A value of $c = 1$ indicates the suspension, a value of $c = 0$ indicates air, and the interface is indicated by a value of $c = 0.5$. The variable c is convected with the fluid velocity **v**. In the Hele-Shaw formulation, the velocity has only the flow-direction component and the front moves with the average velocity $(\bar{v}_r)$ that is averaged through the thickness of the mold. Therefore, the equation for the evolution of c takes the form

$$\frac{\partial c}{\partial t} + \bar{v}_r \frac{\partial c}{\partial r} = 0 \tag{11}$$

Eq. (11) is solved along a boundary in the flow direction. The RK3-TVD scheme [34] is used for time-stepping and the DGFEM [33] for discretization in space. A value of $c = 1$ is prescribed at the inlet boundary and a value of $c = 0$ is used as initial condition inside the simulation domain. This pseudo-concentration variable is used for interpolation between air and the suspension.

3.5 Simulation Results and Discussion

The slowdown in orientation as predicted by the modified versions of the FT model is assessed by comparing the model predictions with the experimentally measured orientation data. Orientation data measured along the flow lines at different heights representative of shell, transition and core layers are used to validate model predictions with coupled and decoupled Hele-Shaw flow solutions. The A_{rr} component of the orientation tensor, considered as representative of the evolution of orientation, is selected for experimental validation in the center-gated disk geometry. The polymer matrix is considered Newtonian with η_s = 350 Pa·s and $\lambda = 1$ is used in all orientation evolution equations. All dimensions of the simulation domain are non-dimensionalized based on the half thickness of the disk. The number of elements in the r-direction is fixed at 100. Mesh refinement was performed in the z-direction to ensure convergence of the simulation results for the FT model. For sufficient accuracy and computational efficiency, it was found that 10 elements in the z-direction are sufficient and this is the number of elements used in all simulations. The predictions in the gate and lubrication region are discussed first followed by the predictions behind the advancing front.

Figure 3.8 shows the orientation predictions with the decoupled Hele-Shaw flow solution in shell, transition and core layers. All three orientation models, FT, slip and RSC are compared with the experimental data averaged from two disks. As shown in Figure 3.8(a), the predictions with all

three models match the experimental data only in the steady region (between r_s/H = 25 and 61) for the shell layer but not in other regions. Near the gate, where high extensional effects are present, all models show a slight drop in the orientation. However, the orientation does not drop to the experimentally observed level at r_s/H = 7.8. The modified orientation models predict a smaller drop in the orientation between r_s/H = 4.8 and 7.8 as compared to the FT model, which seems to be a change in the wrong direction when experimental values are considered. All three models are unable to capture the local peaks and undershoots that are seen in experiments between r_s/H = 4.8 and 25. The steady region (approximately between r_s/H = 25 and 61) has been traditionally used for validation of simulation results using the orientation profile along the thickness direction. This is a region of high shear away from the effects of the gate and the advancing front. Between r_s/H = 25 and r_s/H = 61 orientation predictions with all three models compare well with experiments. In the transition layer, as shown in Figure 3.8(b), the FT model predicts a sudden drop in the orientation near the gate and matches the experimental A_{rr} values at r_s/H = 7.8. However, it is not able to catch up with the fast rise seen in A_{rr} values between r_s/H = 7.8 and 11. The modified models match the orientation at r_s/H = 11 but are unable to capture the sudden drop in the orientation between r_s/H = 4.8 and 7.8. All three models are off from experimental A_{rr} values between r_s/H = 15 and 40. In this region, the FT model under-predicts the orientation while the predictions with the modified versions are even lower. This suggests that the reduced orientation evolution models are not good for the lubrication region in the transition layer and there may be a need to enhance the evolution in this region instead of slowing it down. In the region between r_s/H = 47 and 61, all model predictions are close to experimental values. In the core layer, as shown in Figure 3.8(c), the FT model shows a sudden drop in orientation between r_s/H = 4.8 and 15. However, the model predictions are close to experimental A_{rr} values only at r_s/H = 7.8 and remain lower than the experimental A_{rr} values at all other sampled locations between r_s/H = 4.8 and 15. In the same region, the modified versions predict a too slow evolution of orientation. In the region between r_s/H = 18 and 40, the FT model shows a gradual rise. However, the predictions are lower than the experimental A_{rr} values. In the same region, modified versions predict a relatively flat profile and predictions are closer to experimental A_{rr} values. At radial locations r_s/H = 47 and 54, FT model predictions match the experimental levels while modified versions are slightly above the experimental levels.

Decoupled simulation results with all three models fail to predict the experimentally measured orientation close to the advancing front in all three layers. This is the region downstream of the lubrication region, where the measured orientation values decrease steadily in all three layers.

One of the causes of reduction in the orientation in this region is the fountain flow behind the advancing front that is a characteristic flow feature present in mold filling of polymeric fluids. However, the orientation predictions with the Hele-Shaw flow solution that reach a steady state in the lubrication region, do not show any reduction downstream of the lubrication region. This is most likely because the Hele-Shaw formulation is incapable of reproducing the 2-D flow behind the front and not caused by the orientation models. Because the transverse flow in the *z*-direction is discarded in the Hele-Shaw flow approximation, the predicted orientation shows high flow-direction alignment in the region behind the front. In all three layers, as seen in Figure 3.8, all three models overpredict orientation at $r_s/H = 68$ which is at a distance $r/H = 6$ behind the front. In the core layer, overprediction of orientation goes further back to $r_s/H = 61$, a distance $r/H = 13$ behind the front.

Coupled Hele-Shaw flow simulations were performed to assess the effects of coupling on the velocity field and orientation predictions. The behavior of the modified versions of the FT model in coupled simulation was similar. Therefore, we discuss the effects of coupling for the original FT model and the RSC model only. Figure 3.9 shows the effect of coupling on the velocity field. The change in the velocity due to coupling is clearly visible near the gate ($r_s/H = 11$) and tends to diminish with increasing r. The effect of coupling is most significant in the core layer and decreases as $|z/H|$ increases. This is consistent with the numerical studies conducted before [10, 11, 13, 18]. However, coupling tends to increase the velocity in the core layer as opposed to the decrease in velocity seen in previous studies [13]. This is because of the use of measured inlet orientation at the gate as opposed to random inlet orientation which has been used in previous studies. Measured inlet orientation has A_{zz} values that are one order less than the A_{zz} values for random inlet orientation ($A_{zz} = 0.3333$ for random orientation). Therefore, the extra-stress due to fibers is less with measured orientation which results in a pointed velocity profile with a higher peak as compared to the simulation results with random inlet orientation. In order to verify results from the previous studies, coupled simulations with random orientation assigned at the inlet were also run and the simulations showed a decrease in the velocity profile around the centerline, which is consistent with the findings of Chung and Kwon [13].

Figure 3.10 shows the effects of coupling on the orientation. In the shell and transition layers, where the velocity gradient is higher, the effect of coupling on the orientation is insignificant. In the core layer with minimum velocity gradient in the thickness direction, the effect of coupling on orientation is more prominent, especially at large r/H values where orientation predictions are higher with coupled simulations. For the FT model, this results in a slight

improvement in the lubrication region because the FT model underpredicts the orientation in this region. However, for the modified versions which slightly overpredict the orientation in this region, coupling leads to increased discrepancy with the experimental values. Therefore, coupling is not the primary factor that can account for discrepancies between the experimental data and model predictions.

3.6 Conclusions

The evolution of fiber orientation along the direction of the flow lines (*r*-direction) has been experimentally determined in a center-gated disk in order to evaluate orientation predictions of the delayed versions of the FT model. The orientation is measured at various locations along the *r*-direction at three different *z/H* locations representative of the shell, transition and core layers, respectively at radial locations close to the gate, in the lubrication region, and near the advancing front. The radial locations are distributed along the entire flow length in order to get insight into the evolution of orientation in different regions. The experimental data allows for the assessment of orientation evolution in complex flows.

Orientation predictions with the FT model and two modified versions with slow orientation kinetics have been validated by comparing with experimentally measured fiber orientation data along the flow direction in a center-gated disk in the shell, transition and core layers. A measured inlet orientation was used to provide the correct starting values for assessment of slowdown in orientation. In decoupled Hele-Shaw simulations, all three orientation models match the experimental data in the steady region of the shell layer. The slowdown in orientation shows an improvement over the FT model only for the steady orientation in the lubrication region of the core layer. However, the evolution of orientation is not correctly predicted by any of the three orientation models. In the core and transition layers, the modified models predict very slow evolution of orientation. This is in contrast with the fast evolution observed experimentally which is predicted better by the FT model. Coupled Hele-Shaw flow is not able to reduce the differences between the experimental data and predicted values as the effect of coupling on orientation is small.

3.7 Acknowledgements

The financial support for this work from the National Science Foundation and the Department of Energy through grant No. DMI-0521918 and National Science Foundation through grant No. CMMI-0853537 are gratefully acknowledged. The authors also wish to thank Sabic Americas Inc. for supplying the Valox 420 used in this work. They also gratefully thank the

Material Science and Engineering Department for letting them use the polishing and microscopic facilities. Gregorio M. Vélez-García also acknowledges support from NSF-IGERT through grant No. DGE-0548783, Macromolecular Science and Infrastructure Engineering, and the University of Puerto Rico-Mayagüez. Syed M. Mazahir also acknowledges support from the Doctoral Scholarship program funded by the Institute for Critical Technology and Applied Science, Virginia Tech.

3.8 References

[1] F. Folgar, C.L. Tucker, Orientation behavior of fibers in concentrated suspensions, Journal of Reinforced Plastics and Composites, 3 (1984) 98-119.

[2] M. Sepehr, G. Ausias, P.J. Carreau, Rheological properties of short fiber filled polypropylene in transient shear flow, Journal of Non-Newtonian Fluid Mechanics, 123 (2004) 19-32.

[3] A.P.R. Eberle, G.M. Vélez-García, D.G. Baird, P. Wapperom, Fiber orientation kinetics of a concentrated short glass fiber suspension in startup of simple shear flow, Journal of Non-Newtonian Fluid Mechanics, 165 (2010) 110-119.

[4] A.P.R. Eberle, D.G. Baird, P. Wapperom, G.M. Vélez-García, Using transient shear rheology to determine material parameters in fiber suspension theory, Journal of Rheology, 53 (2009) 685-705.

[5] J. Wang, J.F. O'gara, C.L. Tucker, An objective model for slow orientation kinetics in concentrated fiber suspensions: Theory and rheological evidence, Journal of Rheology, 52 (2008) 1179.

[6] S.G. Advani, Flow and Rheology in Polymer Composites Manufacturing, Elsevier, University of Michigan, 1994.

[7] H.M. Huynh, Improved fiber orientation predictions for injection-molded composites, in: MS Thesis, Universty of Illinois - Urbana Champaign,2001

[8] G.M. Vélez-García, S.M. Mazahir, P. Wapperom, D.G. Baird, Simulation of injection molding using a model with delayed fiber orientation, International Polymer Processing, 26 (2011) 331-339.

[9] J.M. Park, T.H. Kwon, Nonisothermal transient filling simulation of fiber suspended viscoelastic liquid in a center-gated disk, Polymer Composites, 32 (2011) 427-437.

[10] S. Ranganathan, S.G. Advani, A simultaneous solution for flow and fiber orientation in axisymmetric diverging radial flow, Journal of Non-Newtonian Fluid Mechanics, 47 (1993) 107-136.

[11] S.T. Chung, T.H. Kwon, Coupled analysis of injection molding filling and fiber orientation, including in-plane velocity gradient effect, Polymer Composites, 17 (1996) 859-872.

[12] Å. Larsen, Injection molding of short fiber reinforced thermoplastics in a center-gated mold, Polymer Composites, 21 (2000) 51-64.

[13] D.H. Chung, T.H. Kwon, Numerical studies of fiber suspensions in an axisymmetric radial diverging flow: The effects of modeling and numerical assumptions, Journal of Non-Newtonian Fluid Mechanics, 107 (2002) 67-96.

[14] P.F. Bright, R.J. Crowson, M.J. Folkes, A study of the effect of injection speed on fibre orientation in simple mouldings of short glass fibre-filled polypropylene, Journal of Materials Science, 13 (1978) 2497-2498.

[15] T.D. Papathanasiou, Flow-induced alignment in injection molding of fiber-reinforced polymer composites, in: T.D. Papathanasiou, D.C. Guell (Eds.) Flow-induced Alignment in Composite Materials, Woodhead Publishing Limited, Cambridge, England, 1997, pp. 112-165.

[16] J. Azaiez, K. Chiba, F. Chinesta, A. Poitou, State-of-the-art on numerical simulation of fiber-reinforced thermoplastic forming processes, Archives of Computational Methods in Engineering, 9 (2002) 141-198.

[17] R.S. Bay, C.L. Tucker, Fiber orientation in simple injection moldings. Part I: Theory and numerical methods, Polymer Composites, 13 (1992) 317-331.

[18] B.E. Verweyst, C.L. Tucker, Fiber suspensions in complex geometries: Flow/orientation coupling, Canadian Journal of Chemical Engineering, 80 (2002) 1093-1106.

[19] G.M. Vélez-García, P. Wapperom, D.G. Baird, A.O. Aning, V. Kunc, Unambiguous orientation in short fiber composites over small sampling area in a center-gated disk, Composites Part A: Applied Science and Manufacturing, 43 (2012) 104-113.

[20] R.S. Bay, C.L. Tucker, Stereological measurement and error estimates for three-dimensional fiber orientation, Polymer Engineering and Science, 32 (1992) 240-253.

[21] B. Mlekusch, Fibre orientation in short-fibre-reinforced thermoplastics II. Quantitative measurements by image analysis, Composites Science and Technology, 59 (1999) 547-560.

[22] D. Chung, T.H. Kwon, Invariant-based optimal fitting closure approximation for the numerical prediction of flow-induced fiber orientation, Journal of Rheology, 46 (2002) 169.

[23] S.M. Dinh, R.C. Armstrong, A rheological equation of state for semiconcentrated fiber suspensions, Journal of Rheology, 28 (1984) 207-227.

[24] C.L. Tucker III, Flow regimes for fiber suspensions in narrow gaps, Journal of Non-Newtonian Fluid Mechanics, 39 (1991) 239-268.

[25] G.M. Vélez-García, Experimental evaluation and simulations of fiber orientation in injection molding of polymers containing short glass fibers, in: PhD Thesis, Chemical Engineering,Virginia Polytechnic Institute and State University,2012

[26] P.C. Wu, C.F. Huang, C.G. Gogos, Simulation of the mold-filling process, Polymer Engineering and Science, 14 (1974) 223-230.

[27] G.B. Jeffery, The motion of ellipsoidal particles immersed in a viscous fluid, in: Proceedings of the Royal Society of London, Series A, The Royal Society, 1922, pp. 161-179.

[28] R.G. Larson, The Structure and Rheology of Complex Fluids, Oxford University Press, USA, 1999.

[29] D.G. Baird, D.I. Collias, Polymer Processing: Principles and Design, Wiley, 1998.

[30] S.T. Chung, T.H. Kwon, Numerical simulation of fiber orientation in injection molding of short-fiber-reinforced thermoplastics, Polymer Engineering and Science, 35 (1995) 604-618.

[31] F.P.T. Baaijens, Calculation of residual stresses in injection molded products, Rheologica Acta, 30 (1991) 284-299.

[32] I.H. Kim, S.J. Park, S.T. Chung, T.H. Kwon, Numerical modeling of injection/compression molding for center-gated disk: Part i. Injection molding with viscoelastic compressible fluid model, Polymer Engineering & Science, 39 (1999) 1930-1942.

[33] P. Lesaint, P.A. Raviart, On a finite element method for solving the neutron transport equation, in: C.d. Boor (Ed.) Mathematical Aspects of Finite Elements, Academic Press, New York, 1974, pp. 89-123.

[34] C.-W. Shu, S. Osher, Efficient implementation of essentially non-oscillatory shock-capturing schemes, Journal of Computational Physics, 77 (1988) 439-471.

[35] M. Fortin, A. Fortin, A new approach for the FEM simulation of viscoelastic flows, Journal of Non-Newtonian Fluid Mechanics, 32 (1989) 295-310.

[36] G. Haagh, F. Van De Vosse, Simulation of three-dimensional polymer mould filling processes using a pseudo-concentration method, International Journal for Numerical Methods in Fluids, 28 (1998) 1355-1369.

3.9 Figures

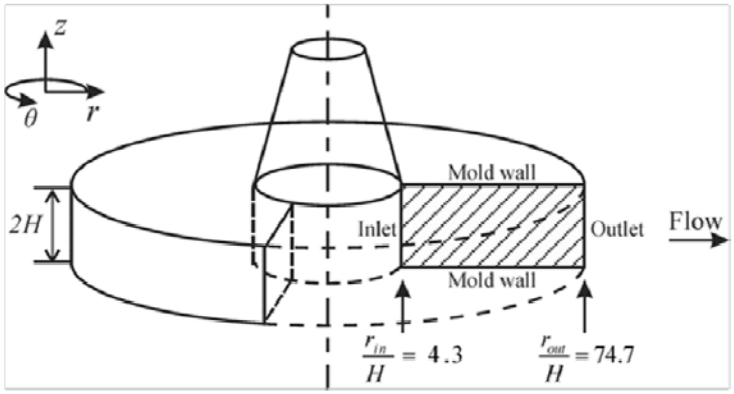

Figure 3.1 Center-gated disk with dimensions normalized by the half thickness *H* of the disk. The shaded area shows the simulation domain and the boundaries.

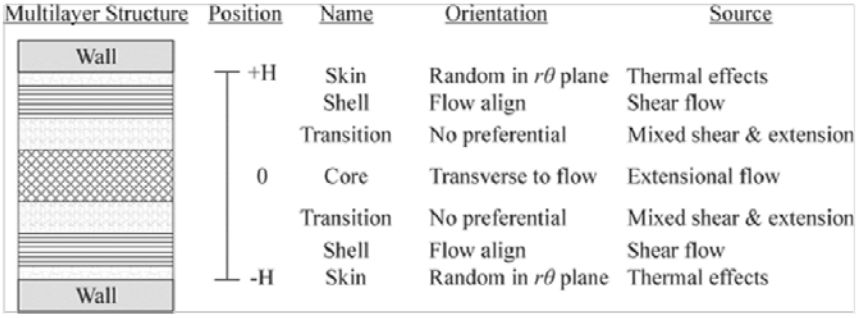

Figure 3.2 Description of the multilayer structure of orientation in a center-gated disk including relative thickness, position, name of the layer, characteristic orientation and physical effects attributed to the orientation.

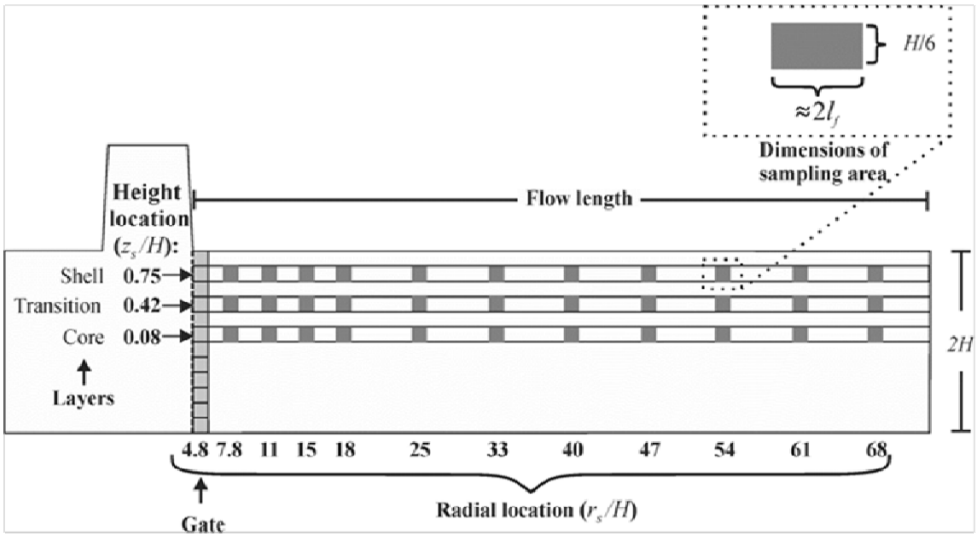

Figure 3.3 Radial locations in a center-gated disk selected for the measurement of fiber orientation. The relative locations of the sampling areas (gray rectangles) for the gate and along different radial locations with constant heights are illustrated in the figure. Insert depicts the dimensions of the sampling area.

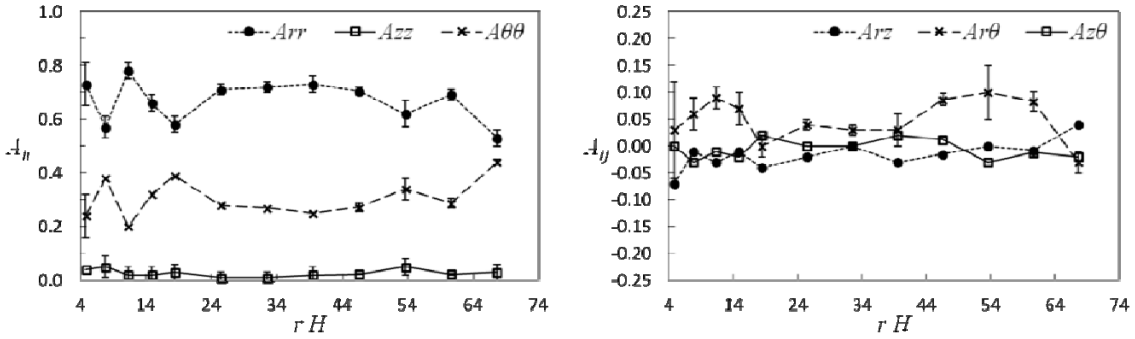

Figure 3.4 Averaged profile of orientation for the upper shell layer (z/H = 0.75) obtained from two center gated disks for (a) diagonal (A_{ii}) and (b) off-diagonal (A_{ij}) components. Standard errors from unequal sample size and assuming unequal variance are shown.

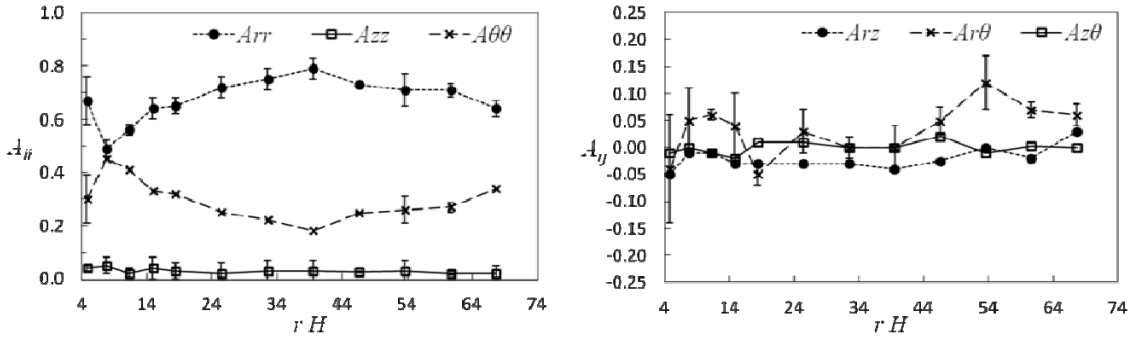

Figure 3.5 Averaged profile of orientation for the upper transition layer (z/H = 0.42) obtained from two center gated disks for (a) diagonal (A_{ii}) and (b) off-diagonal (A_{ij}) components. Standard errors from unequal sample size and assuming unequal variance are shown.

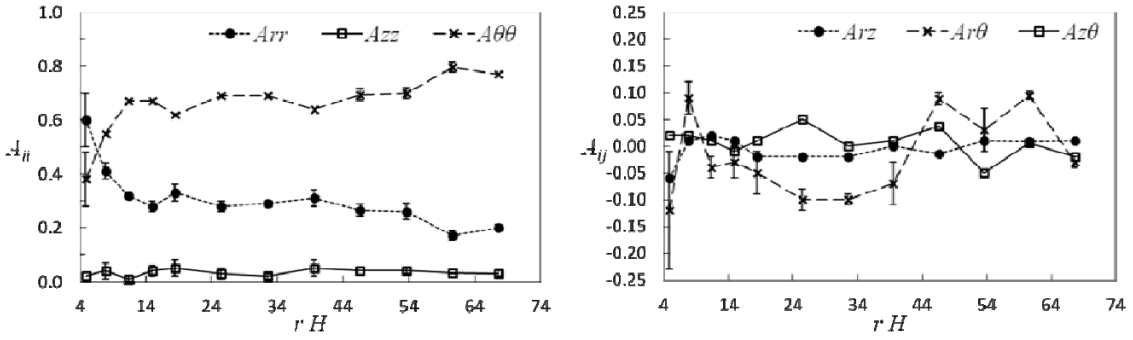

Figure 3.6 Averaged profile of orientation for the upper core layer (z/H = 0.08) obtained from two center gated disks for (a) diagonal (A_{ii}) and (b) off-diagonal (A_{ij}) components. Standard errors from unequal sample size and assuming unequal variance are shown.

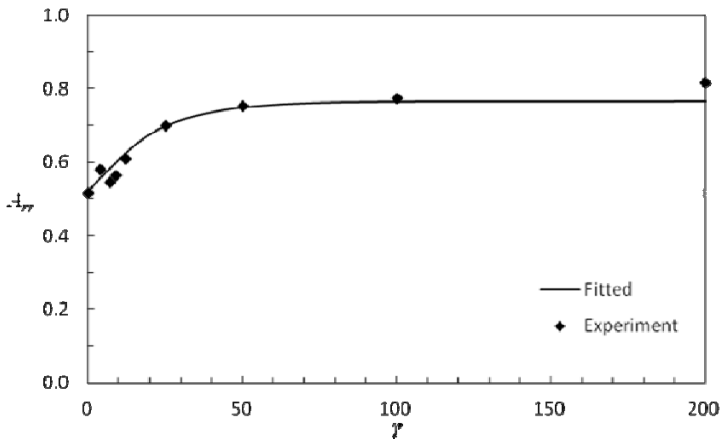

Figure 3.7 Experimentally determined and fitted orientation tensor component A_{rr} in startup of simple shear flow at $\dot{\gamma} = 1\ \mathrm{s}^{-1}$ using model parameters for RSC model determined from rheology (C_I = 0.0112, κ = 0.4) for 30 wt% PBT/glass fiber suspension.

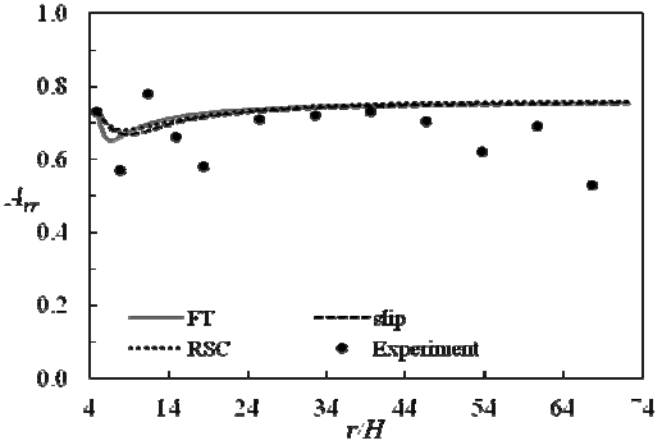

(a)

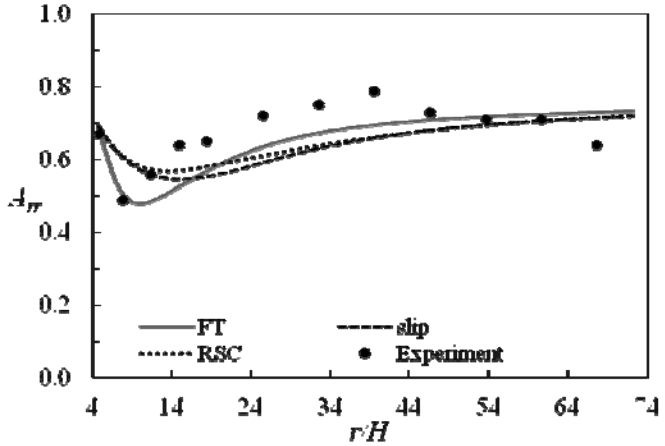

(b)

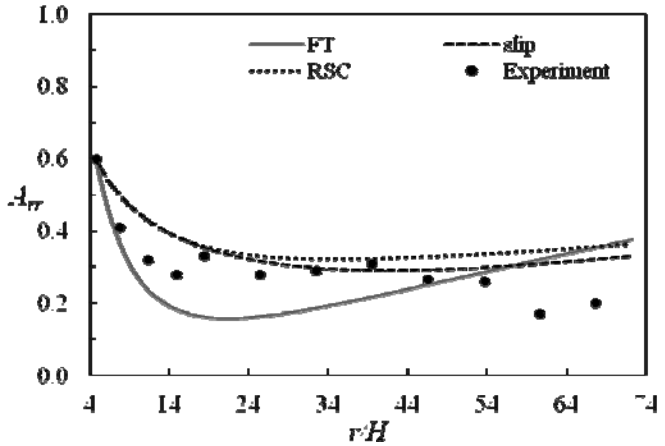

(c)

Figure 3.8 Comparison of A_{rr} predictions with the FT model and its modified versions using decoupled Hele-Shaw simulation with experimentally measured values at (a) z/H = 0.75, (b) z/H = 0.42, and (c) z/H = 0.08.

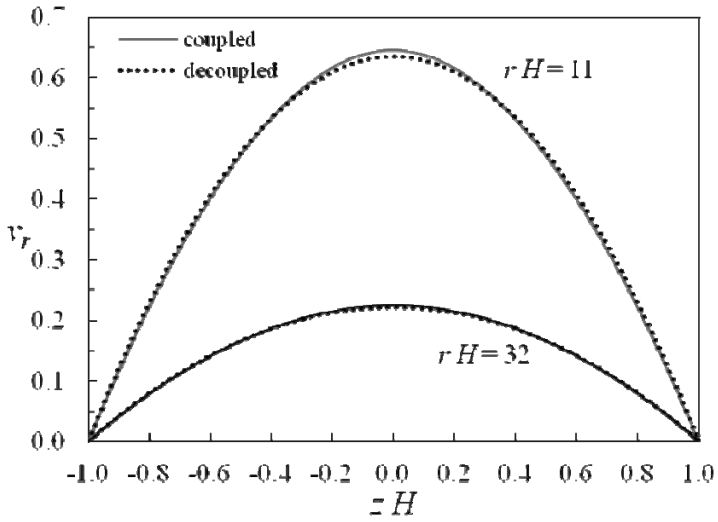

Figure 3.9 Coupled and decoupled velocity profiles through the thickness with the RSC model.

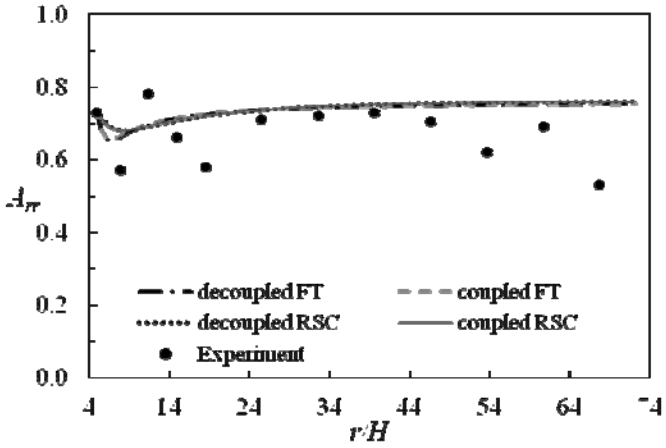

(a)

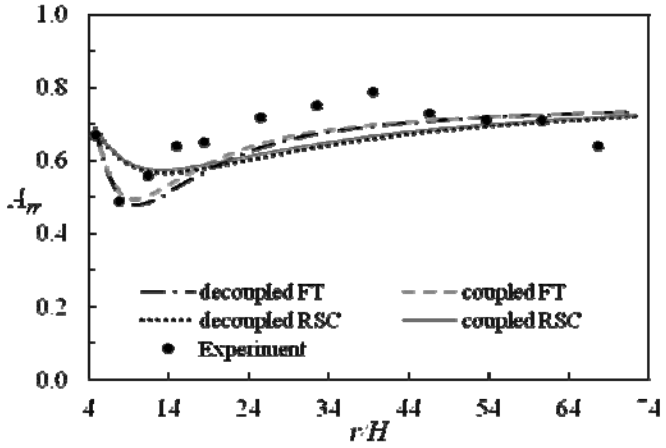

(b)

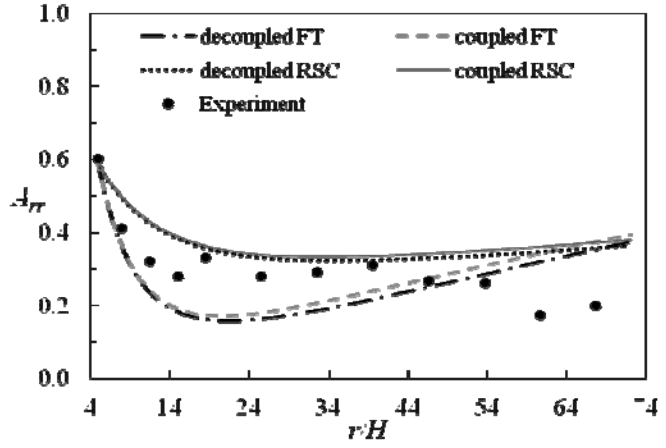

(c)

Figure 3.10 Comparison of A_{rr} predictions in a center-gated disk using coupled and decoupled Hele-Shaw simulations with experimentally measured values at (a) $z/H = 0.75$, (b) $z/H = 0.42$, and (c) $z/H = 0.08$.

CHAPTER 4. FIBER ORIENTATION IN THE FRONTAL REGION OF A CENTER-GATED DISK: EXPERIMENTS AND SIMULATION

*S.M. Mazahir[1], G.M. Vélez-García[2], *P. Wapperom[3], and D. Baird[1]*

[1] Department of Chemical Engineering, Virginia Tech, Blacksburg, VA, 24061, USA

[2] Macromolecules and Interfaces Institute, Virginia Tech, Blacksburg, VA, 24061, USA

[3] Department of Mathematics, Virginia Tech, Blacksburg, VA, 24061, USA

syedm@vt.edu, gvelez@vt.edu, pwappero@math.vt.edu, dbaird@vt.edu

[*] Author to whom correspondence should be addressed; Peter Wapperom, Tel: +1 540 231 7252, Fax: +1 540 231 5960

Abstract

Fiber orientation in the frontal region of a center-gated disk has never been experimentally measured and experimental validation of orientation predictions in this region has never been done. The frontal region of a center-gated disk was studied and its features such as shape, texture and evolution of the layered structure were investigated to understand the evolution of fiber orientation in the frontal region. Fiber orientation was experimentally measured along three different heights representative of shell, transition and core layers, in the region between 90% of fill and 99% of fill in the mold in order to understand the evolution of fiber orientation along radial direction in the frontal region of the disk. Orientation predictions with the Folgar-Tucker model and its modifications, the delayed Folgar-Tucker and reduced strain closure (RSC) models were assessed against the measured experimental data in the frontal region. Pseudo-concentration method was used for the evolution of the advancing front and to include fountain flow effects. Orientation predictions with the fountain flow effects showed a drop in orientation near the front, which was in qualitative agreement with the experimental data. However, Hele-Shaw flow approximation significantly over-predicted orientation in the entire frontal region. The slow versions of the modified Folgar-Tucker model improved predictions at a few locations in the shell layer with no significant improvement in other layers. Coupling of flow and orientation equations did not improve

orientation predictions in combination with model parameters determined from startup of shear experiments but significant improvements were achieved in coupled simulations when a lower value of parameter C_I was used in the standard Folgar-Tucker model.

4.1 Introduction

Short glass fiber thermoplastic composites made by injection molding are finding increased usage as high-strength light-weight materials in various applications. The mechanical, electrical, and thermal properties of these materials are significantly affected by the orientation distribution of reinforcing fibers which develops during the molding operation. Properties of the final solidified part vary throughout the part due to local variations in the orientation of fibers. This is because of the presence of complex flow field inside the mold which induces orientation of fibers, a phenomenon known as flow-induced orientation. Therefore, in order to precisely control fiber orientation in a molded composite part, it becomes necessary to develop theoretical models and numerical schemes that can accurately predict fiber orientation under complex flow fields.

Fountain flow [1], is a characteristic flow feature associated with the advancing front in injection molding operations that plays a prominent role in the orientation of fibers in injection molded geometries [2, 3]. Previous experimental studies on fiber orientation in injection molded geometries such as a center-gated disk have shown some of these effects such as the orientation along the flow direction is not highest at the mold walls but at locations away from the mold walls [4-6]. However, these studies only report experimentally measured fiber orientation data upto a significant distance behind the front and exclude the frontal region of flow. Mazahir et al. [4] have reported fiber orientation measurements along the direction of flow at three different heights representative of the shell, transition and core layers. However, the measured region covers the flow length of the disk only upto 7 *r/H* behind the front. Other publications have reported fiber orientation data measured along the thickness of the disk at sparse radial locations [5, 6]. Bay and Tucker [5] conducted the first experimental study on fiber orientation in a center-gated disk and reported *z/H* profiles only upto a distance 7.5 *r/H* behind the front. Vélez-García et al. [6] reported *z/H* profiles of orientation only upto a distance 7 *r/H* behind the front. In order to gain insights into the effects of the fountain flow on the orientation of fibers in the frontal region of an injection molded geometry such as the center-gated disk, it is crucial to characterize the fiber orientation in the frontal region of the disk. Therefore, measured fiber orientation in the frontal region of a disk is required to understand the effects of the fountain flow on the orientation.

The Folgar-Tucker (FT) [7] model has been the most popular model for fiber orientation predictions in injection molded geometries, with varying degrees of success [8-16]. Folgar and Tucker [7] introduced an isotropic rotary diffusion term in the Jeffery's model [17] to account for interaction between neighboring fibers in a fiber suspension. However, the model is unable to completely account for all fiber-fiber interactions in concentrated fiber suspensions. Rheological studies with glass fiber suspensions have shown that the evolution of fiber orientation in simple flow experiments is much slower than the FT model predicts [18, 19]. It has been suggested that reduction in the rate of rotation of fibers is caused by interactions between fibers, at high fiber concentrations [20, 21]. To slow down orientation kinetics in concentrated fiber suspensions, two modifications to the Folgar-Tucker model have been proposed [19, 21, 22]. One of the proposed modifications is the addition of a delay parameter known as the slip parameter [18, 19] or the strain reduction factor (SRF) [22], which renders the orientation model non-objective. The other modification is the reduced strain closure model (RSC) which achieves the slowdown in orientation evolution while retaining the objectivity of the original model [21]. The modified versions of the Folgar-Tucker model result in improved orientation predictions by slowing down the evolution of orientation in shear flows such as start-up of shear and shear-flow reversal [18, 19, 21].

Initial simulation studies on fountain flow effects in injection molded geometries first calculate the orientation using the Hele-Shaw flow approximation in the lubrication region and then perform a separate simulation for the fountain flow region [10, 23]. Such schemes with separate fountain flow simulations have inherent assumptions such as the distance behind the front where the fountain flow starts and the velocity profile at the start of the fountain flow region. Chung and Kwon [2], and Park and Kwon [3] used the pseudo-concentration method of Haagh and Van De Vosse [24] to include the effects of fountain flow on fiber orientation in a center-gated disk. Chung and Kwon [2] used the Folgar-Tucker model [7] for orientation predictions in a center-gated disk made with nylon 6/6 and 43 wt% (fiber volume fraction $\phi = 0.23$) short glass fibers. However, the parameter C_I that represents inter-fiber interactions in the Folgar-Tucker model was selected as $C_I = 0.001$, which is considerably lower than the typical range for short glass fibers (0.006-0.01), recently proposed by Phelps and Tucker [25]. Values of C_I determined from rheological fitting for fiber suspension with lower volume fraction ($\phi = 0.1766$) have been reported as 0.012 [6] and 0.0112 [4, 21] which are an order of magnitude higher than the value used by Chung and Kwon [2]. Park and Kwon [3] used the RSC model for orientation predictions in a center-gated disk and a phenomenological model for C_I that includes nonlinear viscoelasticity of the polymer and kinematic

interactions between the fibers and the polymer. Moreover, in these two studies, orientation predictions have been compared with the experimental data in the thickness direction only upto a distance 7.5 *r/H* behind the front [2, 3]. Therefore, with these experimental comparisons and parameter selection, it is difficult to quantify the improvements gained in orientation predictions in the frontal region of a center-gated disk.

This paper has two primary objectives. The first objective is to report the measured fiber orientation data in the frontal region of a thin center-gated disk along the radial direction at three different heights representative of the shell, transition, and core layers in order to gain insights into the effects of the fountain flow on fiber orientation in the frontal region. The second objective is to assess predictions of the Folgar-Tucker model and the slow orientation models in the frontal region of a center-gated disk using fountain flow simulation. The model parameters used in the orientation models were determined in previous experimental studies in which the parameters were obtained by performing rheological experiments on fiber suspensions.

4.2 Problem Description

A center-gated disk was injection molded using a 30 wt% (volume fraction ϕ = 0.1766) short glass fiber polybutylene-terephthalate (PBT) suspension (Valox 420). The viscosity of PBT matrix was measured on a Rheometrics Mechanical Spectrometer (RMS-800) from steady shear and dynamic oscillatory measurements conducted at 533 K. The viscosity of the matrix showed a Newtonian behavior between shear rates 0.1 s^{-1} and 100 s^{-1} with η_s = 350 Pa·s [20]. The number average fiber diameter d = 12.9 μm and fiber length l = 362.8 μm were determined from a burn-off process for about 1000 fibers. The measured number average fiber diameter and length correspond to an aspect ratio of a_r = 28.1.

A short-shot disk was made with average measurements, R_{in} = 2.97 mm, outer radius R_{out} = 51.8 mm and thickness $2H$ = 1.38 mm as shown in Figure 4.1(a). In order to exclude the effects of packing, the radial distance filled inside the mold was about 90% of the total radial distance of the mold. The resin was first dried overnight in a vacuum oven at a pressure less than 1.35 kPa and the dried resin was fed to the screw under nitrogen atmosphere at 433 K. The suspension was injected into the mold maintained at 363 K using an injection pressure of approximately 20 MPa, with filling time approximately 1 sec. This corresponds to a volumetric flow rate $q \approx 11.8$ cm^3/s. The disk was allowed to cool and solidify for about 1 min inside the mold to minimize warpage.

4.3 Experimental evaluation of the frontal region

4.3.1. Shape and texture of the advancing front

The shape and the texture of the advancing fronts of 30 wt% short glass fiber / PBT suspension and pure PBT polymer were analyzed under an optical microscope. A center-gated disk was injection-molded with pure PBT under same conditions of temperature and pressure as the disk made with fiber suspension in order to investigate the effect of fibers on the shape and texture of the front. Frontal region of each disk was cut out and mounted in acrylic and observed in the *rz*-plane under an optical microscope at 5X zoom level. Figure 4.2 shows the images of the advancing front of two center-gated disks injection molded with fiber suspension and pure polymer. As can be seen from the figures, the shapes of the two fronts are very different. The front of the suspension shows an almost semi-circular shape and the contact point with the mold wall is at a distance approximately 1.3 *r/H* from the tip of the front. The front of the fiber suspension has a rough texture and voids or bubbles of trapped air can be seen in the frontal region. The front of pure polymer shows a protrusion coming out from the center of the front while the contact point with the mold wall seems to be farther behind than that of the suspension. The front of pure polymer shows a smooth texture and no significant voids or air bubbles can be seen in the frontal region.

4.3.2. Fiber footprints in the frontal region

Figure 4.3 shows the footprints of fibers in the *rz*-plane of a center-gated disk injection molded with 30 wt% short glass fiber / PBT suspension in the region from $r/H = -7$ to the front. The image was obtained by stitching together smaller images taken with an optical microscope at 20X zoom level in the frontal region of the disk. The layered structure can be clearly identified in the region upto radial location $r/H \sim -4$. The shell layers close to the top and bottom mold walls can be easily identified with a sufficient number of fibers aligned in the flow direction. The core layer along the centerline is also easily distinguishable with nearly all fibers aligned in the θ-direction. At $r/H \sim -7$, the core layer is very thin, but grows in the thickness direction as we get closer to the front. In the region between $r/H \sim -4$ and $r/H \sim -3$, the layered structure tends to break down and in the region from $r/H \sim -3$ to the tip of the front, most of the fibers are seen aligned in the θ-direction in all the three layers.

4.3.3. Experimental orientation in the frontal region

Measurements of fiber orientation in the fountain flow region were made at constant thickness-wise positions along the radial direction in the frontal region of the center-gated disk. The

z/H heights that were selected as z_s/H = 0.75, 0.42, and 0.08, are representative of the shell, transition and core layers, respectively. The measurements were made in small rectangular bins with height $H/6$ and width $2l$, respectively, as described by Vélez-García et al. [26]. The sampling bins were centered in the z-direction at the selected z_s/H heights. The skin layer was excluded from the study. As shown in Figure 4.4, six sampling locations were selected in each layer to characterize the evolution of orientation. The positions of these locations are selected along the radial direction are measured from the advancing front. The advancing front (melt-air interface) in this reference frame corresponds to a radial position r/H = 0 (100% fill position in the radial direction). First five locations for sampling were centered in the r-direction at at r_s/H = -7.0, -5.6, -4.9, -3.5, -2.1 from the front. These correspond to flow lengths of 90%, 92%, 93%, 95% and 97% respectively. For the sixth location, we considered a position r_s/H = -0.7 (corresponding to 99% of the flow length) in the core and transition layers and r_s/H = -1.4 (corresponding to 98% of the flow length) in the shell layer. The last location in the shell layer was taken at 98% because at 99%, the sampling bin crossed over the polymer-air interface and the polymer phase covered only a part of the bin. Therefore, the location at 99% in the shell layer would not give reliable orientation information due to very limited number of fibers available for measurement.

The measurement procedure proposed by Vélez-García et al. [26] was used in the characterization of fiber orientation. This is a modified version of the method of ellipses (MoE) [27]. The MoE considers the elliptical footprints of fibers in the polished plane to determine the orientation angles (i.e. in-plane (ϕ_f) and out-of-plane (θ_f) angles) for each individual fiber and estimates the volumetric average of orientation represented through a second-order tensor. Vélez-García et al. [26] modified the MoE to add partially elliptical and rectangular footprints so that reliable orientation data can be obtained from small sampling areas. The modified method also includes a shadow detection that distinguishes between fibers having same footprint in the polished plane but oriented at angles ϕ_f and $\phi_f + \pi$. This correction is achieved by identifying a shadow along the major axis of the elliptical or partially elliptical footprint. The measurements were made on images taken at various radial locations, which were $2l$ wide and contained the sampling area of interest, by optical microscope at 20X magnification. Using an in-house MATLAB program, the wall-to-wall thickness of the disk in each image was divided into 12 equal bins along the z-direction and orientation was determined from elliptical, partially elliptical and rectangular footprints in selected bins.

The measured orientation data is shown in Figure 4.5 through Figure 4.7 for the shell, transition and core layer, respectively. The figures show the diagonal and the off-diagonal components of the orientation tensor at the sampled locations. Figure 4.5(a) shows the diagonal components of the orientation tensor at selected radial locations for the shell layer. Here, A_{rr} values show a steady decrease between radial locations r_s/H = - 5.6 and r_s/H = -1.1. The changes in A_{rr} are complemented by opposite changes in $A_{\theta\theta}$ in the entire region. The primary direction of orientation changes from the r-direction to the θ-direction in the region between r_s/H = -5.6 and r_s/H = -1.1. This suggests that shear flow dominates at r_s/H = -7.0 but it diminishes as we get close to the front in the shell layer. A_{zz} remains close to zero at all sampled locations which means that the orientation is planar in r-θ plane in the region from the front to a distance upto r_s/H = -7.0 behind the front. The A_{rz}, $A_{r\theta}$ and $A_{\theta z}$ components of the orientation tensor in the shell layer behind the front are shown in Figure 4.5(b). The off-diagonal components A_{ij} show the projection of the average tilt of the fibers on the ij-plane. There values of the off-diagonal components fall into three possible categories: $A_{ij} \approx 0, A_{ij} < 0, A_{ij} > 0$. As an example, the possible values of $A_{r\theta} \approx 0$, $A_{r\theta} > 0$, and $A_{r\theta} < 0$ represent negligible tilt, tilt in the counter-clockwise direction, and tilt in the clockwise direction in the $r\theta$-plane, respectively. A_{rz} stays between -0.1 and 0.1 at all sampled locations in the region between r_s/H = -7.0 and r_s/H = -1.1. $A_{z\theta}$ is almost zero in the entire region between r_s/H = -7.0 and r_s/H = -1.1. $A_{r\theta}$ has a small negative value at r_s/H = -7.0 which increases to about 0.2 at r_s/H = -5.6 and after that levels off at around 0.3.

The diagonal components of the orientation tensor for the transition layer are shown in Figure 4.6(a). In the transition layer, A_{rr} shows almost a linear drop from A_{rr} = 0.64 to A_{rr} = 0.09 between r_s/H = -7.0 and r_s/H = -0.7. The increase in $A_{\theta\theta}$ almost matches the reduction in A_{rr} between r_s/H = -7.0 and r_s/H = -2.1, a similar behavior as in the shell layer. However, very close to the front, between r_s/H = -2.1 and r_s/H = -0.7, $A_{\theta\theta}$ is almost flat. In this region, the drop in A_{rr} is complemented by a similar increase in A_{zz} which results in a higher value of A_{zz} compared to A_{rr} at r_s/H = -0.7. A_{zz} remains close to zero at all other sampled locations. The increase in A_{zz} in the region between r_s/H = -2.1 and r_s/H = -0.7 suggests that the extension in the z-direction starts to dominate in this region and causes the fibers to rotate in the z-direction. Figure 4.6(b) shows the off-diagonal components of orientation in the transition layer. A_{rz} and $A_{z\theta}$ stay close to zero in the region between r_s/H = -7.0 and r_s/H = -4.9 and show a slight drop after r_s/H = -4.9. $A_{r\theta}$ increases from values around 0 to about 0.3 in the region between r_s/H = -7.0 and r_s/H = -4.9, stays relatively flat upto r_s/H = -2.1 and slightly drops between r_s/H = -2.1 and r_s/H = -0.7.

Figure 4.7(a) shows the diagonal components of orientation in the core layer at selected radial locations in the frontal region. In this layer, due to the absence of high shear, extension dominates, which tends to align the fibers in the θ-direction. Therefore, A_{rr} is relatively small in this layer as compared to the shell and transition layers at all radial locations between r_s/H = -7.0 and r_s/H = -0.7. Similar to the transition layer, A_{rr} shows a steady decrease along the radial direction. $A_{\theta\theta}$ is relatively constant at around 0.8 which represents high orientation in the θ-direction in the entire region from r_s/H = -7.0 to the front. In this layer, the mirroring behavior is similar to the transition layer with A_{rr} and $A_{\theta\theta}$ mirroring each other near r_s/H = -7.0 which then transitions to A_{rr} and A_{zz} mirroring each other near r_s/H = -0.7. The steady increase in A_{zz} results in A_{zz} being higher than A_{rr} at r_s/H = -0.7. The off-diagonal components of orientation in the core layer are shown in Figure 4.7(b). A_{rz} and $A_{z\theta}$ stay close to zero while $A_{r\theta}$ shows a similar profile as in the transition layer.

4.4 Governing Equations

4.4.1. Orientation evolution equations

For the evolution of orientation of high aspect ratio particles such as glass fibers in semi-dilute fiber concentration regimes, Folgar and Tucker [7] proposed a modification to the Jeffery's model [17] by introducing an isotropic rotary diffusion term that accounts for fiber-fiber interaction. The standard Folgar-Tucker model is given by:

$$\frac{D\mathbf{A}}{Dt} = \left(\mathbf{W}\cdot\mathbf{A} - \mathbf{A}\cdot\mathbf{W}\right) + \lambda\left(\mathbf{D}\cdot\mathbf{A} + \mathbf{A}\cdot\mathbf{D} - 2\mathbf{A}_4 : \mathbf{D}\right) + 2C_I\dot{\gamma}\left(\mathbf{I} - 3\mathbf{A}\right) \tag{1}$$

where $\mathbf{A}$ is the second-order orientation tensor, D/Dt is the material derivative, $\mathbf{W} = [(\nabla\mathbf{v}) - (\nabla\mathbf{v})^T]/2$ the vorticity tensor, $\mathbf{D} = [(\nabla\mathbf{v}) + (\nabla\mathbf{v}^T)]/2$ the rate-of-strain tensor, and $\nabla\mathbf{v} = \partial v_j / \partial x_i$ the velocity gradient. Shape factor $\lambda = \left(a_r^2 - 1\right)/\left(a_r^2 + 1\right)$, where a_r is the fiber aspect ratio, equals one for high aspect ratio particles such as glass fibers. $\mathbf{A}_4$ is the fourth-order orientation tensor, $\mathbf{I}$ the identity tensor, C_I the isotropic interaction coefficient and $\dot{\gamma} = \sqrt{2\mathbf{D}:\mathbf{D}}$.

The orientation evolution predicted by the Folgar-Tucker model has been tested in transient shear flow and it has been observed that the experimentally observed evolution kinetics are much slower than the Folgar-Tucker model predicts [6, 21, 22]. Hence, in order to slow down the evolution of orientation predicted by the Folgar-Tucker model, two modifications were proposed recently [19, 21, 22]. First modification is the introduction of a strain reduction factor (SRF)

proposed by Huynh et al. [22] or a slip parameter (α) proposed by Eberle et al. [19]. The SRF and the slip parameter are two different names for the same parameter which represents the retardation in orientation evolution due to inter-fiber interactions in concentrated suspensions. We will use the term 'slip parameter' for this parameter in this study and 'delayed Folgar-Tucker model' for the Folgar-Tucker model with the slip parameter. The slip parameter is a factor between 0 and 1 and the entire right hand side of the standard Folgar-Tucker model is multiplied with this parameter, thereby slowing down the evolution of orientation:

$$\frac{D\mathbf{A}}{Dt} = \alpha\left[\left(\mathbf{W}\cdot\mathbf{A}-\mathbf{A}\cdot\mathbf{W}\right)+\lambda\left(\mathbf{D}\cdot\mathbf{A}+\mathbf{A}\cdot\mathbf{D}-2\mathbf{A}_4:\mathbf{D}\right)+2C_I\dot{\gamma}\left(\mathbf{I}-3\mathbf{A}\right)\right] \tag{2}$$

However, with this modification, the orientation equation becomes non-objective. Wang et al. [21] followed a different approach and proposed a modification to the standard Folgar-Tucker model that achieves the slowdown in evolution of orientation while retaining the objectivity of the model. The modified model is known as the reduced strain closure (RSC) model and consists of a modification in the closure approximation for $\mathbf{A}_4$ eliminating the problem of non-objectivity. The RSC model is given by:

$$\frac{D\mathbf{A}}{Dt} = \left(\mathbf{W}\cdot\mathbf{A}-\mathbf{A}\cdot\mathbf{W}\right)+\lambda\left(\mathbf{D}\cdot\mathbf{A}+\mathbf{A}\cdot\mathbf{D}-2\left[\mathbf{A}_4+(1-\kappa)(\mathbf{L}_4-\mathbf{M}_4:\mathbf{A}_4)\right]:\mathbf{D}\right)+2\kappa C_I\dot{\gamma}\left(\mathbf{I}-3\mathbf{A}\right) \tag{3}$$

The strain reduction factor κ has a value between 0 and 1 and plays a similar role as the slip parameter α. Two additional fourth-order tensors $\mathbf{L}_4$ and $\mathbf{M}_4$ are introduced which are defined as:

$$\mathbf{L}_4 = \sum_{i=1}^{3}\lambda_i\mathbf{e}_i\mathbf{e}_i\mathbf{e}_i\mathbf{e}_i, \qquad \mathbf{M}_4 = \sum_{i=1}^{3}\mathbf{e}_i\mathbf{e}_i\mathbf{e}_i\mathbf{e}_i \tag{4}$$

where λ_i are the eigenvalues and $\mathbf{e}_i$ the eigenvectors of $\mathbf{A}$.

A closure approximation needs to be used to express $\mathbf{A}_4$ in terms of $\mathbf{A}$. Invariant-based optimal fitting (IBOF) closure approximation was proposed by Chung and Kwon [28] to express $\mathbf{A}_4$ in terms of $\mathbf{A}$. The accuracy of IBOF closure is as good as eigenvalue-based closures, but required computational time is less. We use the IBOF closure approximation for $\mathbf{A}_4$ in all simulations.

4.4.2. Equations of motion

The mass and momentum equations for the flow of an incompressible fluid under creeping flow conditions are:

$$\nabla \cdot \mathbf{v} = 0 \tag{5}$$

$$\nabla \cdot \left(-p\mathbf{I} + 2\eta_s \mathbf{D} + \mathbf{T}_{fiber} \right) = \mathbf{0} \tag{6}$$

where ∇ is the gradient operator, $\mathbf{v}$ the velocity, p the pressure, $\mathbf{I}$ the identity tensor, and η_s the matrix viscosity. $\mathbf{T}_{fiber}$ is the viscous extra-stress contribution from the fibers to the total stress in the fluid. The general form of $\mathbf{T}_{fiber}$ is

$$\mathbf{T}_{fiber} = 2\nu\zeta_{str}\mathbf{D} : \mathbf{A}_4 \tag{7}$$

where ν is the concentration of the fibers and ζ_{str} is the viscous drag coefficient between the fibers and the polymer matrix [29]. We refer to $\nu\zeta_{str}$ as the coupling parameter. Dinh and Armstrong [29] proposed a model for the viscous drag coefficient ζ_{str} in thermoplastic composites:

$$\zeta_{str} = \frac{\pi\eta_s L_f^3}{12\ln\left(2a_c / d_f\right)} \tag{8}$$

where a_c is the average inter-fiber distance that depends on the fiber orientation. For $\mathbf{A}_4$ appearing in the extra-stress term, we use the IBOF closure approximation in all simulations.

Isothermal filling conditions are assumed in this work because of fast filling conditions, (about one second filling time), in agreement with the findings of Wu et al. [30]. Amount of heat dissipated through viscous heating was approximately equal to the heat loss due to conduction through the mold walls. The maximum temperature rise due to viscous dissipation was estimated to be about 3.5 K.

The flow equations are solved in a non-dimensional framework. Velocities are scaled with the average radial velocity $v_{avg}(R_{in})$ at the inlet of the mold, lengths are scaled with the half-thickness of the disk H, and time with $v_{avg}(R_{in})/H$. The coupling parameter $\nu\zeta_{str}$ is scaled with the matrix viscosity η_s.

4.4.3. Model parameters

The model parameters for Valox 420 obtained by Mazahir et al. [4] for all the three orientation models. The parameter values are C_I = 0.0112 for the standard Folgar-Tucker model, (C_I, α) = (0.0112, 0.40) for the delayed Folgar-Tucker model, and (C_I, κ) = (0.0112, 0.40) for the RSC model. The value of the coupling parameter $\nu\zeta_{str}$, is in general, obtained either from theory or

from rheological experiments of fiber suspensions. Mazahir et al. [4] fitted a non-dimensional value of $\nu\zeta_{str} = 6.18$ to stress data of Eberle et al. [20].

For fibers with $a_r = 20$, $\nu\zeta_{str} = 7.75$ and 19.36 for suspensions with $\phi = 0.1$ and $\phi = 0.2$, respectively based on Dinh and Armstrong's theory [13]. Extrapolating from these values, the theoretical value of $\nu\zeta_{str}$ for our fiber suspension, with $a_r = 28$ and $\phi = 0.1766$ comes out to be $\nu\zeta_{str} = 37$. For coupled simulations, we use both fitted and theoretical values of $\nu\zeta_{str}$. Simulation results using $\nu\zeta_{str} = 6.18$, which is fitted to rheological experiments and $\nu\zeta_{str} = 37$, which is extrapolated using theoretical values are compared.

4.5 Numerical Methods

Filling of a center-gated disk mold with a short glass fiber suspension is simulated by solving a transport equation for the evolution of the advancing front, equations of motion for the velocity and pressure and orientation equations for the fiber orientation. In the time-stepping scheme, these three equations are solved in a decoupled fashion at every time step. For the spatial discretization of velocity, continuous biquadratic polynomials are used, while pressure is represented by continuous bilinear polynomials. For the orientation and extra-stress, we use discontinuous biquadratic and discontinuous bilinear polynomial representation, respectively. The pseudo-concentration variable in the transport equation is discretized in space with discontinuous biquadratic polynomials. The choice of discontinuous polynomials for the orientation, extra-stress and pseudo-concentration is due to the hyperbolic nature of the orientation and transport equations. The details of solution schemes for these equations are given below. Equations of motion are discussed first, followed by the orientation and transport equations.

4.5.1. Equations of motion

The equations of motion (5), (6) are solved simultaneously at every time step to obtain the velocity $\mathbf{v}^{n+1}$ and pressure p^{n+1} at time level t^{n+1}.

$$\nabla \cdot \mathbf{v}^{n+1} = 0 \tag{9}$$

$$\nabla \cdot \left(-p^{n+1}\mathbf{I} + 2\eta_s \mathbf{D}^{n+1} + \tilde{\mathbf{T}}_{fiber}^{n+1} \right) = \mathbf{0} \tag{10}$$

For coupled simulations, viscous extra-stress contribution from fibers is considered through the term $\tilde{\mathbf{T}}_{fiber}^{n+1} = 2\nu\zeta_{str}\mathbf{D}^{n+1} : \mathbf{A}_4^n$, where $\mathbf{D}$ is implicit at time level t^{n+1} and $\mathbf{A}_4$ is explicit at time level t^n.

Spatial discretization is performed with the Galerkin finite element method. Because the equations of motion are solved in the entire simulation domain which consists of polymer as well as air, η_s is taken to be polymer viscosity in the polymer phase and air viscosity in the air phase. Near the polymer-air interface, η_s is linearly interpolated between the values for the polymer and air phase

$$\eta_s = c \times \eta_p + (1 - c) \times \eta_a \tag{11}$$

where η_p is the polymer viscosity and η_a is the air viscosity. The pseudo-concentration variable c, has values in the range [0, 1]. A value of $c = 1$ indicates polymer, a value of $c = 0$ air and a value $c = 0.5$ defines the polymer-air interface. The value of c is determined at every integration point and $c = 0$ is used if $c < 0$, and $c = 1$ if $c > 1$ in order to eliminate non-physical values of c due to non-linear-interpolation. At the inlet of the mold, a parabolic velocity profile is prescribed. At other boundaries, the boundary conditions are prescribed as [24]

$$\begin{aligned} &a v_t + \sigma_t = 0 \qquad \forall x \in \Gamma_{\mathrm{w}} \cup \Gamma_{\mathrm{o}} \\ &a v_n + \sigma_n = 0 \qquad \forall x \in \Gamma_{\mathrm{o}} \\ &v_n = 0 \qquad\quad \forall x \in \Gamma_{\mathrm{w}} \end{aligned} \tag{12}$$

where $a = 10^{10}$ for $c \geq 0.5$ and $a = 0$ for $c < 0.5$, Γ_{w} is the boundary along the mold walls and Γ_{o} is the outlet for air as shown in Figure 4.1(b). With these boundary conditions, neither air nor polymer is allowed to pass through the mold walls. Air is allowed to slip freely along the mold walls while the slip velocity for the polymer along the mold walls is negligible which effectively acts as a no-slip boundary condition for the polymer phase.

4.5.2. Orientation equations

The orientation equations can be written as

$$\begin{aligned} &\frac{\partial \mathbf{A}}{\partial t} + \mathbf{v} \cdot \nabla \mathbf{A} - c\mathbf{F}(\nabla \mathbf{v}, \mathbf{A}) = \mathbf{0} \\ &\mathbf{A}(\Gamma_{\mathrm{i}}, t) = \mathbf{A}_{\mathrm{i}} \end{aligned} \tag{13}$$

where c is the pseudo-concentration variable, and $\mathbf{F}(\nabla \mathbf{v}, \mathbf{A})$ is the model-specific term given by the right-hand sides of Eqs. (1), (2) and (3) for the standard Folgar-Tucker, the delayed Folgar-Tucker model and the RSC model, respectively. Γ_{i} is the inlet boundary of the simulation domain and $\mathbf{A}_{\mathrm{i}}$ is the orientation state prescribed at the inlet boundary. The orientation is determined in the entire

simulation domain which consists of air as well as polymer. The distinction between the two phases is made by the pseudo-concentration variable c which is multiplied with the model-specific term $\mathbf{F}(\nabla\mathbf{v}, \mathbf{A})$.

The orientation evolution equations in the form of Eq. (13) are spatially discretized using the discontinuous Galerkin finite element method (DGFEM) of Lesaint and Raviart [31]. The weak formulation for the orientation equations with appropriate functional spaces for the test functions and the solution on an element K is given by: Find $\mathbf{A}$ such that for all admissible weighting functions $\mathbf{\Lambda}$

$$\left\langle \frac{\partial \mathbf{A}}{\partial t}, \mathbf{\Lambda} \right\rangle_{\mathrm{K}} + \left\langle \mathbf{v}\cdot\nabla\mathbf{A}, \mathbf{\Lambda} \right\rangle_{\mathrm{K}} + \left\langle \mathbf{v}\cdot\mathbf{n}\left[\mathbf{A}\right], \mathbf{\Lambda} \right\rangle_{\Gamma_{\mathrm{K,i}}} - \left\langle c\mathbf{F}(\mathbf{A}, \nabla\mathbf{v}), \mathbf{\Lambda} \right\rangle_{\mathrm{K}} = 0 \quad (14)$$

where $\langle \mathbf{P}, \mathbf{Q} \rangle_{\mathrm{K}}$ and $\langle \mathbf{P}, \mathbf{Q} \rangle_{\Gamma_{\mathrm{K,i}}}$ are proper L^2 inner products on the element domain Ω_{K} and on the element boundary $\Gamma_{\mathrm{K,i}}$, respectively. The boundary integral is applied only on those boundaries of the element K for which $\mathbf{v}\cdot\mathbf{n} < 0$, where $\mathbf{n}$ is the outward unit normal along the element boundary. $\left[\mathbf{A}\right]$ is the discontinuity across inter-element boundaries given by $\left[\mathbf{A}\right] = \mathbf{A}_{\Gamma_{\mathrm{K,u}}} - \mathbf{A}_{\Gamma_{\mathrm{K,e}}}$, where $\mathbf{A}_{\Gamma_{\mathrm{K,u}}}$ is the value of $\mathbf{A}$ along the boundary $\Gamma_{\mathrm{K,i}}$ in the upstream element and $\mathbf{A}_{\Gamma_{\mathrm{K,e}}}$ the value of $\mathbf{A}$ inside element K along the boundary $\Gamma_{\mathrm{K,i}}$. If a boundary $\Gamma_{\mathrm{K,i}}$ of element K is along the inlet boundary, $\mathbf{A}_{\Gamma_{\mathrm{K,u}}} = \mathbf{A}_{\mathrm{i}}$. The value of c is determined at every integration point and $c = 0$ is used if $c < 0$, and $c = 1$ if $c > 1$ in order to eliminate non-physical values of c due to non-linear-interpolation. The advantage of the DGFEM formulation is reduced computational time and memory requirements as compared to the solution for the entire domain at once. In the DGFEM method, interpolation functions are defined locally on an element and the equations are solved separately on each element. Discretization in time is achieved by means of the explicit Runge Kutta third order total variance diminishing (RK3-TVD) scheme [32]. The choice of RK3-TVD is made because it provides a stable solution, even with a relatively large time step as compared to the single step explicit methods, and computational time and memory requirements are low as compared to single step implicit methods [33].

4.5.3. Transport equation

The evolution of the advancing front is captured by the pseudo-concentration method [24]. The pseudo-concentration variable c evolves according to the transport equation

$$\frac{\partial c}{\partial t} + \mathbf{v} \cdot \nabla c = 0 \qquad (15)$$
$$c(\Gamma_i, t) = 1$$

Air is considered to have zero density and viscosity about 0.1% of the fiber suspension. With this selection of material properties for air, the contribution of air to pressure buildup in the mold is negligible as compared to that of the suspension. Eq. (15) is spatially discretized with the DGFEM [31] as described in section 4.5.2 with no model-specific terms. Discretization in time is achieved by means of the RK3-TVD scheme [32].

4.6 Results

Orientation predictions in the frontal region of a center-gated disk are compared with experimentally measured orientation data. The full thickness of the disk is simulated and all the quantities are made dimensionless. The dimensions of the disk are shown in Figure 4.1, non-dimensionalized by the half thickness H of the disk. Simulation results are validated along the radial direction at three different heights, $z_s/H = 0.75$, $z_s/H = 0.42$, and $z_s/H = 0.08$, representative of the shell, transition and core layers, respectively. Measured orientation data in the frontal region of a disk as shown in Figure 4.5-Figure 4.7 is used for experimental validation. The component of the orientation tensor along the main flow direction, A_{rr}, considered as representative of fiber orientation, is used for validation of all simulation results.

Mesh refinement is performed in both r- and z-directions with the decoupled simulation of RSC model to ensure convergence of results. Figure 4.8 shows the convergence of A_{rr} along the radial direction in the shell and core layers. Five meshes are considered with elements in r- and z-directions as 100x20, 200x30, 400x30, 400x40 and 600x40. The results are almost identical for the last three meshes. Therefore, we select the 400x30 mesh for all our simulations in order to have sufficient accuracy as well as computational efficiency. A time step of 0.02 was selected for all simulations. Smaller time steps showed no significant differences in orientation predictions.

First, we discuss the shape of the front and velocity profile as predicted by the pseudo-concentration method. Next, comparison of fountain flow simulation with Hele-Shaw

approximation is discussed followed by an assessment of the slow versions of the Folgar-Tucker model and effects of coupling with the RSC model.

4.6.1. Advancing front with the pseudo-concentration method

Figure 4.9 shows the shape of the front at 90% fill length of the mold alongwith the A_{rr} predictions of the RSC model in a decoupled simulation, The streamlines are shown in two reference frames. Figure 4.9(a) shows the streamlines in a stationary reference frame and Figure 4.9(b) shows the streamlines in a moving reference frame attached to the tip of the front. The shape of the front is almost semi-circular. The pseudo-concentration value drops at the melt-air interface from approximately $c = 1$ in the polymer region to approximately $c = 0$ over a distance of about two elements giving an accurate description of the interface. In a stationary reference frame, streamlines are parallel to the main direction of flow upto a radial location ~ -2 r/H. In the region between r/H ~ -2 and r/H ~ -1, streamlines diverge outwards towards the walls and become parallel again at ~ r/H = -1. In the reference frame moving with the tip of the front, the streamlines show the fluid coming towards the front, following the curvature of the melt-air interface and going backwards along the walls, creating a fountain-like flow. The streamlines in the air phase stay in air and the streamlines in the polymer phase stay within the polymer, and there is no mixing between the two phases.

The contour of A_{rr} shows a drop in orientation near the walls due to which A_{rr} peaks at a location away from the wall. This drop in orientation near the walls is due to the effects of fountain flow, which transports the fibers from the inner layers to the outer layers. The contour plot of A_{rr} closely follows the streamlines in the moving reference frame, especially near the centerline and the walls.

4.6.2. Fountain flow vs Hele-Shaw flow

Figure 4.10 shows the standard Folgar-Tucker model predictions in a decoupled simulation in the shell, transition and core layers in the frontal region of a center-gated disk. Orientation predictions with fountain flow and Hele-Shaw flow approximation are compared with the experimental data of section 4.3. Figure 4.10(a) shows the orientation evolution along the shell layer. Fountain flow simulation shows better qualitative agreement with the experimental data than Hele-Shaw flow approximation. Fountain flow simulation predicts a drop in orientation near the front, followed by a slight increase and then a final drop to levels at frontal orientation values very close to the front. This is very similar to the trend seen in the experimental data. Hele-Shaw flow approximation, on the other hand, predicts steady values with no drop in orientation in the frontal

region. However, there are significant quantitative differences in fountain flow predictions and the experimental data as the predicted evolution of orientation from high steady values to low values near the front is too fast compared to experimental evolution. Fountain flow simulation starts to show a decrease in orientation at approximately r/H = -4, followed by a rapid drop at approximately r/H = -2.5. Between r/H = -2 and -1, orientation predictions with the fountain flow simulation shows a slight increase followed by another rapid drop between r/H = -1 and the front. Experimental data, on the other hand shows much gradual evolution with the first drop in orientation from A_{rr} = 0.69 at r_s/H = -14 (not shown here, available in a previous study [4]) to A_{rr} = 0.52 at r_s/H = -7.0, followed by a rise between r_s/H = -7.0 and r_s/H = -5.6. Also, the final drop in experimental orientation, which starts at distance approximately r/H = -5.5, is much gradual than the drop seen in fountain flow predictions.

In the transition and core layers also, as shown in Figure 4.10(b) and Figure 4.10(c) respectively, orientation predictions with fountain flow simulation show improved qualitative agreement with the experimental data near the front while predictions with the Hele-Shaw flow approximation do not show any decrease in orientation. In the transition layer, the predicted drop in orientation values with fountain flow simulations qualitatively matches the trend in experimental data. Also, in the core layer, there is good qualitative agreement between fountain flow predictions and the experimental data as both show a drop in orientation followed by a relatively flat profile very close to the front. A_{rr} predictions very close to the front almost coincide with the experimental data at r_s/H = -0.7 in both layers. However, as in the shell layer, there are significant quantitative differences between fountain flow predictions and experimental data. Fountain flow predictions show much too fast evolution compared to the experimental data. In fountain flow simulation, the transition from high steady values to low orientation values near the front starts only at approximately r/H = - 2 in both layers while the experimental data shows a much gradual transition starting as far back as r_s/H = -7.0.

4.6.3. Assessment of delay in orientation evolution

In this section and the next, all orientation predictions are with fountain flow simulation. Figure 4.11 shows fiber orientation predictions with the standard Folgar-Tucker, the delayed Folgar-Tucker model and the RSC model using a decoupled simulation in the frontal region of a center-gated disk. In the shell layer, as shown in Figure 4.11(a), evolution of orientation with the RSC model does not show a slowdown compared to the evolution predicted with the standard Folgar-Tucker model. Both the models predict a rapid drop in orientation starting approximately

r/H = -2. However, the delayed Folgar-Tucker model predicts a slowdown in orientation evolution with first gradual drop in orientation starting at approximately r/H = -5. This is in relatively good agreement with the experimental data. However, this is the second drop in orientation data while the first decrease in experimental data starts even before r_s/H = -7. Even though the delayed Folgar-Tucker model improves orientation predictions in the frontal region, none of the models is able to fully capture the slow evolution of orientation in the frontal region.

In the transition and core layers, shown in Figure 4.11(b) and Figure 4.11(c), predictions with all three models almost coincide with a drop in orientation starting at approximately r/H = -2. Predictions are in good qualitative agreement in both layers with orientation values at r_s/H = -0.7 being predicted very well with the slow models. However, none of the slow versions is able to achieve the slowdown in orientation evolution seen in the experimental data in both layers. The predicted transition in orientation from steady values to orientation values near the front starts only at approximately r/H = -2 and happens over a much shorter distance while experimental data shows the decline from steady values to values near the front starting much earlier, at r_s/H = -7 and happening over a much longer distance.

4.6.4. Effects of coupling and C_I on orientation in the frontal region

The effects of coupling on orientation predictions in the frontal region of a center-gated disk were investigated by comparing coupled and decoupled simulations with the experimental orientation values. Both the standard Folgar-Tucker model and the RSC model were considered in coupled simulations and the coupling parameters determined from rheological fitting as well as theoretical calculations based on Dinh-Armstrong theory were considered. Figure 4.12 shows the velocity profiles through the thickness direction at r/H = 11.3 with the RSC model in coupled and decoupled simulations. The effect of coupling on velocity profile is higher near the gate and diminishes with increasing r. The change in velocity due to coupling is most significant in the core layer and decreases with increasing $|z/H|$ value. Coupling tends to make the velocity profile more pointed with higher velocity in the center as compared to the decoupled solution, which is in contrast with the decrease in the velocity seen in the core layer in a previous study [2]. This is because of the measured orientation that is prescribed at the inlet boundary of the disk, instead of equilibrium orientation that was used at the gate in the previous study. Measured inlet orientation shows a planar orientation with very small values of A_{zz} which are an order of magnitude less than the A_{zz} values for equilibrium orientation [6]. Therefore, the extra-stress due to fibers is smaller with

the measured inlet orientation as compared to the extra-stress with the equilibrium values. As a result, the velocity in the core layer is higher with measured values.

Figure 4.13 shows the effect of coupling on orientation with the standard Folgar-Tucker model and the RSC model. Coupled simulations with the Folgar-Tucker model were performed with $\nu\zeta_{str}$ = 6.18, which is fitted to rheological experiments and $\nu\zeta_{str}$ = 37, which is determined theoretically. Coupled simulations with the RSC model were performed only with $\nu\zeta_{str}$ = 37. In the shell layer, as shown in Figure 4.13(a) and (b), evolution of orientation is slower in coupled simulations as compared to decoupled simulations. Orientation in coupled simulations starts to decrease further upstream than in decoupled simulations and a local increase in orientation very close to the front is almost absent in coupled simulations with $\nu\zeta_{str}$ = 37. However, coupled simulations show quantitative differences with the experimental trend. Even though coupled simulations start to decrease further upstream than decoupled simulations, the reduction in orientation is very small. Moreover, very close to the front, coupled simulations predict higher values of orientation than decoupled simulations, while the experimental data has much lower values. In the transition layer, the differences between decoupled and coupled simulations are negligible except that the evolution of orientation from high orientation values in the steady lubrication region to low orientation values in the frontal region is slower in coupled simulations than in decoupled simulations. In the core layer, both coupled and decoupled simulations are able to capture the experimental orientation value at r_s/H = -0.7, which is closest to the front, very well. The slowdown in orientation evolution due to coupling, is more in the core layer as compared to the transition layer. Maximum slowdown in orientation evolution is achieved with RSC model in coupled simulation with $\nu\zeta_{str}$ = 37, which shows a gradual decrease starting at approximately r/H = -5.5, considerably upstream than the locations where all other simulations start to show a drop. However, coupled simulations predict slightly higher steady values of orientation as compared to decoupled simulations in the region close to r/H = -7 and are still far off from orientation evolution seen in the frontal region.

Simulations with the standard Folgar-Tucker model and two different values of C_I were also performed to see the effects of C_I on orientation in coupled and decoupled simulations. Two values of C_I, 0.0112, fitted to rheological data in startup of shear by Mazahir et al. [4] and 0.001, used by Chung and Kwon [2] were considered to understand the effects of C_I on fiber orientation in radial diverging flow in a center-gated disk. Figure 4.14 shows a comparison of orientation predictions

with these C_I values in coupled and decoupled simulations. In the shell layer, decoupled simulation with smaller C_I predicts a decreasing orientation profile as far back as r/H = -7 while larger C_I predicts relatively steady values. Effect of smaller C_I is significantly different in coupled simulations. While the larger C_I value predicts almost steady values with a negligible drop upto r/H ~ -1 followed by a steep drop very close to the front, the smaller C_I predicts a uniform decrease in orientation even as far back as r/H ~ -6, which is significantly closer to the trend in the experimental data. However, the increase in orientation between r_s/H = -7.0 and r_s/H = -5.6 is not captured by the coupled simulation with the smaller C_I value. Motivated with a good agreement between orientation predictions with smaller C_I in a coupled simulation and experimental data in the frontal region, orientation predictions with the two C_I values (not shown here) were compared with the experimental data in the lubrication region reported in a previous study [4]. It was observed that smaller C_I value in both coupled and decoupled simulations does not provide a good match with experimental orientation evolution in the lubrication region while the larger C_I value, fitted to rheological data provides a much better agreement with the orientation data, especially in the shell layer. This suggests that the larger C_I value, which has been obtained by fitting to rheological data in startup of shear is better suited for the lubrication region, which has a relatively high amount of shear. However, in the frontal region, with high extension and less shear relative to the lubrication region, it is suggested that C_I needs to be determined from extensional flow experiments and a value of C_I determined from startup of shear experiments is not appropriate.

In the transition layer, both C_I values predict similar orientation profiles in decoupled simulations with steady values upto r/H ~ -2 followed by a sudden drop to low orientation values near the front. In coupled simulations, smaller C_I predicts the orientation trend qualitatively better than the larger C_I. Especially, at r_s/H = -2.1 and r_s/H = -0.7, orientation predictions with smaller C_I in coupled simulation are in close proximity with the measured data. However, predictions at upstream locations are still significantly off from the experimental data. In the core layer, smaller C_I lowers orientation predicts in the entire region from r/H = -7 to the front in both coupled and decoupled simulations. These lower predictions are in much better agreement with the experimental data than the predictions with the larger C_I. Decoupled simulation with smaller C_I predicts steady values upto r/H ~ -2, capturing the experimental data very well at r_s/H = -5.8 and r_s/H = -4.9, followed by a drop near the front, with good agreement with experimental data at r_s/H = -2.1 and r_s/H = -0.7. In coupled simulation with smaller C_I, orientation predictions at r_s/H = -7 and r_s/H = -

0.7 are in close proximity to measured values. However, the evolution from high orientation to low orientation between these locations is only in qualitative agreement with the experimental trend.

4.7 Conclusions

Experimental measurements in the frontal region of a center-gated disk injection molded with 30 wt% short glass fiber suspension are done in order to investigate the evolution of orientation in the frontal region of the disk. The front of a disk made with fiber suspension is compared with that of a disk made with pure polymer. The front of the suspension shows an almost-semi-circular shape which is significantly different from that of the pure polymer. Moreover, in case of fiber suspension, texture of the front is rough and trapped air is present in the frontal region while with pure polymer, front is smooth with no trapped air. In the disk made with fiber suspension, layered structure with the core, transition and shell layers is clearly visible upto a distance approximately $4r/H$ behind the front followed by a widening of the core layer towards the front. The evolution of fiber orientation along the radial direction at three different heights in the frontal region of the disk has been measured in order to evaluate orientation predictions with the standard Folgar-Tucker model, its delayed version and the RSC model in the frontal region. The effects of fountain flow on orientation are seen in all the three layers with a drop in orientation from steady values representative of lubrication region to significantly lower values near the front.

Orientation predictions with the standard Folgar-Tucker model, its delayed version and the RSC model have been validated by comparing experimentally measured fiber orientation in the frontal region of a center-gated disk. Model parameters are obtained from a previous study in which rheological data under startup of shear was used for parameter fitting. Fountain flow simulation shows a drop in orientation in the frontal region of the disk and provides qualitative agreement with the experimental trend while Hele-Shaw flow approximation significantly over-predicts orientation in the frontal region with no drop near the front. An assessment of slowdown in orientation evolution in the frontal region was done by comparing model predictions with the standard Folgar-Tucker model, delayed Folgar-Tucker model and the RSC model in decoupled simulations using model parameters obtained by fitting to shear flow experiments. It was observed that none of the models is able to provide a good agreement with the experimental data at all sampled regions. The delayed Folgar-Tucker model performed better than the other two models in locations further behind the front while the RSC model provided better predictions at sampled locations much closer to the front. Effects of coupling were also investigated and it was observed that coupled simulations

resulted in a smooth transition from high orientation values further behind the front to low values in the region near the front. However, when predictions are compared against the experimental data, there are no significant improvements in orientation predictions with coupled simulations. The effects of C_I on fiber orientation predictions were significant. A smaller value of C_I resulted in significantly better agreement with the experimental data in coupled simulation suggesting that a larger C_I which was obtained from startup of shear experiments is not appropriate for orientation predictions in the frontal region. Extension dominates over shear in the frontal region and there is a need to measure C_I in extensional flow to improve predictions in the frontal region.

4.8 Acknowledgements

The authors wish to gratefully acknowledge the financial support for this work from the Department of Energy and the National Science Foundation through grants No. DMI-0521918 and No. CMMI-0853537, respectively. The authors also like to thank Sabic Americas Inc. for providing the Valox 420 material used in experimental studies in this work. The access to polishing and microscopic facilities at the Material Science and Engineering Department and to the microscope at Institute of Critical Technology and Applied Sciences (ICTAS) at Virginia Tech is gratefully acknowledged. Syed Mazahir gratefully acknowledges the support provided by ICTAS through the Doctoral Scholars program. Gregorio M. Vélez-García would like to thank NSF-IGERT for funding through grant No. DGE-0548783, the Macromolecular Science and Infrastructure Engineering, and the University of Puerto Rico-Mayagüez.

4.9 References

[1] W. Rose, Fluid-fluid interfaces in steady motion, Nature, 191 (1961) 242-243.

[2] D.H. Chung, T.H. Kwon, Numerical studies of fiber suspensions in an axisymmetric radial diverging flow: The effects of modeling and numerical assumptions, Journal of Non-Newtonian Fluid Mechanics, 107 (2002) 67-96.

[3] J.M. Park, T.H. Kwon, Nonisothermal transient filling simulation of fiber suspended viscoelastic liquid in a center-gated disk, Polymer Composites, 32 (2011) 427-437.

[4] S.M. Mazahir, G.M. Vélez-García, P. Wapperom, D.G. Baird, Evolution of fiber orientation in radial direction in a center-gated disk: Experiments and simulation, Composites Part A: Applied Science and Manufacturing, (under review).

[5] R.S. Bay, C.L. Tucker, Fiber orientation in simple injection moldings. Part II: Experimental results, Polymer Composites, 13 (1992) 332-341.

[6] G.M. Vélez-García, S.M. Mazahir, P. Wapperom, D.G. Baird, Simulation of injection molding using a model with delayed fiber orientation, International Polymer Processing, 26 (2011) 331-339.

[7] F. Folgar, C.L. Tucker, Orientation behavior of fibers in concentrated suspensions, Journal of Reinforced Plastics and Composites, 3 (1984) 98-119.

[8] R.S. Bay, C.L. Tucker, Fiber orientation in simple injection moldings. Part I: Theory and numerical methods, Polymer Composites, 13 (1992) 317-331.

[9] B.E. Verweyst, C.L. Tucker, Fiber suspensions in complex geometries: Flow/orientation coupling, Canadian Journal of Chemical Engineering, 80 (2002) 1093-1106.

[10] K.H. Han, Y.T. Im, Numerical simulation of three-dimensional fiber orientation in injection molding including fountain flow effect, Polymer Composites, 23 (2002) 222-238.

[11] J. Ko, J.R. Youn, Prediction of fiber orientation in the thickness plane during flow molding of short fiber composites, Polymer Composites, 16 (1995) 114-124.

[12] M. Gupta, K.K. Wang, Fiber orientation and mechanical properties of short-fiber-reinforced injection-molded composites: Simulated and experimental results, Polymer Composites, 14 (1993) 367-382.

[13] S.T. Chung, T.H. Kwon, Coupled analysis of injection molding filling and fiber orientation, including in-plane velocity gradient effect, Polymer Composites, 17 (1996) 859-872.

[14] S.T. Chung, T.H. Kwon, Numerical simulation of fiber orientation in injection molding of short-fiber-reinforced thermoplastics, Polymer Engineering and Science, 35 (1995) 604-618.

[15] M. Vincent, E. Devilers, J.F. Agassant, Fibre orientation calculation in injection moulding of reinforced thermoplastics, Journal of Non-Newtonian Fluid Mechanics, 73 (1997) 317-326.

[16] S. Ranganathan, S.G. Advani, A simultaneous solution for flow and fiber orientation in axisymmetric diverging radial flow, Journal of Non-Newtonian Fluid Mechanics, 47 (1993) 107-136.

[17] G.B. Jeffery, The motion of ellipsoidal particles immersed in a viscous fluid, in: Proceedings of the Royal Society of London, Series A, The Royal Society, 1922, pp. 161-179.

[18] M. Sepehr, G. Ausias, P.J. Carreau, Rheological properties of short fiber filled polypropylene in transient shear flow, Journal of Non-Newtonian Fluid Mechanics, 123 (2004) 19-32.

[19] A.P.R. Eberle, G.M. Vélez-García, D.G. Baird, P. Wapperom, Fiber orientation kinetics of a concentrated short glass fiber suspension in startup of simple shear flow, Journal of Non-Newtonian Fluid Mechanics, 165 (2010) 110-119.

[20] A.P.R. Eberle, D.G. Baird, P. Wapperom, G.M. Vélez-García, Using transient shear rheology to determine material parameters in fiber suspension theory, Journal of Rheology, 53 (2009) 685-705.

[21] J. Wang, J.F. O'gara, C.L. Tucker, An objective model for slow orientation kinetics in concentrated fiber suspensions: Theory and rheological evidence, Journal of Rheology, 52 (2008) 1179.

[22] H.M. Huynh, Improved fiber orientation predictions for injection-molded composites, in: MS Thesis, Universty of Illinois - Urbana Champaign,2001

[23] B.E. VerWeyst, C.L. Tucker, P.H. Foss, J.F. O'Gara, Fiber orientation in 3-D injection molded features: Prediction and experiment, International Polymer Processing, 4 (1999) 409-420.

[24] G. Haagh, F. Van De Vosse, Simulation of three-dimensional polymer mould filling processes using a pseudo-concentration method, International Journal for Numerical Methods in Fluids, 28 (1998) 1355-1369.

[25] J.H. Phelps, C.L. Tucker III, An anisotropic rotary diffusion model for fiber orientation in short- and long-fiber thermoplastics, Journal of Non-Newtonian Fluid Mechanics, 156 (2009) 165-176.

[26] G.M. Vélez-García, P. Wapperom, D.G. Baird, A.O. Aning, V. Kunc, Unambiguous orientation in short fiber composites over small sampling area in a center-gated disk, Composites Part A: Applied Science and Manufacturing, 43 (2012) 104-113.

[27] A.R. Clarke, C.N. Eberhardt, Microscopy techniques for materials science, CRC Press, 2002.

[28] D. Chung, T.H. Kwon, Invariant-based optimal fitting closure approximation for the numerical prediction of flow-induced fiber orientation, Journal of Rheology, 46 (2002) 169.

[29] S.M. Dinh, R.C. Armstrong, A rheological equation of state for semiconcentrated fiber suspensions, Journal of Rheology, 28 (1984) 207-227.

[30] P.C. Wu, C.F. Huang, C.G. Gogos, Simulation of the mold-filling process, Polymer Engineering and Science, 14 (1974) 223-230.

[31] P. Lesaint, P.A. Raviart, On a finite element method for solving the neutron transport equation, in: C.d. Boor (Ed.) Mathematical Aspects of Finite Elements, Academic Press, New York, 1974, pp. 89-123.

[32] C.-W. Shu, S. Osher, Efficient implementation of essentially non-oscillatory shock-capturing schemes, Journal of Computational Physics, 77 (1988) 439-471.

[33] W.R. Hwang, W.-Y. Kim, S.H. Kang, S.J. Kim, Direct simulations on 2D mold-filling processes of particle-filled fluids, Korea-Australia Rheology Journal, 21 (2009) 193-200.

4.10 Figures

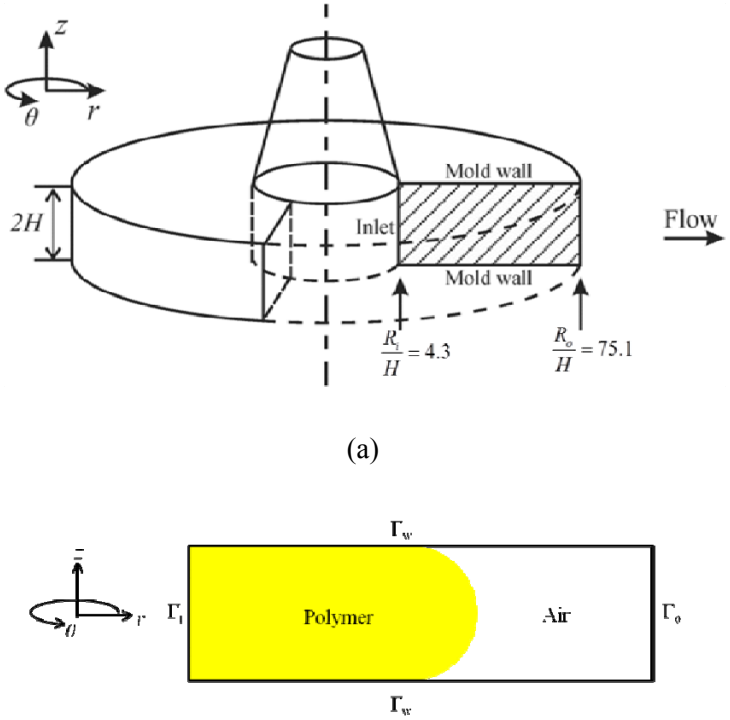

(a)

(b)

Figure 4.1 Center-gated disk with dimensions normalized by the half thickness H of the disk (a) and the simulation domain and boundaries (b).

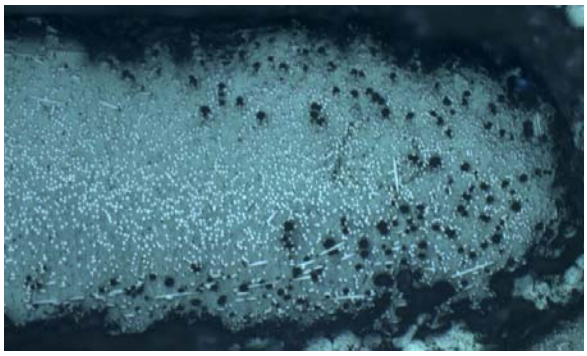

(a)

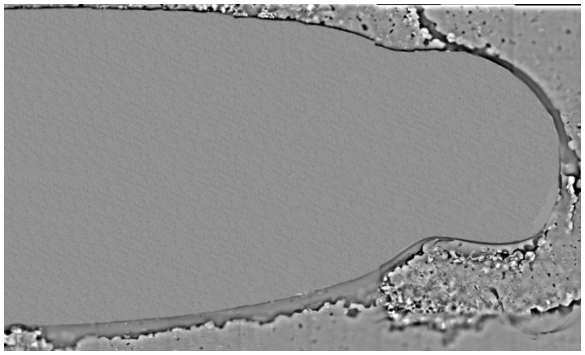

(b)

Figure 4.2 Microscopic image at 5X zoom of the frontal region of a center-gated disk made with (a) PBT/30 wt% short glass fiber suspension and (b) pure PBT.

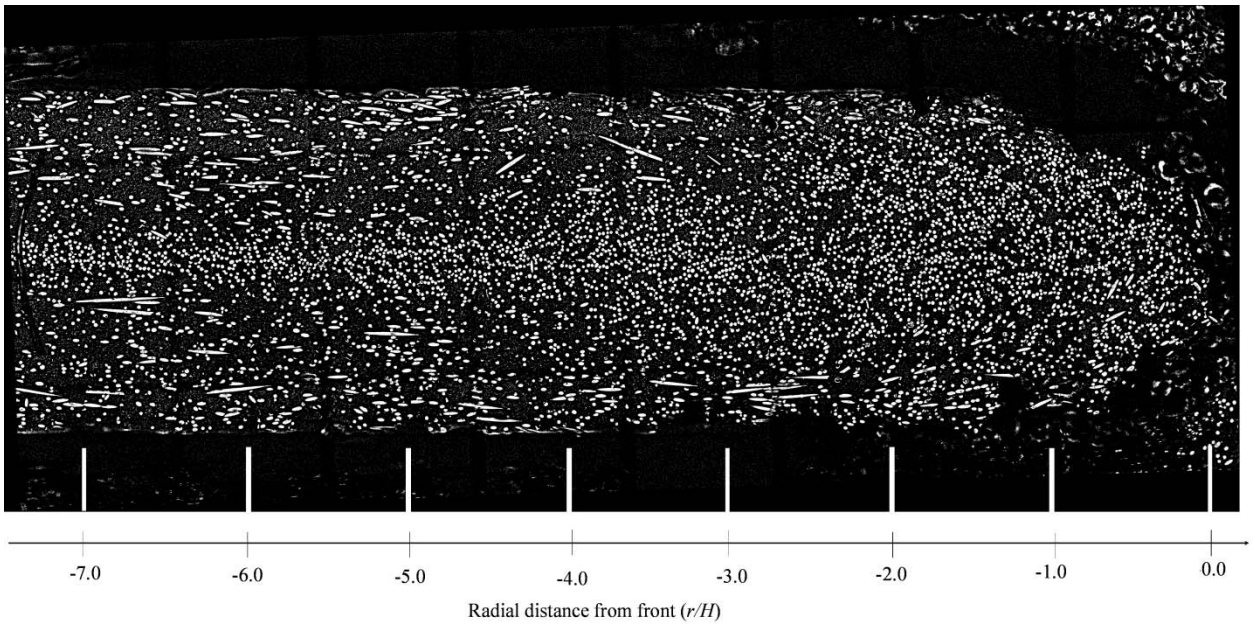

Figure 4.3 Microscopic image of a PBT / 30 wt% short glass fiber suspension center-gated disk showing the fiber footprints in the frontal region upto a distance approximately *r/H* = -7 *r/H* from the front. The image was taken at 20X zoom and the footprints were identified by an image analysis software.

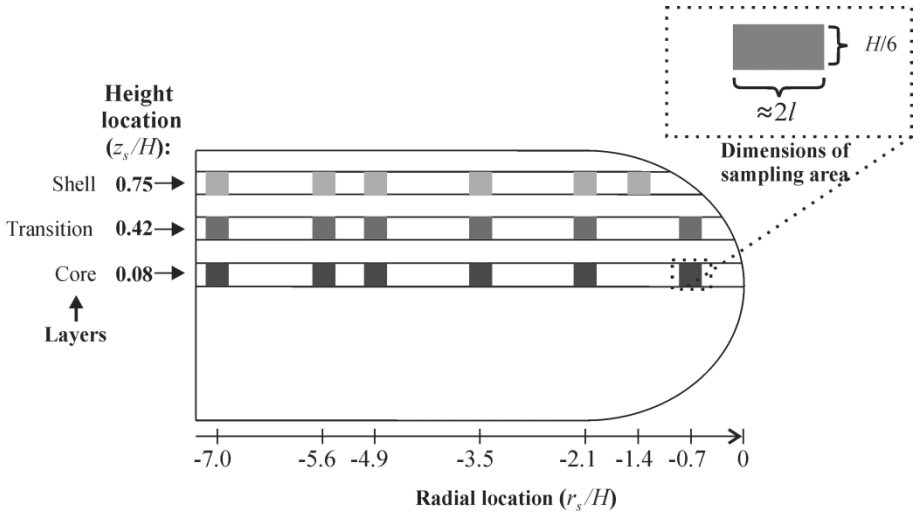

Figure 4.4 Radial locations in the frontal region of a center-gated disk selected for measurement of fiber orientation. Radial locations are shown in terms of non-dimensional distance from the front. Insert shows the dimensions of the sampling area.

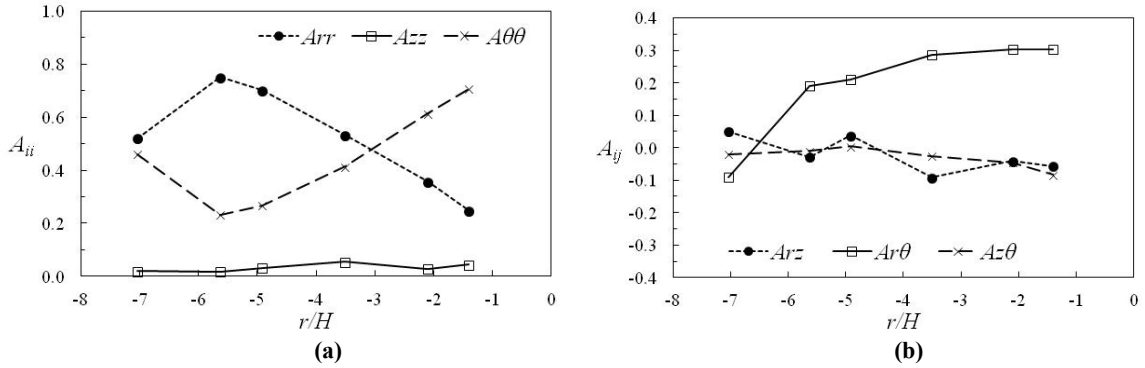

Figure 4.5 Orientation profile in the frontal region of a center-gated disk for the upper shell layer (z_s/H = 0.75) obtained from a center-gated disk for (a) diagonal A_{ii} and (b) off-diagonal A_{ij} components.

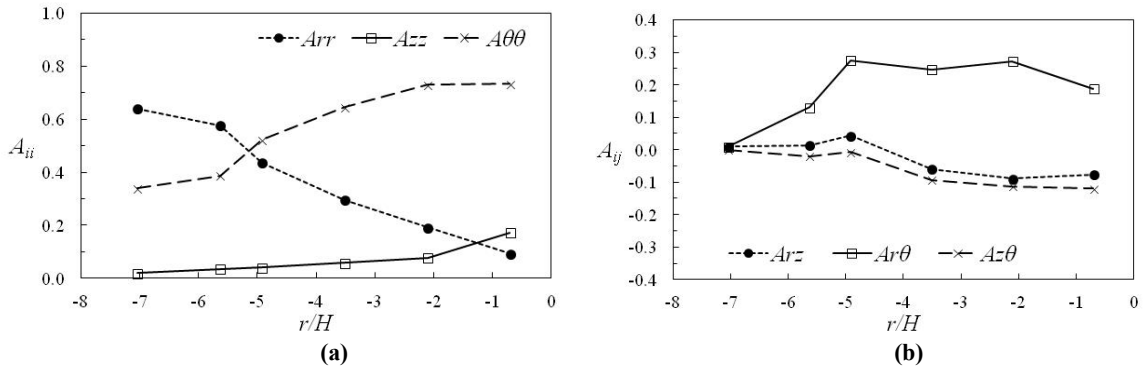

Figure 4.6 Orientation profile in the frontal region of a center-gated disk for the upper transition layer (z_s/H = 0.42) obtained from a center-gated disk for (a) diagonal A_{ii} and (b) off-diagonal A_{ij} components.

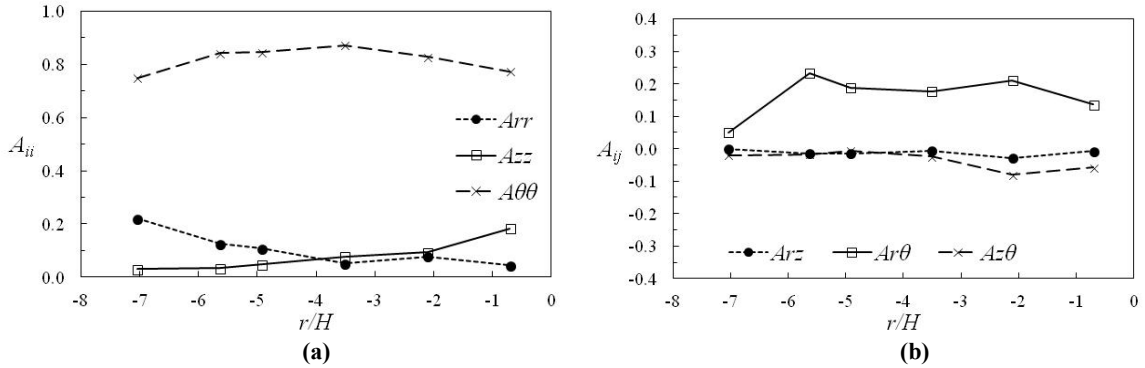

Figure 4.7 Orientation profile in the frontal region of a center-gated disk for the upper core layer (z_s/H = 0.08) obtained from a center-gated disk for (a) diagonal A_{ii} and (b) off-diagonal A_{ij} components.

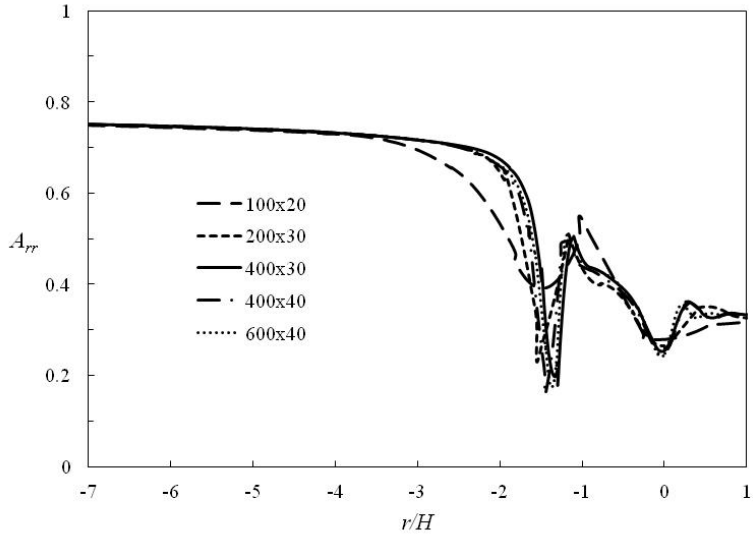

(a)

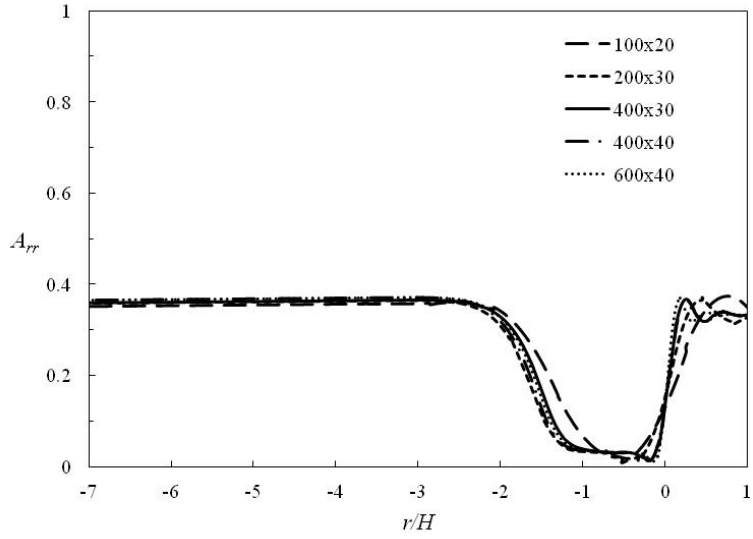

(b)

Figure 4.8 Convergence of predicted A_{rr} with the RSC model in decoupled fountain flow simulation. Fives meshes are considered with mesh refinement in both *r*- and *z*- directions. A_{rr} predictions are shown at (a) z_s/H = 0.75, (b) z_s/H = 0.08.

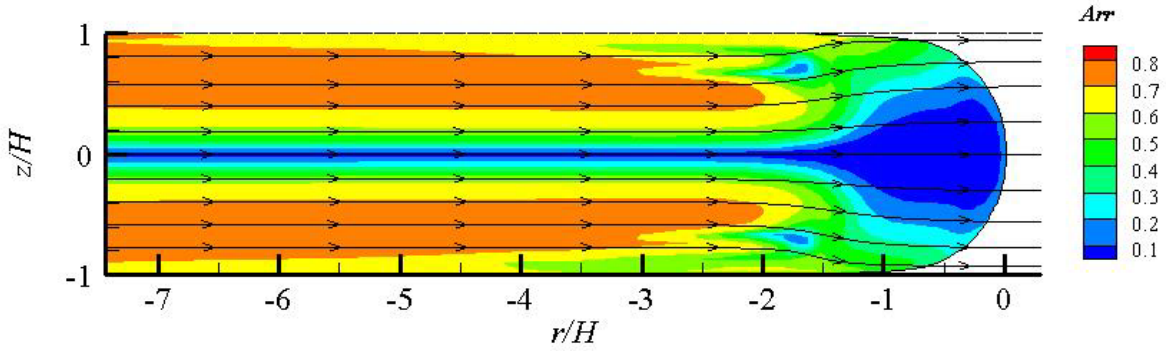

(a)

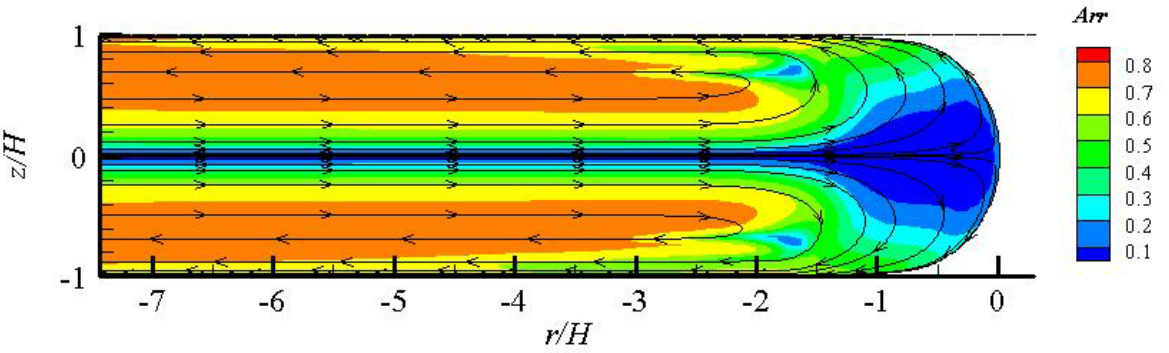

(b)

Figure 4.9 Contour plot of A_{rr} predictions with the RSC model in a decoupled simulation in the frontal region of a center-gate disk and streamlines in (a) a stationary reference frame, and (b) a moving reference frame attached to the tip of the front.

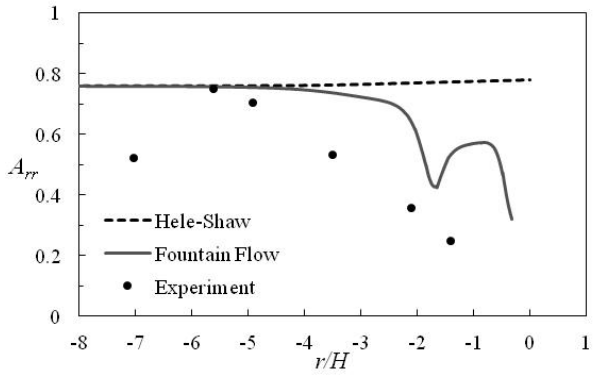

(a)

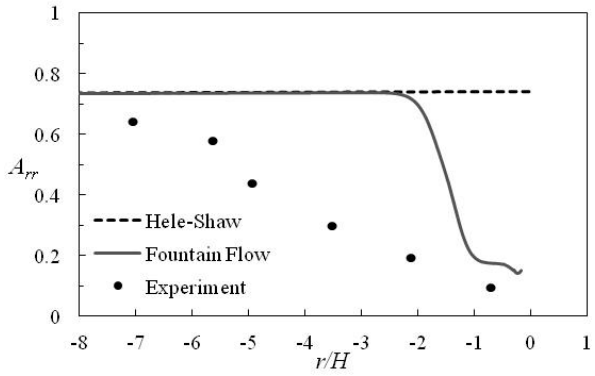

(b)

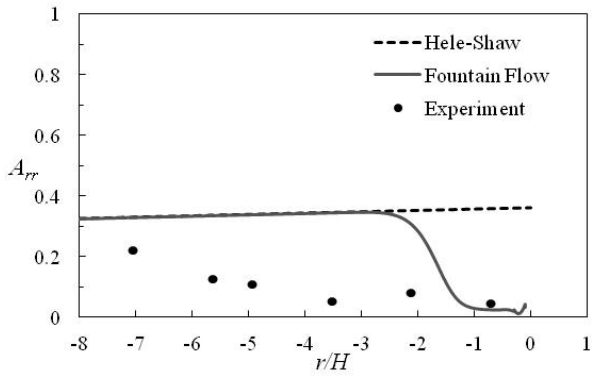

(c)

Figure 4.10 A_{rr} predictions with the standard Folgar-Tucker model using Hele-Shaw flow approximation and fountain flow simulation in a decoupled scheme, compared with experimentally measured values at (a) z_s/H = 0.75, (b) z_s/H = 0.42, and (c) z_s/H = 0.08.

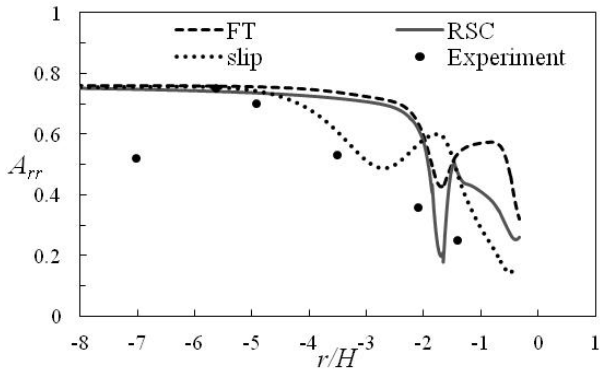

(a)

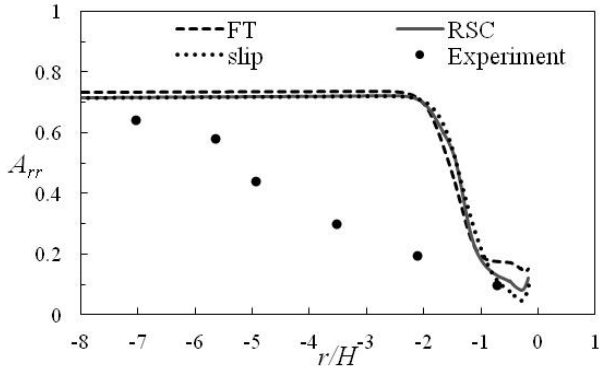

(b)

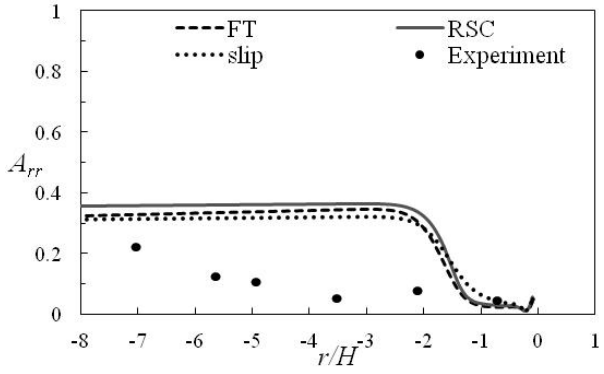

(c)

Figure 4.11 Comparison of A_{rr} predictions with the standard Folgar-Tucker model and its slow versions using decoupled fountain flow simulation with experimentally measured values at (a) $z_s/H = 0.75$, (b) $z_s/H = 0.42$, and (c) $z_s/H = 0.08$.

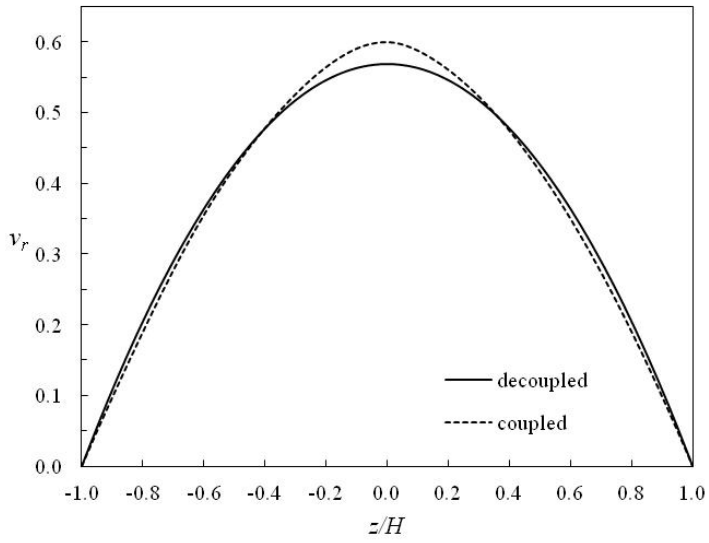

Figure 4.12 Coupled and decoupled velocity profiles through the thickness with the RSC model at *r/H* = 11.3.

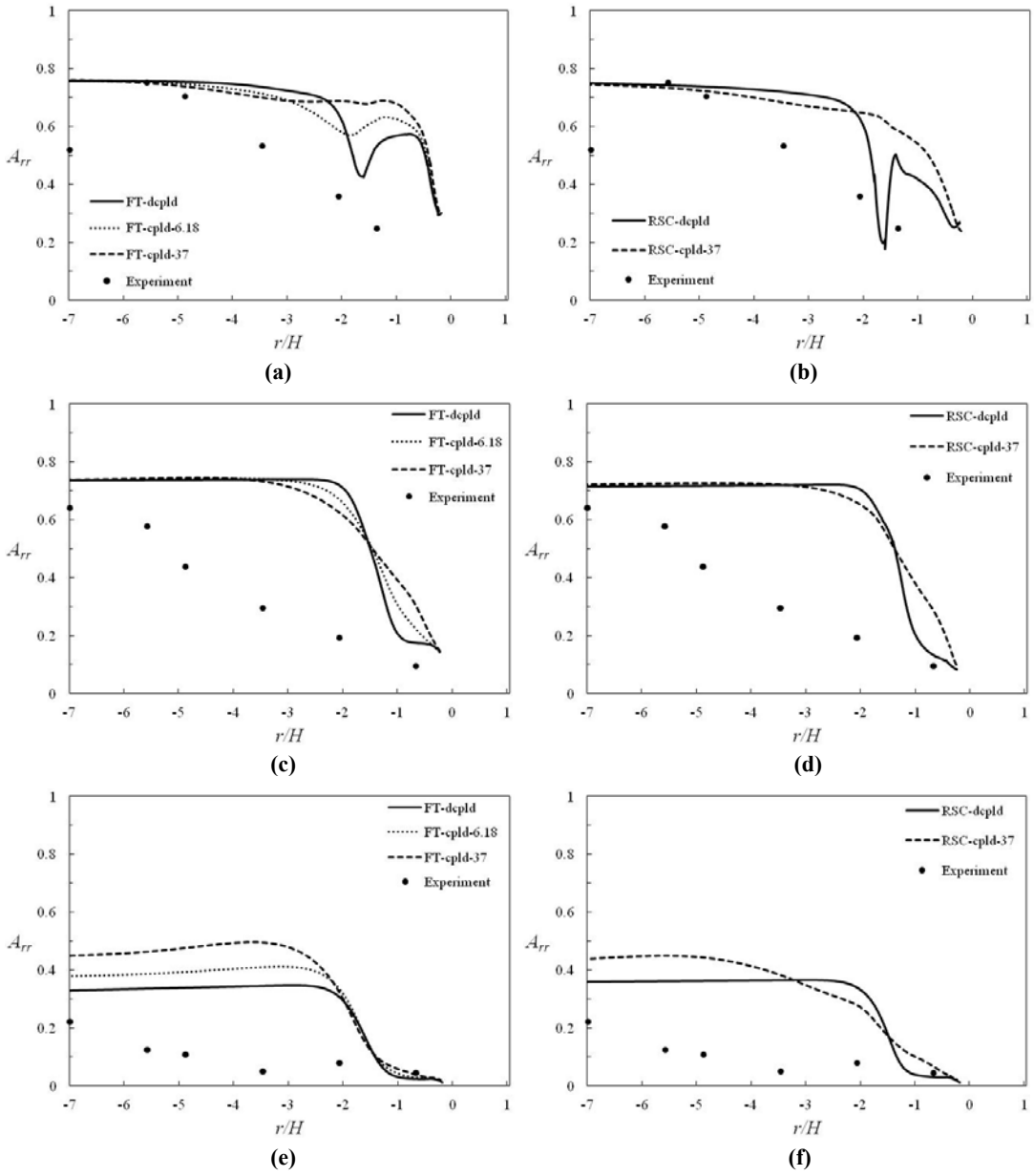

Figure 4.13 Comparison of A_{rr} predictions with the standard Folgar-Tucker (FT) model (left) and the RSC model (right) using decoupled (dcpld) and coupled (cpld) simulations with experimentally measured values at (a),(b) $z_s/H = 0.75$, (c),(d) $z_s/H = 0.42$, and (e),(f) $z_s/H = 0.08$. Coupled (cpld) simulations with the standard Folga-Tucker model are performed using two values of the coupling parameter $\nu\zeta_{str} = 6.18$ (value fitted from rheology) and $\nu\zeta_{str} = 37$ (theoretically determined)

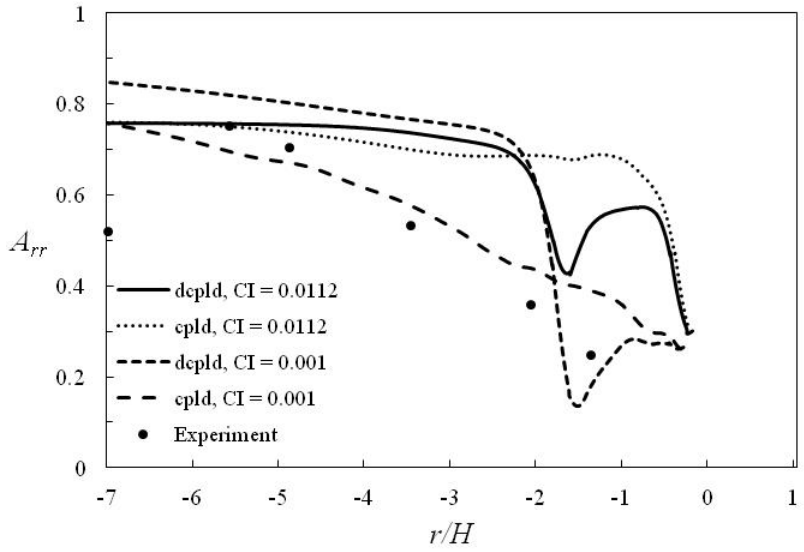
1
0.8
0.6
0.4
0.2
0
A_{rr}
dcpld, CI = 0.0112
cpld, CI = 0.0112
dcpld, CI = 0.001
cpld, CI = 0.001
Experiment
-7
-6
-5
-4
-3
-2
-1
0
1
r/H

(a)

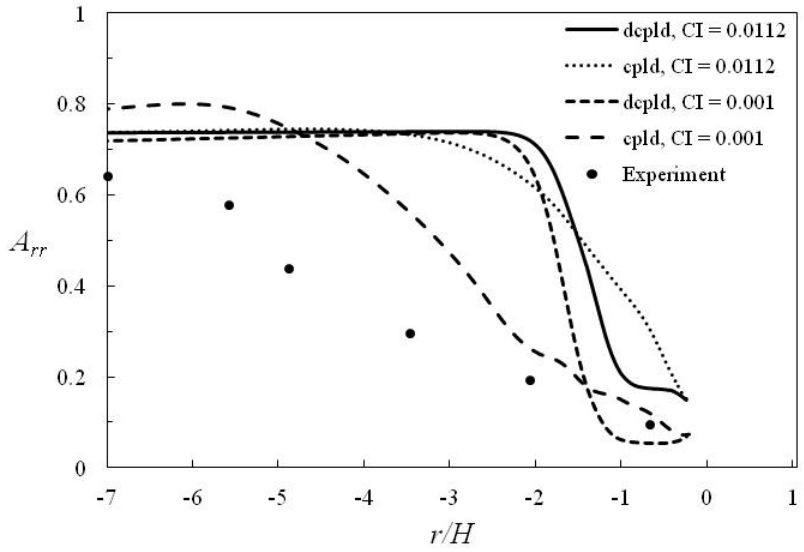
1
0.8
0.6
0.4
0.2
0
A_{rr}
dcpld, CI = 0.0112
cpld, CI = 0.0112
dcpld, CI = 0.001
cpld, CI = 0.001
Experiment
-7
-6
-5
-4
-3
-2
-1
0
1
r/H

(b)

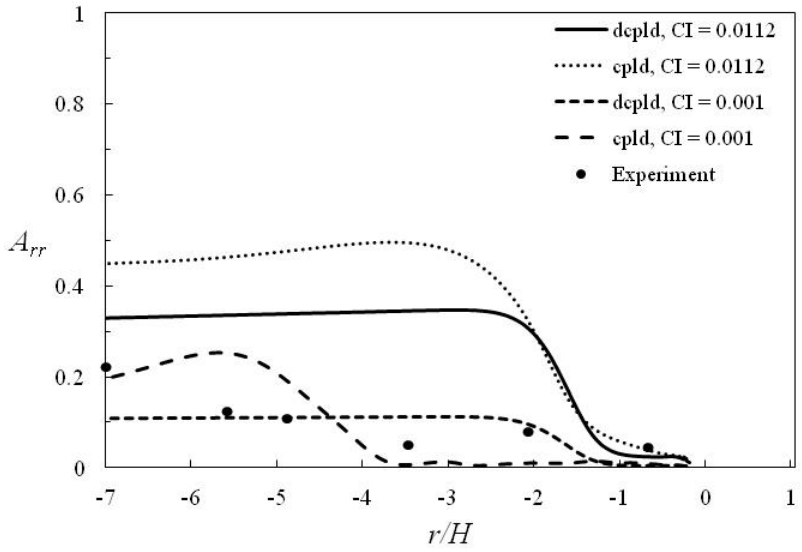

(c)

Figure 4.14 Comparison of A_{rr} predictions with the standard Folgar-Tucker (FT) with two different values of C_I (0.001 and 0.012) using decoupled and coupled simulations with experimentally measured values at (a) z_s/H = 0.75, (b) z_s/H = 0.42, and (c) z_s/H = 0.08. Decoupled (dcpld) simulations are compared with coupled (cpld) simulations using theoretical value of the coupling parameter, $\nu\zeta_{str}$ = 37.

CHAPTER 5. FIBER ORIENTATION PREDICTIONS FOR LONG FIBER SUSPENSIONS IN INJECTION MOLDING SYSTEMS

*S.M. Mazahir[1], G.M. Vélez-García[2], *P. Wapperom[3], and D. Baird[1]*

[1] Department of Chemical Engineering, [2] Macromolecules and Interfaces Institute, [3] Department of Mathematics, Virginia Tech, Blacksburg, VA, 24061, USA

syedm@vt.edu, gvelez@vt.edu, pwappero@math.vt.edu, dbaird@vt.edu

[*] Author to whom correspondence should be addressed; Peter Wapperom, Tel: +1 540 231 7252, Fax: +1 540 231 5960

Abstract

Evolution of orientation for long semi-flexible fiber suspensions during the filling phase of a center-gated disk was simulated. The orientation of long semi-flexible fibers was predicted using the Folgar-Tucker model, which was originally developed for short rigid fibers, and with the Bead-Rod model, which has been recently proposed for semi-flexible fibers. Model parameters for both the models were obtained from previous rheological study in which the parameters were determined by fitting the rheological response of fiber suspension under startup of shear in a sliding plate rheometer. Orientation predictions were compared with the experimental data in both the thickness direction and the direction of flow. Both models performed very well in the core layer in almost entire flow length. However, close to the walls, Bead-Rod model performed significantly better than the Folgar-Tucker model in almost entire lubrication region. Bending of fibers with the Bead-Rod model was not significant and occurred only in the region close to the gate. Effects of fountain flow on orientation predictions near the front were also assessed against Hele-Shaw flow approximation. It was shown that fountain flow simulation is able to predict the drop in flow direction component of orientation in the frontal region while Hele-Shaw flow overpredicts orientation in almost entire frontal region.

5.1 Introduction

Glass fiber / polymer suspensions are injection molded to make high-strength light-weight materials for use in various applications. Glass fibers used in these materials act as reinforcing materials and enhance the mechanical, electrical, and thermal properties of these composite materials. However, the properties of the final solidified part depend on two primary factors. The first is the orientation distribution of these fibers and the second is the flexibility of fibers. Fiber flexibility, which is exhibited by long fibers, accounts for additional enhancement in mechanical properties as compared to short fibers which are rigid.. Glass fibers can be classified as 'short' and 'long' based on their length. Fibers with length $L < 1$ mm are said to be short and fibers with length $L > 1$ mm are said to be long [1].

The distinguishing feature of long fibers is the flexibility exhibited by these fibers. The term 'flexibility' describes the ability of long fibers to bend under a given flow field. A fiber with higher flexibility or equivalently lower 'stiffness' shows higher degree of bending when placed in a flow field that induces bending. The effective stiffness (S^{eff}) of a fiber in a viscous medium was quantified by Switzer and Klingenberg [2] with the introduction of a dimensionless group that depends on the properties of the fiber and the surrounding matrix

$$S^{eff} = \frac{E_Y \pi}{64 \eta_s \dot{\gamma} a_r^4} \tag{1}$$

where E_Y is the Young's modulus of the fiber, η_s is the matrix viscosity, $\dot{\gamma}$ is the shear rate, and a_r is the fiber aspect ratio, given by $a_r = L/d$, L being the fiber length and d the fiber diameter.

Folgar and Tucker [3] proposed a modification to the Jeffery's model [4] to describe the evolution of orientation of rigid fibers in non-dilute fiber suspensions. The model proposed by Folgar and Tucker attempted to capture fiber interactions in non-dilute fiber suspensions by introducing an isotropic rotary diffusion term. Orientation predictions with the Folgar-Tucker model have been tested in transient shear flow experiments and it has been observed that the evolution of orientation seen in the experiments is much slower than the Folgar-Tucker model predictions [5-7]. Wang et al. [5] proposed the reduced strain closure (RSC) model which slows down the evolution of orientation in simple flows. However, the RSC model is more complex than the Folgar-Tucker model because of the need for determining the eigenvalues and eigenvectors of the orientation tensor that describes the orientation state of the fibers. A second modification has been proposed

that achieves the slowdown in the evolution of orientation by adding a parameter known as the strain reduction factor [8] or the slip parameter [6, 7]. The term 'slip parameter' will be used here for this parameter. These two modifications have been shown to improve orientation predictions in rheological experiments such as start-up of shear and shear-flow reversal [5-7]. However, none of these models take into account fiber flexibility and are therefore not suitable for orientation prediction of long glass fibers which are considered semi-flexible.

The Bead-Rod model, originally proposed by Strautins and Latz [9] is a first step towards describing the evolution of semi-flexible fibers using a continuum approach. The model takes into account the flexibility of semi-flexible fibers that show small bending angles. In this model, a semi-flexible fiber is described by two rods, each of length l_B and orientation **p** and **q** connecting three beads as shown in Figure 5.1. The rods are free to rotate around the central bead, which acts as a pivot point. Semi-flexible fibers have an inherent resistance to bending which is captured by a resistance potential that exists between the two rods. For a perfectly straight fiber, no restorative force is present in the fiber. When a semi-flexible fiber is subjected to a flow field that induces bending or curvature, the Bead-Rod model predicts bending of the fiber due to drag flow on the beads. The Bead-Rod model was originally formulated for dilute suspensions and did not account for fiber-fiber interactions in non-dilute suspensions. Ortman et al. [10] added an isotropic rotary diffusion term to the model in order to include fiber-fiber interactions and a 'slip' parameter with the same definition and purpose as in the context of the Folgar-Tucker model [3]. From here on, the Bead-Rod model, including the modifications proposed by Ortman et al. [10], will be referred to as the Bead-Rod model and the Folgar-Tucker model with the slip parameter will be referred to as the Folgar-Tucker model.

Orientation predictions with the Bead-Rod model have been shown to be better than the Folgar-Tucker model predictions at radial locations greater than 20% fill position in a center-gated disk [11]. However, at fill positions 50% -100% of fill, both models over-predicted the fiber orientation near the walls. This was attributed to the Hele-Shaw flow approximation which was used in the simulations. Hele-Shaw flow has previously been shown to result in over-prediction of orientation in the frontal region, especially near the walls and therefore inclusion of fountain flow in the simulation becomes important [12].

The objective of this paper is to assess the improvement in orientation predictions with the Bead-Rod model over the Folgar-Tucker model predictions for long semi-flexible fiber suspensions

in a center-gated disk. The model parameters are from an earlier experimental study on a sliding plate rheometer [10] and the experimental data reported in the thickness direction by Ortman et al. [11] is used for experimental validation in this study. Profiles of orientation along the radial direction in the shell, transition and core layers are generated for comparison of orientation evolution along the direction of flow. The second objective is to experimentally validate the improvements in orientation predictions with the fountain flow simulations over Hele-Shaw flow predictions by comparing simulation results with the orientation data along the thickness and radial directions.

5.2 Governing equations

5.2.1. Orientation evolution equations

The orientation of a rigid fiber can be described by a vector **p** along the axis of the fiber. For a given orientation distribution function ψ, where ψ represents the probability of finding a fiber with a given orientation in a differential volume of space, the second moment of **p** with respect to a given probability distribution function can be evaluated to form a second order orientation tensor **A**, which conveniently describes the orientation for a population of fibers

$$\mathbf{A}(t) = \iint \mathbf{pp}\,\psi(\mathbf{p},t)\,d\mathbf{p} \quad (2)$$

The evolution of **A** for high aspect ratio particles can be described by the Folgar-Tucker model

$$\frac{D\mathbf{A}}{Dt} = \alpha\left[\mathbf{A}\cdot\mathbf{L}^T + \mathbf{L}\cdot\mathbf{A} - 2\mathbf{A}_4 : \mathbf{D} + 2C_I\dot{\gamma}\left(\mathbf{I} - 3\mathbf{A}\right)\right] \quad (3)$$

where D/Dt is the material derivative, α the slip parameter, $\mathbf{L} = \nabla\mathbf{v}^T$, $\mathbf{D} = 1/2\left(\mathbf{L} + \mathbf{L}^T\right)$, $\nabla\mathbf{v} = \partial v_j / \partial x_i$ being the velocity gradient. $\mathbf{A}_4$ is the fourth-order orientation tensor, **I** the identity tensor, C_I the isotropic interaction coefficient and $\dot{\gamma} = \sqrt{2\mathbf{D}:\mathbf{D}}$. A closure approximation is needed to express $\mathbf{A}_4$ in terms of **A**. Chung and Kwon [13] proposed Invariant-based optimal fitting (IBOF) closure approximation to express $\mathbf{A}_4$ in terms of **A**. The IBOF closure is as good as eigenvalue-based closures in accuracy, but requires less computational time. We use the IBOF closure approximation for $\mathbf{A}_4$ in all simulations.

In the Bead-Rod model, the fiber orientation is represented by three moments of vectors **p** and **q** according to [9]

$$\mathbf{A}(t) = \iint \mathbf{pp}\,\psi(\mathbf{p},\mathbf{q},t)\,d\mathbf{p}d\mathbf{q} \tag{4}$$

$$\mathbf{B}(t) = \iint \mathbf{pq}\,\psi(\mathbf{p},\mathbf{q},t)\,d\mathbf{p}d\mathbf{q} \tag{5}$$

$$\mathbf{C}(t) = \iint \mathbf{p}\,\psi(\mathbf{p},\mathbf{q},t)\,d\mathbf{p}d\mathbf{q} \tag{6}$$

Eq. (4) describes the second order orientation tensor given by the second moment of the orientation vector of one of the rods shown in Figure 5.1, with respect to the orientation distribution function ψ. This is similar to the second order orientation tensor described for rigid fibers. The flexibility of fibers can be defined as their bending capacity. In the above form of the Bead-Rod model, the solution of the Bead-Rod model equations provides a way to estimate the bending of fibers. A measure for the degree of bending is trace of **B**, denoted as *tr*(**B**). For a perfectly straight fiber, vectors **p** and **q**, point in opposite directions, which can be written mathematically as **q** = **-p**. Based on this, orientation tensors **A** and **B** for a population of perfectly straight fibers can be written as **B** = **-A** in which case *tr*(**B**) = -1.0. As the fibers bend, *tr*(**B**) gets smaller in magnitude based on the degree of bending of the fiber. For a fiber that is completely bent, in which case **q** = **p**, **B** = **A**, and *tr*(**B**) = 1.0. For fibers with the two rods perpendicular to each other, *tr*(**B**) = 0.0.

The evolution of orientation of semi-flexible fibers, according to the Bead-Rod model, including the modifications proposed by Ortman et al. [10] is given by

$$\frac{D\mathbf{A}}{Dt} = \alpha\left[\mathbf{A}\cdot\mathbf{L}^T + \mathbf{L}\cdot\mathbf{A} - 2\mathbf{A}_4 : \mathbf{D} + 2C_I\dot{\gamma}\left(\mathbf{I} - 3\mathbf{A}\right) + \frac{l_B}{2}\left(\mathbf{Cm} + \mathbf{mC} - 2(\mathbf{m}\cdot\mathbf{C})\mathbf{A}\right) - 2\kappa\left(\mathbf{B} - \mathbf{A}tr(\mathbf{B})\right)\right] \tag{7}$$

$$\frac{D\mathbf{B}}{Dt} = \alpha\left[\mathbf{B}\cdot\mathbf{L}^T + \mathbf{L}\cdot\mathbf{B} - 2(\mathbf{A} : \mathbf{D})\mathbf{B} - 4C_I\dot{\gamma}\mathbf{B} + \frac{l_B}{2}\left(\mathbf{Cm} + \mathbf{mC} - 2(\mathbf{m}\cdot\mathbf{C})\mathbf{B}\right) - 2\kappa\left(\mathbf{A} - \mathbf{B}tr(\mathbf{B})\right)\right] \tag{8}$$

$$\frac{D\mathbf{C}}{Dt} = \alpha\left[\mathbf{L}\cdot\mathbf{C} - (\mathbf{A} : \mathbf{L})\mathbf{C} - 2C_I\dot{\gamma}\mathbf{C} + \frac{l_B}{2}\left(\mathbf{m} - \mathbf{C}(\mathbf{m}\cdot\mathbf{C})\right) - \kappa\mathbf{C}\left(1 - tr(\mathbf{B})\right)\right] \tag{9}$$

$$\mathbf{m} = \sum_i\sum_j\sum_k \frac{\partial^2 v_i}{\partial x_j \partial x_k} A_{jk}\mathbf{e}_i \tag{10}$$

where κ is the resistive bending potential coefficient, *tr*(**B**) is the trace of **B** and **e** is a unit vector. The slip parameter α accounts for the slowdown in evolution of orientation, and plays the same role as in the Folgar-Tucker model. The terms in Eq. (7)-(9) containing the parameter C_I are the

isotropic rotary diffusivity terms that account for fiber-fiber interactions. The terms containing **m** account for bending due to non-uniform velocity gradients along the length of the fiber.

5.2.2. Equations of motion

The flow of an incompressible fluid under creeping flow conditions is governed by the balance equations

$$\nabla \cdot \mathbf{v} = 0 \tag{11}$$

$$\nabla \cdot \left(-p\mathbf{I} + 2\eta_s \mathbf{D} \right) = \mathbf{0} \tag{12}$$

where ∇ is the gradient operator, **v** the velocity, p the pressure, **I** the identity tensor, and η_s the matrix viscosity. The filling conditions are assumed to be isothermal because of fast filling time (approximately two second fill time). Due to such a short filling time, cooling effects due to conduction are small. Heating due to viscous dissipation offsets the cooling effects due to conduction inside the polymer. Ortman et al. [11] estimated the change in melt temperature due to viscous dissipation to be less than 1 ^{O}C. Non-dimensionalization of the flow equations is performed. Velocities are non-dimensionalized with the average radial velocity $v_{avg}(R_{in})$ at the mold inlet, lengths are non-dimensionalized with the half-thickness of the disk H, and time with $v_{avg}(R_{in})/H$.

5.2.3. Model parameters

The model parameters for 30wt % long glass fiber reinforced polypropylene were obtained by Ortman et al. [11] for the Folgar-Tucker model with the slip parameter, and the Bead-Rod model. The parameter values are (C_I, α) = (0.005, 0.25) for the Folgar-Tucker model and (C_I, α) = (0.053, 0.13) for the Bead-Rod model. These parameters were determined by fitting the orientation and stress model predictions to experimental stress data under startup of steady shear in a sliding plate rheometer. The resistive bending potential coefficient κ was determined to be κ = 218 s^{-1} by considering the physical properties of glass fibers and fiber length distribution, and l_B was taken to be $L_N/2$, where L_N is the number average fiber length. L_N was experimentally determined to be L_N = 2.92 mm [11].

5.3 Numerical Methods

Filling of long glass fiber suspension in a center-gated disk mold and the evolution of fiber orientation is simulated by solving a transport equation for the evolution of the advancing front, equations of motion for the velocity and pressure and orientation equations for the fiber orientation.

In the time-stepping scheme, these three equations are solved in a decoupled fashion at every time step. Continuous biquadratic polynomials are used for the discretization of velocity and continuous bilinear polynomials for pressure. For the orientation and pseudo-concentration, discontinuous biquadratic polynomial representation is used. The discontinuous polynomials for the orientation and pseudo-concentration are selected due to the convective nature of the orientation and transport equations. The solution schemes for each equation are described in detail below.

5.3.1. Equations of motion

The equations of motion (5), (6) are solved simultaneously to determine the velocity $\mathbf{v}^{n+1}$ and pressure p^{n+1} at time level t^{n+1}.

$$\nabla \cdot \mathbf{v}^{n+1} = 0 \tag{13}$$

$$\nabla \cdot \left(-p^{n+1}\mathbf{I} + 2\eta_s \mathbf{D}^{n+1} \right) = \mathbf{0} \tag{14}$$

Galerkin finite element method is used for the spatial discretization. The equations of motion are solved in the entire simulation domain which consists of polymer as well as air. Therefore, viscosity η_s is taken to be polymer viscosity in the polymer phase and air viscosity in the air phase. Viscosity η_s is linearly interpolated between the polymer viscosity and air viscosity near the polymer-air interface

$$\eta_s = c \times \eta_p + (1-c) \times \eta_a \tag{15}$$

where c is the pseudo-concentration variable, η_p is the polymer viscosity and η_a is the air viscosity. The pseuodo-concentration variable c has values in the range [0, 1]. A value of c = 1 indicates polymer, a value of c = 0 air and a value c = 0.5 defines the polymer-air interface. The value of c is determined at every integration point and c = 0 is used if c < 0, and c = 1 if c > 1 in order to eliminate non-physical values of c due to non-linear-interpolation. At the inlet of the mold, a Newtonian velocity profile based on the given flow rate is prescribed. At the other boundaries, the boundary conditions are prescribed as [14]

$$\begin{aligned} &a v_t + \sigma_t = 0 \qquad \forall x \in \Gamma_{\mathrm{w}} \cup \Gamma_{\mathrm{o}} \\ &a v_n + \sigma_n = 0 \qquad \forall x \in \Gamma_{\mathrm{o}} \\ &v_n = 0 \qquad\quad \forall x \in \Gamma_{\mathrm{w}} \end{aligned} \tag{16}$$

where $a = 10^{10}$ for $c \geq 0.5$ and $a = 0$ for $c < 0.5$, Γ_w is the boundary along the mold walls and Γ_o is the outlet for air as shown in Figure 5.2. With the use of these boundary conditions, air and polymer are not allowed to pass through the mold walls. Air is allowed to slip freely along the mold walls while the slip velocity for the polymer along the mold walls is negligible which effectively acts as a no-slip boundary condition for the polymer phase.

5.3.2. Orientation equations

The orientation equations can be written as

$$\begin{aligned} &\frac{\partial \mathbf{P}}{\partial t} + \mathbf{v} \cdot \nabla \mathbf{P} - c\mathbf{F}(\mathbf{L}^T, \mathbf{P}) = \mathbf{0} \\ &\mathbf{P}(\Gamma_i, t) = \mathbf{P}_i \end{aligned} \tag{17}$$

where $\mathbf{P}$ is the orientation tensor $\mathbf{A}$ in the Folgar-Tucker model or $\mathbf{A}$, $\mathbf{B}$, $\mathbf{C}$ in the Bead-Rod model, and $\mathbf{F}(\mathbf{L}^T, \mathbf{P})$ is the model-specific term given by the right-hand sides of Eqs. (3), (7)-(9), Γ_i is the inlet boundary of the simulation domain and $\mathbf{P}_i$ is the orientation state prescribed at the inlet boundary. Because the orientation is determined in the entire simulation domain at each time step, the distinction between the air and polymer phase is made by multiplying the model-specific term $\mathbf{F}(\mathbf{L}^T, \mathbf{P})$ in Eq. (13) by the pseudo-concentration variable.

Eq. (13) is spatially discretized using the discontinuous Galerkin finite element method (DGFEM) of Lesaint and Raviart [15]. The weak formulation for the orientation equations with appropriate functional spaces for the test functions and the solution on an element K is given by: Find $\mathbf{P}$ such that for all admissible weighting functions $\mathbf{\Lambda}$

$$\left\langle \frac{\partial \mathbf{P}}{\partial t}, \mathbf{\Lambda} \right\rangle_K + \left\langle \mathbf{v} \cdot \nabla \mathbf{P}, \mathbf{\Lambda} \right\rangle_K + \left\langle \mathbf{v} \cdot \mathbf{n}[\mathbf{P}], \mathbf{\Lambda} \right\rangle_{\Gamma_{K,i}} - \left\langle c\mathbf{F}(\mathbf{P}, \mathbf{L}^T), \mathbf{\Lambda} \right\rangle_K = 0 \tag{18}$$

where $\langle \mathbf{P}, \mathbf{Q} \rangle_K$ and $\langle \mathbf{P}, \mathbf{Q} \rangle_{\Gamma_{K,i}}$ are proper L^2 inner products on the element domain Ω_K and on the element boundary $\Gamma_{K,i}$, respectively. The boundary integral is applied on those boundaries of the element K where $\mathbf{v} \cdot \mathbf{n} < 0$, $\mathbf{n}$ being the outward unit normal along the boundary. The discontinuity across the elements is given by $[\mathbf{P}] = \mathbf{P}_{\Gamma_{K,u}} - \mathbf{P}_{\Gamma_{K,e}}$, where $\mathbf{P}_{\Gamma_{K,u}}$ is the value of $\mathbf{P}$

along the boundary $\Gamma_{K,i}$ in the upstream element and $\mathbf{P}_{\Gamma_{K,e}}$ is the value of **P** inside element K along the boundary $\Gamma_{K,i}$. For element boundaries along the inlet boundary of the simulation domain, $\mathbf{P}_{\Gamma_{K,u}} = \mathbf{P}_i$. The value of c is determined at every integration point and $c = 0$ is used if $c < 0$, and $c = 1$ if $c > 1$ in order to eliminate non-physical values of c due to non-linear-interpolation. With this formulation, the orientation solution is determined locally within each element, which significantly reduces the computational time and memory as compared to solving for orientation in the entire domain at once. The explicit Runge-Kutta third order total variance diminishing (RK3-TVD) scheme is used for discretization in time [16]. With RK3-TVD, the solution is stable even with a relatively large time step as compared to the single step explicit methods, while computational time and memory requirements are low as compared to the single step implicit methods [17].

At the inlet boundary of the mold geometry, $\mathbf{A}_i$ is prescribed as the experimentally measured inlet orientation for both the models. For the Bead-Rod model, additional inlet values are needed for Eqs. (8) and (9). Because the fiber curvature is not reported by Ortman et al. [11], we assume that all the fibers are initially straight before entering the mold. Therefore, we use $\mathbf{B}_i = -\mathbf{A}_i$ and $\mathbf{C}_i = \mathbf{0}$. Inside the mold geometry, we initialize the orientation values with equilibrium values, which is represented by $\mathbf{A}_i = 1/3\mathbf{I}$ and $\mathbf{B}_i = -1/3\mathbf{I}$ and $\mathbf{C}_i = \mathbf{0}$.

5.3.3. Transport equation

The pseudo-concentration method is used to predict the evolution of the advancing front [14]. The solution of the transport equation determines the evolution of the pseudo-concentration variable c

$$\begin{aligned} &\frac{\partial c}{\partial t} + \mathbf{v} \cdot \nabla c = 0 \\ &c(\Gamma_i, t) = 1 \end{aligned} \tag{19}$$

The polymer-air interface moves according to this equation and polymer fills the region initially filled with air. The material properties of air are selected such that the contribution of air to pressure buildup in the mold is negligible as compared to that of the polymer. The density of air is chosen to be zero and viscosity about 0.1% of the fiber suspension. Spatial discretization of Eq. (15) is performed with the DGFEM scheme, as described in section 4.5.2 without model-specific terms. Time discretization is achieved by means of RK3-TVD scheme [16].

5.4 Experimental Data

5.4.1. Test geometry and material data

The simulations results were compared with the experimental orientation data in a center-gated disk geometry reported by Ortman et al. [11]. Figure 5.2 shows the geometry of the center-gated disk which was injection molded using 30 wt% long glass fibers polypropylene suspension, provided by SABIC Innovative Plastics. The disk had an internal radius R_i = 2.97 mm, outer radius R_o = 45 mm, and thickness $2H$ = 2.05 mm. The radial distance filled inside the mold corresponded to about 90% of the total radial length inside the mold. Fill time was approximately 2 seconds, corresponding to a volumetric flow rate Q = 6.52 cm^3/s. The volume fraction of fibers in the suspension was φ = 0.145 which is classified as a concentrated suspension using the theory of Doi and Edwards [18]. The initial fiber length was determined to be 13 mm, which was significantly reduced during the extrusion to an average fiber length L_N = 2.92 mm. The average diameter of fibers was d = 14.5 μm. This corresponds to an aspect ratio of a_r = 201.4.

5.4.2. Experimental fiber orientation

Ortman et al. [11] used the micrographic technique of Hine et al. [19] for measurement of fiber orientation and reported fiber orientation data at radial locations in 10% increments of the total fill length starting from the gate of the center-gated disk. Three independent samples were cut and polished in the *r-z* plane to measure fiber orientation along the thickness at each radial location. The sample width was taken to be 5.5 mm and images were taken with an optical microscope on this sample width covering the thickness of the disk, which corresponds to an imaged area of 5.5 mm × 2.05 mm. The measurements of the elliptical footprints of the fibers in the *r-z* plane were used to determine the components of the orientation tensor **A**. The orientation data was then separated into 12 bins along the thickness to provide a profile of the orientation along the thickness of the disk.

Ortman et al. [11] have reported thickness-wise profiles of orientation at 11 radial locations, starting at the gate and moving out in the radial direction in 10% increments of the total fill length. The fill positions r/H = 12.46, 22.03, 31.60, 41.16 and 45.95, corresponding to 20%, 40%, 60%, 80% and 90% of total fill length are considered for comparison with the experimental data in the thickness direction. In order to understand the evolution of fiber orientation along the radial direction in different layers, radial profiles at z/H = 0.93, 0.8, 0.67, 0.40, 0.13 and 0.0 were selected. These layers at different z/H locations were selected because of presence of varying degrees of shear and extension. This has been done in order to understand the evolution of fiber orientation

along the radial direction in different layers which have varying degrees of shear and extension. The component of the orientation tensor along the main flow direction, A_{rr}, considered as representative of fiber orientation, is used for validation of all simulation results.

5.5 Results

Orientation predictions with the Bead-Rod model and the Folgar-Tucker model are compared with the experimental data of Ortman et al. [11]. Full thickness of the disk is simulated and all quantities are made dimensionless. The dimensions, non-dimensionalized by the half thickness H of the disk, are shown in Figure 5.2. A mesh with 300 elements in the r-direction and 30 elements in the z-direction is used. This mesh is an optimum mesh and provides sufficiently accurate results with computational efficiency [20].

5.5.1. Effects of fountain flow on fiber orientation

Decoupled fountain flow and decoupled Hele-Shaw simulations were performed with the Bead-Rod model using model parameters obtained by Ortman et al. [11] from rheological experiments in a sliding plate rheometer. Figure 5.3 shows orientation predictions with the fountain flow and Hele-Shaw flow simulations plotted against the measured orientation data along the thickness direction of the disk. Orientation predictions with fountain flow simulation match the predictions with Hele-Shaw flow approximation upto $r/H = 31.60$, which corresponds to 60% of the total flow length. Also, when compared against the experimental data, both the simulation schemes perform reasonably well throughout the thickness of the mold upto $r/H = 31.60$. However, as we get closer to the front, though the characteristic shell-core-shell layer structure is seen in the z/H-profiles, Hele-Shaw flow approximation over-predicts orientation near the walls at radial locations close to the front and does not match the drop in orientation near the walls. Fountain flow simulation, on the other hand, starts to show a drop in orientation near the walls, which is in qualitative agreement with the trend seen in experimental data. At $r/H = 45.95$, fountain flow shows very good agreement with the experimental orientation near the wall. However, the simulations predict a much narrower core layer at radial locations close to the front, while the experimental data shows a relatively wider core. Although the simulations show good agreement with the experimental data near $z/H = 0.0$, orientation in the transition region is overpredicted.

The radial evolution of fiber orientation and orientation predictions with the Bead-Rod model using the fountain flow simulation and Hele-Shaw flow approximation at selected z/H positions are shown in Figure 5.4. At $z/H = 0.93$, orientation predictions with both simulation

schemes match in the region near the gate and the lubrication region where the orientation data is relatively flat. The effect of fountain flow starts to appear at $r/H \sim 35$ after which fountain flow simulation predicts a drop in orientation values, qualitatively following the trend seen in the experimental data and is in very good agreement with the experimental data at $r/H = 45.95$. Hele-Shaw flow approximation, on the other hand, significantly over-predicts orientation in the region near the front as the predicted orientation values level off and do not show any drop.

In layers corresponding to a thickness location $z/H = 0.80$, fountain flow predicts a similar behavior as in the layer corresponding to $z/H = 0.93$ with a gradual drop in orientation, starting at around $r/H = 38$ followed by a steep drop very close to the front. This qualitatively matches the trend in experimental data while Hele-Shaw flow approximation over-predicts orientation in the region close to the front. However, the predicted drop in orientation with fountain flow simulation starts much further downstream when compared to the drop seen in the experimental data. In the layer at $z/H = 0.67$, the region of gradual orientation drop is smaller compared to layers close to the wall, and tends to get smaller towards the core, disappearing in the layers at $z / H \leq 0.4$. In the layers at $z / H \leq 0.4$, the effects of the fountain flow are observed only in a very thin region close to the front. Experimental data does not show a distinct drop in the region close to the front and both fountain flow simulation and Hele-Shaw flow approximation are able to capture the orientation evolution reasonably well.

5.5.2. Assessment of semi-flexible and rigid fiber models

Orientation predictions with the Bead-Rod model and the Folgar-Tucker model were assessed by comparing model predictions with the experimental data in both the thickness direction and the evolution of orientation along the radial direction. Figure 5.5 shows the comparison of orientation predictions with the Bead-Rod model and the Folgar-Tucker model along the thickness direction at selected radial locations. Both the models show the characteristic shell-core-shell layer structure and are able to predict the thickness-wise profiles reasonably well upto $r/H = 31.60$. At $r/H = 41.16$, both models show a decrease in orientation near the walls. However, the Bead-Rod model shows a local minimum in orientation at the walls while the Folgar-Tucker model shows a local minimum at $|z/H| \sim 0.8$, which is slightly away from the walls. At radial location $r/H = 45.95$, both models are in very good agreement with the experimental data close to the walls, at $|z/H| = 0.93$. Also, in the core layer, both models are in close proximity with the experimental data, at $z/H =$

0.0 and $|z/H| = 0.13$. However, both models predict a narrower core layer compared to a relatively wider core seen in the experimental data.

Figure 5.6 shows the comparison of orientation predictions with the Bead-Rod model and the Folgar-Tucker model along the radial direction at selected thickness-wise locations. The Bead-Rod model is able to predict the evolution of orientation in the lubrication region along the radial direction at $z/H = 0.93$ better than the Folgar-Tucker model. In the region upto $r/H = 31.6$, the Folgar-Tucker model slightly overpredicts the orientation while the Bead-Rod model is able to match the experimental evolution relatively well. The effects of the fountain flow are observed starting at approximately $r/H = 31.6$. There is a qualitative agreement between the predicted evolution of orientation with both models and experimental evolution in the region between $r/H = 31.6$ and $r/H = 41.16$. Both model predictions almost coincide in the region close to the front and show very good comparison with the experimental data at $r/H = 45.95$. In the layer corresponding to $z/H = 0.8$, Bead-Rod model again provides slightly better predictions than the Folgar-Tucker model in most part of the lubrication region. In the region close to the front, both the models predict a drop in orientation starting at $r/H \sim 38$ with the Folgar-Tucker model predicting a much steeper drop than the Bead-Rod model. In all other layers, there is no significant difference in orientation predictions with the two models and both the models capture the evolution of orientation relatively well in almost entire lubrication region with some discrepancies near the frontal region in the layer corresponding to $z/H = 0.4$. In the layer corresponding to $z/H = 0.0$, the Bead-Rod model performs slightly better than the Folgar-Tucker model starting at $r/H = 17$, which is in the lubrication region, upto $r/H = 45.95$, which is in the frontal region.

5.5.3. Bending predictions with the Bead-Rod model

The amount of fiber curvature induced as a result of rotary diffusion and the complex flow field present in the mold was determined by calculating $tr(\mathbf{B})$. Figure 5.7 shows the evolution of $-tr(\mathbf{B})$ along the radial direction at three thickness-wise locations, $z/H = 0.93$, $z/H = 0.40$, and $z/H = 0.0$. A value of $-tr(\mathbf{B}) = 1.0$ indicates straight fibers and a reduction in $-tr(\mathbf{B})$ indicates the extent of bending. Fiber bending is higher in the region near the gate with a maximum occurring near the walls. This is due to high shear rates $(\dot{\gamma})$ in the region near the gate close to the walls compared to other locations in the simulation domain. In the layer corresponding to $z/H = 0.93$, $-tr(\mathbf{B})$ reduced from 1.0 at the gate to a minimum of about 0.93 at $r/H \sim 3.6$. In the layers close to the center-line, the extent of bending is relatively smaller and is lowest in the layer corresponding to $z/H = 0.0$.

Fiber bending gradually diminishes with increasing radius in all the three layers and -*tr*(**B**)- converges to steady values which are close to 1.0.

5.6 Conclusions

Performance of the Folgar-Tucker model and the Bead-Rod model in injection molding was assessed against experimental long fiber orientation data obtained from a center-gated disk. Model parameters for both the models were obtained from a previous experimental study in which rheological response of the fiber suspension under startup of shear was used to determine model parameters. Fountain flow simulation performed significantly better than Hele-Shaw flow approximation in the region near the front as it showed the characteristic drop in orientation along the radial direction which was in qualitative agreement with the experimental data while Hele-Shaw flow approximation over-predicted the orientation in the region close the front. Along *z/H*-profiles, both simulation schemes predicted the typical shell-core-shell layer structure. However, at radial locations close to the front, fountain flow simulation showed the characteristic drop in orientation near the walls in *z/H*-profiles and the predicted values were closer to the experimental data. Hele-Shaw flow approximation, on the other hand, overpredicted orientation near the walls and did not show any drop close to the walls. Fountain flow simulations were performed with the Bead-Rod model and the Folgar-Tucker model to assess the performance of these models. Both the models predicted the characteristic shell-core-shell layer structure in *z/H*-profiles and predicted orientation was in good agreement with the experimental data upto $r/H = 31.60$. However, at radial locations close to the front, the predicted core layer was narrower compared to the core layer in the experimental data. Bead-Rod model performed better than the Folgar-Tucker model in the radial direction in most of the lubrication region, especially along the layers close to the walls and along the layers in the core region. Along the layers in the transition region, both models were able to predict experimental evolution reasonably well. Fiber bending was estimated through *tr*(**B**) and slight bending was observed in the gate region near the walls, where shear rates are higher compared to other locations.

5.7 Acknowledgements

The authors wish to gratefully acknowledge the financial support for this work from the Department of Energy and the National Science Foundation through grants no. No. DMI-0521918 and No. CMMI-0853537, respectively. Syed Mazahir also acknowledges the financial support

provided by Institute of Critical Technology and Applied Science (ICTAS) at Virginia Tech through the ICTAS Doctoral Scholars program.

5.8 References

[1] J.M. Crosby, Long-fiber molding materials, in: L.A. Carlsson (Ed.) Thermoplastic composite materials, Elsevier, Amsterdam, 1991, pp. 139-168.

[2] L.H.S. III, D.J. Klingenberg, Rheology of sheared flexible fiber suspensions via fiber-level simulations, Journal of Rheology, 47 (2003) 759-778.

[3] F. Folgar, C.L. Tucker, Orientation behavior of fibers in concentrated suspensions, Journal of Reinforced Plastics and Composites, 3 (1984) 98-119.

[4] G.B. Jeffery, The motion of ellipsoidal particles immersed in a viscous fluid, in: Proceedings of the Royal Society of London, Series A, The Royal Society, 1922, pp. 161-179.

[5] J. Wang, J.F. O'gara, C.L. Tucker, An objective model for slow orientation kinetics in concentrated fiber suspensions: Theory and rheological evidence, Journal of Rheology, 52 (2008) 1179.

[6] M. Sepehr, G. Ausias, P.J. Carreau, Rheological properties of short fiber filled polypropylene in transient shear flow, Journal of Non-Newtonian Fluid Mechanics, 123 (2004) 19-32.

[7] A.P.R. Eberle, G.M. Vélez-García, D.G. Baird, P. Wapperom, Fiber orientation kinetics of a concentrated short glass fiber suspension in startup of simple shear flow, Journal of Non-Newtonian Fluid Mechanics, 165 (2010) 110-119.

[8] H.M. Huynh, Improved fiber orientation predictions for injection-molded composites, in: MS Thesis, Universty of Illinois - Urbana Champaign,2001

[9] U. Strautins, A. Latz, Flow-driven orientation dynamics of semiflexible fiber systems, Rheologica Acta, 46 (2007) 1057-1064.

[10] K. Ortman, D. Baird, P. Wapperom, A. Whittington, Using startup of steady shear flow in a sliding plate rheometer to determine material parameters for the purpose of predicting long fiber orientation, Journal of Rheology, 56 (2012) 955-981.

[11] K. Ortman, D. Baird, P. Wapperom, A. Aning, Prediction of fiber orientation in the injection molding of long fiber suspensions, Polymer Composites, 33 (2012) 1360-1367.

[12] D.H. Chung, T.H. Kwon, Numerical studies of fiber suspensions in an axisymmetric radial diverging flow: The effects of modeling and numerical assumptions, Journal of Non-Newtonian Fluid Mechanics, 107 (2002) 67-96.

[13] D. Chung, T.H. Kwon, Invariant-based optimal fitting closure approximation for the numerical prediction of flow-induced fiber orientation, Journal of Rheology, 46 (2002) 169.

[14] G. Haagh, F. Van De Vosse, Simulation of three-dimensional polymer mould filling processes using a pseudo-concentration method, International Journal for Numerical Methods in Fluids, 28 (1998) 1355-1369.

[15] P. Lesaint, P.A. Raviart, On a finite element method for solving the neutron transport equation, in: C.d. Boor (Ed.) Mathematical aspects of finite elements, Academic Press, New York, 1974, pp. 89-123.

[16] C.-W. Shu, S. Osher, Efficient implementation of essentially non-oscillatory shock-capturing schemes, Journal of Computational Physics, 77 (1988) 439-471.

[17] W.R. Hwang, W.-Y. Kim, S.H. Kang, S.J. Kim, Direct simulations on 2D mold-filling processes of particle-filled fluids, Korea-Australia Rheology Journal, 21 (2009) 193-200.

[18] M. Doi, S.F. Edwards, The Theory of Polymer Dynamics, Oxford University Press, New York, 1988.

[19] P.J. Hine, N. Davidson, R.A. Duckett, A.R. Clarke, I.M. Ward, Hydrostatically extruded glass-fiber-reinforced polyoxymethylene. I: The development of fiber and matrix orientation, Polymer Composites, 17 (1996) 720-729.

[20] S.M. Mazahir, G.M. Vélez-García, P. Wapperom, D.G. Baird, Fiber orientation in the frontal region of a center-gated disk: Experiments and simulation, (submitted).

5.9 Figures

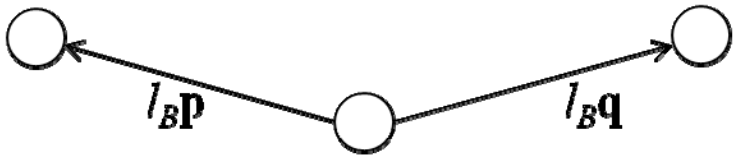

Figure 5.1 Bead-rod model proposed by Strautins and Latz [9] for semi-flexible fibers. Three beads are connected with two rods with length l_B and orientation vectors p and q.

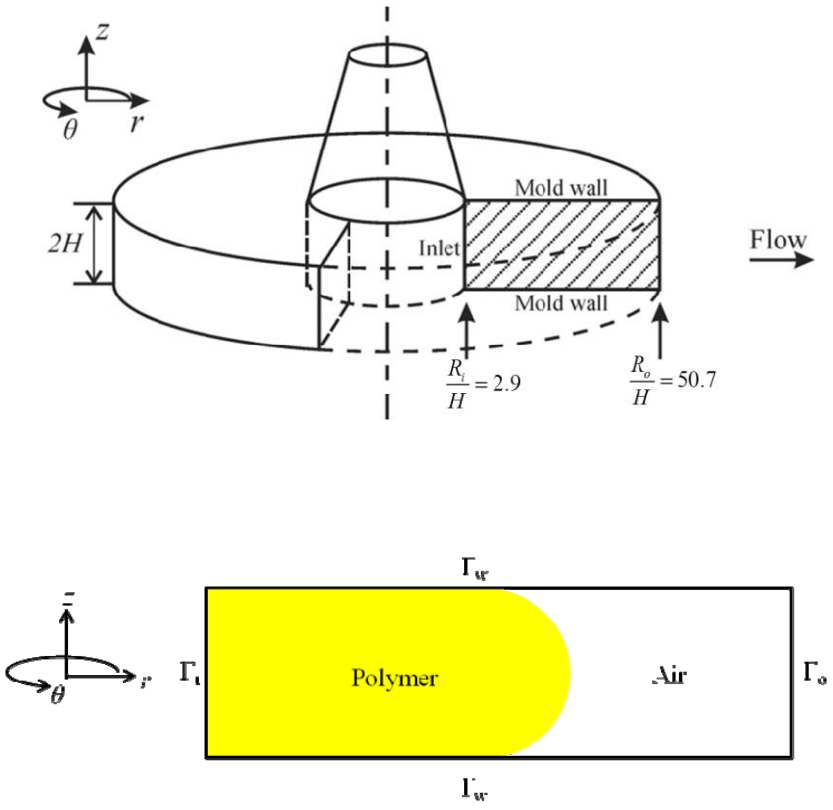

Figure 5.2 Center-gated disk with dimensions normalized by the half thickness H of the disk (a) and the simulation domain and boundaries (b).

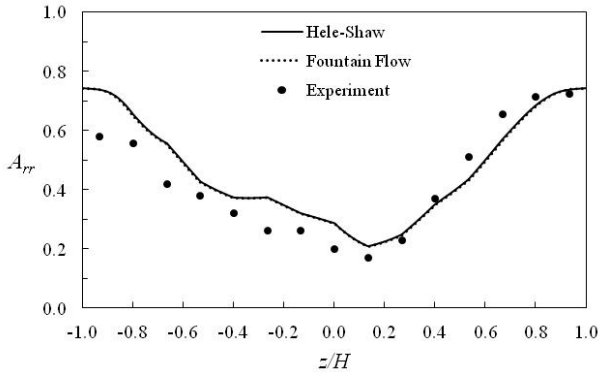
Hele-Shaw
Fountain Flow
Experiment
A_{rr}
z/H
1.0
0.8
0.6
0.4
0.2
0.0
-1.0 -0.8 -0.6 -0.4 -0.2 0.0 0.2 0.4 0.6 0.8 1.0

(a)

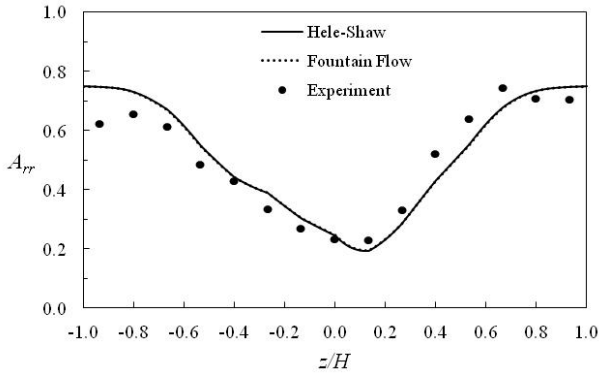
Hele-Shaw
Fountain Flow
Experiment
A_{rr}
z/H
1.0
0.8
0.6
0.4
0.2
0.0
-1.0 -0.8 -0.6 -0.4 -0.2 0.0 0.2 0.4 0.6 0.8 1.0

(b)

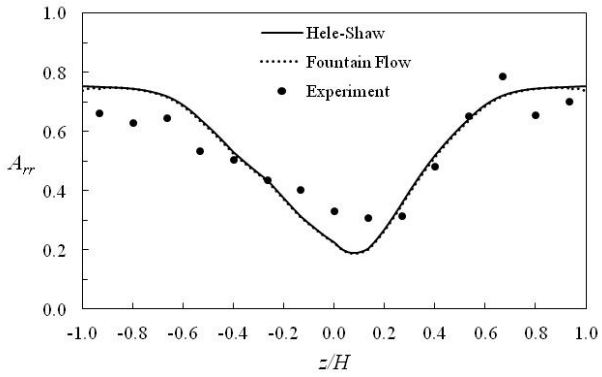
Hele-Shaw
Fountain Flow
Experiment
A_{rr}
z/H
1.0
0.8
0.6
0.4
0.2
0.0
-1.0 -0.8 -0.6 -0.4 -0.2 0.0 0.2 0.4 0.6 0.8 1.0

(c)

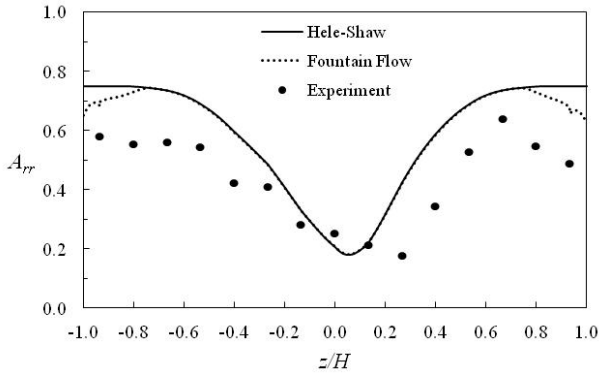

(d)

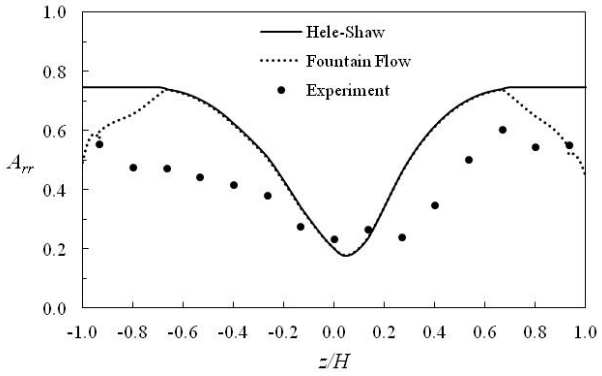

(e)

Figure 5.3 Comparison of A_{rr} predictions with the Bead-Rod model using fountain flow simulation and Hele-Shaw flow approximation along the thickness direction at radial locations (a) r/H = 12.46, (b) r/H = 22.03, (c) r/H = 31.60, (d) r/H = 41.16, and (e) r/H = 45.95.

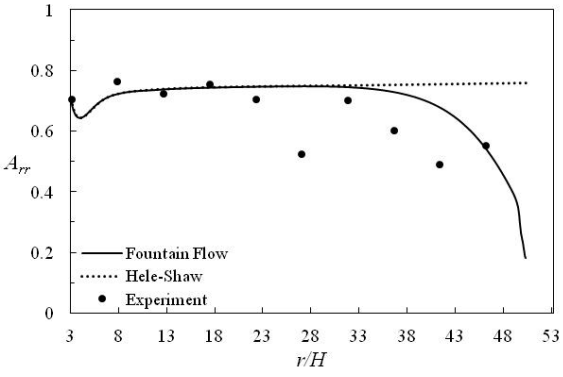

(a)

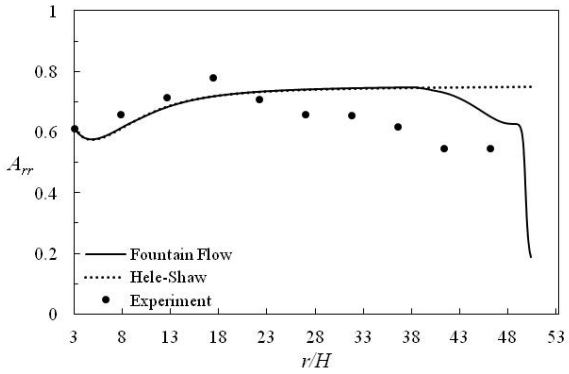
1
0.8
0.6
A_{rr}
0.4
0.2
0
3 8 13 18 23 28 33 38 43 48 53
r/H
Fountain Flow
Hele-Shaw
Experiment

(b)

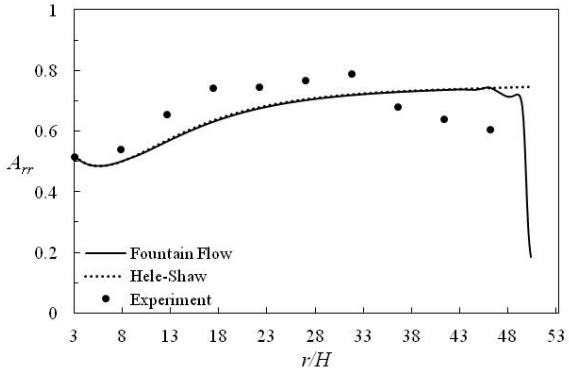
1
0.8
0.6
A_{rr}
0.4
0.2
0
3 8 13 18 23 28 33 38 43 48 53
r/H
Fountain Flow
Hele-Shaw
Experiment

(c)

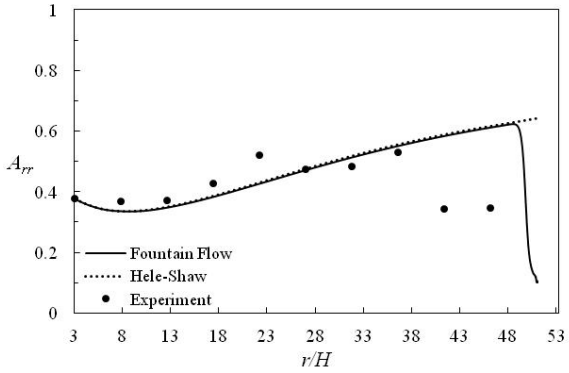
1
0.8
0.6
A_{rr}
0.4
0.2
0
3 8 13 18 23 28 33 38 43 48 53
r/H
Fountain Flow
Hele-Shaw
Experiment

(d)

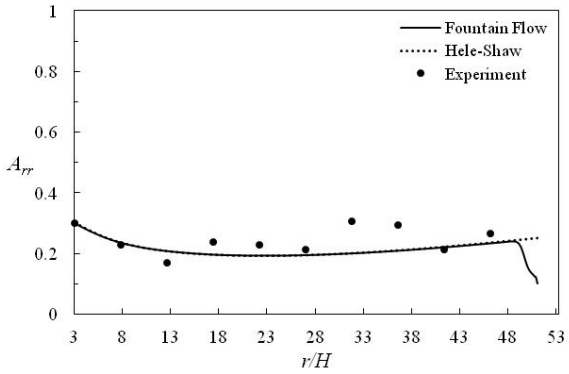

(e)

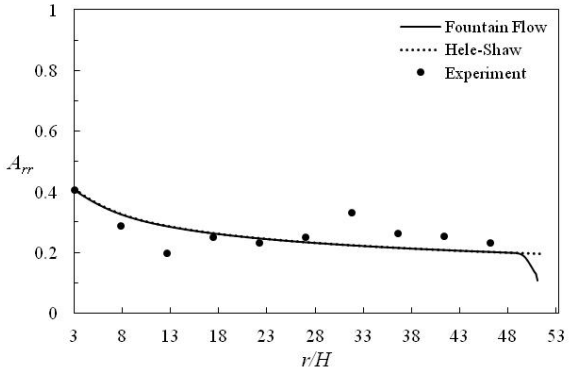

(f)

Figure 5.4 Comparison of A_{rr} predictions using the Bead-Rod model with the fountain flow simulation and Hele-Shaw flow approximation along the radial direction at thickness locations (a) z/H = 0.93, (b) z/H = 0.80, (c) z/H = 0.67, (d) z/H = 0.40, (e) z/H = 0.13, and (f) z/H = 0.0.

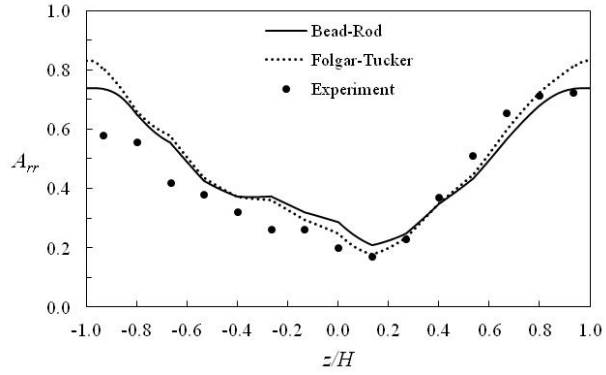

(a)

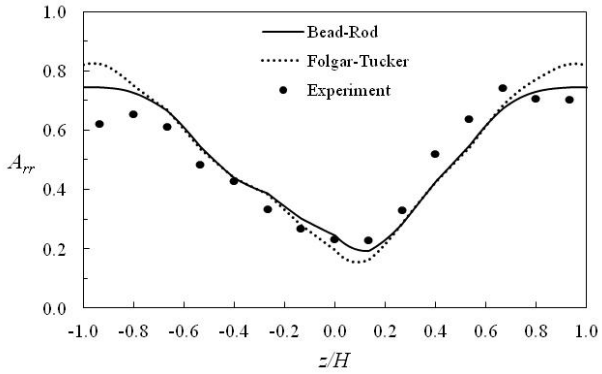
Bead-Rod
Folgar-Tucker
Experiment
A_{rr}
z/H

(b)

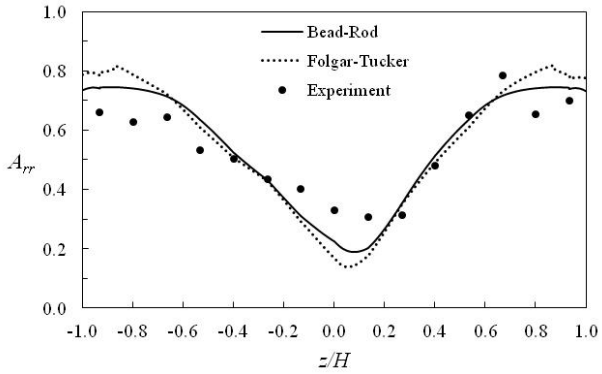
Bead-Rod
Folgar-Tucker
Experiment
A_{rr}
z/H

(c)

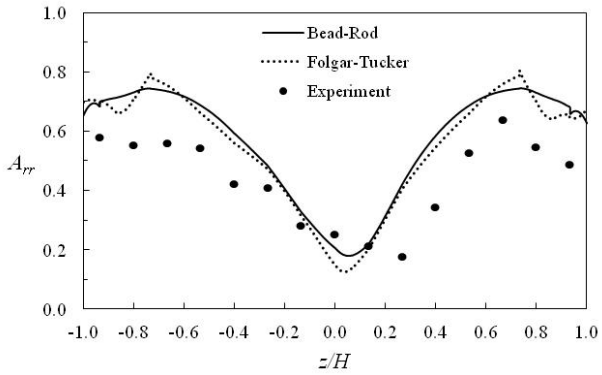
Bead-Rod
Folgar-Tucker
Experiment
A_{rr}
z/H

(d)

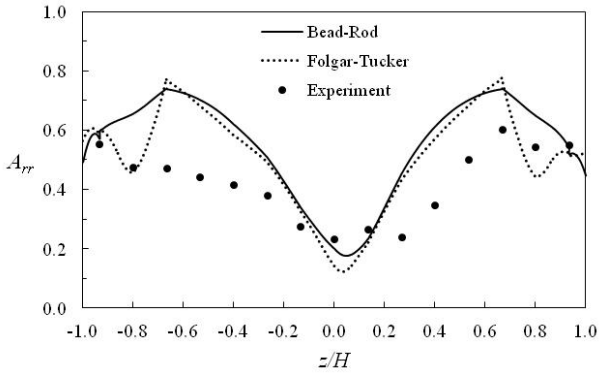

(e)

Figure 5.5 Comparison of A_{rr} predictions with the Bead-Rod model and the Folgar-Tucker model along the thickness direction using fountain flow simulation at radial locations (a) r/H = 12.46, (b) r/H = 22.03, (c) r/H = 31.60, (d) r/H = 41.16, and (e) r/H = 45.95.

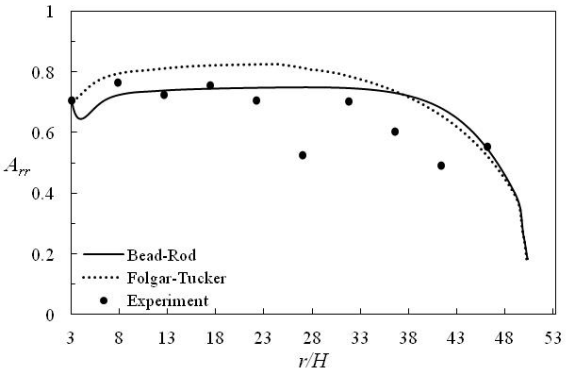

(a)

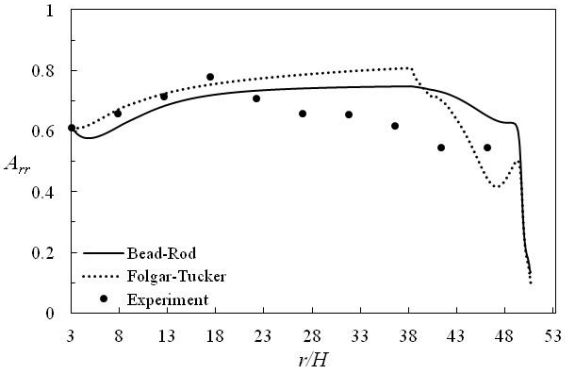

(b)

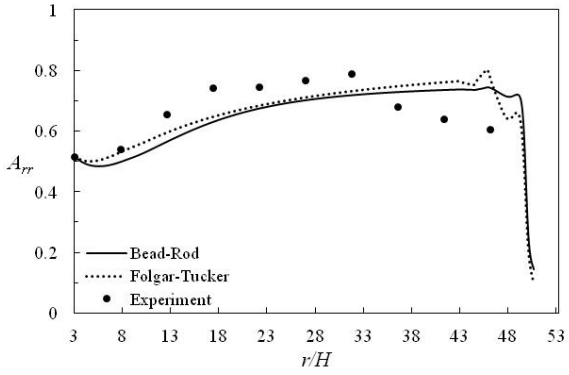
1
0.8
0.6
0.4
0.2
0
A_{rr}
Bead-Rod
Folgar-Tucker
Experiment
3
8
13
18
23
28
33
38
43
48
53
r/H

(c)

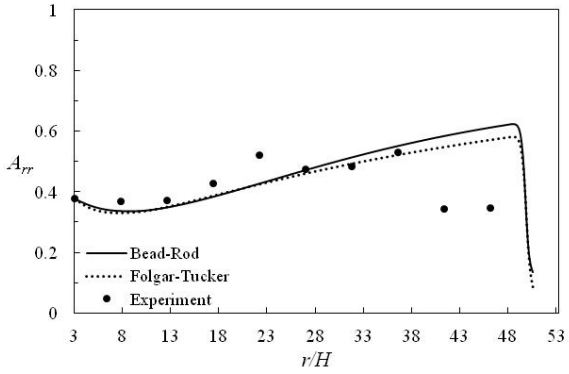
1
0.8
0.6
0.4
0.2
0
A_{rr}
Bead-Rod
Folgar-Tucker
Experiment
3
8
13
18
23
28
33
38
43
48
53
r/H

(d)

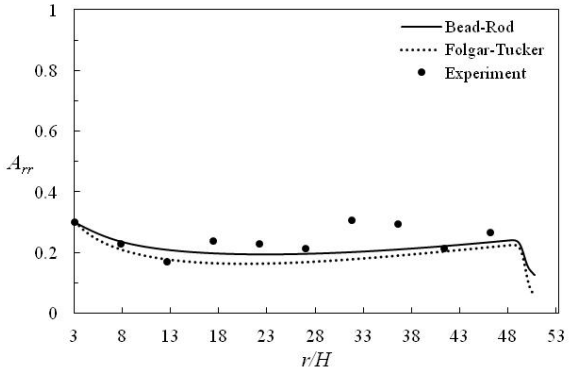
1
0.8
0.6
0.4
0.2
0
A_{rr}
Bead-Rod
Folgar-Tucker
Experiment
3
8
13
18
23
28
33
38
43
48
53
r/H

(e)

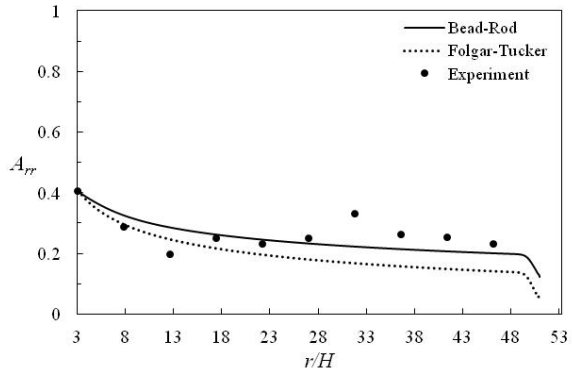

(f)

Figure 5.6 Comparison of A_{rr} predictions with the Bead-Rod model and the Folgar-Tucker model using fountain flow simulation scheme along the radial direction at thickness locations (a) z/H = 0.93, (b) z/H = 0.80, (c) z/H = 0.67, (d) z/H = 0.40, (e) z/H = 0.13, and (f) z/H = 0.0.

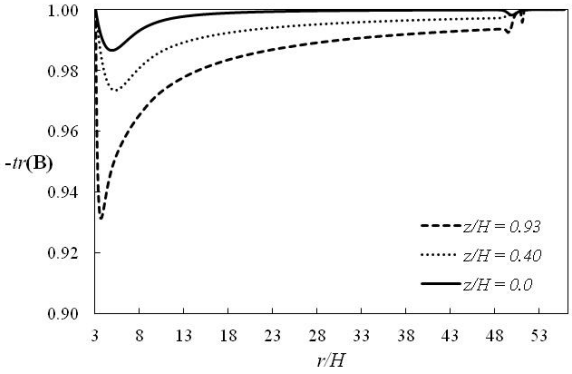

Figure 5.7 Bending predictions with the Bead-Rod model along the radial direction, estimated through |*tr*(B)|, at z/H = 0.93, z/H = 0.40, and z/H = 0.0.

CHAPTER 6. CONCLUSIONS

6.1 Conclusions

In this research work, fiber orientation predictions were validated against experimental data in a center-gated disk geometry. Experimental data was generated from center-gated disks which were injection molded with PBT 30 wt% short glass fiber suspension. Experimental measurements were made along the direction of the flow lines (r-direction) in the disk in order to characterize the evolution of fiber orientation during mold filling stage. The objective of measuring fiber orientation along the direction of flow was to understand the evolution of orientation along the entire fill length of the disk geometry. Experimental characterization of orientation evolution was done separately for the lubrication region and the frontal region using an improved version of the method of ellipses, which includes contributions of partially elliptical and rectangular objects, in addition to elliptical objects. The improved version also includes consideration of a shadow along the primary axis of the ellipses in order to eliminate the ambiguity problem of two fibers having identical cross sections in the plane of measurements but with orientations 180^{O} apart. In the lubrication region, fiber measurements were made at various radial locations along the entire fill length at three different z/H heights representative of the shell, transition and core layers, respectively. Experimental data near the gate showed high extension effects in all the three layers with a sudden drop in A_{rr} (and a corresponding increase in $A_{\theta\theta}$). This was followed by an increase in A_{rr} to steady levels due to relatively high shear along the shell and transition layers in the lubrication region. However, in the core layer, a continued effect of high extension was observed with orientation diminishing further with radial distance inside the mold.

In the frontal region, fountain flow plays a significant role on evolution of fiber orientation and the effects are localized within small radial distance of the front, which makes it critical to measure fiber orientation in greater detail in this region. Therefore, sampling bins were spaced closely apart in the radial direction in all three layers in the frontal region. Experimental data along the radial direction in the frontal region showed a drop in flow-direction component of orientation at all z/H heights with different characteristic shapes of orientation profiles at each height. Also, features such as shape and texture of the advancing front, evolution of the shell and core layers, and

presence of trapped air in the region were qualitatively studied by analyzing microscopic image of the frontal region. It was observed that the core layers grows in thickness towards the front as almost all fibers get oriented along the θ-direction.

First part of the simulation study focused on an assessment of slowdown in orientation by comparing model predictions of the standard Folgar-Tucker model with two other models, a delayed Folgar-Tucker model and reduced strain closure (RSC) model which predict slower evolution of orientation under transient shear conditions. Model predictions of these three orientation models were assessed in coupled and decoupled Hele-Shaw flow simulations against the experimental data along the direction of flow at three z/H heights in the lubrication region. Model parameters for all the orientation models were obtained independently from injection molding experiments by fitting model predictions to rheological data under startup of shear. A measured inlet orientation was used at the inlet of the mold to provide the correct starting values of orientation for an objective assessment of the slowdown in orientation evolution. Slow orientation models showed improvement over Folgar-Tucker model in the lubrication region of the core layer with no significant improvement in other regions. In the transition layer, slow orientation models slowed down the evolution of orientation compared to the standard Folgar-Tucker model. However, the experimental data showed a need for speeding up evolution instead of slowing it down. Effects of coupling on fiber orientation were also investigated. The effect of coupling with velocity in Hele-Shaw flow simulations was small. It was observed for the first time that measured inlet orientation results in an increase in maximum velocity at the center of the mold as compared to a drop in the maximum velocity with random inlet orientation, which has been the standard inlet condition used in most previous studies. However, with such minimal effects on velocity, coupled simulations showed insignificant differences in orientation predictions from decoupled simulations in all three layers. Near the front, orientation predictions with all the models leveled off to steady values and in Hele-Shaw flow simulations, none of the models was able to capture the drop in experimental orientation.

Second part of the simulation study focused on orientation predictions in the frontal region of a center-gated disk, covering a region from 90% of the total fill length to 99% of the total fill length inside the mold. Model predictions with the Hele-Shaw flow approximation and fountain flow simulation were compared and it was observed that the fountain flow simulation shows a drop in orientation in all the three layers, which is in qualitative agreement with the trend seen in the experimental data. Also, fountain flow simulations with all three orientation models showed the

characteristic drop, followed by a rise and then another drop in the shell layer which qualitatively agrees with the experimental data. Predictions with fountain flow simulation were in close proximity with the experimental data at 99% of the flow length in the transition layer and especially the core layer. Hele-Shaw flow approximation, on the other hand, significantly over-predicted orientation values in the entire frontal region and orientation leveled off at steady values without showing a drop in orientation in any layer. An assessment of the slowdown in orientation was carried out by comparing model predictions of the standard Folgar-Tucker model with the delayed Folgar-Tucker model and the RSC model in decoupled fountain flow simulations. It was observed that the delayed Folgar-Tucker model showed a slowdown in orientation in the shell layer, which was in relatively better agreement with the gradual drop observed in the experimental data. RSC model, on the other hand, did not show a significant slowdown in orientation in the shell layer. In the transition and core layers, however, none of the slow orientation models was able to achieve a slowdown in the evolution of orientation. All the three orientation models showed a drop in orientation near the front which was relatively fast as compared to the slow evolution in experimental data. Effects of coupling on fiber orientation were investigated and it was observed that coupling slows down the evolution of fiber orientation. However, in case of all the three orientation models, when model parameters determined from startup of shear were used, coupled simulations did not show any significant improvements over decoupled simulations. A smaller value of model parameter C_I , taken from a previous study was tried in coupled simulations and the predictions showed significant improvements in the frontal region. However, this value of C_I does not show good predictions in the lubrication region where C_I fitted from rheological data (in startup of shear) gives better predictions.

The objective of the third part of simulation study was to extend the numerical scheme developed for short rigid fiber systems to long semi-flexible fiber systems, for which the Bead-Rod model has been proposed. In this study, model parameters were obtained from an earlier experimental study in which rheological response of a semi-flexible fiber suspension under startup of shear was used to determine model parameters. Orientation predictions with the Folgar-Tucker model and the Bead-Rod model using decoupled fountain flow simulations and decoupled Hele-Shaw flow approximation were compared with the experimental data from an earlier study. When compared against the z-profiles of experimental data, fountain flow simulations were able to capture the characteristic drop in orientation near the walls while Hele-Shaw flow approximation over-predicted orientation in the region near the walls at radial locations near the advancing front.

However, in both simulation schemes, the predicted core layer at radial locations above 70% of fill length was narrow as compared to a much wider core seen in experimental *z*-profiles. The evolution of orientation in *r*-direction along the shell and core layers in the lubrication region was better captured by the Bead-Rod model as compared to the Folgar-Tucker model. In the region near the advancing front, both models predicted a drop in orientation near the front, which was in qualitative agreement with the *r*-profiles of experimental data. However, the predicted drop in orientation was relatively fast as compared to more gradual drop in orientation observed in experimental data. Bead-Rod model predictions were not significantly different from Folgar-Tucker model predictions in the region near the front.

6.2 Recommendations

In rigid fiber systems, the Folgar-Tucker model and its variations, namely the delayed Folgar-Tucker model and the RSC model have been shown to provide good agreement with experimental data in the lubrication region along the shell layer using model parameters determined from transient shear flow experiments. However, orientation predictions using model parameters from shear flow experiments do not capture the orientation profiles in the region near the advancing front. This is due to presence of high extension in this region which requires parameters determined from extensional flow experiments. Therefore, it is recommended to measure model parameters in extensional flow experiments for improvement in orientation predictions in the frontal region.

In semi-flexible fiber systems, experimental orientation data that is available has been measured using measurement techniques which were originally developed for short fiber systems. For semi-flexible fibers, which show bending, this method is not the most appropriate method and there is a need to improve experimental measurement techniques for semi-flexible fiber systems. Also, experimental data in the region near the front from 90% of the flow length to 99% of the flow length should be measured separately and coupled simulations with the Bead-Rod model along with model parameters determined from extensional flow experiments should be explored in this region. Another limitation with the long fiber systems is the fiber breakage inside the mold which results in a distribution of fiber length in the final part. Therefore, the Bead-Rod model should be tested with different fiber length distributions when comparing against experimental data from injection molded geometries.

APPENDICES

Appendix A: Solution scheme for orientation equations

The set of governing equations for the second order orientation tensor **A** is given by:

$$\begin{aligned} &\frac{\partial \mathbf{A}}{\partial t} + \mathbf{v}\cdot\nabla\mathbf{A} - c\mathbf{F}(\nabla\mathbf{v},\mathbf{A}) = \mathbf{0} \\ &\mathbf{A}(\Gamma_i, t) = \mathbf{A}_i \end{aligned} \tag{20}$$

where c is the pseudoconcentration variable, $\mathbf{F}(\nabla\mathbf{v},\mathbf{A})$ is the model-specific term, Γ_i is the inlet boundary of the simulation domain and $\mathbf{A}_i$ is the orientation state prescribed at the inlet boundary of the simulation domain. The orientation is determined in the entire simulation domain which consists of air as well as polymer. Therefore, distinction needs to be made between the polymer phase and air phase because we want to include the effects of the velocity gradient and fiber interaction on the orientation in the polymer phase but not in air. This distinction between the two phases is made by the pseudoconcentration variable c. In our numerical scheme, we multiply the model-specific term, $\mathbf{F}(\nabla\mathbf{v},\mathbf{A})$, with the pseudoconcentration variable c.

For rigid short glass fiber models, the model-specific term equals

Folgar-Tucker model:

$$\mathbf{F}(\nabla\mathbf{v},\mathbf{A}) = \left(\mathbf{W}\cdot\mathbf{A} - \mathbf{A}\cdot\mathbf{W}\right) + \lambda\left(\mathbf{D}\cdot\mathbf{A} + \mathbf{A}\cdot\mathbf{D} - 2\mathbf{A}_4 : \mathbf{D}\right) + 2C_I\dot{\gamma}\left(\mathbf{I} - 3\mathbf{A}\right) \tag{21}$$

Slip version of the Folgar-Tucker model:

$$\mathbf{F}(\nabla\mathbf{v},\mathbf{A}) = \alpha\left[\left(\mathbf{W}\cdot\mathbf{A} - \mathbf{A}\cdot\mathbf{W}\right) + \lambda\left(\mathbf{D}\cdot\mathbf{A} + \mathbf{A}\cdot\mathbf{D} - 2\mathbf{A}_4 : \mathbf{D}\right) + 2C_I\dot{\gamma}\left(\mathbf{I} - 3\mathbf{A}\right)\right] \tag{22}$$

RSC model:

$$\begin{aligned} \mathbf{F}(\nabla\mathbf{v},\mathbf{A}) = &\left(\mathbf{W}\cdot\mathbf{A} - \mathbf{A}\cdot\mathbf{W}\right) + \lambda\left(\mathbf{D}\cdot\mathbf{A} + \mathbf{A}\cdot\mathbf{D} - 2\left[\mathbf{A}_4 + (1-\kappa)(\mathbf{L}_4 - \mathbf{M}_4 : \mathbf{A}_4)\right] : \mathbf{D}\right) \\ &+ 2\kappa C_I\dot{\gamma}\left(\mathbf{I} - 3\mathbf{A}\right) \end{aligned} \tag{23}$$

The orientation evolution equations are discretized in space using the discontinuous Galerkin finite element method (DGFEM). These equations are hyperbolic in nature because of the presence of the convective term $\mathbf{v}\cdot\nabla\mathbf{A}$, and upwinding needs to be employed to get stable and convergent solutions for such systems. In the DGFEM method, the equations are solved separately on each element and a discontinuity is considered in the solution at inter-element boundaries to achieve necessary upwinding. The interpolation functions in the DGFEM are discontinuous across elements, which allows for discrete solution in each element. The advantage of this formulation is that at each time step, we solve for orientation values at the element level which significantly reduces the computational time and memory requirements as compared to the solution for the entire domain at once.

Spatial discretization

In the DGFEM formulation for the orientation equations, we start with the weak formulation on an element K in the simulation domain. With appropriate functional spaces for the test functions and the solution, the weak formulation for Eq. (13) on an element K is given by: Find **A** such that for all admissible weighting functions **Λ**:

$$\left\langle \frac{\partial \mathbf{A}}{\partial t}, \mathbf{\Lambda} \right\rangle_{\mathrm{K}} + \left\langle \mathbf{v}\cdot\nabla\mathbf{A}, \mathbf{\Lambda} \right\rangle_{\mathrm{K}} - \left\langle c\mathbf{F}(\mathbf{A}, \nabla\mathbf{v}), \mathbf{\Lambda} \right\rangle_{\mathrm{K}} = 0 \tag{24}$$

where $\langle \mathbf{P}, \mathbf{Q} \rangle_{\mathrm{K}}$ is proper L^2 inner product on the element domain Ω_{K}. In the numerical integration of Eq. (24), the pseudoconcentration variable c is calculated at every integration point, a correction is applied to it and the corrected value of c is multiplied with the model-specific term. The correction involves limiting the pseudoconcentration variable c in the range [0, 1]. This is done by making c = 1 if $c > 1$, and $c = 0$ if $c < 0$. This correction aims to eliminate non-physical values of c due to non-linear interpolation. The second step is integration by parts of the convective term:

$$\left\langle \mathbf{v}\cdot\nabla\mathbf{A}, \mathbf{\Lambda} \right\rangle_{\mathrm{K}} = \left\langle \mathbf{v}\cdot\mathbf{n}\mathbf{A}, \mathbf{\Lambda} \right\rangle_{\Gamma_{\mathrm{K}}} - \left\langle \nabla\cdot\mathbf{v}\mathbf{A}, \mathbf{\Lambda} \right\rangle_{\mathrm{K}} - \left\langle \mathbf{v}\mathbf{A}, \nabla\mathbf{\Lambda} \right\rangle_{\mathrm{K}} \tag{25}$$

where $\langle \mathbf{P}, \mathbf{Q} \rangle_{\Gamma_{\mathrm{K}}}$ is proper L^2 inner product on the element boundary Γ_{K}, and **n** is the outward unit normal along the boundary Γ_{K}. In the next step, parts of the element boundary Γ_{K} where $\mathbf{v}\cdot\mathbf{n} < 0$ are classified as inflow boundaries denoted by $\Gamma_{\mathrm{K,i}}$. Once the inflow boundaries of an element are identified, we impose weak inflow boundary condition in the boundary integral at the inflow

boundaries, which is given by $\mathbf{A} = \mathbf{A}_{\Gamma_{K,i}}$. The imposed boundary condition specified by $\mathbf{A}_{\Gamma_{K,i}}$ is the value of **A** along the inflow boundary in the neighboring upstream element or the inlet orientation $\mathbf{A}_i$ prescribed at the inlet boundary of the simulation domain. Finally, after integration by parts the weak formulation for the orientation equations with appropriate functional spaces for the test functions and the solution on an element K is given by: Find **A** such that for all admissible weighting functions **Λ**

$$\left\langle \frac{\partial \mathbf{A}}{\partial t}, \mathbf{\Lambda} \right\rangle_{\mathrm{K}} + \left\langle \mathbf{v} \cdot \nabla \mathbf{A}, \mathbf{\Lambda} \right\rangle_{\mathrm{K}} + \left\langle \mathbf{v} \cdot \mathbf{n}\left[\mathbf{A}\right], \mathbf{\Lambda} \right\rangle_{\Gamma_{K,i}} - \left\langle c\mathbf{F}(\mathbf{A}, \nabla \mathbf{v}), \mathbf{\Lambda} \right\rangle_{\mathrm{K}} = 0 \tag{26}$$

where $\left[\mathbf{A}\right] = \mathbf{A}_{\Gamma_{K,i}} - \mathbf{A}$. We use discontinuous quadratic polynomials for spatial discretization of orientation.

Time discretization

Discretization in time is performed with explicit third order accurate time variance diminishing scheme (RK3-TVD) with a fixed time step Δt. The scheme comprises three explicit Euler steps and two linear interpolation steps:

$$\begin{aligned}
&\mathbf{M}\left(\frac{\tilde{\mathbf{A}}^{n+1} - \mathbf{A}^{n}}{\Delta t}\right) = \mathbf{g}\left(c^{n+1}, \nabla \mathbf{v}^{n}, \mathbf{A}^{n}\right) \\
&\mathbf{M}\left(\frac{\tilde{\mathbf{A}}^{n+2} - \tilde{\mathbf{A}}^{n+1}}{\Delta t}\right) = \mathbf{g}\left(c^{n+1}, \nabla \mathbf{v}^{n+1}, \tilde{\mathbf{A}}^{n+1}\right) \\
&\tilde{\mathbf{A}}^{n+0.5} = \frac{3}{4}\mathbf{A}^{n} + \frac{1}{4}\tilde{\mathbf{A}}^{n+2} \\
&\mathbf{M}\left(\frac{\tilde{\mathbf{A}}^{n+1.5} - \tilde{\mathbf{A}}^{n+0.5}}{\Delta t}\right) = \mathbf{g}\left(c^{n+1}, \nabla \tilde{\mathbf{v}}^{n+0.5}, \tilde{\mathbf{A}}^{n+0.5}\right) \\
&\mathbf{A}^{n+1} = \frac{1}{3}\mathbf{A}^{n} + \frac{2}{3}\tilde{\mathbf{A}}^{n+1.5}
\end{aligned} \tag{27}$$

where **M** denotes the mass matrix and **g** is the force vector which comprises of the convection term and the model-specific term. The superscripts denote the time step and a tilda (˜) over a variable denotes the intermediate values determined locally within the Euler scheme. The values of c^{n+1} and $\nabla \mathbf{v}^{n+1}$ are known at time t^{n+1} because the pseudoconcentration and velocity equations are solved before the orientation equations. Pseudoconcentration variable is taken at time t^{n+1} in all three Euler steps because with this scheme, the orientation evolution and the evolution of the melt-air interface

always exactly match each other. In a test problem of pure convection of pseudoconcentration and orientation, this scheme shows exact match between the evolution of pseudoconcentration and orientation. In every Euler step, velocity gradient $\nabla \mathbf{v}$ is taken at the same time level as the orientation tensor **A** because they appear simultaneously in the model-specific term and their evolution in time has to match in each Euler step. Therefore, in the third Euler step, $\nabla \tilde{\mathbf{v}}^{n+0.5}$ at intermediate time step $t^{n+0.5}$ is determined as an intermediate value by linear interpolation between $\nabla \mathbf{v}^n$ and $\nabla \mathbf{v}^{n+1}$.

Orientation tensor correction

At each time step, after the orientation solution is determined, sometimes the values of the components of the orientation tensor **A** are physically unrealistic such as negative values or values greater than 1 that tend to introduce errors which build up over time. In order to eliminate these errors, we apply a correction to the orientation tensor at each time step. This correction involves making the orientation tensor positive definite and dividing the principal components of **A** by $tr(\mathbf{A})$ that limits the values to the range [0, 1].

Appendix B: Experimental orientation in the frontal region of a center-gated disk

Orientation along the radial direction at three different heights in the frontal region of a center-gated disk from the front to a distance r/H = -7.0 behind the front was measured in a short-shot disk. The measurements of the disk are available in section 4.2. A modified version of the method of ellipses (MoE) was used for orientation measurement. In this method, partially elliptical and rectangular footprints are also considered in addition to the elliptical footprints, and a shadow along the major axis of of elliptical or partially elliptical footprints is identified for determining the off-diagonal components of the orientation tensor. Measurements were made on optical images at 20X magnification in small rectangular bins with height $H/6$ and width $2l$, respectively, where H is half thickness of the disk and l is the average fiber length. The method is described in more detail in section 4.3.3.

Appendix B.1: Orientation along the radial direction at z/H = 0.75 (representative of the shell layer) in the frontal region from the front to a distance r/H = -7.0 behind the front

Flow length	***r/H* behind front**	A_{rr}	A_{zz}	$A_{\theta\theta}$	A_{rz}	$A_{r\theta}$	$A_{z\theta}$
90%	(7.0)	0.5200	0.0200	0.4600	0.0500	-0.0900	-0.0200
92%	(5.6)	0.7504	0.0176	0.2320	-0.0292	0.1914	-0.0097
93%	(4.9)	0.7023	0.0310	0.2666	0.0381	0.2114	0.0038
95%	(3.5)	0.5325	0.0548	0.4126	-0.0917	0.2871	-0.0252
97%	(2.1)	0.3577	0.0278	0.6145	-0.0408	0.3036	-0.0458
98%	(1.4)	0.2486	0.0445	0.7069	-0.0570	0.3039	-0.0835

Appendix B.2: Orientation along the radial direction at z/H = 0.42 (representative of the transition layer) in the frontal region from the front to a distance r/H = -7.0 behind the front

Flow length	***r/H* behind front**	A_{rr}	A_{zz}	$A_{\theta\theta}$	A_{rz}	$A_{r\theta}$	$A_{z\theta}$
90%	(7.0)	0.6400	0.0200	0.3400	0.0100	0.0100	0.0000
92%	(5.6)	0.5774	0.0364	0.3862	0.0132	0.1304	-0.0194
93%	(4.9)	0.4369	0.0414	0.5217	0.0428	0.2746	-0.0070
95%	(3.5)	0.2955	0.0591	0.6454	-0.0601	0.2473	-0.0936
97%	(2.1)	0.1915	0.0782	0.7303	-0.0895	0.2728	-0.1124
99%	(0.7)	0.0933	0.1734	0.7333	-0.0762	0.1885	-0.1204

Appendix B.3: Orientation along the radial direction at z/H = 0.08 (representative of the core layer) in the frontal region from the front to a distance r/H = -7.0 behind the front

Flow length	***r/H* behind front**	A_{rr}	A_{zz}	$A_{\theta\theta}$	A_{rz}	$A_{r\theta}$	$A_{z\theta}$
90%	(7.0)	0.2200	0.0300	0.7500	0.0000	0.0500	-0.0200
92%	(5.6)	0.1245	0.0334	0.8421	-0.0144	0.2325	-0.0177
93%	(4.9)	0.1074	0.0474	0.8452	-0.0146	0.1881	-0.0053
95%	(3.5)	0.0509	0.0773	0.8718	-0.0057	0.1764	-0.0241
97%	(2.1)	0.0782	0.0940	0.8278	-0.0284	0.2114	-0.0810
99%	(0.7)	0.0449	0.1822	0.7729	-0.0077	0.1356	-0.0574